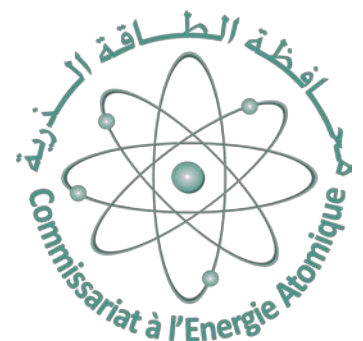




## Proceedings of the First International Conference and School on Radiation Imaging (ICSRI-2021)

---



SETIF, SEPTEMBER 26-30, 2021

---

Ferhat Abbas-Setif1 University-UFAS

Faculty of Sciences

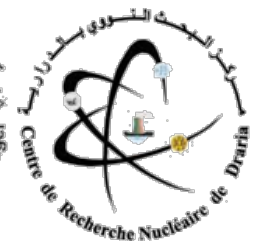
In partnership with the Atomic Energy Commission-COMENA

ALGERIA

Edited by: Prof. Fayçal KHARFI

# Proceedings of the First International Conference and School on Radiation Imaging

Setif, September 26-30, 2021



Editor

Pr. Fayçal KHARFI

Ferhat Abbas-Setif1 University, Algeria

Co-editor

Dr. Layachi BOUKERDJA

Nuclear Research Centre of Birine, Algeria

---

**LEGAL NOTICE:** Papers compiled in this volume are printed in a unique format keeping unaltered the content of the submitted manuscripts. Inclusions does not constitute endorsement by the editors or conference organizers. Readers should assume responsibility for any use to which the information is put.

**Proceedings of the First International Conference and School on Radiation Imaging (ICSRI-2021)**

Setif, Algeria

September 26-30, 2021

Edited by Pr. Fayçal KHARFI

2022 Ferhat Abbas-Setif1 University

Laboratory of Dosing, Analysis and Characterisation with high resolution

Campus El-Bèz, Setif-19000, Algeria

All rights reserved ©2022

**ISSN 2800-1362**

Printed in Algeria by Founoune Printing Press

---

## **Local Organizing Committee**

### **General Chair:**

Pr. Fayçal Kharfi (Ferhat Abbas-Setif1 University, Algeria)

### **Deputy Chair:**

Dr. Layachi Boukerdja (Nuclear Research Centre of Birine, Algeria)

### **Committee Members**

Dr. Belkhiat Djamel Edine Chouaib (Ferhat Abbas-Setif1 University, Algeria)

Pr. Azizi Hacene (Ferhat Abbas-Setif1 University, Algeria)

Pr. Moussaoui Adelouahab (Ferhat Abbas-Setif1 University, Algeria)

Dr. Hamici Melia (Ferhat Abbas-Setif1 University, Algeria)

Dr. Chouaba Seif Eddine (Ferhat Abbas-Setif1 University, Algeria)

Dr. Mosbah Ammar (Ferhat Abbas-Setif1 University, Algeria)

Dr. Khelfi Djilali (Atomic Energy Commission, Algeria)

Dr. Bilal Sari (Ferhat Abbas-Setif1 University, Algeria)

Mrs. Benachour Lilia (Ferhat Abbas-Setif1 University, Algeria)

## **Scientific Committee**

Pr. Atef El-Taher (Al-Azhar University, Eg)

Pr. Amrani Naima (Ferhat Abbas-Setif1 University, Dz)

Pr. Azizi Hacene (Ferhat Abbas-Setif1 University, Dz)

Pr. Babahenini Mohamed Chaouki (Biskra University, Dz)

Pr. Benamrane Nacéra (Oran Sciences and Technology Univesity, Dz)

Pr. Boucenna Ahmed (Ferhat Abbas-Setif1 University, Dz)

Pr. Bouchareb Yassine (Sultan Qaboos University, Om)

Pr. Bouyoucef Salahedine (Bab El Oued HUC, Dz)

Pr. Cherfa Yazid (SD-Blida University, Dz)

Pr. Djedi Nouredine (Biskra University, Dz)

Pr. Doghmane Nouredine (BM-Annaba University, Dz)

Pr. Draï Redouane (Research Centre on Industrial Technology, Dz)

Pr. Guemmmaz Mohamed (Ferhat Abbas-Setif1 University, Dz)

Pr. Hadid Abdenour (Oulu University, Fi)

Pr. Hachouf Fella (Constantine University, Dz)

Pr. Hamidatou Algham Lylia (Nuclear Research Centre of Birine, Dz)

Pr. Kambiz Shahnazi (PHIC, China)

Pr. Kharfi Fayçal (Ferhat Abbas-Setif1 University, Dz)

Pr. Maalej Nabil (King Fahd University PM, KSA)

Pr. Maouche Djamel (Ferhat Abbas-Setif1 University, Dz)

Pr. Merouani Hayet Farida (Annaba University, Dz)

Pr. Meziane Abdelkrim (CERIST, Dz)

Pr. Mimi Malika (Mostaghanem University, Dz)

Pr. Mongy Tarek (Egyptian Commission of Atomic Energy, Eg)

Pr. Moussaoui Adelouahab (Ferhat Abbas-Setif1 University, Dz)

---

Pr. Meriç Niyazi (Ankara University, Tr)  
Pr. Oussalah Mourad (Oulu University, Fi)  
Pr. Saint-Gregoire Jean-pierre (ASCA, Fr)  
Dr. Şahiner Eren (Ankara University, Tr)  
Pr. Schillinger Burkhard (TUM, De)  
Pr. Seghier Mohamed (ECAE, Abu Dhabi, UAE)  
Pr. Seghour Abdessalem (Nuclear Research Centre of Algiers, Dz)  
Pr. Taleb-Ahmed Abdelmalik (Valencienns University, Fr)  
Pr. Zaidi Habib (Geneva University Hospital, Ch)  
Dr. Zidi Tahar (Atomic Energy Commission, DZ)

---

## Preface

The International Conference and School on Radiation Imaging (ICSRI-2021) is a biennial scientific event organized by the dosing, analysis, and characterisation with high-resolution laboratory of Ferhat Abbas-Sétif1 university. The ICSRI-2021 was held for the first time at the University of Setif1. Setif is one of the most active and beautiful cities of Algeria. Due to the COVID-19 pandemic, the conference took place virtually while the school was face-to-face. This year scientists met to explore the development and application of radiation imaging and image processing in the domains of medicine and industry. As it is well known, radiation imaging is a field of science that cover a wide variety of disciplines such as imaging principles and methodologies, development of applications, imaging technologies, design of imaging systems...The recent progress in radiation imaging has been accelerated by advances in computer technology. Some imaging techniques are replacing other less efficient in terms of examination capability while some are able to provide almost perfect internal details with high contrast and resolution. As an example from medical imaging, techniques using radioisotopes provide functional and metabolic information that can be used to complement the morphological information provided by X-ray CT-scan. Image processing has always played a major role in the development and use of radiation imaging techniques. Image processing in radiation imaging is, indeed, a science field presenting up-to-date detailed treatment techniques and algorithms for the registration, segmentation, reconstruction, and evaluation of imaging data. The ICSRI-2021 was focused on all above-mentioned radiation imaging topics and moreover on: non-medical radiation imaging, imaging methods and systems development, radiation imaging simulation and modelling, molecular imaging and nuclear medicine, medical radiation imaging, advanced imaging methods, image processing, and imaging data analysis.

Ferhat Abbas-Setif1 University, Setif, Algeria, organized the ICSRI-2021 from 26 to 30 September 2021. The Algerian Atomic Energy Commission (COMENA) kindly supported the organisation of conference. The conference has included plenary sessions with conferences presented by eminent scientists, and orally and in poster sessions covering the different conference topics. The invited talks were selected to review recent advances in the different topics covered by the conference. The conference was followed by a three (3) days school for doctorate students and newly qualified academics and researchers in the field of radiation imaging and application. The program of the school included lectures and practical sessions on three topics: 1- 3D Tomography, 2- Scanning Electron Microscopy (SEM), and 3- Image processing in radiation imaging. Engineers, scientists and medical professionals from industry, government, healthcare and academia have used this opportunity to improve their technical skills and expand their knowledge in the field of radiation imaging and image processing by attending the school and interacting with experts. I would like to thank and highlight the outstanding efforts of the local organizing committee, the staff of Ferhat Abbas-Setif1 University, and the International scientific and advisory committee. Thanks are also extended to our partners: the Atomic Energy Commission (COMENA), the Nuclear Research Centre of Birine, the Nuclear Research Centre of Algiers (CRNA), and the Nuclear Research Centre of Draria (CRND), Algeria.

**Pr. Fayçal KHARFI**


General Chair of the ICSRI-2021 Conference  
Director of the School on Radiation Imaging and Image Processing

---







## The Editor

Prof. Fayçal Kharfi is Professor of Physics at the Department of Physics of Ferhat Abbas-Setif1 University. He teaches several courses on molecular imaging, computed tomography, radiation physics and application, and medical physics. He is also the actual Director of the Dosing, Analysis, and Characterisation with high resolution Laboratory (LDAC). The focus of his actual research activities is on ionizing radiation application. His research crosscuts a range of areas in radiation dosimetry, radiation therapy, computed tomography, archaeology, and nuclear medicine. His overarching goals are to understand how ionizing radiations act on matter and how they could effectively be applied for many purposes and applications such as therapy, and archaeological dating and imaging. He is an associated editor of the “Technology in Cancer Research & Treatment” SAGE journal. He published many research and educational works in various international journals, books, and conference proceedings. He is frequent reviewer, expert in radiation application, and member of many international associations such as the international society of neutron radiography (ISNR) and the international association on engineers (IAENG). He supervised many doctorate thesis and research projects in the fields of radiation dosimetry and application, radiation therapy, and medical imaging. He contributes to the organisation of numerous national and international conferences and workshops on medical physics and radiation application.





**First International Conference and School on  
Radiation Imaging (ICSRI - 2021)**  
26 - 30 Septembre 2021, Setif, Algeria




---

## Content

Breast cancer classification .....	10
Applications of artificial intelligence in radiation therapy .....	20
Performance of machine learning for face recognition .....	25
Convolutional neural network for detecting alzheimer’s disease in the early stages from magnetic resonance imaging .....	29
A robust deep model based on the attention mechanism for the classification of x-ray images chest of covid-19’s patients .....	33
Intelligent vision navigation of pioneer 3-dx mobile robot .....	42
Multi-agents segmentation for mammography .....	54
Segmentation of MRI images by the algorithm FPSO-FPCM for detection of multiple sclerosis .....	60
Evaluation of effective delivered dose from computed tomography head scans by OSL&TL dosimetry .....	73
Simulation of dynamic 18FDG-PET images for lesion detectability investigation using kinetic modeling and 4D-XCAT phantom .....	85
Commissioning of a brachytherapy treatment planning system and its validation with Gafchromic film EBT3 using 2D gamma index distribution .....	90
Monte-Carlo code for modeling and simulation of tomographic image .....	93
Neutron imaging denoising with a deep learning method .....	101
Neutron beam characterization at the neutron radiography facility of Es-Salam research reactor by SCALE 6.1 simulations .....	108
Neutron irradiation effects on topological properties of CZ-Silicon .....	112
Overview of tracers’ techniques using in CFD modeling of boron behaviour and pressurized thermal shock .....	116



2021

## Breast cancer classification

Ahmed Zoubir Messalti<sup>a,\*</sup>, Sadik Bessou<sup>a</sup>

<sup>a</sup>Department of Computer Science, University of Farhat Abbas Sétif1, Sétif-19000, Algeria

**ABSTRACT:** Worldwide, breast cancer is the most common type of cancer in women and the second highest in terms of mortality. Diagnosis of breast cancer is performed when an abnormal lump is found (from self-examination or x-ray) or a tiny speck of calcium is seen (on an x-ray). After a suspicious lump is found, the doctor conduct a diagnosis to determine whether it is cancerous and, if so, whether it has spread to other parts of the body. In this research, we trained five different classifier models to develop a benchmark breast cancer classification where we have adopted two different sub-tasks, in which we used the breast cancer dataset obtained from the University of Wisconsin Hospital at Madison, USA, which has a large number of features. Not all of the features we find in the dataset are helpful in building an Artificial intelligence (AI) model to make the necessary prediction. Using certain features can make predictions worse. Therefore, the selection of features plays a huge role in building a machine-learning model. In this work, we explore the correlation metric to choose the right features in building a High accurate model. The following study provides very good results, the best model as found in our experiment is the random forest model with the use of correlation matrix to extract the best features, and it gives a prediction accuracy equal to 97, 59%.

**Keywords:** Machine learning; Classification; breast cancer; X-ray; Artificial Intelligence.

## INTRODUCTION

Medical images are an important means to assist doctors in making judgments. It is certainly one of the fields of medicine that has undergone a real revolution over the past twenty years. These recent findings not only allow for better diagnosis but also offer new hope for treatment for many diseases like breast cancer, which is the most common type of cancer worldwide. Breast cancer has now surpassed lung cancer as the leading cause of global cancer incidence in 2020, with an estimated 2.3 million new cases, representing 11.7% of all cancer cases (as shown in Fig. 1-A). It is the fifth leading cause of cancer mortality worldwide, with 685,000 deaths (as shown in Fig.1-B). Among women, breast cancer accounts for 1 in 4 cancer cases and for 1 in 6 cancer deaths, ranking first for incidence and mortality in the vast majority of countries<sup>1</sup>. These figures show the importance of early detection of this disease, and its late diagnosis often results in cumbersome, mutilating and expensive treatment with a high mortality rate. This study aims to develop a benchmark Breast cancer classification based on Wisconsin

(Diagnostic) Data Set, and to apply existing approaches on the proposed data to predict if a given set of symptoms lead to breast cancer. The task is often a classification problem where the classes are simply benign/maligned; In addition to classification techniques, as well some machine learning algorithms, we rely on feature extraction and selection, which are important steps in breast cancer detection and classification. An optimum feature set should have effective and discriminating features, while mostly reduce the redundancy of features pace to avoid “curse of dimensionality” problem. The “curse of dimensionality” suggests that the sampling density of the training data is too low to promise a meaningful estimation of a high dimensional classification function with the available finite number of training data. For some advanced classification methods, such as artificial neural network and support vector machine, the dimension of feature vectors not only highly affects the performance of the classification, but also determines the training time of the algorithm. Thus, how to extract useful

features and make a good selection of the features is a crucial task for an AI model.

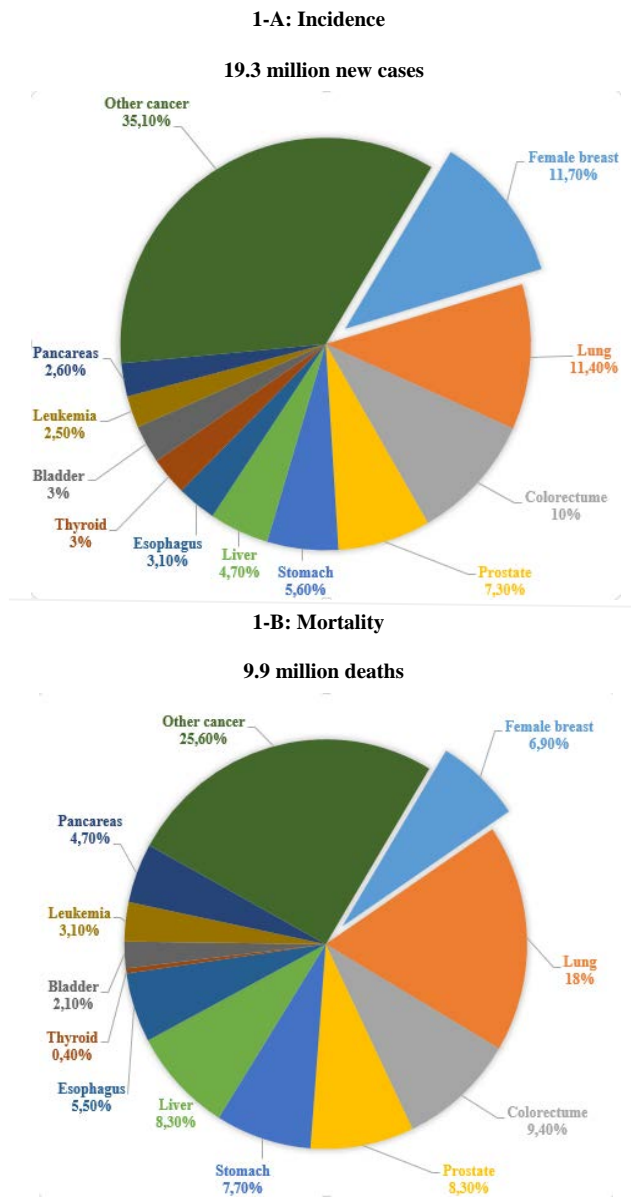


Fig. 1 Distribution of Cases and Deaths for the Top Most Common Cancers in 2020<sup>1</sup>

## BACKGROUND

Conventional methods of monitoring and diagnosing the diseases rely on detecting the presence of particular signal features by a human observer. Due to large number of patients in intensive care units and the need for continuous observation of such conditions, several computer aided-diagnosis (CAD)

approaches for automated diagnostic systems have been developed in the past years to attempt to solve this problem. Among these systems, we find<sup>2</sup>:

- Image Checker M1000, from the company R2 technology (FDA approved in June 1998, CE marked).
- Second Look, from CADX Medical Systems (request for approval FDA registered, CE marked).
- Mammex TR, from Scanis (FDA approval request filed, CE marked).

Such techniques work by transforming the mostly qualitative diagnostic criteria into a more objective quantitative feature classification problem. Fig.2 illustrates the high-level decomposition of automatic detection processes. In certain cases, a pre-processing of the data making it possible to highlight the sought signs can be used.

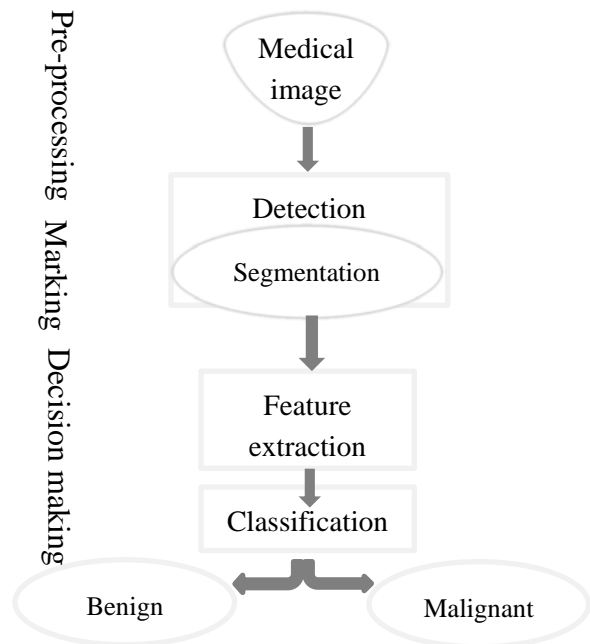


Fig. 2 General Diagram of a detection chain for micro calcifications in the medical image

### Pre-processing

The approach commonly used in image processing is to work on the histogram in order to define a transfer function on the gray levels to highlight the details present in the image. Other methods have also been proposed such as the use of sharpening filters<sup>3</sup>, or even the removal of the background of the image<sup>4</sup>. The latter approach involves subtracting a low pass filtered version of the original image.

## **Marking**

### **Detection of micro calcifications**

The first class of radiological signs that are looked for are the foci of micro calcifications. In fact, since calcium clumps are made up of small, contrasting objects, this kind of approach seems to have real potential. For example,<sup>5</sup> propose to model the problem as the detection of Gaussian objects in Markovian noise using a filter bank decomposition. Another approach consists in carrying out a filtering with a Mexican hat in order to measure the contrast of structures of dimension compatible with the core of the filter<sup>6</sup>. Other formalisms are also possible, so we can find the use of fuzzy logic for the detection of calcifications<sup>7-8</sup> or even approaches using filtering of the dynamics of the image using mathematical morphology tools<sup>9</sup>.

### **Opacity detection**

Detecting opacities is a little more complex than for micro calcifications, especially because of the variability that exists between different types of tumor.

### **Extraction of markers**

Detecting areas of over-density is a first step in detecting suspicious areas in the breast. Thus<sup>10</sup> propose to use a measurement of detection of over densities by calculating the proportion of pixels located around a lesion, which have an intensity lower than the minimum of the intensity inside. With the same aim of detecting over-densities, other approaches attempt to detect contrasting areas using a Mexican hat in the same way as for micro calcifications. However, this kind of approach does not seem to be well suited to the size of the objects to be detected<sup>11</sup>. Indeed, an opacity is generally much more extensive than a micro calcification, with a greater variability in terms of shape. <sup>12</sup>Proposed the use of mathematical morphology tools for the automatic extraction of opacities.

### **Segmentation**

It is necessary to extract the form of lesion potentially detected. The simplest approaches rely on global image thresholds <sup>13</sup>an iterative algorithm has been developed for the automatic detection of masses in mammograms.

### **Decision-making**

Decision-making is generally made after a characterization step. From a high-level point of view, we take measurements from the results of detection and / or segmentation (depending on whether we are working on micro calcifications or opacities) in order to subsequently take a decision to using standard classification methods.

### **Feature extraction**

In the case of micro calcifications, a preliminary characteristic

extraction step is therefore require<sup>14</sup>.

Among these characteristics, one can find those which relate to the texture such as the analysis of the neighboring regions, the spatial dependence of the levels of gray, the statistics of lengths on the levels of gray or the difference of levels of gray<sup>15</sup>. Regarding opacities, the first class of characteristics used is based on the shape of the object. We can cite for example the compactness, the Ferret report, or the perimeter. An important characterization of certain lesions is the presence of spicules at the level of their periphery. To consider this, a series of measurements to assess how well the lesion is speculated have also been proposed. They are essentially based on the analysis of the local orientations of the contours. These orientations can for example be obtained from a wavelet decomposition<sup>16</sup>. On the same principle, works propose to evaluate the complexity of a contour by fractal analysis<sup>17</sup>. The information provided by the association of contour and image content can also be exploited by extracting and analyzing a more or less wide band that follows the contour of the lesion<sup>18</sup>. This strip is usually stretched to make the contour linear before fractal analysis.

The information provided by the association of contour and image content can also be exploited by extracting and analyzing a more or less wide band that follows the contour of the lesion .This strip is generally stretched so as to make the outline linear before analysis. The analysis is done by extracting measurements on this band, such as studying the orientations of the contour<sup>19</sup>. This type of approach is therefore dependent on the contour, so the measurements obtained are strongly linked to the characteristics of the segmentations considered. For example, if you use an outline that follows the spicules well, the spicules appear linearly in the band image.

### **Classification of anomalies**

The purpose of the classification step is to give the final answer on what is detected and considered to be a sign of injury. The idea is to combine the information extracted previously to get a decision. You can see this in a similar way to what the radiologist does to make his decision.

The classification phase uses the supervised classification tools of artificial intelligence. Techniques such as neural networks (RN), fuzzy logic (FL), support vector machines (SVM), and nearest neighbor type methods are most commonly used. The work related to this field is outlined shortly as follows.

In<sup>20</sup>, Vikas Chaurasia and Saurabh Pal achieve accuracy of (96.84%) using SVM-RBF kernel in Wisconsin Breast Cancer (original) datasets. They obtained this result after comparing the performance criterion of supervised learning classifiers such as Naïve Bayes, SVM-RBF kernel, RBF neural networks.

In<sup>21</sup>, Authors show that each algorithm performs in a different way depending on the dataset and the features selection, to find

the best classifier in breast cancer datasets. SVM using Gaussian kernel is the most suited technique for recurrence/non-recurrence prediction of breast cancer.

In<sup>22</sup>, an optimized KNN model is proposed for breast cancer prediction using a grid search approach for searching the best hyper-parameter. The result shows that the performance significantly improves when best hyper parameter or K value is used for training the KNN. The performance of the KNN with default parameters is 90.10%. Better breast cancer detection accuracy is achieved by the KNN using best hyper-parameter or K value is chosen using a grid search approach when the algorithm is trained and the highest performance achieved using hyper-parameter tuning is 94.35%.

## EXPERIMENTAL

In this section, we describe the used dataset as well as the main steps of pre-processing and feature extraction, the development tools and environment, the proposed approaches and algorithms.

### Dataset

The real-world databases for this study come from the field of pathology, regarding the cytodiagnosis of breast cancer (Fig.3) using a technique called fine-needle aspiration of the breast lesion (FNAB).

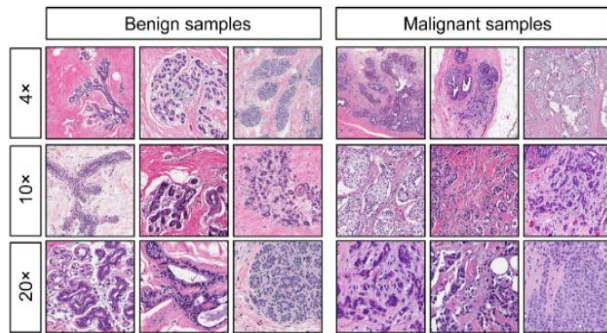


Fig .3 FNA result for benign and malignant tumor under the microscope

The original dataset was obtained by Dr. William H. Wolberg, physician at the University of Wisconsin Hospital at Madison, Wisconsin, USA<sup>23</sup>.

To create the dataset Dr. Wolberg used fluid samples, taken from patients with solid breast masses and an easy-to-use graphical computer program called Xcyt 7, which is capable of perform the analysis of cytological features based on a digital scan.

The dataset contains 569 instances, with benign 357 (62.75%) and 212 (37.25%) malignant cases (as shown in fig.4).

The Dataset has 10 principal attributes described as following:

- *Radius*: mean of distances from center to points on the perimeter.
- *Texture*: standard deviation of gray-scale values.
- *Perimeter*: The total distance between the snake points constitutes the nuclear perimeter.
- *Area* : Number of pixel on the interior of the snake and adding one-half of the pixel in the perimeter.
- *Smoothness*: Local variation in radius lengths.
- *Compactness*:  $\text{Perimeter}^2 / \text{area}$ .
- *Concavity*: Severity of concave portions of the contour.
- *Concave points*: Number of concave portions of the contour.
- *Symmetry*: The length difference between lines perpendicular to the major axis to the cell boundary.

*Fractal dimension*: Coastline approximation. A higher value corresponds to a less regular contour and thus to a higher probability of malignancy.

For each of the 10 features, there are three numerical variables, representing the mean, the standard deviation and the “worst” (mean of three largest values).

As well to the previous features, we find in the studied data set: The very first feature is the patient *ID*. For building a predictive model, this feature is irrelevant and therefore is discarded. The second variable, *diagnosis*, is binary and categorical with the values B (benign) and M (malignant).

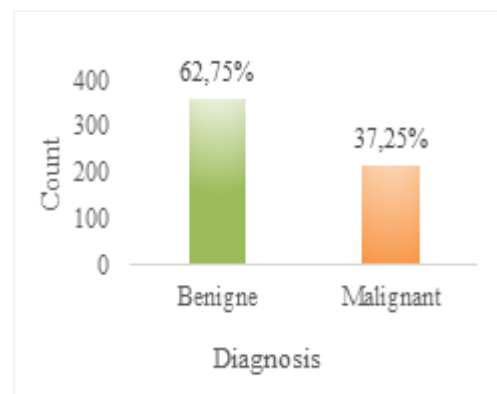


Fig.4 Standard dataset statistics

**Data availability:** The Wisconsin Diagnostic Breast Cancer dataset was obtained from the UCI machine-learning depository (available at: <http://archive.ics.uci.edu/ml>).

## ***Development Environment***

In this section, we present the different frameworks used to develop and execute our proposed models and approaches.

### ***Python***

Python is an interpreted high-level programming language released in 1991 by Guido van Rossum. It is widely used in all types of disciplines such as general programming, web development, software development, data analysis and machine learning due to its multi paradigm, which include functional, procedural, object-oriented programming<sup>24</sup>.

### ***Jupyter***

The Jupyter Notebook is an open source application that enables users to create interactive, shareable notebooks that contain live code, equations, visualizations, and text<sup>25</sup>.

### ***Pandas***

Pandas is a Python package providing fast, flexible, and expressive data structures designed to make working with “relational” or “labeled” data both easy and intuitive. It aims to be the fundamental high-level building block for doing practical, real world data analysis in Python<sup>26</sup>.

### ***Sklearn***

Scikit-learn is a free Python library dedicated to machine learning. It is intended to connect to the Python NumPy and SciPy computer and logical libraries. Simple and successful devices for data mining and data analysis. It is open to all and reusable in different contexts<sup>27</sup>.

### ***Matplotlib***

Matplotlib is a python 2D plotting library that produces publication quality figures in a variety of hardcopy formats and interactive environments across platforms. Matplotlib can be used in Python scripts, the Python and IPython shells, the Jupyter notebook, web application servers, and four graphical user interface toolkits.

### ***Seaborn***

Statistical data visualization is a Python visualization library based on Matplotlib. It provides a high-level interface for drawing attractive statistical graphics.

### ***Time***

The Python time module provides many ways of representing time in code, such as objects, numbers, and strings. It also provides functionality other than representing time, like waiting during code execution and measuring the efficiency of your code.

## ***Algorithms***

We used five different types of classification models: Support

Vector Machines, Random forest, Naïve-Bayes, Logistic regression and k-Nearest Neighbor.

Our choice of models for this study is partially motivated by the list of benchmark models outlined in the previous section. What follows is a short description of these classification model types and their specific implementations for this research.

### ***Logistic-Regression***

The application of the Logistic regression model has featured prominently in many domains such as the biological sciences. The Logistic regression algorithm is used when the objective is to classify data items into categories. Usually in logistic regression, the target variable is binary, which means that it only contains data classified as 1 or 0, which in our case refers to a patient that is positive or negative for diabetes. The purpose of our logistic regression algorithm is to find the best fit that is diagnostically reasonable to describe the relationship between our target variable and the predictor variables.

### ***Support Vector Machines***

Support Vector Machines is a widely used as supervised learning technique that is remarkable for being practical and theoretically sound, simultaneously. The approach of SVM is rooted in the field of statistical learning theory, and is systematic: e.g., training a SVM has a unique solution (since it involves optimization of a concave function).

### ***Random Forest***

Random forest is an ensemble method that creates many independent decision tree classifiers trained on different bootstrapped resamples of training data and then allows them to ‘vote’ on unseen data, which is an idea behind bagging. This trick allows dealing with overfitting that regular decision trees are prone to, by reducing variance of the model and therefore increasing its performance.

### ***Naïve-Bayes***

Naive Bayes classifier uses training data and Bayes’ theorem to assign a probability that an unseen data point belongs to each possible class. This classifier is very fast and simple, but it usually provides poor classification performance, partially because of its assumption of feature independence, which is very strong and is seldom true in real life applications.

### ***K-Nearest Neighbor***

The K-Nearest Neighbor is a learning method bases on instances that does not required a learning phase it is one of the most used algorithms in machine learning. The training sample, associated with a distance function and the choice function of the class based on the classes of nearest neighbors is the model developed. Before classifying a new element, we must compare it to other elements using a similarity measure. Its k-nearest neighbors are

then considered, the class that appears most among the neighbors is assigned to the element to be classified. The neighbors are weighted by the distance that separate it to the new elements to classify.

**Techniques**

In this section, we discuss some of the accompanying techniques of machine learning algorithms in building an IA model.

**Correlation**

Correlation is a statistical term, which in common usage refers to how close two variables are to having a linear relationship with each other. Features with high correlation are more linearly dependent and hence have almost the same effect on the dependent variable. Therefore, when two features have high correlation, we can drop one of them.

**Cross-validation**

Cross-validation is one of the most important techniques used for evaluate machine learning classifier. The classifier’s evaluation is most often based on prediction model accuracy. The K-fold cross validation algorithm works as follows (Fig. 5).

The training set is divided into mutually exclusive and equal-sized subsets and for each subset; the classifier is trained on the union of all the other subsets. The average of the error rate of each subset is therefore an estimate of the classifier error rate<sup>28</sup>.

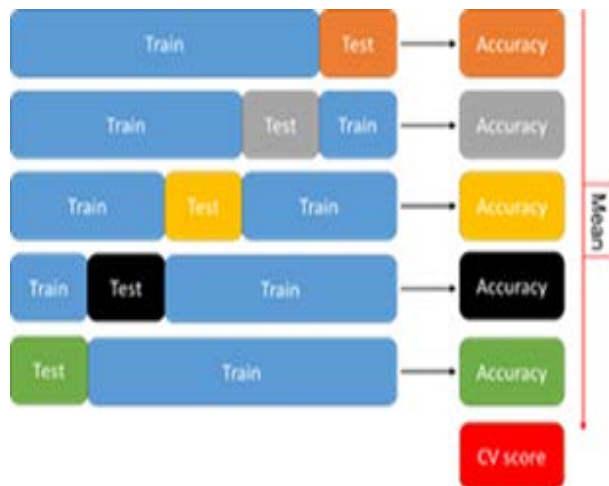


Fig. 5 Crosse validation

**Measures for performance evaluation**

Confusion matrix is a way to summarize classifier performance. Thus, we used it to measure our models performance. Figure 6 shows a basic representation of a confusion matrix.



Fig. 6 The confusion matrix

A confusion matrix for actual and predicted class is formed comprising of TP, FP, TN, and FN to evaluate the parameter. The significance of the terms is given below.

*True positive:* Sick people correctly diagnosed as sick TP.

*False positive:* Healthy people incorrectly identified as sick FP.

*True negative:* Healthy people correctly identified as healthy TN.

*False negative:* Sick people incorrectly identified as healthy FN.

In this task, we focus on the accuracy and medical testing to evaluate the performance of the proposed system.

**Medical Testing**

The act of diagnosing a medical condition is extremely involved. When done right, the process is a complex blend of clinical evidence, data, probabilistic rationale and pattern matching, with the consequences of different courses of action kept in mind from a cost and patient care perspective. When done poorly, a range of tests is performed (often without justification), and conclusions drawn on scant evidence.

Medical tests are designed to detect, diagnose or monitor disease in a patient, and take on many different formats, including clinical examinations, imaging, biopsies, genetic analysis, and blood tests. Beyond their cost and usability, the most important question for any test is its effectiveness. In other words, how good is a particular test at detecting, diagnosing or monitoring the condition in question?

Diagnostic tests are often sold, marketed, cited and used with sensitivity and specificity as the headline metrics. Sensitivity and specificity are defined as:

- **Sensitivity:**

Sensitivity is the probability that a test is correctly identify a person with the disease when in fact, they do have the disease or sensitivity is the system’s ability in truly identifying the sick people. It can be estimated as:

$$\text{Sensitivity} = \frac{TP}{TP+FN} \quad (1)$$

- **Specificity:**

Specificity is the probability that a test is correctly identify a person whom does not have the disease when in fact they are disease free. Specificity is calculated by the following formula:

$$\text{Specificity} = \frac{TN}{TN+FP} \quad (2)$$

Notice the denominators. For sensitivity, we have 'true positives', which are of course positives, and 'false negatives', which are also positives. Therefore, sensitivity only deals with positive cases, and the logic is the same with specificity for negative cases. The result is that sensitivity is a measure of the probability of getting a positive result out of all the positive cases, and that specificity is a measure of the probability of getting a negative result out of all the negative cases. Another way of phrasing this is that sensitivity is the probability of getting a positive result, given that you have the disease. Note that in practice, we are interested in the opposite of this, namely the probability of having the disease, given a positive test result (and similarly for not having the disease). For these measures, we use the positive predictive value (PPV) and negative predictive value (NPV), respectively:

$$PPV = \frac{TP}{TP+FP} \quad (3)$$

$$NPV = \frac{TN}{TN+FN} \quad (4)$$

Ideally, Systems that rely on medical image dataset should have high sensitivity and high specificity, but usually there are some tradeoffs between sensitivity and specificity.

Figure 2 shows the heat-map analysis of the nine attributes to show their correlation. The colors show how one parameter is associated with another parameter through the colors displayed. Lighter colors show that two attributes are highly correlated, white being the most correlated with a value of 1.00. Darker colors, on the other hand, show that two parameters are poorly correlated

A medical image system might have a high sensitivity but lower specificity and vice versa, this is due to limitations on hardware manufacturing and available materials, which affect the performance of the system diversely.

- **Accuracy:**

Accuracy shows the performance of the diagnostic system is determined based on the combination of sensitivity and specificity and is calculated by the following formula:

$$\text{Accuracy} = \frac{TP+TN}{TP+TN+FN+FP} \quad (5)$$

## Building models

Our project is broken down into the following tow subtasks:

### Sub-task A: using all the features

This section presents the methodology that we follow to build our machine learning models using all the features in Wisconsin breast cancer dataset, below are the steps to follow.

- **Loading the data**
- **Removing the unwanted columns**

Before feeding the data into the machine learning models, a pre-processing is applied. The aim of pre-processing is to reduce dimensions and clean up the data from noisy and unwanted columns. This step can improve the accuracy of classification.

- **Encoding the categorical variable**

Machines, cannot understand the raw text. Therefore, we need to convert diagnostic column into numbers (0, 1). This variable is the label for the supervised learning problem as defined above.

- **Splitting dataset**

In order to form the confusion matrix, the dataset was divided into training set and testing set, 80% of the data is used to train the system and the remaining 20% for testing

- **Training machine learning models**

The final step in the classification task is to train the machine learning classifier, using the features created in the previous step and using the 10-fold validation. Here, five supervised learning algorithms are utilized to build models to perform classification, namely, logistic Regression, Random Forest, Naïve-Bayes, Support vector machine, and K-Nearest Neighbor.

### Sub-task B: features selecting based on correlation

In this subsection, we repeat all the above steps and we explore our most prominent and most important step in our research, which is “*features Selecting based on correlation*” where it is in the penultimate rank in terms of implementation.

- **Selecting features based on correlation**

Often when we get a dataset, we might find a plethora of features. Not all of them might be useful in building a machine-learning model to make the necessary prediction.

Using some of the features might even make the predictions worse. Therefore, feature selection plays a huge role in building a machine-learning model. In this step, we explore correlation matrix to select the right features:

First, we create the correlation matrix (Fig.7).



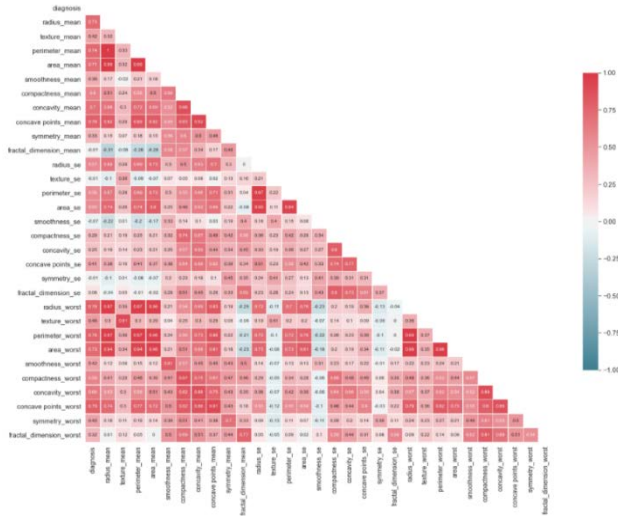


Fig.7 Correlation matrix heatmap

Next, we drop variables that have a very low correlation with the target. Then we rank and select the top 15 features that correlate with the diagnosis column.

Finally we compare every two features separately then we drop one of the two features that have a correlation higher than 0.9 (Fig.8). (Between the two ends of the comparison, we drop the feature that is least correlated to the target column).

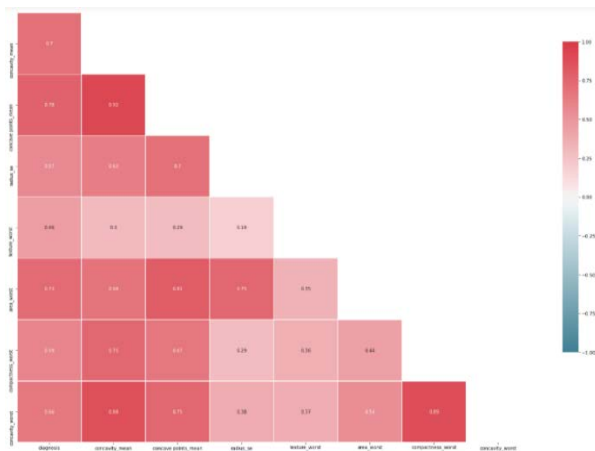


Fig.8 Correlation matrix heatmap (without irrelevant features)

## RESULTS AND DISCUSSION

Throughout the previous section, we have presented the different steps of our work development. This section describes all the results obtained from the study and introduces the best performance according to various performance metrics. First performance was obtained by using all features; Second performance was obtained by using features selection.

### Result for Sub-task A: using all the features

After evaluating our five algorithms (Logistic Regression, SVM, Random Forests, NB and KNN), we summarized the results in the Table 1.

Table 1. Result of sub-task A

	LR	SVM	RF	NB	KNN
<b>Accuracy (%)</b>	90,78	86,83	<b>94,74</b>	94,07	88,37
<b>Sensitivity (%)</b>	91,04	<b>98,51</b>	97,01	94,03	95,52
<b>Specificity (%)</b>	91,49	72,34	<b>91,49</b>	85,11	85,11
<b>PPV (%)</b>	93,85	83,54	<b>94,2</b>	90	90,14
<b>NPV (%)</b>	87,76	<b>97,14</b>	95,56	90,91	93,02
<b>Time (Second)</b>	0,335	0,076	1,688	1,456	<b>0,058</b>

From the Table 1, it can be seen that the best accuracy achieved is 94.74 % by Random Forest, the last row of Table 1 shows the time required to build the classification algorithms.

The results show that KNN achieved less timing for building a model. In addition, SVM require more time, but it shows that his training time is much less than other classification algorithms.

### Result for Sub-task B: features selection

In this subsection, we show the results of applying classifiers using the correlation matrix to choose the best features on dataset (Table.2) and we introduce the best performance according to various performance metrics.

Table 2. Result of sub-task B

	LR	SVM	RF	NB	KNN
<b>Accuracy (%)</b>	94,74	91	<b>97,59</b>	96,5	89,66
<b>Sensitivity (%)</b>	95,52	98,51	<b>98,51</b>	94,03	97,01
<b>Specificity (%)</b>	97,87	85,11	<b>97,87</b>	91,49	95,74
<b>PPV (%)</b>	98,46	90,41	<b>98,51</b>	94,03	97,01
<b>NPV (%)</b>	93,88	97,56	<b>97,87</b>	91,49	95,74
<b>Time (Second)</b>	0,329	0,073	1,593	1,453	0,07

From the Table 2 it can be seen that the best accuracy achieved is 97.59 % by Random Forest, also it is the best one for the other metrics, except for training time.

### Results summary

To conclude, figures below (9 and 10) show a comparison between the results obtained previously in terms of training time and accuracies.

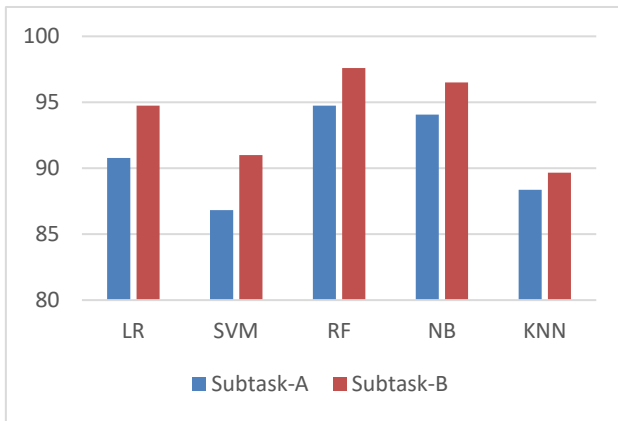


Fig.9. Accuracies Comparisons

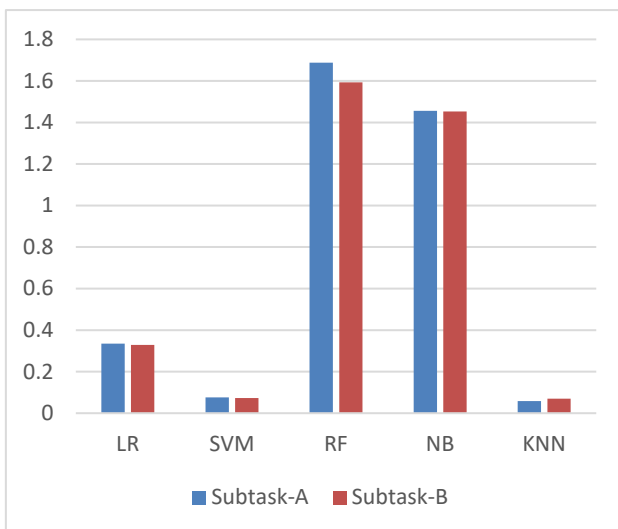


Fig.10 Training Time Comparisons

We compare results of different methods, it is clear that when we used features selection (correlation matrix) we get best results in all methods. As we noticed an improvement in the performance of all classifiers especially the random forest model, which overtake the 97% threshold in most performance measures.

While the KNN model remained the fastest in terms of training time, we note that our best model in terms of accuracy (RF) took more time to train and vice versa.

All these improvement results are due to the reduction of high dimensional correlated features to low dimensional features. Dimension reduction consists of projecting all data from the original space onto a new space of reduced dimensions, which is a commonly used step in machine learning, especially when faced with very high dimensional features space.

The main reasons for using dimension reduction in machine learning are as follows:

- Improve the performance of the prediction, to improve the learning efficiency.
- Provide faster predictors possibly using less information on the original data.
- Reduce the complexity of the results produced and allow a better understanding of the classification process.

## CONCLUSIONS

All the work we did during this challenge showed the benefit of using Feature selection technics in machine learning Algorithm. The most well-known feature selection technique is correlation matrix; it is good at reducing the high dimensional correlated features into low dimensional features.

The results of classifying the data obtained by the approach were very promising and the best model as found in our analysis is a random forest model with using of correlation matrix to extract the best features, it gives a prediction accuracy equal to 97, 59%.

## AUTHOR INFORMATION

### Corresponding Author

\*Ahmed Zoubir Messalti

Email address: [ahmedzoubir.messalti@univ-setif.dz](mailto:ahmedzoubir.messalti@univ-setif.dz)

Sadik Bessou

Email address: [bessou.s@univ-setif.dz](mailto:bessou.s@univ-setif.dz)

## REFERENCES

1. Sung H, Ferlay J, Siegel RL, et al. World Cancer Statistics 2020: GLOBOCAN Estimates of Incidence and Mortality Worldwide for 36 cancers in 185 countries. *CA Cancer J Clin* 2021. doi: 10.3322
2. <http://www.imanord.fr/>
3. H.-P. CHAN et al(1987). Digital mammography. ROC studies of the effects of pixel size and unsharp-mask filtering on the detection of subtle microcalcifications. *Investigative Radiology*, 22(7):581–589.
4. X. H. ZHOU et R. GORDON (1989). Detection of early breast cancer: an overview and future prospects. *Critical Reviews in Biomedical Engineering (CRBE)*, 17(3):203–255.
5. R. STRICKLAND, et H. I. HAHN, (1997). Wavelet transform methods for object detection and recovery. *IEEE Transactions on Medical Imaging*, 6(5):724–735.
6. S. BERNARD et al (2006). Microcalcification detection on simple backprojection reconstructed slices using wavelets. *Computer Assisted Radiology and Surgery (CARS)*, 1:84– 86.

7. H.-D. CHENG et al (1998). A novel approach to microcalcification detection using fuzzy logic technique. *IEEE Transactions on Medical Imaging*, 17(3):442–450.
8. A. RICK, (1999). Représentation de la variabilité dans le traitement d'images flou. Thèse de doctorat, université Paris VI.
9. M. GRIMAUD (1991). La géodésie numérique en morphologie mathématique. Application à la détection automatique des microcalcifications. Thèse de doctorat, Ecole nationale supérieure des mines de Paris.
10. M. D. HEATH et , K. W. BOWYER (2000). Mass detection by relative image intensity. *International Workshop on Digital Mammography (IWDM)*. Medical Physics Publishing (Madison, WI).
11. G. PETERS (2007). Computer-aided Detection for Digital Breast Tomosynthesis. Thèse de doctorat, Ecole Nationale Supérieure des Télécommunications.
12. C. VACHIER (1995). Extraction de caractéristiques, segmentation d'image et morphologie mathématique. Thèse de doctorat, Ecole nationale supérieure des mines de Paris.
13. V. G. MARTINEZ et al (1999). Iterative method for automatic detection of masses in digital mammograms for computer-aided diagnosis. *SPIE Symposium on Medical Imaging*, volume 3661, pages 1086–1093.
14. H. D.CHENG et al (2003). Computer-aided detection and classification of microcalcifications in mammograms : a survey. *Pattern Recognition*, 36(12):2967 – 2991.
15. J. K. KIM et H.W. PARK (1999). Statistical textural features for detection of microcalcifications in digitized mammograms. *IEEE Transactions on Medical Imaging*, 18(3):231–238.
16. Li, L.,MAO, F, W. QIAN, et L. CLARKE (1997). Wavelet transform for directional feature extraction in medical imaging. *IEEE International Conference on Image*
17. H. KIM, et W. KIM, (2005). Automatic detection of spiculated masses using fractal analysis in digital mammography. *Computer Analysis of Images and Patterns (CAIP)*, pages 256–263.
18. N. MUDIGONDA, R. RANGAYYAN, et J. LEO DESAUTELS, (2001). Detection of breast masses in mammograms by density slicing and texture flow-field analysis. *IEEE Transactions on Medical Imaging*, 20(12):1215– 1227.
19. A. R. DOMINGUEZ, et , A. K. NANDI (2009). Toward breast cancer diagnosis based on automated segmentation of masses in mammograms. *Pattern Recognition*, 42(6):1138 – 1148. *Digital Image Processing and Pattern Recognition Techniques for the Detection of Cancer*.
20. Chaurasia, V., & Pal, S. (2014). Data mining techniques: to predict and resolve breast cancer survivability. *International Journal of Computer Science and Mobile Computing IJCSMC*, 3(1), 10-22.
21. Rana, M., Chandorkar, P., Dsouza, A., & Kazi, N. (2015). Breast cancer diagnosis and recurrence prediction using machine learning techniques. *IJRET: International Journal of Research in Engineering and Technology* eISSN, 2319-1163.
22. Assegie, T. A. (2021). An optimized K-Nearest Neighbor based breast cancer detection. *Journal of Robotics and Control (JRC)*, 2(3), 115-118. Wolberg WH, Mangasarian OL. Multisurface method of pattern separation for medical diagnosis applied to breast cytology. In: *Proceedings of the National Academy of Sciences*, vol. 87. Washington, DC, 1990. p. 9193-6.
23. Wolberg WH, Mangasarian OL. Multisurface method of pattern separation for medical diagnosis applied to breast cytology. In: *Proceedings of the National Academy of Sciences*, vol. 87. Washington, DC, 1990. p. 9193-6.
24. D Kuhlman. A python book: Beginning python. *Advanced Python, and Python Exercises*, 2012.
25. Intel. jupyter notebook. [jupyter.org/](https://jupyter.org/), Accessed on 2018-5-15.
26. pandas package. <https://pandas.pydata.org/pandas-docs/version/0.20/>, Accessed on 2018-5-10.
27. scikit learn. <https://en.wikipedia.org/wiki/Scikit-learn>, . Accessed on 2018-5-10.
28. Sotiris B Kotsiantis, I Zaharakis, and P Pintelas. Supervised machine learning: A review of classification techniques. *Emerging artificial intelligence applications in computer engineering*.



2021

## Applications of Artificial Intelligence in Radiation Therapy

Dorea Maria Khalal<sup>a,\*</sup>, Hacene Azizi<sup>a</sup>

<sup>a</sup>Laboratory of dosing, analysis and characterization in high resolution, Department of Physics, Faculty of Sciences, Ferhat Abbas Sétif 1 University, El Bèz campus 19137, Sétif, Algeria

**ABSTRACT:** The increase of computing power, the development of mathematical algorithms and the growth of data encouraged the use of Artificial Intelligence (AI) in different fields such as industry, medicine, robotics and social media. Indeed, AI becomes more and more present in our everyday lives. Machine Learning (ML) is a subunit of AI that allows machines to learn from past data to provide accurate results. Deep learning (DL) is a form of ML that trains a model to perform human-like tasks such as speech recognition and image identification.

Many applications of ML and DL are present in the field of Radiation Oncology. AI algorithms allow optimization and automation of the radiotherapy workflow. The impact of AI tools is important in terms of efficiency and consistency in treatment.

In this paper, we present the different AI methods that can be applied to radiation therapy. We give recent examples related to each step of the radiation therapy workflow where different anatomic locations and imaging modalities are considered. A particular attention is devoted to automatic segmentation.

**Keywords:** Artificial intelligence; Machine learning; Deep learning; Radiation therapy; Radiotherapy.

## INTRODUCTION

Artificial intelligence (AI) is a branch of computer science where smart machines are capable to display human-like capabilities and thus performing tasks that typically require human intelligence such as learning, planning and reasoning. These tasks can be performed using machines without being explicitly instructed. Three components are needed to achieve this goal: powerful computers, advanced AI algorithms and data. Machine Learning (ML) is a part of AI that allows a machine to be capable to learn and improve from data without being explicitly programmed. By using these data, the programs can thus learn for themselves. Deep learning (DL) is a specialized subset of machine learning. DL algorithms are based on the use of neural networks which are composed of layers. These networks, called artificial neural networks, attempt to mimic the behavior of the human brain. Thus, DL can learn from large amounts of data in order to classify, infer and predict the outcome. By increasing the data size, the performance of the algorithms is adaptively improved.

AI has numerous and varied applications, in particular with the

use of a multidisciplinary approach based on computer science and mathematics. AI is introduced in the financial field<sup>1,2</sup> (to evaluate the risks of different financial operations), robotics<sup>3</sup>, industrial sector<sup>4</sup> (solutions to deal with production problems) and many other fields.

Recently, AI has been widely used in the medical field. This is due to the important advances in computing performance, and also to the growth and sharing of data. Indeed, in the medical field, AI can contribute to accelerate the drug development, to improve diagnosis and for remote consultations<sup>5,6</sup>. In this study, we present the applications of AI that are used in the different steps of the radiotherapy workflow. Particular interest is devoted to automatic segmentation of medical images where some examples are given.

## APPLICATIONS OF ARTIFICIAL INTELLIGENCE IN RADIATION THERAPY

Radiation therapy (RT) is used as a local cancer treatment. More than half of all people with cancer receive RT as part of their cancer treatment<sup>7</sup>. In RT treatment, beams of electrons, photons or ions, with a given energy, are used to kill cancer cells. To ensure an efficient RT treatment, precise targeting of the tumour should be performed by the oncologist. Moreover, organs at risk (OARs) should be protected during irradiation.

The number of scientific publications on applications of AI in RT is constantly increasing. Using the following search phrases: “Machine Learning” and (“radiation oncology” or radiotherapy) and “Deep Learning” and (“radiation oncology” or radiotherapy) on the PubMed library, we obtain the results presented in figure 1. This figure shows clearly the rapid augmentation of the corresponding publications number over time. As an example, the number of these publications has been multiplied by a factor F, where F=57 corresponds to ML and F=177.5 to DL during the period (2013-2020).

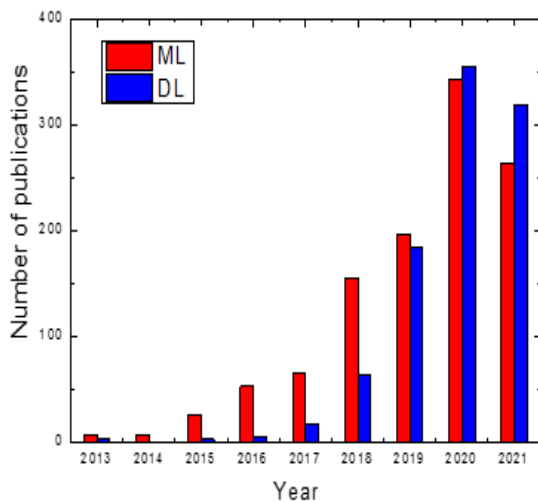


Fig. 1 Yearly published articles corresponding to applications of ML and DL in RT, until August 2021 (PubMed, see text for details).

ML and DL models allow automation and optimization of the RT workflow which is represented in figure 2 with its different steps: patient assessment, simulation, treatment planning, quality assurance (QA) and treatment delivery. In the following sections, we present some examples of the use of AI tools in the RT workflow.

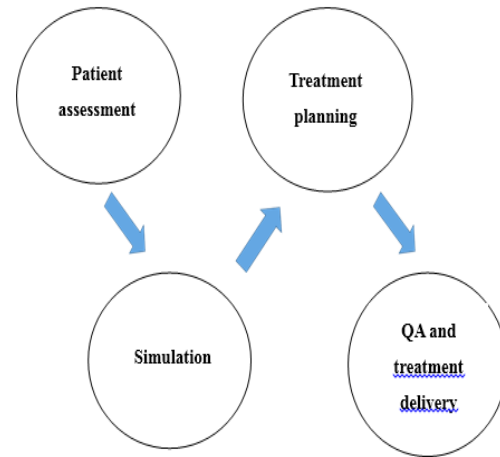


Fig. 2 Different steps of a radiotherapy workflow.

### Patient assessment

#### Patient evaluation

The first step of the RT workflow corresponds to the clinical evaluation of the patient by the oncologist. During this step, a physical examination of the patient is performed with a review of his medical history. A treatment plan, which takes into account all these data, is then proposed to the patient. This step can be significantly simplified with the use of AI algorithms. Indeed, data extraction and analysis can be performed with AI tools which can help as an important decision support for doctors<sup>8</sup>. AI tools are also very helpful to automate structured documentation about electronic health records of patients<sup>9</sup>.

#### Dose prescription

The dose of radiation to be administered to the patient should be determined and prescribed by the radiation oncologist. The treatment plan takes into account the tumor shape and the surrounding healthy organs. Using AI tools, it is possible to offer personalized treatment for each patient with an optimal dose prescription<sup>10</sup>.

### Simulation

#### Image registration

Registration corresponds to the overlaying of medical images that have been obtained of the same region shot from different imaging modalities (e.g. computer tomography (CT) and magnetic resonance (MR)). This process can improve significantly the precision of the diagnostic by providing additional information about the anatomy of the explored region of the patient<sup>11</sup>. Registration of medical images performed with high accuracy allows a clear segmentation of the planning target volume (PTV) and the organs at risk (OARs). Thus, registration

of medical images constitutes an important step of the RT workflow.

Commercial mathematical algorithms are available for medical images registration, but they are used in particular cases related to solving problems specific to a given modality. Moreover, the obtained results with these algorithms are sensitive to artifacts that can be present in medical images. It has been shown that registration performed using AI algorithms leads to better performance<sup>12</sup>. In addition, these algorithms can be applied for different imaging modalities<sup>12,13</sup> and they appear to mitigate the effects of artifacts<sup>14,15</sup>.

Han et al. developed a DL-based model for deformable CT-CBCT (Cone Beam Computed Tomography) registration for radiation treatment<sup>16</sup> (pancreatic cancer). This model was compared to two intensity-based algorithms. These authors showed that the proposed deep network model improved segmentation accuracy compared to the other models with a sensitive reduction in processing time.

Koen et al. proposed an automatic supervised method, based on a convolutional neural network, to estimate registration errors in the case of nonlinear registration of 3D images<sup>17</sup>. It has been shown that this method can be trained to robustly estimate registration errors in a predetermined range, with subvoxel accuracy.

### **Contouring**

Before starting the radiotherapy planning step, the radiotherapist should segment accurately the target volumes (TV) and the OARs. This operation is an important part of the radiotherapy workflow and constitutes one of the most time-consuming tasks. The precision of the delineation has an impact on the obtained results: in case of an incorrect segmentation of the tumor, we can have under-dosing or overdosing. In such situations, there is a decreased likelihood of controlling the tumor or a significant risk of toxicity. Furthermore, the segmentation of organs is also subject to inter-observer variation<sup>18,19</sup>. It is possible that the same radiotherapist may not be able to reproduce his own segmentation very well<sup>20-22</sup>; hence the need to use automatic segmentation of medical images. First, semi-automatic methods, based essentially on the 'Atlas data' were proposed<sup>23</sup>. In this case, one should match the image to be segmented, to one of the atlas data images. This operation is performed using registration techniques. However, it has been shown that atlas-based methods are sensitive to the atlas-data choice<sup>24</sup> and also to the used registration techniques.

At present, several researchers have applied AI models to delineate OARs and target volumes for different cases as head and neck tumors, lung and breast cancers. AI-based auto-segmentation algorithms have been shown to improve significantly this operation for different imaging modalities: CT,

CBCT<sup>25</sup> (Cone Beam Computed Tomography), PET<sup>26</sup> (Positron Emission Tomography) and MRI<sup>27</sup> (Magnetic Resonance Imaging).

In Ref<sup>28</sup>, an algorithm, called LL-CNN (lifelong learning-based convolutional neural network) was presented. This algorithm was used for automatic segmentation of head and neck organs-at-risk where good results were obtained. In another work<sup>25</sup>, a novel DL network, called BibNet, was used to segment bladder, prostate, rectum and seminal vesicles from CT and cone beam CT scans. This model was scored either equally good (for prostate and seminal vesicles) or better (for bladder and rectum) than the structures from routine clinical practice.

### **Treatment planning**

After the segmentation of tumor and OARs and the dose prescription, the optimal treatment plan for the patient should be generated by achieving sufficient tumor coverage and avoiding the surrounding tissues. This step is considered as a problem of optimization where many parameters (e.g. positioning and machine settings) are to be determined to ensure a better management of the patient's cancer.

One of the most important aspects of AI-based treatment planning corresponds to the generation of plans and the prediction of an acceptable dose distribution for individual patients based on their anatomy. Using DL algorithms, optimal dose distributions have been predicted allowing acceleration of dose calculations<sup>29</sup>.

It was shown, in Ref<sup>30</sup>, that the presented DL method can predict clinically acceptable dose distributions. There is no statistically significant difference between DL prediction and real clinical plan for all clinically relevant dose volume histogram (DVH) indices, except brainstem, right and left lens. This DL-based method constitutes a promising approach to prepare automated treatment planning in the future.

In Ref<sup>31</sup>, a comparison of automatically generated plans (AP) to plans generated manually (MP) was performed showing the auto planning method to be a robust clinical tool. This study concerned the following sites: head-neck, high-risk prostate and endometrial cancer. AP plans were judged of equal or better quality compared to MP plans in more than 90% of the evaluations concerning dosimetric results. By considering dosimetric and clinical advantages, this auto planning method can generate high quality treatment plans for VMAT (Volumetric modulated arc therapy) according to institutional specific planning protocols.

### **QA and treatment delivery**

#### **Quality assurance**

Intensity modulated radiation therapy (IMRT) and Volumetric arc radiation therapy (VMAT) are two techniques used to deliver

high-precision radiotherapy. In order to verify the accuracy of the dose calculation and the delivery system, it is important to perform patient-specific quality assurance before delivering the calculated dose to the patient. The precedent procedure, which consists to measure the dose in a phantom, is expensive and time consuming. Recently, ML and DL algorithms have been developed to predict patient-specific QA results<sup>32-34</sup>. Moreover, many models have been proposed to detect errors. Different errors have been investigated as the detection of multileaf collimator (MLC) positional errors in the case of static beam IMRT dosimetry QA<sup>35</sup>. In another paper<sup>36</sup>, a DL model has been used to detect errors of MLC transmission and effective source size for static beam IMRT QA dosimetry.

### Treatment delivery

Patients treated with RT should attend the radiation oncology department several times and sometimes, they have to wait for long times. These long waiting times can affect negatively the patients. AI tools can be used in order to organize the different steps of the RT treatment which could further optimize appointment scheduling<sup>10</sup>.

Furthermore, kV-CBCT was implemented to verify the patient's positioning on the treatment table before the irradiation session. However, images provided by CBCT have a much lower quality than the planning CT images. In order to ensure more accurate positioning of patients for treatment, AI tools were used to improve the quality of CBCT image<sup>37</sup>.

Moreover, in the case of the image-guided RT (IGRT), we have the incorporation of imaging techniques as the on-board MRI and optical surface imaging. The patient motions during the treatment (respiration and/or digestion) should be taken into account in the prediction of the radiation dose to be delivered to the patient. In Ref<sup>38</sup>, a DL model was developed for the external respiration signal prediction for RT treatment. This study showed the potential of this DL algorithm to predict the respiratory signal.

## CONCLUSIONS

Several papers have been published on applications of AI tools in the radiotherapy workflow. These studies clearly explained the important contribution of AI models to ameliorate RT treatment in terms of efficiency and consistency. Using ML and DL algorithms, gains in time during segmentation and planning are performed. Other benefits are also obtained when performing QA and delivering treatment.

However, significant challenges and problems remain before the implementation of these models in the clinical setting. Moreover, large datasets should be prepared and shared between centers to train AI models.

## AUTHOR INFORMATION

### Corresponding Author

\*Dorea Maria Khalal

Email address: [doreamaria.khalal@univ-setif.dz](mailto:doreamaria.khalal@univ-setif.dz)

## REFERENCES

1. C. Milana and A. Ashta, Artificial intelligence techniques in finance and financial markets: A survey of the literature. *Strategic Change*, 2021, 30, 189–209.
2. J. W. Goodell, S. Kumar, W. M. Lim, D. Pattnaik, Artificial intelligence and machine learning in finance: Identifying foundations, themes, and research clusters from bibliometric analysis. *Journal of Behavioral and Experimental Finance*, 2021, 32, 100577.
3. V. Kaartemo, A. Helkkula, A Systematic Review of Artificial Intelligence and Robots in Value Co-creation: Current Status and Future Research Avenues. *Journal of Creating Value*, 2018, 4, 211–228.
4. Bo-hu Li, Bao-cun Hou, Wen-tao Yu, Xiao-bing Lu and Chun-wei Yang, Applications of artificial intelligence in intelligent manufacturing: a review. *Frontiers Inf Technol Electronic Eng*, 2017, 18, 86–96.
5. R. Liu, Y. Rong, Z. Peng, A review of medical artificial intelligence. *Global Health Journal*, 2020, 4, 42–45.
6. E. Racine, W. Boehlen, M. Sample, Healthcare uses of artificial intelligence: Challenges and opportunities for growth, *Healthcare Management Forum*, 2019, 32, 272–275.
7. R. Atun, D. A. Jaffray, M. B. Barton, F. Bray, M. Baumann, B. Vikram, T. P. Hanna, F. M. Knaul, Y. Lievens, T. Y. M. Lui, M. Milosevic, B. O'Sullivan, D. L. Rodin, E. Rosenblatt, J. Van Dyk, M. L. Yap, E. Zubizarreta, M. Gospodarowicz, Expanding global access to radiotherapy. *Lancet Oncol*, 2015, 16, 1153–1186.
8. M. Feng, G. Valdes, N. Dixit, T.D. Solberg, Machine learning in radiation oncology: Opportunities, requirements, and needs. *Front Oncol*, 2018, 8, 1–7.
9. F. Jiang, Y. Jiang, H. Zhi, Y. Dong, H. Li, S. Ma, Y. Wang, Q. Dong, H. Shen, Y. Wang, Artificial intelligence in healthcare: past, present and future. *Stroke and Vascular Neurology*, 2017, 2, 230–243.
10. E. Huynh, A. Hosny, C. Guthier, D. S. Bitterman, S. F. Petit, D. A. Haas-Kogan, B. Kann, H. J. W. L. Aerts and R. H. Mak, Artificial intelligence in radiation oncology. *Nat Rev Clin Oncol*, 2020, 17, 771–781.
11. P. Czajkowski, T. Piotrowski, Registration methods in radiotherapy. *Reports of Practical Oncology & Radiotherapy*, 2019, 24, 28–34.
12. R. Liao, S. Miao, P. Tournemire, S. Grbic, A. Kamen, T. Mansi, D. Comaniciu, An Artificial Agent for Robust Image Registration. *Proceedings of the Thirty-First AAAI Conference on Artificial Intelligence*, 2017, 4168–4175.
13. G. Wu, M. Kim, Q. Wang, B. C. Munsell, D. Shen, Scalable High-Performance Image Registration Framework by Unsupervised Deep Feature Representations Learning. *IEEE Trans Biomed Eng*, 2016, 63, 1505–1516.
14. S. Miao, S. Piat, P. Fischer, A. Tuysuzoglu, P. Mewes, T. Mansi, and R. Liao, Dilated FCN for Multi-Agent 2D/3D Medical Image Registration. *Thirty-Second AAAI Conference on Artificial Intelligence*, 2018, 3501–3509.

- intelligence, 2018, 4694–4701.
15. B. Hou, A. Alansary, S. McDonagh, A. Davidson, M. Rutherford, J. V. Hajnal, D. Rueckert, B. Glocker, B. Kainz, Predicting Slice-to-Volume Transformation in Presence of Arbitrary Subject Motion. *International Conference on Medical Image Computing and Computer-Assisted Intervention*, 2017, 296–304.
  16. X. Han, J. Hong, M. Reyngold, C. Crane, J. Cuaron, C. Hajj, J. Mann, M. Zinovoy, H. Greer, E. Yorke, G. Magerasa, M. Niethammer, Deep-learning-based image registration and automatic segmentation of organs-at-risk in cone-beam CT scans from high-dose radiation treatment of pancreatic cancer. *Med Phys*, 2021, 48, 3084–3095.
  17. K. A. J. Eppenhof, J. P. W. Pluim, Error estimation of deformable image registration of pulmonary CT scans using convolutional neural networks. *J Med Imag*, 2018, 5, 024003.
  18. J. Van de Steene, N. Linthout, J. de Mey, V. Vinh-Hung, C. Claessens, M. Noppen, A. Bel, G. Storme, Definition of gross tumor volume in lung cancer: inter-observer variability. *Radiother Oncol*, 2002, 62, 37–49.
  19. Y. Cui, W. Chen, F. M. Kong, L. A. Olsen, R. E. Beatty, P. G. Maxim, T. Ritter, J. W. Sohn, J. Higgins, J. M. Galvin, Y. Xiao, Contouring variations and the role of atlas in non-small cell lung cancer radiation therapy: Analysis of a multi-institutional preclinical trial planning study. *Pract Radiat Oncol*, 2015, 5, 67–75.
  20. J. Zhu, Y. Liu, J. Zhang, Y. Wang, L. Chen, Preliminary Clinical Study of the Differences Between Interobserver Evaluation and Deep Convolutional Neural Network-Based Segmentation of Multiple Organs at Risk in CT Images of Lung Cancer. *Front Oncol*, 2019, 9, 627.
  21. L. Lin, Q. Dou, Y. M. Jin, G. Q. Zhou, Y. Q. Tang, W. L. Chen, B. A. Su, F. Liu, C. J. Tao, N. Jiang, J. Y. Li, L. L. Tang, C. M. Xie, S. M. Huang, J. Ma, P. A. Heng, J. T. S. Wee, M. L. K. Chua, H. Chen, Y. Sun, Deep Learning for Automated Contouring of Primary Tumor Volumes by MRI for Nasopharyngeal Carcinoma. *Radiology*, 2019, 291, 677–686.
  22. M. Kosmin, J. Ledsam, B. Romera-Paredes, R. Mendes, S. Moinuddin, D. de Souza, L. Gunn, C. Kelly, C. O. Hughes, A. Karthikesalingam, C. Nutting, R. A. Sharma, Rapid advances in auto-segmentation of organs at risk and target volumes in head and neck cancer. *Radiother Oncol*, 2019, 135, 130–140.
  23. M. Cabezas, A. Oliver, X. Lladó, J. Freixenet, M. B. Cuadra, A review of atlas-based segmentation for magnetic resonance brain images. *Comput Methods Programs Biomed*, 2011, 104, e158–177.
  24. D. Peressutti, B. Schipaanboord, J. Soest, T. Lustberg, W. Elmpt, T. Kadir, A. Dekker, M. Gooding, TU-AB-202-10: How Effective Are Current Atlas Selection Methods for Atlas-Based Auto-Contouring in Radiotherapy Planning?. *Medical Physics*, 2016, 43, 3738–3739.
  25. J. Schreier, A. Genghi, H. Laaksonen, T. Morgas, B. Haas, Clinical evaluation of a full-image deep segmentation algorithm for the male pelvis on cone-beam CT and CT. *Radiotherapy and Oncology*, 2020, 145, 1–6.
  26. Y. Lu, J. Lin, S. Chen, H. He and Y. Cai, Automatic Tumor Segmentation by Means of Deep Convolutional U-Net With Pre-Trained Encoder in PET Images, *IEEE Access*, 2020, 8, 113636–113648.
  27. M.H.F. Savenije, M. Maspero, G.G. Sikkes, J. R. N. van der Voort van Zyp, A. N. T. J. Kotte, G. H. Bol, C. A. T. van den Berg, Clinical implementation of MRI-based organs-at-risk auto-segmentation with convolutional networks for prostate radiotherapy. *Radiat Oncol*, 2020, 15, 104.
  28. J. W. Chan, V. Kearney, S. Haaf, S. Wu, M. Bogdanov, M. Reddick, N. Dixit, A. Sudhyadhom, J. Chen, S. S. Yom, T. D. Solberg, A convolutional neural network algorithm for automatic segmentation of head and neck organs at risk using deep lifelong learning. *Med Phys*, 2019, 46, 2204–2213.
  29. D. Nguyen, T. Long, X. Jia, W. Lu, X. Gu, Z. Iqbal, S. Jiang, A feasibility study for predicting optimal radiation therapy dose distributions of prostate cancer patients from patient anatomy using deep learning. *Sci Rep*, 2019, 9, 1076.
  30. J. Fan, J. Wang, Z. Chen, C. Hu, Z. Zhang, W. Hu, Automatic treatment planning based on three-dimensional dose distribution predicted from deep learning technique. *Med Phys*, 2019, 46, 370–381.
  31. S. Cilla, A. Ianiro, C. Romano, F. Deodato, G. Macchia, M. Buwenge, N. Dinapoli, L. Boldrini, A. G. Morganti, V. Valentini, Template-based automation of treatment planning in advanced radiotherapy: a comprehensive dosimetric and clinical evaluation. *Sci Rep*, 2020, 10, 423.
  32. A. F. I. Osman, N. M. Maalej, Applications of machine and deep learning to patient-specific IMRT/VMAT quality assurance. *Journal of Applied Clinical Medical Physics*, 2021, 22, 20–36.
  33. G. Valdes, R. Scheuermann, C. Y. Hung, A. Olszanski, M. Bellerive, T. D. Solberg, A mathematical framework for virtual IMRT QA using machine learning. *Med Phys*, 2016, 43, 4323–4334.
  34. S. Tomori, N. Kadoya, Y. Takayama, T. Kajikawa, K. Shima, K. Narazaki, K. Jingu, A deep learning-based prediction model for gamma evaluation in patient-specific quality assurance. *Med Phys*, 2018, 45, 4055–4065.
  35. L. S. Wootton, M. J. Nyflot, W. A. Chaovalitwongse, E. Ford, Error Detection in Intensity-Modulated Radiation Therapy Quality Assurance Using Radiomic Analysis of Gamma Distributions. *Int J Radiat Oncol Biol Phys*, 2018, 102, 219–228.
  36. N. J. Potter, K. Mund, J. M. Andreozzi, J. G. Li, C. Liu, G. Yan, Error detection and classification in patient-specific IMRT QA with dual neural networks. *Med Phys*, 2020, 47, 4711–4720.
  37. S. Kida, T. Nakamoto, M. Nakano, K. Nawa, A. Haga, J. Kotoku, H. Yamashita, K. Nakagawa, Cone beam computed tomography image quality improvement using a deep convolutional neural network. *Cureus*, 2018, 10, e2548.
  38. H. Lin, C. Shi, B. Wang, M. F. Chan, X. Tang, W. Ji, Towards real-time respiratory motion prediction based on long short-term memory neural networks. *Phys. Med. Biol*, 2019, 64, 085010.
-





## Performance of machine learning for face recognition

Fella Berrimi,<sup>a\*</sup> Riadh Hedli,<sup>b</sup> Chafia Kara-mohamed<sup>a</sup>

<sup>a</sup>Department of Computer Science, Faculty of Sciences, University of Ferhat ABBAS, Setif, Algeria

<sup>b</sup>Department of Mathematics, Faculty of Sciences, University of Ferhat ABBAS, Setif, Algeria

**ABSTRACT:** The image can be noised during the acquisition and transmission despite the most advanced development of vision systems. Thus, the preprocessing of digital image is required to suppress as much as possible the parasite degradation, while at the same time preserving the maximum amount of relevant information in order to obtain a better restitution of the image. To cope with these challenges, we propose an algorithm that consists of two fundamental stages, feature extraction and image denoising. The first step consists of using the Schur decomposition to extract the main features and dissimilate the small features from the large ones. The second one permits to denoise these features by an adaptive wiener filter, such that, the small features are smoothed with 3x3 wiener filter mask and the large features are enhanced by 5x5 wiener filter mask in order to increase the recognition rate. The performance of the proposed method is demonstrated using the ORL database and two objective metrics PSNR and SSIM. The experiments show that the proposed method gives better results than state of the art classical machine learning competitors.

**Keywords:** Machine learning; Schur decomposition; Image denoising; Wiener filter; Face recognition.

## INTRODUCTION

Face recognition is a challenging problem that has been widely studied in the field of pattern recognition and computer vision. Nowadays, face recognition has made great progress for various potential applications in security and emergency<sup>1,2,3</sup>, law enforcement<sup>4</sup>, video surveillance<sup>5,6</sup>, and access control<sup>7</sup>, etc. Most of these methods failed to handle the various degradations under certain uncontrolled conditions, including varying lighting, poses, facial expressions, and noise, where the performance of face recognition system would drop significantly. Several works have been carried out towards the illumination, pose, and noise problems and also achieve good results<sup>8,9,10</sup>.

Existing research studied the effects of face image denoising and enhancement methods on the face recognition performance. In<sup>11</sup>, the authors propose an algorithm for denoising the degraded face image sequence in the principal component analysis (PCA) domain for recognizing this face. They first apply a temporal

filter that performs motion compensation combined with a weighted average filter, then an adaptive spatial filter realized by PCA transformation.

In the work<sup>12</sup>, the authors show that the solution of denoising process using the autoencoder networks based on the ORL face database. The proposed method can support face recognition systems designed for use in an outdoor environment as the preprocessing stage and it can provide the effective results after training process.

The authors in<sup>13</sup> propose a carefully designed deep neural network coined noise-resistant network (NR-Network) for face recognition under noise. They present a multi-input structure in the final fully connected layer of the proposed NR-Network to extract a multi-scale and more discriminative feature from the input image. To address the noise problems, we propose in this paper a novel method to recognize the degraded face images. Since the various features contained in image are different, it

may manipulate these features differently. Therefore, the proposed approach uses the schur decomposition to separate the small features from the large ones. The Schur decomposition method is widely used for face recognition<sup>14-15</sup> for its numerical stability<sup>16</sup>. The face recognition approach proposed in<sup>17</sup> uses the schur decomposition with PCA and their experiments showed the discriminate power of the schur decomposition for face recognition.

## EXPERIMENTAL

### Proposed method

Most of face recognition methods suffer from degradations such as noise and blur that can affected image.

To address these problems, we have proposed a method to recognize the noised face images.

The structures contained in an image are different, so, it is appropriate to treat them differently. The diagram of the proposed method is shown in the figure (Fig1).

The main tasks of the proposed noisy facial image recognition algorithm are the following:

*Features extraction:* we utilize the schur decomposition for computing schurvalues and schurvectors that are used to separate the small features from the large ones. To show the efficiency of this method for face representation, we compared it with the learning methods that are in the same context: Eigenfaces<sup>18</sup>, Fisherfaces<sup>18</sup> and Laplacianfaces<sup>19</sup>.

*Features denoising:* the used filter called adaptive wiener filter (AW filter) is adapted according to each feature (small and large) where noise is removed smoothly in the small features for preserving the details and edges using 3x3 wiener filter mask, and it is removed strongly in the large features using 5x5 wiener filter mask.

*Features classification:* the face recognition is performed using the Nearest Neighbors classifier with Euclidiene distance for the four machine learning methods. It is the standard method for classification and often used in many pattern recognition applications.

### Test of the experimental results

The proposed algorithm is tested on the ORL database<sup>20</sup>. These images are corrupted by white additive Gaussian noise with various levels of standard deviation  $\sigma= 5, 10, 15, 20, 25$  and  $30$ . They are denoised with an adaptive wiener filter (AW filter by 3x3 & 5x5) for the following machine learning methods used for features extraction: Eigenfaces, Fisherfaces, Laplacianfaces as well as the proposed method.

The performance of the proposed algorithm for filtering noised facial images (NF image) is evaluated using the PSNR and the SSIM<sup>21</sup>, which provided the quantitative quality evaluation of results.

## RESULTS AND DISCUSSION

We show in table 1 and 2 the quality in terms of PSNR and SSIM of the denoised images using the proposed method.

**Table 1 PSNR of images treated by different algorithms with different Gaussian noise levels**

$\sigma$	5	10	15	20	25	30
NF image	29.73	27.06	25.82	23.76	22.03	19.40
AW filter+ Eigenfaces	30.45	30.74	28.62	26.44	23.82	20.95
proposed method	35.52	34.24	33.75	31.55	29.21	26.78
AW filter+ Fisherface	34.10	33.56	31.60	29.45	27.20	26.22
AW filter+ Laplacianfaces	35.12	33.85	32.35	30.10	29.05	26.20

**Table 2 SSIM of images treated by different algorithms with different Gaussian noise levels**

$\sigma$	5	10	15	20	25	30
NF image	0.957	0.954	0.948	0.936	0.897	0.865
AW filter+ Eigenfaces	0.970	0.968	0.962	0.957	0.934	0.917
proposed method	0.975	0.972	0.967	0.963	0.946	0.941
AW filter+ Fisherface	0.971	0.966	0.961	0.955	0.947	0.937
AW filter+ Laplacianfaces	0.970	0.968	0.963	0.948	0.934	0.931

Experimental results demonstrate a significant improvement of the proposed algorithm over the tested ones, due to its ability to separate the various features effectively and to perform an adaptive denoising process for each feature in the facial image.

**Table 3 Recognition rate of facial image attracted with Gaussian**

noise $\sigma=2$	
Methods	Recognition rates
AW filter+Eigenfaces	87.9
proposed method	91.8
AW filter+Fisherfaces	88.2
AW filter+Laplacianfaces	89.7

The face recognition rates are shown in table above and from that, it is obvious that Schurfaces outperforms the other approaches in the same context. So, the denoised image with good quality leads to a better recognition rate.

## CONCLUSIONS

Image denoising is a preprocessing step in the face recognition field. In this work, we developed a denoised facial image algorithm for face recognition, where the schur decomposition is used to learning the subspace and to dissimilate the small features from the large ones. Then, each feature is filtered by an adaptive wiener filter, so that, the small features are smoothed with 3x3 wiener filter mask, and the large features are enhanced with 5x5 wiener filter. The recognition process uses the Nearest Neighbors classifier to determine the identity of query facial image.

The experimental results show the performance of machine learning in biometric systems that the Schurfaces has the high discriminate power and the denoising algorithm has achieved higher noise removal gain as compared with the tested algorithms. The quantitative metrics (PSNR and SSIM) and the recognition rate demonstrate these results. In future, we will focus on deep subspace learning techniques to improve face recognition accuracy.

## AUTHOR INFORMATION

### Corresponding Author

\*Fella BERRIMI

Email address: [fellaber@yahoo.fr](mailto:fellaber@yahoo.fr)

## REFERENCES

1. Z. Xu, C. Hu and L. Mei, Video structured description technology based intelligence analysis of surveillance videos for public security applications, *Multimed. Tools Appl.*, 2015, 75(19), 1-18.
2. Z. Xu, Y. Liu and H. Zhang et al., Building the multi-modal

- storytelling of urban emergency events based on crowdsensing of social media analytics, *Mob. Netw. Appl.*, 2017, 22(2), 218-227.
3. Y. Yang and Z. Xu et al., A security carving approach for AVI video based on frame size and index, *Multimedia Tools Appl.*, 2017, 76(3), 3293-3312.
4. D. Mcallister, Law Enforcement Turns to Face-Recognition Technology, *Information Today*, 2007, 24(5).
5. Z. Yan, Z. Xu and JD, The Big Data Analysis on the Camera-based Face Image in Surveillance Cameras, *Intell. Autom. Soft Comput.*, 2016, doi: 10.1080/10798587.2016.1267251.
6. Z. Xu, et al., The big data analytics and applications of the surveillance system using video structured description technology, *Clust. Comput.*, 2016, 19(3), 1283-1292.
7. S.J. Mckenna and S. Gong, Non-intrusive person authentication for access control by visual tracking and face recognition, *Lect. Notes Comput. Sci.*, 2006, 1206, 177-183.
8. H. Roy and D. Bhattacharjee, Local-gravity-face (LG-face) for illumination-invariant and heterogeneous face recognition, *Info. Forensics Secur. IEEE Trans.*, 2016, 11(7), 1-1.
9. X. Wang, Q. Ruan and Jin, et al., Three-dimensional face recognition under expression variation, *EURASIP J. Image Video Process.*, 2014, 54(1), 1-11.
10. M.H. Siddiqi et al., Human facial expression recognition using curvelet feature extraction and normalized mutual information feature selection, *Multimedia Tools Appl.*, 2016, 75(2), 935-959.
11. F. Berrimi, K. Benmahammed and R. Hedli, Denoising of degraded face images sequence in PCA domain for recognition, *Journal of King Saud University - Computer and Information Sciences*, 2021, 33(7), 836-843.
12. N. M. Tun, A. I. Gavrilov and N. L. Tun, Facial Image Denoising Using Convolutional Autoencoder Network, 2020 International Conference on Industrial Engineering, Applications and Manufacturing (ICIEAM), Sochi, Russia, 2020, doi: 10.1109/ICIEAM48468.2020.9112080
13. H. Ge, Y. Dai, Z. Zhu and B. Wang, Robust face recognition based on multi-task convolutional neural network, *Math Biosci Eng*, 2021, 18(5), 6638-6651, doi: 10.3934/mbe.2021329.
14. F. Song, D. Zhang, and J. Yang, A novel dimensionality - reduction approach for face recognition, *Neurocomputing*, 2006, 69, 13-15, 1683-1687.
15. G. Wang and W. Zhang, Neighborhood preserving schur discriminant analysis, *Inf. Technol. J.*, 2011, 10, 12, 2464-2469.
16. S. Michael and P. Van Dooren, Stability issues in the factorization of structured matrices, *SIAM J. Matrix Anal. Appl.*, 1997, 18, 1, 104-118.
17. R. Balakrishnan, R. Kannan, S. Kannaiyan, and S. Swaminathan, Deity face recognition using schur decomposition and hausdorff distance measure, In *Proc. IEEE 56th Int. Midwest Symp. Circuits Syst. (MWSCAS)*, Aug. 2013, 1184-1187.
18. P. N. Belhumeur, J. P. Hespanha, and D. Kriegman, Eigenfaces vs. Fisherfaces: Recognition using class specific linear projection, *IEEE Trans. Pattern Anal. Mach. Intell.*, Jul. 1997, 19, 7, 711-720.
19. X. He, S. Yan, Y. Hu, P. Niyogi, and H.-J. Zhang, Face recognition using laplacianfaces, *IEEE Trans. Pattern Anal. Mach. Intell.*, Mar. 2005, 27, 3, 328-340.
20. <https://www.face-rec.org/databases/>
21. F. Weber, Some Quality Measures for Face Images and Their Relationship to Recognition Performance, Technical report, National Institute of Standards and Technology, Gaithersburg, MD (2006).

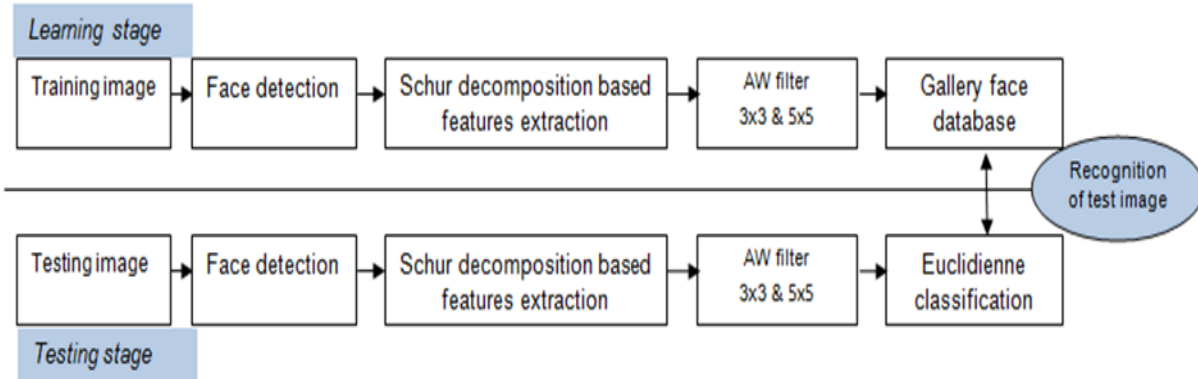


Fig. 1 Diagram of proposed method



# Convolutional Neural Network for detecting Alzheimer's disease in the early stages from Magnetic Resonance Imaging

Skander Hamdi,<sup>a,\*</sup> Abdelouahab Moussaoui,<sup>a</sup> Mourad Ousalah,<sup>b</sup> Mohamed Saidi<sup>b</sup>

<sup>a</sup>Department of Computer science, University of Ferhat Abbas Setif 1, Setif-19000, Algeria

<sup>b</sup>Department of Computer science and engineering, University of Oulu, Oulu, Finland

**ABSTRACT:** Alzheimer's disease has taken a large healthcare concern nowadays, with about 50 million people living with the disease in 2020. The development of the disease can be slowed down by early diagnose. Brain MRI images have been exploited for early diagnosing due to their availability of a set disease related features. In this work, a deep learning model was proposed to classify four (4) early stages of Alzheimer's disease. Our model reached an accuracy of 95.66%.

**Keywords:** Alzheimer's disease; Artificial intelligence; Medical imaging; Magnetic Resonance Imaging (MRI); Deep learning; Convolutional neural networks.

## INTRODUCTION

Alzheimer's disease (AD), the most prevalent form of dementia, is a significant healthcare concern in the 21st century. According to the AD international federation, the number of people living with this disease has reached about 50 million in 2020. Efforts have been undertaken to create early detection techniques, particularly at pre-symptomatic phases, to limit or prevent disease development. Neuroimaging solutions including Magnetic Resonance Imaging (MRI) and Positron Emission Tomography (PET) have been exploited to detect early cases of Alzheimer's dementia. With the development of artificial intelligence techniques, brain images have been collected and exploited to classify several diseases, including Alzheimer's using deep learning and transfer learning techniques. Kanghan O. et al.<sup>1</sup> proposed a volumetric convolutional neural network (CNN) model for four binary classification tasks AD vs. normal control (NC), progressive mild cognitive impairment (pMCI) vs. NC, stable mild cognitive impairment (sMCI) vs. NC and pMCI vs. sMCI using ADNI dataset, a convolutional autoencoder based unsupervised learning is used for AD vs. NC, a supervised transfer learning for pMCI vs. sMCI classification task. After, a gradient-based visualization method that approximates the spatial influence of the CNN model's decision was applied to detect the most important biomarkers related to AD and pMCI.

As results, the classification rate of AD is reached at 86.60% and pMCI at 73.95%. Silvia B. et al.<sup>2</sup> used a convolutional neural networks (CNNs) on 3D T1-weighted images from ADNI and privately collected subjects to diagnose AD and mild cognitive impairment who will convert to AD (c-MCI), healthy controls (HC) and stable -MCI (s-MCI). AD vs HC classification test using ADNI dataset only achieved 99% and the combined ADNI + non-ADNI dataset reached 98%. The accuracy of CNNs in distinguishing c-MCI patients from s-MCI patients was up to 75%. Iago Richard R. S. et al.<sup>3-4</sup>, tried to distinguish Alzheimer's patients from those who are healthy. Alzheimer's Disease Interval Minimum Resonance (MIRIAD) database was utilized to validate the suggested technique. Convolution layers in the proposed CNN architecture are designed to extract the best features from the chosen region. Selected features are then placed in a vector for learning and pattern detection by another classifier in the proposed architecture's final layer. Finally, the data is partitioned using the 10-fold cross-validation technique and trained with different parameters using the random forest, support vector machine (SVM), and k-nearest neighbor (k-NN) algorithms. For these methods, the precision results are 0.8832, 0.9607, and 0.8745, respectively. Another study from J. Venugopalan et al. in reference <sup>5</sup>, proposed multimodal deep

learning models, stacked denoising auto-encoders for feature extraction from clinical and genetic data and 3D-convolutional neural networks (CNNs) for imaging data. The proposed method outperforms baseline models. T. Anh Tuan et al.<sup>6</sup> proposed an efficient diagnosing system from brain MRI scans, divided into two phases: segmentation and classification. Segmentation is performed by a model that combines Gaussian Mixture Model (GMM) and Convolutional Neural Network (CNN) while the classification is done by combining Extreme Gradient Boosting (XGBoost) and Support Vector Machine (SVM). In this work, we will propose a new convolutional neural network (CNN) architecture for early classifying AD stages: Moderate-Dementia, Non-Dementia, Very-Mild-Dementia, and Mild-Dementia. The goal is to achieve the best performance metrics in terms of Accuracy, Precision, Recall, Area Under Curve (AUC), and F1-Score.

## EXPERIMENTAL

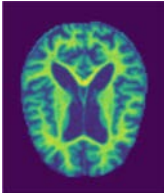
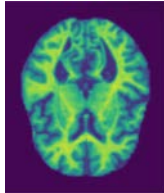
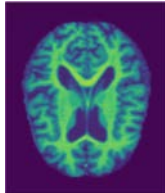
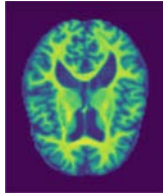
### Dataset

In this work, we used a recently published dataset available on Kaggle platform<sup>7</sup>. The dataset contains 6400 MRI images belonging to the 4 above-mentioned classes. Table.1 shows samples of each class with the total number of samples for each one.

### Data augmentation

As our proposition is a deep learning technique, the training

**Table 1. Sample of each class and the corresponding number of classes**

Moderate-Dementia	Non-Dementia	Very-Mild-Dementia	Mild-Dementia
64 images	3200 images	2240 images	896 images
			

phase needs a sufficient set of data. Therefore, some of image data augmentation techniques are applied (mirror, scale,

rotation). Figure.1 illustrates the applied techniques.

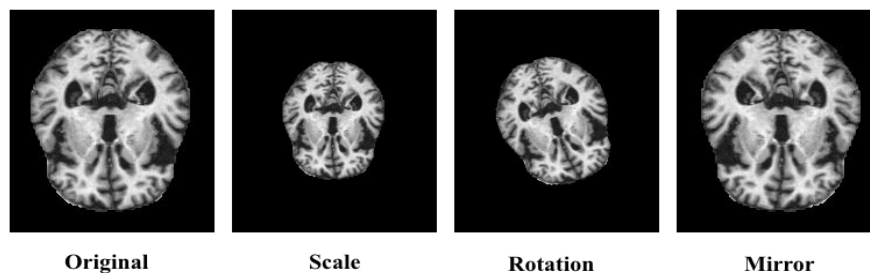


**Fig.1 Example and illustration of the applied data augmentation**

### CNN architecture

We propose a CNN architecture presented in Table.2. Our model is trained on Kaggle platform due to the available hardware resources. To validate our proposition, K-Fold cross-validation with  $k = 5$  is used. The used hyper-parameters are described in Table.3. Data is split into 80% for training and the rest for

validation and test.

## RESULTS AND DISCUSSION

After training and validating our model in around 5.25 hours, the overall of the above-mentioned evaluation metrics (Accuracy, Precision, Recall, AUC, F1-Score) are obtained and calculated. Table.4 summarized all obtained results at each fold for

validation as well as the average of training performance. We note the importance of using regularization and normalization

blobs (Dropout and Batch Normalization) in preventing overfitting.

**Table 2. The proposed CNN architecture has 4 blocs, the first three blocks are used for auto feature extraction while the latest one is for feature learning phase. We note that all activation functions are ReLU and only the latest one is softmax.**

Bloc_1	Bloc_2	Bloc_3	Bloc_4
Input (224x224x3)	Conv2D (256, (3,3))	Conv2D (512, (3,3))	Dense (256)
Conv2D (128, (3,3))	MaxPool2D(2,2)	MaxPool2D(2,2)	BatchNorm
MaxPool2D(2,2)	BatchNorm	BatchNorm	Activation
BatchNorm	Activation	Activation	Dropout(0.3)
Activation	Dropout(0.3)	Dropout(0.3)	Dense(4)
Dropout(0.3)			Activation(softmax)

**Table 3. The used hyper-parameters. We reduce the learning rate after 20 epochs if there is no improvement in the model accuracy i.e.  $new\_lr = 0.7 * current\_lr$ .**

Optimizer	Batch size	Epochs	Learning rate reduction factor
Adam	64	270	0.7 after every 20 epochs if there is no improvement

**Table 4. Proposed CNN model training and validation results.**

	Accuracy	Precision	Recall	AUC	F1-Score
<b>Train</b>	<b>0.9997</b>	<b>0.9994</b>	<b>0.9993</b>	<b>0.9999</b>	<b>0.9994</b>
<b>Fold-1</b>	0.9511	0.9030	0.9012	0.9700	0.9021
<b>Fold-2</b>	0.9589	0.9178	0.9178	0.9727	0.9179
<b>Fold-3</b>	0.9594	0.9188	0.9188	0.9799	0.9188
<b>Fold-4</b>	0.9574	0.9149	0.9149	0.9736	0.9149
<b>Fold-5</b>	0.9565	0.9130	0.9130	0.9732	0.9129
<b>Avg+Std</b>	<b>0.95666 ± 0.0029</b>	<b>0.9135 ± 0.0056</b>	<b>0.9131 ± 0.0063</b>	<b>0.9738 ± 0.0032</b>	<b>0.9133 ± 0.0059</b>

## CONCLUSIONS

Deep learning architectures, especially CNN, have proven their effectiveness in dealing with medical images. Many models have been built to classify many diseases. In this work, we trained a CNN model that classifies AD dementia MRI images into four early disease-stage classes: Mild-Dementia, No-Dementia, Very-Mild-Dementia, and Moderate-Dementia. It is very important to early diagnose AD to attribute the appropriate treatment which can slow the disease development. Our proposed model reached an accuracy of 95.66%, 91.35%, 91.31%, 97.38%, and 91.33% for precision, recall, AUC, and F1-Score respectively.

## AUTHOR INFORMATION

### Corresponding Author

\*Skander Hamdi

Email address: [skander.hamdi@univ-setif.dz](mailto:skander.hamdi@univ-setif.dz)

## REFERENCES

1. K. Oh, Y.-C. Chung, K.W. Kim, W.-S. Kim, I.-S. Oh, Classification and Visualization of Alzheimer's Disease using Volumetric Convolutional Neural Network and Transfer Learning, Sci. Rep. 9 (2019) 18150. <https://doi.org/10.1038/s41598-019-54548-6>.
2. S. Basaia, F. Agosta, L. Wagner, E. Canu, G. Magnani, R. Santangelo, M. Filippi, Automated classification of Alzheimer's disease and mild cognitive impairment using a single MRI and deep neural networks, NeuroImage Clin. 21 (2019) 101645.

- <https://doi.org/https://doi.org/10.1016/j.nicl.2018.101645>.
3. I.R.R. da Silva, G. dos S.L. e Silva, R.G. de Souza, M.A. de Santana, W.W.A. da Silva, M.E. de Lima, R.E. de Souza, R. Fagundes, W.P. dos Santos, Chapter four - Deep learning for early diagnosis of Alzheimer's disease: a contribution and a brief review, in: H. Das, C. Pradhan, N.B.T.-D.L. for D.A. Dey (Eds.), Academic Press, 2020: pp. 63–78. <https://doi.org/https://doi.org/10.1016/B978-0-12-819764-6.00005-3>.
  4. D. Pan, A. Zeng, L. Jia, Y. Huang, T. Frizzell, X. Song, Early Detection of Alzheimer's Disease Using Magnetic Resonance Imaging: A Novel Approach Combining Convolutional Neural Networks and Ensemble Learning, *Front. Neurosci.* . 14 (2020) 259. <https://www.frontiersin.org/article/10.3389/fnins.2020.00259>.
  5. J. Venugopalan, L. Tong, H.R. Hassanzadeh, M.D. Wang, Multimodal deep learning models for early detection of Alzheimer's disease stage, *Sci. Rep.* 11 (2021) 3254. <https://doi.org/10.1038/s41598-020-74399-w>.
  6. T.A. Tuan, T.B. Pham, J.Y. Kim, J.M.R.S. Tavares, Alzheimer's diagnosis using deep learning in segmenting and classifying 3D brain MR images, *Int. J. Neurosci.* (2020) 1–10. <https://doi.org/10.1080/00207454.2020.1835900>.
  7. Kaggle platform <https://www.kaggle.com/yasserhessein/dataset-alzheimer>
-





2021

# A Robust Deep Model Based on the Attention Mechanism for the Classification of X-ray images Chest of Covid-19's Patients

Nabila Frahta,<sup>a,\*</sup> Abdelouahab Moussaoui,<sup>b</sup> Khier Benmahammed<sup>c</sup>

<sup>a</sup> Sciences and Technology Department, Ferhat Abbas University, Sétif 19000, Algeria

<sup>b</sup> Computer Sciences Department, Ferhat Abbas University, Sétif 19000, Algeria

<sup>c</sup> Electronics Department, Ferhat Abbas University, Sétif 19000, Algeria

**ABSTRACT:** Medical imaging has become an indispensable tool for any clinical examination. In fact, the diagnosis has become much more precise with the use of images, like pathologies such as Covid-19 pandemic which continues to have a big influence on the health and daily life of the global population. The most important step for stopping Covid-19 is to detect infected patients effectively and impose immediate isolation. Patients infected by Covid-19 were found to present abnormalities in X-ray images chest, which makes it possible to detect Covid-19 cases in clinical medicine were computed X-ray images chest provides useful information for radiologists to diagnose Covid-19. In this paper, we propose a new deep neural architecture to classify a Covid-19 patient. Our architecture is based on attention model and EfficientNet architecture. We propose a new deep architecture based on EfficientNetB3-V2 to which we have added an attention mechanism. Our results are more reliable and explainable than those of traditional deep learning-based classification models. Experimental results show that our approach is able to achieve a good performance with an accuracy of 0.98 in comparison with other models such as VGG16, DenseNet21, Inception V3, Resnet50 and MobileNet V2.

**Keywords:** Covid-19; X-ray images chest; Deep learning; Attention mechanism; CNN models, EfficientNet.

## INTRODUCTION

Coronaviruses, a family of viruses, cause infection and consequently illness ranging from the common cold to severe diseases like Severe Acute Respiratory Syndrome (SARS) and Middle East Respiratory Syndrome (MERS). A novel coronavirus, COVID-19, is the infection caused by SARS-CoV-2. A study by World Health Organization (WHO) proves that COVID-19 virus like SARS cause open holes in lungs and appear like a honeycomb. The first outbreak of Covid-19 was identified in Wuhan, Hubei, China, in December. Within three months (On March 11, 2020) of the first outbreak, WHO declared the COVID-19 a pandemic. By 09 April 2020, this virus affects more than 15.5 lakhs people and more than 90 thousand people lost their lives. The report from Imperial College, London

suggests that more than 90% percent of the world population could have been affected and could have killed 40.6 million people if no mitigation measures have been taken to combat the virus<sup>1</sup>.

People suffering from COVID-19 have moderate respiratory illness that can be cured without any special treatment of antibiotics. However, people facing from medical complications like diabetes, chronic respiratory diseases, and cardiovascular diseases are more likely to suffer from this virus. According to the reports of WHO, common symptoms of COVID-19 are same as that of common flu, which include fever, tiredness, dry cough, and shortness of breath, aches, pains and sore throat<sup>2</sup>. These common symptoms make difficult to detect the virus at an early stage. As this is a virus, so there is no chance that it can be

limited by anti-biotics, which works on bacterial or fungal infections.

The National Institute of Allergy and Infectious Diseases (NIAID) and Rocky Mountain Laboratories (RML) have released some images of COVID-19 virus using scanning and transmission electron microscopy. Figure 2.1 shows the sample images of COVID-19 virus captured by NIAID and RML using different microscopes. Image in Figure 2.1(a) shows the COVID-19 virus captured by scanning electron microscope from a US patient where virus particles are shown in yellow color and emerge from the cells that are shown in blue and pink color. Image shown in Figure 2.1(b) is captured by the transmission electron microscope. This figure is clearly able to illustrate that COVID-19 virus looks similar form outside as most of the corona viruses including SARS and MERS, sharing the bump covered spherical surface<sup>1-2</sup>.

## RELATED WORKS

With the COVID-19 virus affecting the world since December 2019, and the need to identify infections faster, many studies have been carried out especially on the detection of COVID-19 with computer-aided systems. Most of the studies have been carried out using deep learning approaches that have become popular in the last few years, which can speed up the analysis of various medical images. Therefore in the study of Barstugan et al.<sup>3</sup> where classical learning methods are preferred, a new approach has been proposed for the classification of COVID-19. They have extracted features with the help of patches of different sizes as 16x16, 32x32, 48x48, 64x64 from 150 CT images. The best classification accuracy was obtained as 99.68% by classifying the obtained features with an SVM (Support Vector Machines) classifier, with 10-fold cross-validation and GLSZM feature extraction method.

Wang et al.<sup>4</sup> designed a special deep learning-based framework called COVID-Net (a new architecture of CNN). They applied the 1\*1 convolutional deep learning method to the data sets consisting of chest X-ray images into normal, pneumonia, and COVID-19, they use a much larger dataset consisting of 13, 800 CXR images across 13, 645 patient cases from which 182 images belong to COVID-19 patients. The authors report an accuracy of 92.4% overall and sensitivity of

80% for COVID-19.

Nihad et al.<sup>5</sup> proposed a CNN-based method, called PDCOVIDNet Parallel-Dilated convolution-based COVID-19 detection network, for detecting COVID-19 from chest X-ray images. PDCOVIDNet can effectively capture COVID-19 features by dilated convolution in the parallel stack of convolution blocks, we used a total of 2905 chest X-ray images, comprising three cases (such as COVID-19, normal, and viral

pneumonia). The authors claimed the effectiveness of the model compared with some well known CNN architecture and showed precision and recall of 96.58% and 96.59% respectively in a case of COVID-19 detection.

In<sup>6</sup> five pre-trained convolutional neural network-based models (ResNet50, ResNet101, ResNet152, InceptionV3 and Inception-ResNetV2) have been proposed for the detection of COVID-19 using chest X-ray images. We have implemented three different binary classifications (COVID-19, normal, viral pneumonia and bacterial pneumonia). Performance results show that ResNet50 pre-trained model yielded the highest accuracy among five models for used three different datasets (Dataset-1: 96.1%, Dataset-2: 99.5% and Dataset-3: 99.7%).

Halgurd et al.<sup>7</sup> introduced a simple yet an effective CNN model together with testing pre-trained AlexNet for the detection of COVID-19 disease, using their own chest X-ray and CT scan data set while providing accuracy up to 98% via modified pre-trained model and 94.1% accuracy by using the modified CNN.

Farooq et al.<sup>8</sup> developed COVID-ResNet, a deep learning framework for the problem of classifying CXRs into normal, COVID-19, bacterial pneumonia and viral pneumonia. COVIDResNet was trained on a publicly available dataset COVIDx that consists of 68 COVID-19 radiographs from 45 COVID-19 patients, 1,203 healthy patients, 931 patients with a bacterial pneumonia and 660 patients with Non COVID-19 viral pneumonia. This framework is highly sensitive to normal 96.58 % and COVID-19 100 % classes.

Aplostolopoulos et al.<sup>9</sup> transferred some existing object classification models into the COVID-19 classification area. They compared five currently existing models, namely, VGG-19, MobileNet v2, Inception, Xception, and Inception ResNet-v2 were trained using transfer learning on ImageNet, and different neural network architectures were used on top of each architecture. VGG-19 outperforms the other models and has an accuracy of 98.75 % in the two class classification scheme and 93.48 % in the three-class classification scheme.

Kumar et al.<sup>10</sup> presented the use of ResNet152 and seven traditional machine learning classifiers, for the effective classification of COVID-19, including logistic regression, nearest neighbors, decision tree, random forest, AdaBoost classifier, naive Bayes, and XGBoost classifier.

This model has an accuracy of 97.7 % on the XGBost classifier. Boyi Liu et al.<sup>11</sup> proposed an experiment to compare the performance of federated machine learning, between four popular models (Mobile Net, ResNet18, MobileNet-v2, and COVID-Net), by applying them to the patient chest images CXR dataset. These models are designed to recognize COVID-19 pneumonia, the authors used the same parameters for all models, after 100 rounds the authors found that the ResNet18 model is

the fastest model and gives the highest accuracy rate (96.15%, 91.26%), second, the COVID-Net and MobileNet-v2 had the same loss value as COVID-Net and Mobile Net. Non-federated learning was conducted on the same data and it was found that the loss convergence rate caused by using federated learning decreased slightly.

Fatima M Salman et al.<sup>12</sup> proposed deep learning model to identify COVID-19 cases using patient’s chest x-rays images by implementing convolutional neural network CNN deep learning algorithm which based on the algorithm of InceptionV3, they used patient’s chest x-rays datasets contains 130 images of COVID-19 x-ray cases and 130 images for normal cases x-ray, their prediction machine learning model gives 100% prediction accuracy.

From the above Table and the previous literature review study, we notice that most of the studies have used machine learning and deep learning to predict the COVID-19 pandemic.

It can be seen also that all the earlier seen studies used different methods such as GLSZM+SVM and XG-Boos like in<sup>2-10</sup>, CNN and AlexNe like in<sup>7</sup> also one of the previous studies used ensemble on heterogeneous models, i.e, VGG19, ResNet50, MobileNetv2, Inception, Xception in<sup>6-9</sup>, but that approach has some limitations such as that each model requires a separate training session, and an individual model suffers from training many parameters.

To address the most problems, we use a lightweight but effective model EfficientNet since it is 8.4 times smaller and 6.1 times faster than the best existing CNN. Also, to extenuate the limitation related to the computational cost of training multiple deep learning models for ensemble prediction, we force large changes in model weights through the recurrent learning rate, creating model snapshots in the same training, and further apply an ensemble to make the proposed architecture more robust.

### PROPOSED METHOD

Convolutional neural networks (CNNs) are commonly developed at a fixed resource cost, and then scaled up in order to achieve better accuracy when more resources are made available. For example, ResNet can be scaled up from ResNet-18 to ResNet-200 by increasing the number of layers, and recently, GPipe achieved 84.3% ImageNet top-1 accuracy by scaling up a baseline CNN by a factor of four. The conventional practice for model scaling is to arbitrarily increase the CNN depth or width, or to use larger input image resolution for training and evaluation

#### EfficientNet Architecture

The effectiveness of model scaling also relies heavily on the baseline network. So, to further improve performance, we have

also developed a new baseline network by performing a neural architecture search using the AutoML MNAS framework, which optimizes both accuracy and efficiency (FLOPS). The resulting architecture uses mobile inverted bottleneck convolution (MBConv), similar to MobileNetV2 and MnasNet, but is slightly larger due to an increased FLOP budget. We then scale up the baseline network to obtain a family of models, called EfficientNets.

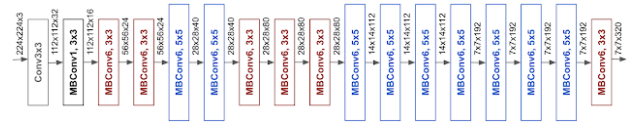


Fig. 1 The architecture for our baseline network EfficientNet-B0 is simple and clean, making it easier to scale and generalize

The other EfficientNet CNN models are defined through the model scaling idea and are, hence, deeper and wider. For example, EfficientNet-B3-V2 model is shown in Fig. 2, where IRC means that the MBConv block uses an inverted residual connection. Similar, to EfficientNet-B0 it used MBConv1 and MBConv6 modules.

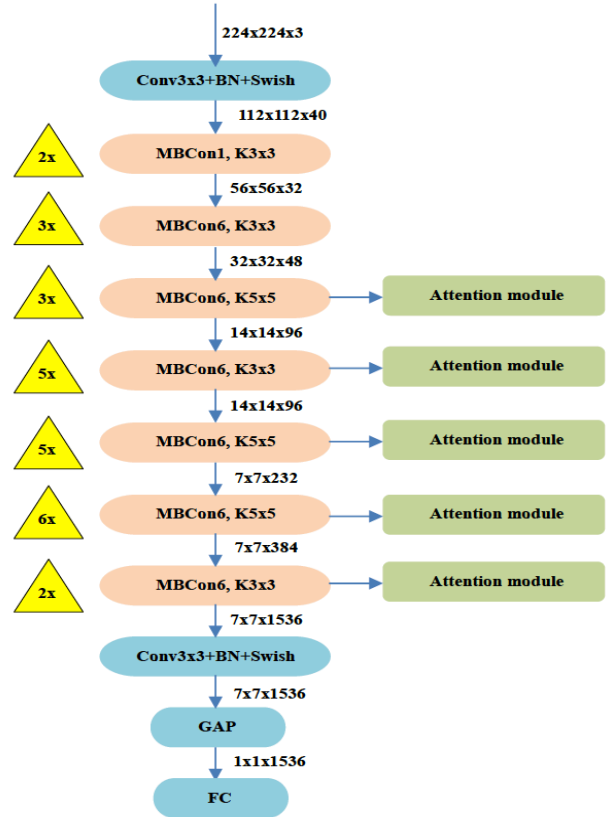


Fig. 2 The proposed EfficientNet-B3-V2 where the attention mechanism is incorporated at some intermediate layer of the model

Notice that the neurons in the first convolutional layer capture the features in a small area in the image. If the size of the filters used is 3x3 than that will be the size of this area.

We call this area the receptive field of that neuron in the image. In the next layer of the CNN each neuron is convolved with the same 3x3 area in the previous layer but that translates to a large receptive field in the input image. As we go deeper and deeper into the network each neuron corresponds to a larger and larger receptive field.

However, another idea is to incorporate the attention module at lower convolutional layers because the higher layers' features represent very large receptive fields with highly overlapping regions, which means the attention mechanism may not be effective with these features. Thus, we also propose to investigate other options as shown in Fig. 1, where the attention module is added as a second branch in the network starting from different MBConv blocks.

As can be seen in Fig. 2, we investigate several positions for the attention branch including MBConv blocks 9,14, 19, 25, and the last 27th block. In other words, the model now has two separate branches. This also means that the model has two outputs which must be optimized jointly. The final proposed model called EfficientNet-B3, is shown in Fig. 2, where the attention module is connected to Block 19.

## EXPERIMENTAL

### Dataset description

In this work, two types of COVID-19 datasets were used:

Dataset 01— We have used the chest x ray images dataset from [47]. There are 9545 images in this dataset and is split into two partitions. 4045 for covid images and 5500 for non covid. 80% of them made up the training phase, 10% the testing phase and 10% the validation phase, as shown in table1 and Fig. 3.

**Table 1. Distribution of images in training testing and validation sets for Dataset 1**

Dataset 1	Training	Testing	Validation	Total
Covid	3033	506	506	4045
Non Covid	4125	688	687	5500
Total	7158	1194	1193	9545

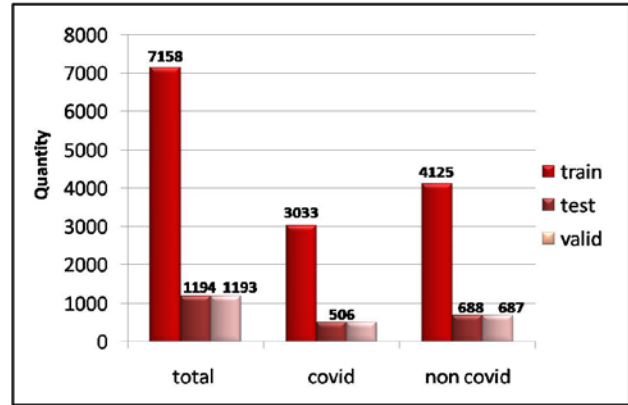


**Fig 3 Bar chart showing the distribution of images in training testing and validation sets for Dataset 1**

Dataset 02 — is the dataset used to train and evaluate model by merging two other public datasets: RSNA Pneumonia Detection Challenge dataset And COVID-19 Image Data Collection. The new dataset, called COVIDx, is designed for a classification problem and contemplates three classes:

Normal, Pneumonia, and COVID-19. The dataset has a total of 13 677 images, approximately 80% of them made up the training phase, 10% the testing phase and 10% the validation phase, as shown in Table 2 and Fig 4.

**Table 2. Distribution of images in training testing and validation sets for Dataset 2**

Dataset 1	Training	Testing	Validation	Total
Covid	2568	428	428	3424
Pneumonia	1009	168	168	1345
Normal	6680	1114	1114	8908
Total	10257	1710	1710	13677

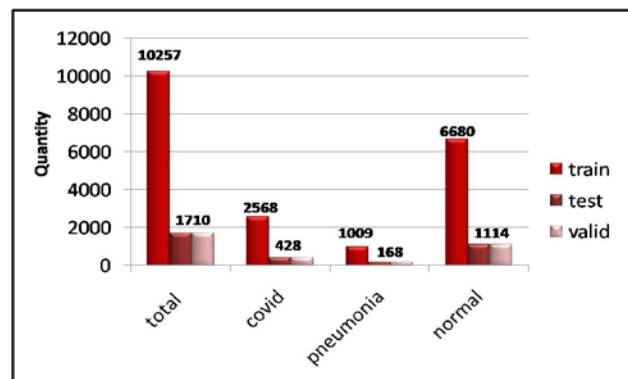


**Fig 4 Bar chart showing the Distribution of images in training testing and validation sets for Dataset 2**

### Data preparation

In the present study, there is a need to make X-ray scan images compatible with the pre-trained transfer learning-based model. For this, pre-processing steps: change in input image data type, resizing of the input images, and normalization of input images. Initially, the input images are read into a numerous image format (jpeg, jpg, png) and resized to 224x224x3. In the preprocessing stage, X-ray scan images in the input dataset are of different sizes, thus to maintain the uniformity the input images are resized to 224x224x3, and the order of the color channels was changed from the default BGR to RGB to prepare the images for processing.

### Data augmentation

data augmentation is an important step to achieve meaningful information and accurate classification. which the values of the pixels of each image were scaled by transferring to (0,255) such that the images would be standard during training, and in order to enhance the size and quality of the training dataset. Specifically, we utilized the Image Data Generator class of Keras (<https://keras.io>). The augmentation options included geometrical distortions such as small rotations, shearing and zooming up to a factor of 20%.

### Model and architecture interpretation

The main task in the experiment is image classification. There are already many classic neural networks in this field, and there are models specifically designed for the recognition of COVID-19 pneumonia CXR images. 6 models are used in the experiments (EfficientNetB3-V2, DenseNet121, Vgg16, ResNet50, InceptionV3, MobileNetV2). The model is a sequential which allows us to create the model layer-by-layer. In these layers, flatten layers, batch normalization layers, and dropout layers with 30% dropout rate were performed as well in our case. We will be using the Rectified linear unit (ReLU) activation function for all the layers except the final output layer. ReLU is the most common choice for activation function in the hidden layers and has shown to work pretty well. The final output layer is another dense layer which has number of neurons equal to the number of classes. we employed a SoftMax for a multi-class classification problem, and sigmoid for binary class classification problem. The model is compiled with categorical cross entropy loss function (multi-class classification).

We set the number of epochs to 21 epochs, the learning grate is 1e-5, and the optimizer we used Nadam. Training-related parameters are shown in Table 3.

We trained the model using a GPU for SpeedSup the training process, also we used the accuracy metric is used to evaluate the model. We save the best model to be used to make predictions accuracy By applying two different attention (lime attention and grad cam attention).

Table 3. Parameters related to model training

Parameter	Value
Dropout Rate	0.30
Batch size	50
# Epochs	21
Optimize	Nadam
Learning rate	0.005

### Attention maps

Although the modular architecture of EfficientNetB0 model provides encouraging recognition performance for image classification, there are still several issues where it is challenging to reveal why and how to produce such impressive results. Due to its black-box nature, it is sometimes contrary to apply it in a medical diagnosis system where we need interpretable system visualization techniques assist in illustrating the basis of prediction of the model. There are many attention maps and visualization techniques for example Gradient-weighted Class Activation Mapping (Grad-CAM), saliency maps (SM), local interpretable model-agnostic explanations (LIME), and a lot more. In this article, Grad-CAM and LIME techniques are utilized to present the model perception of identifying and classifying and to distinguish between different categories (such as COVID-19, normal, and pneumonia), from X-ray images, where EfficientNetB0 emphasizes correct classification of these photos.

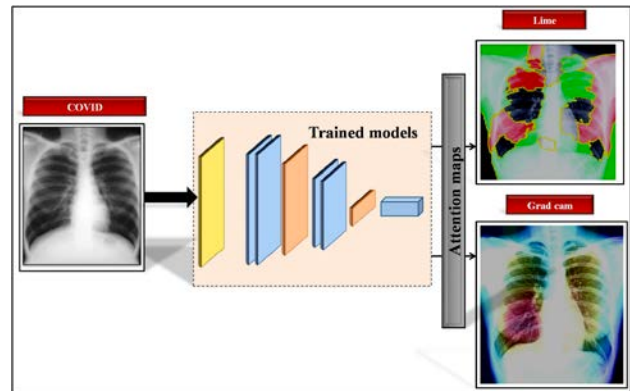


Fig 5 Explanatory scheme for attention maps of dataset 1

Accurate and definitive salient region detection is crucial for the analysis of classification

decisions as well as for assuring the trustworthiness of the results. In order to locate the salient area, Grad-CAM with various illuminations related to feature importance are used, as show in Fig 5 and Fig 6. Bright regions could be defined as regions containing the features that had the most effective role in making

decisions about whether or not to have a disease. As for the Lime method, it works by making alterations on different features on a particular input and seeing which of those alterations make the biggest difference to the output classification.

Thus, highlighting the features most relevant to the network decision. Where the red and green areas in the LIME generated explanation correspond to the regions that contributed against the predicted class and towards the predicted class respectively (Green represents healthy areas, while red represents diseased areas) as we show in Fig 5 and Fig 6.

In this two-way, causality and explainability were included in the study. It was concluded that the developed model could be used in healthcare centers so that would no need to wait long times for the radiologists to interpret the images.

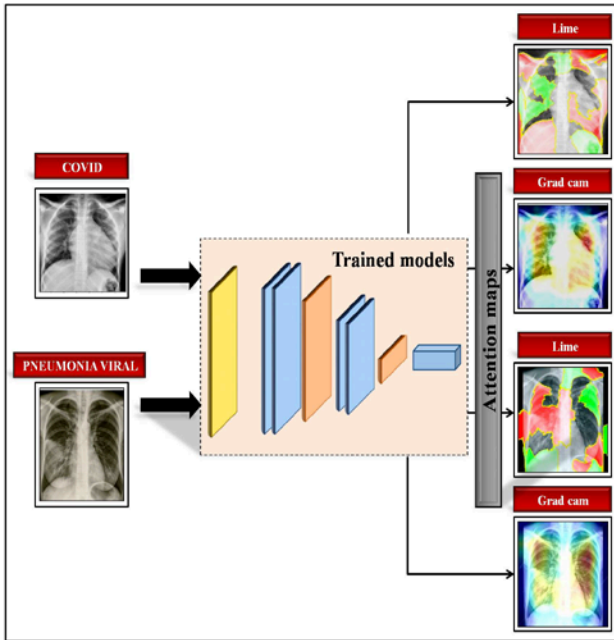


Fig 6 Explanatory scheme for attention maps of dataset 2

## RESULTS AND DISCUSSION

In order to show the results obtained for the six models, we illustrate in what follows the results in terms of precision and error as well as confusion matrix for each of the six models. After analyzing the results obtained, the following remarks are noted: **1.** From Fig 6 and Fig 7 the accuracy of training and testing increases with the number of epochs, this reflects that with each epoch the model learns more information. If the precision is reduced then we will need more information to make our model learn and therefore we must increase the number of epochs and vice versa. Similarly, the decline of loss during the training processes the with the number of epochs.

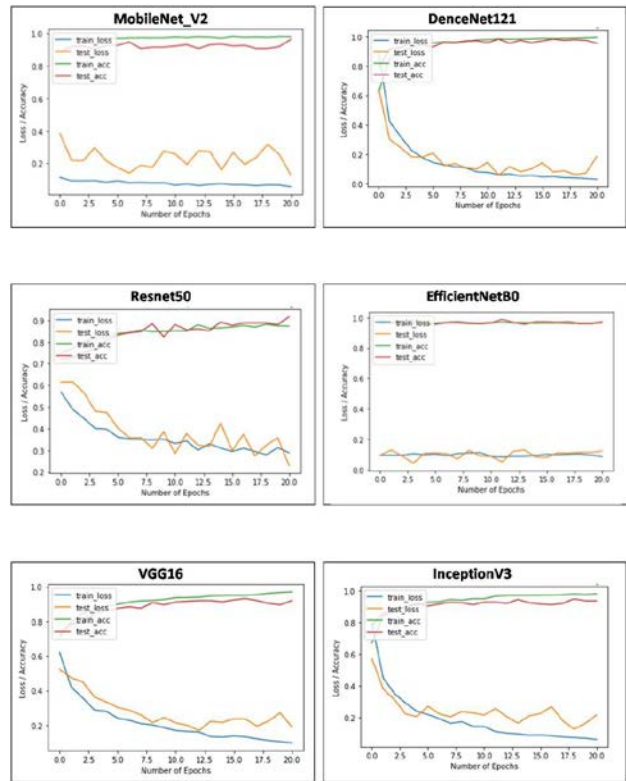


Fig 6 Accuracy and error for six different binary class models [8]

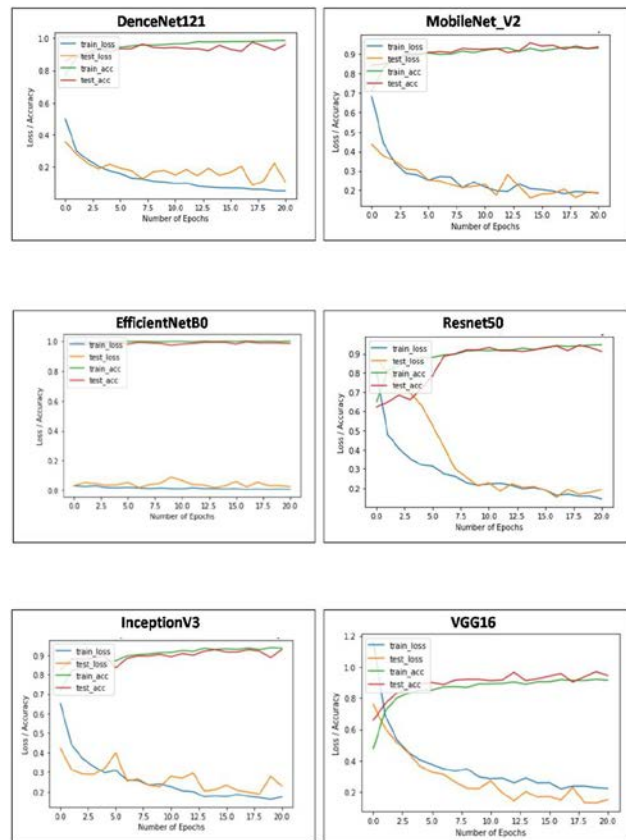


Fig 7 Accuracy and error for six different multi class models

2. Fig 6 and Fig 7 curves showed clear evidence of the absence of overfitting. We also note the convergence in the results of the six models for each of Binary Class and Multiclass in terms of accuracy and loss, as it turns out that the percentage of loss achieved a small percentage in most of the models.

### Confusion matrix

In this study, we used traditional measures to evaluate the performance of the proposed model, using a confusion matrix. Where:

- The True Positive (TP): is the number of correctly predicted COVID-19 /images.
- The False Positive (FP): is the number of mistakenly predicted COVID-19/images and the Positive is the number of cases/images of COVID-19 patients.
- The True Negative (TN): is the number of correctly predicted non-COVID-19 pneumonia cases/images.
- The False Negative (FN): is the number of mistakenly predicted non-COVID-19 /images and The Negative is the number of non-COVID-19 /images enrolled.

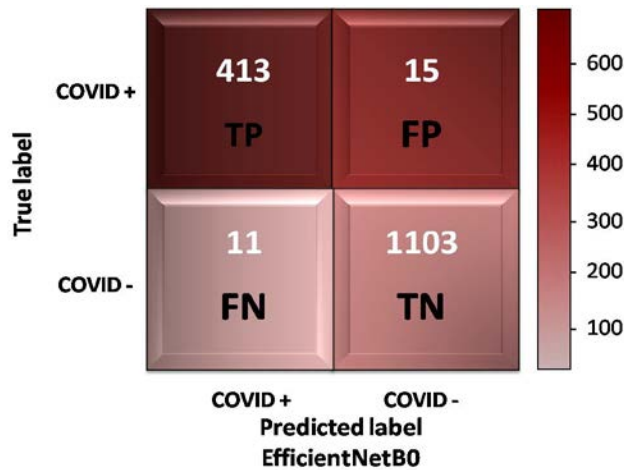


Fig 8 Confusion matrix of EfficientNetB0

By applying the Efficient NetNetB3-V2 model, 314 correctly predicted COVID-19 images were obtained, 11 incorrectly predicted images were obtained, 1103 non-COVID images were correctly predicted and 15 incorrectly predicted non-COVID-19 images were obtained.as show in Fig 8.

Confusion matrix of models are presented in Fig 9 and Fig 10 for Dataset 1 and Dataset 2 respectively.

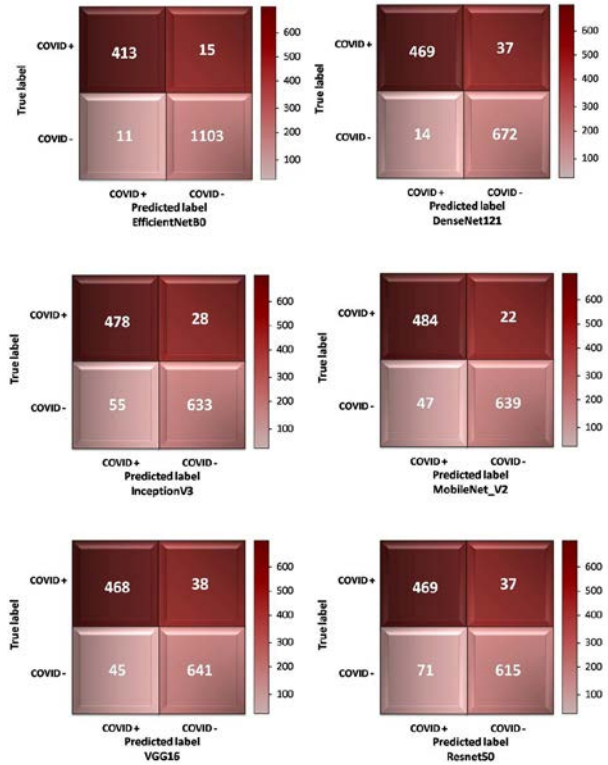


Fig 9 Confusion matrix for each model from dataset 1

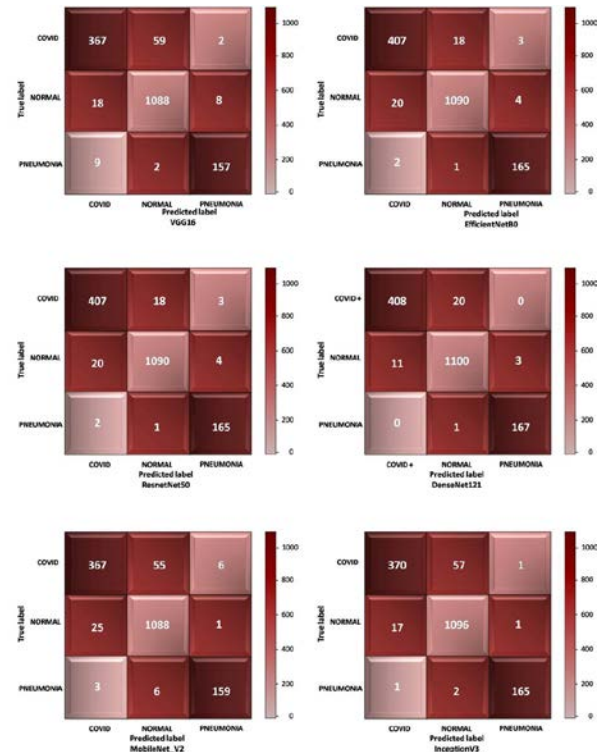


Fig 10 Confusion matrix for each model from dataset 2

Based on this confusion matrix, the sensitivity, specificity, accuracy and F1 score were calculated. Here, sensitivity was defined as the ratio of COVID-19 cases correctly detected by the model to all the actual COVID-19 cases. Specificity was defined as the ratio of the Non COVID-19 cases correctly detected by the model to all the actual Non COVID-19 cases. Moreover, accuracy was defined as the rate of all the COVID-19 and non-COVID-19 cases accurately detected on the basis of the Xray images. In Table 4, we have summarized the proposed model’s comparison for two datasets different (binary class, multi class).

**Table 4. Comparison table of models**

Data Set	Architecture	Accuracy
<b>DataSet 1</b> <b>Binary Class</b>	EfficientNetB3-V2	98.40
	VGG16	92.00
	DenseNet21	96.00
	Inception V3	92.80
	Resnet50	91.60
	MobileNet V2	96.40
<b>DataSet 2</b> <b>Multi Class</b>	EfficientNetB3-V2	97.20
	VGG16	94.40
	DenseNet21	95.60
	Inception V3	93.60
	Resnet50	91.20
	MobileNet V2	93.60

## CONCLUSIONS

This paper presents a brief review of the usage of deep learning and Based on the results, it is demonstrated that deep learning with CNNs may have significant effects on the automatic detection and automatic extraction of essential features from X-ray images, related to the diagnosis of the Covid-19. We conducted X-Ray images training architecture based on EfficientNetB3 augmented with an attention mechanism. This architecture baptized EfficientNetB3-V2 is compared to five different models such as DenseNet21, VGG16, ResNet50, Inception V3 and MobileNetV2.

The experimental results of the comparison between them showed that the EfficientNetB3-V2 produced the best classification accuracy identification among the five popular

models in both binary classification and multiclassification.

This model can be used to help the radiologist to make clinical decisions, due to its unbiased high-accuracy and correctly identified focus region. Attention mapping technology was also used to find out which part of the chest x-ray was most important in diagnosing whether a patient had COVID-19 infection or not, as it greatly helps doctors in detecting and predicting COVID-19 at an early stage.

Future developments include combining the proposed method with some of the novel techniques introduced in the very recent work Channel-Attention-Based mechanism. A second direction is inserting the attention mechanism in every MBConv block of the EfficientNetB3-V2 model.

Finally, another possible improvement is adding attention mechanism by using both CAM and GRAD-CAM at every training epoch to visualize and explain the deep networks via these two techniques in order establish appropriate trust in predictions performance from any stage of models.

## AUTHOR INFORMATION

### Corresponding Author

\*Nabila Frahta

Email address: [frahta.nabila@gmail.com](mailto:frahta.nabila@gmail.com)

## ACKNOWLEDGMENT

This paper and the research behind it would not have been possible without the exceptional support of Professor Abdelouahab Moussaoui. His enthusiasm, knowledge and exacting attention to detail have been an inspiration and kept my work on track from my first encounter with the medical imaging researchers to the final draft of this paper. His generosity and expertise have improved this study in innumerable ways and saved me from many errors; those that inevitably remain are entirely my own responsibility.

## REFERENCES

1. G. Jain, D. Mittal, D. Thakur, MK. Mittal, A deep learning approach to detect Covid-19 coronavirus with X-Ray images.



- Biocybern Biomed Eng*, 2020., 40(4):1391-1405.
2. M. Barstugan, U. Ozkaya, S. Ozturk, Coronavirus (covid-19) classification using ct images by machine learning methods. arXiv preprint arXiv:2003.09424.(2020).
  3. Y. Mohamed, Y. Abdallah, A. Alqahtani, Research in Medical Imaging Using Image Processing Techniques, 2019.
  4. L. Wang, Q.L. Zhong, and A. Wong, Covid-net: A tailored deep convolutional neural network design for detection of covid-19 cases from chest x-ray images. *Scientific Reports* 10.1 (2020): 1-12.
  5. K. Nihad Chowdhury, M. Muhtadir Rahman, and M. Ashad Kabir, PDCOVIDNet: a parallel-dilated convolutional neural network architecture for detecting COVID-19 from chest X-ray images. *Health information science and systems* 8.1 (2020): 1-14.
  6. A. Narin, K. Ceren, and P. Ziyet, Automatic detection of coronavirus disease (covid-19) using x-ray images and deep convolutional neural networks. *Pattern Analysis and Applications*, (2021): 1-14.
  7. S. Halgurd Maghdid, et al., Diagnosing COVID-19 pneumonia from X-ray and CT images using deep learning and transfer learning algorithms. *Multimodal Image Exploitation and Learning* 2021. Vol. 11734. *International Society for Optics and Photonics*.
  8. M. Farooq, and A. Hafeez, Covid-resnet: A deep learning framework for screening of covid19 from radiographs. *arXiv preprint arXiv:2003.14395*.31 Mar 2020.
  9. D. Ioannis Apostolopoulos, and A. Tzani, Mpesiana. Covid-19: automatic detection from x-ray images utilizing transfer learning with convolutional neural networks. *Physical and Engineering Sciences in Medicine* 43.2, 2020.
  10. R. Kumar, R. Arora, V. Bansal, et al., Accurate prediction of COVID-19 using chest X-Ray images through deep feature learning model with SMOTE and machine learning classifiers. *MedRxiv*, 2020.
  11. L. Boyi, Y. Bingjie, Z. Yize, et al., Experiments of federated learning for covid-19 chest x-ray images. arXiv preprint arXiv:2007.05592, 5 Jul 2020.
  12. F. M. Salman, S. S. Abu-Naser, E. Alajrami, B. S. Abu-Nasser, B. A. M. Ashqar, COVID-19 Detection using Artificial Intelligence, 3rd March 2020. *Department of Information Technology. Meshkat*.
-



2021

## Intelligent Vision Navigation of Pioneer 3-DX Mobile Robot

Salim Refoufi,<sup>a,\*</sup> Guezout Farouk,<sup>a</sup> Laghmara Youcef,<sup>a</sup> Doukhi Oualid<sup>b</sup>

<sup>a</sup> Intelligent Systems Laboratory . Faculty of Technology. Ferhat Abbas University, 19000. Setif, Algeria

<sup>b</sup> Center for Artificial Intelligence & Autonomous Systems, Kunsan National University, 558 Daehak-ro, Naun 2(i)-dong, Gunsan 54150, Jeollabuk-do, Korea.

**ABSTRACT:** The work done was about the autonomous navigation of the “Pioneer 3DX” mobile robot, the aim of this project was to remotely control the robot to perform various tasks such as navigation obstacles avoidance, using distance measurement, in addition to visualization using the camera. Our work deals with the issue of autonomous navigation of mobile robots in static or dynamic in door environments like the hospitals. This framework is defined by the specificities of the envisaged applications, which we can summarize by navigation for mobile robots near obstacles.

The work consists of studying and applying the algorithms for the autonomous navigation of mobile robots in a construction site, in order to allow the robot to move from one initial position to another final while avoiding obstacles and collisions.

Our strategy concerns the development of methods inspired by artificial intelligence to ensure optimized navigation while avoiding obstacles in the environment where robots must operate.

We will simulate autonomous navigation in an unknown environment to reach the goal we want to reach while avoiding obstacles, where we will use a Pioneer 3-DX mobile robot equipped with a camera, which will help achieve the desired goals.

We have written a code in Python that gives the robot instructions that allow it to navigate to any place, we specify in our code while avoiding obstacles if there are any. We use ROS (Robot Operating System) that provides services similar to an operating system for robotics as well as operating systems for computers (hardware abstraction, management of competition, processes, etc.) but also functionalities of high level (asynchronous calls, synchronous calls, centralized database, robot configuration system, etc.). Simulation results prove the effectiveness of this method.

**Keywords:** Mobile robot ; Obstacles avoidance; Vision navigation; Mobile camera.

## INTRODUCTION

In recent years, robots have become an important and effective factor in the development of human society. Because of its importance in our daily life.

Robotics is a branch of engineering and science that includes electronics engineering, mechanical engineering and computer science and so on. This branch deals with the design, construction, use to control robots, sensory feedback and information processing<sup>4-7</sup>.

A robot is a reprogrammable, multifunctional manipulator

designed to move material, parts, tools or specialized devices through variable programmed motions for the performance of a variety of tasks<sup>2</sup>.

Interest in mobile robots has increased dramatically in recent years. Men realize that some work previously carried out by humans could be carried out by machines equipped with more or less complex means depending on the type of work to be carried out. These jobs can be arduous, tiring, dangerous or impracticable for humans. Examples include those that must be performed in

hostile environments where the air is unbreathable, in nuclear power plants, in space, in the oceans, or certain repetitive work involving little human intellectual capacity. Various reasons have contributed to the development of Artificial Intelligence and Robotics<sup>3-9</sup>:

- From a purely scientific point of view, techniques and methods have matured and refined.
- Economic needs, within the framework of the capitalist mode of production, pushing towards an increase in profit, the improvement of productivity has always been an imperative for the functioning of the system. This has been further accentuated by economic crises and global competition.

This work is part of the problem of autonomous mobile robot navigation and focuses mainly on a specific type of system and application, in this case, using vision to avoiding obstacles. He thus comes to producing a specific robotic environment where autonomou mobile robots must use camera to support the tasks under this site.

Our work offers a partial view of research topics related to the field of mobile robotics and presents the scientific barriers that remain to be overcome lead to the development of an autonomous robot. The autonomy of the latter requires the perception of the environment. Among these, navigation plays a fundamental role in the interaction of the robot with its changing environment. It consists of determining the path for the robot basing to the data giving by the camera, skirting the fixed obstacles. To perform this task, our approach is to use a mobile camera to detect all the obstacles in front, left or right the robot, the aim being to allow this latter to change position while avoiding obstacles. This method is simulated and several scenarios were tested. The results obtained demonstrate the robustness of the method as well as extended performance.

In this work, we will work on this aspect of mobile robotics by presenting three sections and several steps:

The first section is devoted to the presentation of mobile robots. A general overview on the field of mobile robotics is approached to examine the typology of mobile robots, the different constituent parts and the existing control architectures for a mobile robot.

In the second section, we present an introduction to the program we used: ROS (Android Operating System) and the Python programming language, in addition to an idea of the concept of

open source.

The third section deals with discussing and analyzing simulation results and various experiments to accomplish the task defined by the robot, which is convergence towards the goal and avoiding obstacles.

## EXPERIMENTAL

### *A mobile robot*

An automatic machine that is capable to move around in its environment and is not fixed to one physical location (Fig.1).

Following the degree of autonomy, the means of perception and reasoning, certain robots are capable, under reduced human control, to model their workspace and to plan a trajectory in an environment they did not necessarily know before<sup>8</sup>.

Actually, most sophisticated mobile robots are essentially destined to applications in variable or uncertain environments, often full of obstacles, needing adaptability<sup>1</sup>.



Fig.1 Pioneer P3-AT equipped with arm manipulator

### *Rolling without sliding and non holonomy*

Consider a vertical wheel that rolls without sliding on a level ground, the rolling without sliding results in the zero speed of the point I of the wheel in contact with the ground (Fig.2).

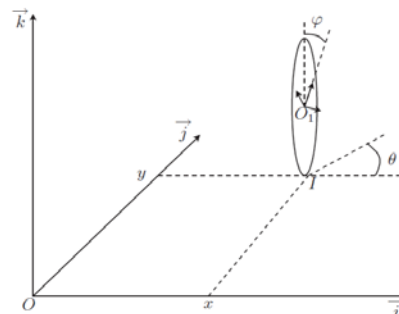


Fig.2 Description of a wheel

With the notations of figure 2, we obtain:

$$\begin{aligned} \vec{v}(I/R_0) &= \dot{x}\vec{i} + \dot{y}\vec{j} + \left( \dot{\theta}\vec{k} + \dot{\varphi}(-\sin\theta\vec{i} + \cos\theta\vec{j}) \right) \wedge (-r\vec{k}) \\ &= (\dot{x} - r\dot{\varphi}\cos\theta)\vec{i} + (\dot{y} - r\dot{\varphi}\sin\theta)\vec{j} = 0 \end{aligned} \quad (1)$$

Where:  $r$  is the radius of the wheel and  $(x, y)$  is the coordinate of the point  $o_1$  in the fixed reference  $R_0 = (o, \vec{i}, \vec{j}, \vec{k})$ . We deduce two constraints:

$$\begin{cases} \dot{x} - r\dot{\varphi}\cos\theta = 0 \\ \dot{y} - r\dot{\varphi}\sin\theta = 0 \end{cases} \quad (2)$$

The model (2) can be transformed to show the speed components in the planes of the wheel and perpendicular to the wheel, the following kinematic constraints are then obtained:

$$\begin{cases} \dot{x}\cos\theta + \dot{y}\sin\theta = r\dot{\varphi} \\ -\dot{x}\sin\theta + \dot{y}\cos\theta = 0 \end{cases} \quad (3)$$

It is interesting to note that by introducing  $v = r\dot{\varphi}$  the rolling speed of the wheel and  $w = \dot{\theta}$  its speed of rotation around the axis  $\vec{k}$ , we form the following model:

$$\begin{bmatrix} \dot{x} \\ \dot{y} \\ \dot{\theta} \end{bmatrix} = \begin{bmatrix} \cos\theta & 0 \\ \sin\theta & 0 \\ 0 & 1 \end{bmatrix} \begin{bmatrix} v \\ w \end{bmatrix} \quad (4)$$

### The differential type robot

We consider the mobile robot of the uni-cycle type shown schematically in Figure 3 this robot is equipped with two fixed drive wheels controlled independently and idle wheels ensuring its stability.

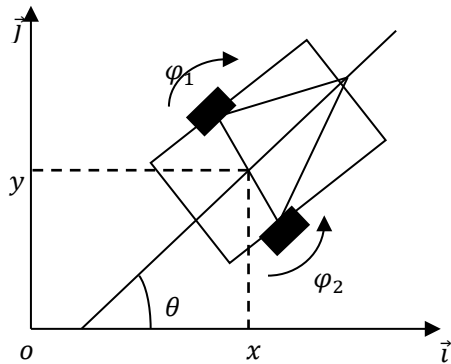


Fig.3 Uni-cycle type robot

Let the abscissa and ordinate  $(x, y)$  of the middle of the axis of

the two drive wheels,  $\theta$  the orientation of the robot,  $r$  the radius of the wheels and  $2R$  the distance between the two drive wheels. Returning to equation (1) and it is easily shown that the non-sliding rolling constraints of each of the controlled wheels are written:

- for the left wheel

$$\dot{x} - R\dot{\theta}\cos\theta - r\dot{\varphi}_1\cos\theta = 0 \quad (5)$$

$$\dot{y} - R\dot{\theta}\sin\theta - r\dot{\varphi}_1\sin\theta = 0 \quad (6)$$

- for the right wheel

$$\dot{x} - R\dot{\theta}\cos\theta - r\dot{\varphi}_2\cos\theta = 0 \quad (7)$$

$$\dot{y} - R\dot{\theta}\sin\theta - r\dot{\varphi}_2\sin\theta = 0 \quad (8)$$

These four constraints are not independent since the difference of the left-hand sides of the equalities (5) and (7) is proportional to that associated with (6) and (8). The last constraint, for example can therefore be omitted. In addition, a constraint is completely integrable. Indeed, we have:

$$\begin{cases} \dot{x}\cos\theta + \dot{y}\sin\theta - R\dot{\theta} = r\dot{\varphi}_1 \\ \dot{x}\cos\theta + \dot{y}\sin\theta + R\dot{\theta} = r\dot{\varphi}_2 \end{cases} \quad (9)$$

Thus, we obtain:

$$2R\dot{\theta} = r(\dot{\varphi}_2 - \dot{\varphi}_1) \quad (10)$$

Which implies:

$$2R\theta = r(\varphi_2 - \varphi_1) + \text{constant} \quad (11)$$

Consequently, there are only two independent constraints left, (5) and (6), of which an equivalent writing is:

$$\begin{cases} \dot{x} = v\cos\theta \\ \dot{y} = v\sin\theta \\ \dot{\theta} = w \end{cases} \quad (12)$$

Where:

- The linear speed of the robot is

$$v = \frac{r}{2}(\dot{\varphi}_1 - \dot{\varphi}_2) \quad (13)$$

- The angular speed of the robot is

$$w = \frac{r}{2R}(\dot{\varphi}_2 - \dot{\varphi}_1) \quad (14)$$

The fact that this system is the same as the model (4) obtained for a single wheel (uni-cycle), which justifies the qualifier uni-cycle often used in the literature.

### Robotic Development Environment

Robotic systems involve many skills such as mechanics, electrical engineering, control, computer vision, and many areas of computing such as real-time computing, parallelism, and networking. Often advances in robotics depend on technological obstacles solved in these scientific fields.

In this section, we begin by describing the software platform and hardware platform used, and then we present the suggested communication mechanisms, simulation programs, and programming language used in the experiment.

### ROS (Robot Operating System)

It is a system that provides services similar to an operating system for robotics as well as operating systems for computers (hardware abstraction, management of competition, processes, etc.) but also functionalities of high level (asynchronous calls, synchronous calls, centralized database, robot configuration system, etc.). ROS is completely open-source and free to users, initially developed by the Stanford Artificial Intelligence Laboratory in 2007, the ROS project was adopted by Willow Labs in 2008 and remains their responsibility<sup>10</sup>.

The basic principle of a robotic OS is to operate in parallel a large number of executable that must be able to exchange information synchronously or asynchronously. For example, a robotic OS must interrogate the robot's sensors at a defined frequency (ultrasonic or infrared distance sensor, pressure sensor, temperature sensor, gyroscope, accelerometer, cameras, microphones, etc.), retrieve this information, process it ( data fusion), pass them to processing algorithms (speech processing, artificial vision, simultaneous localization and mapping, etc.) and finally, control the motors in return. This whole process is carried out continuously and in parallel. On the other hand, the robotic OS must ensure the management of competition to ensure efficient access to the robot's resources<sup>11</sup>.

The ROS Computation Graph is the peer-to-peer network of ROS systems that processes data. The basic features of ROS Computation Graph are nodes, ROS Master, the parameter server, messages, and services<sup>10</sup>.

The following diagram (Fig.4) shows how topics and services work between the nodes and the Master:

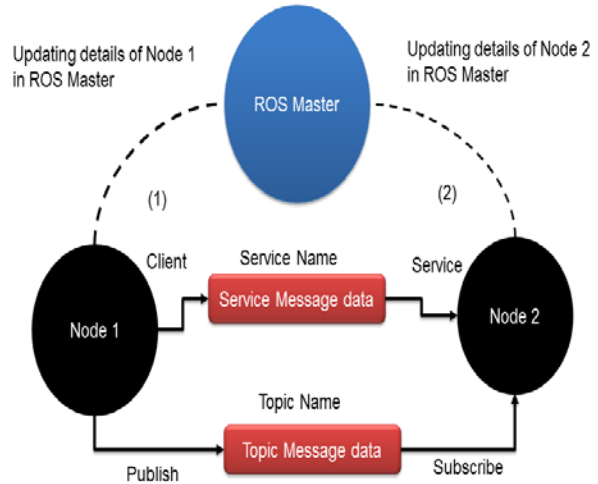


Fig.4 Communication between the ROS nodes and the ROS Master

### Gazebo simulator

Simulation of the basic chassis and function of the robotic system allowed for the rapid development and testing of the obstacle avoidance algorithm. Requirements for the simulation program included the ability to integrate well with the ROS network, have support for the sensors used, specifically the LRF, and provide the ability to add or remove objects while the simulation was in progress in order to simulate dynamic obstacles. The simulator chosen, based on these requirements, was Gazebo. Dr Andrew Howard and Nate Koenig originally developed this 3D simulator in 2002 at the University of Southern California. Since then it has been continually improved, and the development of the simulator was taken over by the OSRF in 2012. According to the overview of Gazebo on its webpage, “Gazebo is a 3D dynamic simulator with the ability to accurately and efficiently simulate populations of robots in complex indoor and outdoor environments,” and offers “physics simulation at a much higher degree of fidelity, a suite of sensors, and interfaces for both users and programs”. This simulator includes a large library of robot models, supports many different sensors via plugins, and since it was developed alongside ROS, provides a ROS package called *gazebo\_ros\_pkgs* to facilitate communications between the simulator and the ROS network. This package, authored by John Hsu, Nate Koenig, and Dave Coleman, is a wrapper for the standalone Gazebo program that provides an interface with ROS using “ROS messages, services, and dynamic reconfigure”.

The Gazebo simulator provides user interfaces for designing

worlds and robot models for use in simulation. For this work research, a robot model was developed utilizing two existing open-source models from the Gazebo model library—one for the P3-AT chassis, authored by Dereck Wonnacott, and one for the Hokuyo LRF, authored by John Hsu. These two models were combined using the model editor, and plugins for the robot's skid-steer drive and the laser data from the LRF were added. Since the only sensor required to implement the obstacle avoidance algorithm was the LRF, no additional sensors were modelled for simulation. The resultant robot model used for simulation is shown in figure 5.



Fig.5 Gazebo Model of P3-AT with LRF Attached

#### *Testing Gazebo with the ROS interface*

Assuming that the ROS environment is properly set up, we can start to **roscore** before starting Gazebo using the following command:

**\$ roscore**

The following command will run Gazebo using ROS:

**\$ rosrunc gazebo\_ros gazebo**

Gazebo runs two executables—the Gazebo server and the Gazebo client. The Gazebo server will execute the simulation process and the Gazebo client can be the Gazebo GUI. Using the previous command, the Gazebo client and server will run in parallel.

The Gazebo GUI is shown in the following screenshot (Fig.6).

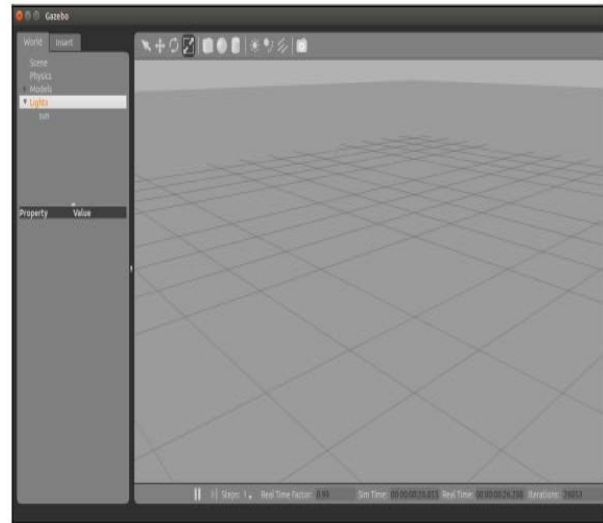


Fig.6 The Gazebo simulator

#### *Using Gazebo*

The Gazebo GUI is similar to rviz in many ways. The central window provides the view for Gazebo's 3D world environment. The grid is typically configured to be the ground plane of the environment on which all the models are held due to gravity in the environment.

Gazebo also has the same cursor/mouse control as rviz, described in the Using rviz section.

#### *Gazebo robotics simulator with ROS*

This tutorial is intended for roboticists that want to have realistic simulations of their robotic scenarios. Gazebo is a 3D simulator, while ROS serves as the interface for the robot. Combining both results in a powerful robot simulator. With Gazebo, you are able to create a 3D scenario on your computer with robots, obstacles and many other objects. Gazebo also uses a physical engine for illumination, gravity, inertia, etc. You can evaluate and test your robot in difficult or dangerous scenarios without any harm to your robot. Most of the time it is faster to run a simulator instead of starting the whole scenario on your real robot.

Originally, Gazebo was designed to evaluate algorithms for robots. For many applications, it is essential to test your robot application, like error handling, battery life, localization, navigation and grasping. As there was a need for a multi-robot simulator Gazebo was developed and improved.

## RVIZ

RVIZ is a 3D visualization tool for ROS applications. It provides a view of your robot model, capture sensor information from robot sensors, and replay captured data. It can display data from camera, lasers, from 3D and 2D devices including pictures and point clouds.

The purpose of RIVZ is to enable you to visualize the state of a robot. It uses sensor data to try to create an accurate depiction of what is going on in the robot's environment (Fig.7).

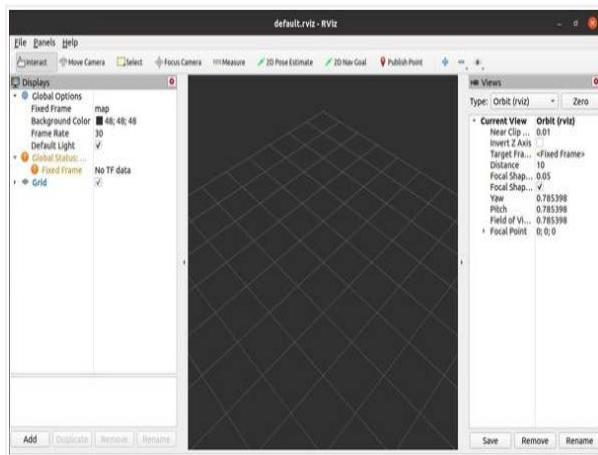


Fig.7 The RVIZ Simulator

## Programming Language

Starting with the research of the programming language, which will be used to develop the idea, is usually the first thing to do. After taking a deep and careful general look at many programming languages, Python was the one catching the interest. To justify this choice the following section covers an introduction about Python, firstly, and secondly a comparison between Python and few others programming languages.

### What is Python?

Python is an interpreted, object-oriented, high-level programming language with dynamic semantics. Its high-level built-in data structures, combined with dynamic typing and dynamic binding, make it very attractive for Rapid Application Development, as well as for use as a scripting or glue language to connect existing components. Python is simple, easy to learn as the syntax emphasizes readability and therefore reduces the cost of program maintenance. Python supports modules and

packages, which encourages program modularity and code reuse. The Python interpreter and the extensive standard library are available in source or binary form without charge for all major platforms and can be freely distributed<sup>13</sup>.

Often, programmers choose to work with Python because of the increased productivity it provides. Since there is no compilation step, the edit-test-debug cycle is incredibly fast. Debugging Python programs is easy, a bug or bad input will never cause a segmentation fault. Instead, when the interpreter discovers an error, it raises an exception. When the program does not catch the exception, the interpreter prints a stack trace. A source-level debugger allows inspection of local and global variables, evaluation of arbitrary expressions, setting breakpoints, stepping through the code a line at a time, and so on. The debugger is written in Python itself, testifying to Python's introspective power. On the other hand, often the quickest way to debug a program is to add a few print statements to the source, the fast edit-test-debug cycle makes this simple approach very effective<sup>13</sup>.

Python is a general-purpose programming language started by Guido van Rossum that became very popular very quickly, mainly because of its simplicity and code readability. It enables the programmer to express ideas in fewer lines of code without reducing readability<sup>13</sup>.

## OpenCV

OpenCV was started at Intel in 1999 by Gary Bradsky, and the first release came out in 2000. Vadim Pisarevsky joined Gary Bradsky to manage Intel's Russian software OpenCV team. In 2005, OpenCV was used on Stanley, the vehicle that won the 2005 DARPA Grand Challenge. Later, its active development continued under the support of Willow Garage with Gary Bradsky and Vadim Pisarevsky leading the project. OpenCV now supports a multitude of algorithms related to Computer Vision and Machine Learning and is expanding day by day<sup>12</sup>.

## RESULTS AND DISCUSSION

### First application (Pioneer 3-AT)

#### Visual navigation without obstacle environment

In this first simple example, let's say there are no obstacles in the

path, so we don't implement the obstacle avoidance algorithm. Now, by specifying the position the robot should go to with "Goal x" and "Goal y", the robot will launch from the position (x = 0, y = 0), and make its way to the given position. We'll use (x = 5, y = -5) in this example (Fig.8).

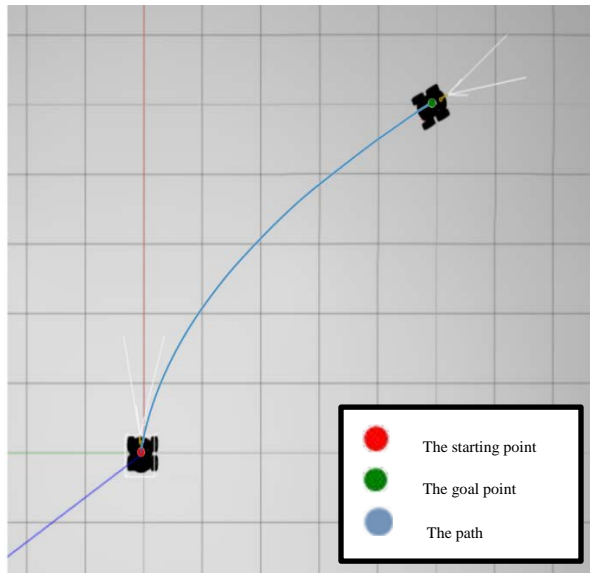


Fig.8 Simulation without Obstacles and Goal at (5, -5)

#### Visual navigation in an environment with obstacles

In the beginning, the camera of the Pioneer robot was fixed and did not moving, and when executing the simulations we noticed that the robot could not avoid obstacles due to the narrow space covered by the camera because when avoiding the obstacle it had to return to the path that allows it to reach the desired target, so the obstacle becomes very close from the camera, and thus the field of view becomes narrower than before, and this makes the robot not find the necessary space to avoid the obstacle so collide with it, and because of this problem we decided to add a mechanical hand that allows the camera to rotate relative to the axis of Z to make the camera rotate to the obstacle when seeing it and This is to better avoid the obstacle and no collide with it. Goal coordinates used (x = 5; y = -5) (Fig.9).

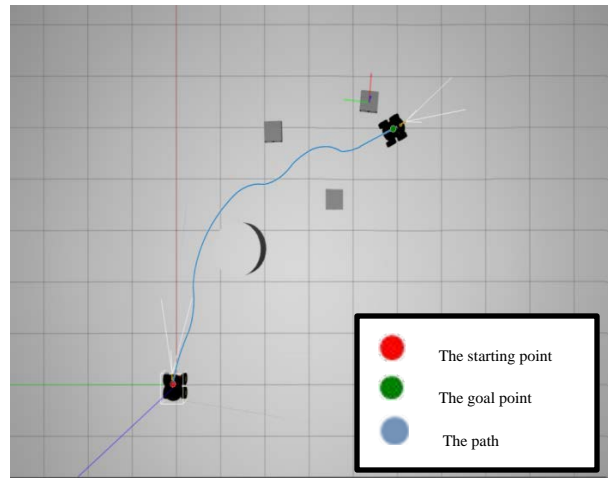


Fig.9 Simulation with multiple Obstacles and Goal at (5, -5)

#### Second application (Pioneer 3-DX)

Before starting the practical work, we encountered several problems, most notably:

- The lack of an exact description of the robot in the **urdf file** as shown in figure 10.
- Note that the robot runs intermittently.

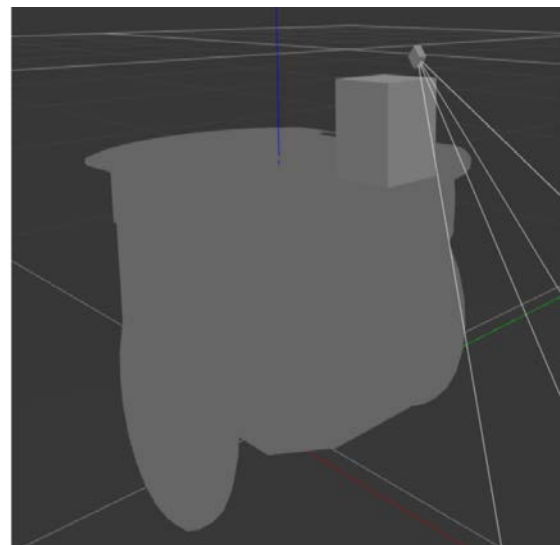


Fig.10 Pioneer 3-DX before modification

- And to fix this bug, we modified several commands in the urdf file, so it became as follows (Fig.11):
- We added a robotic hand to allow the camera to rotate



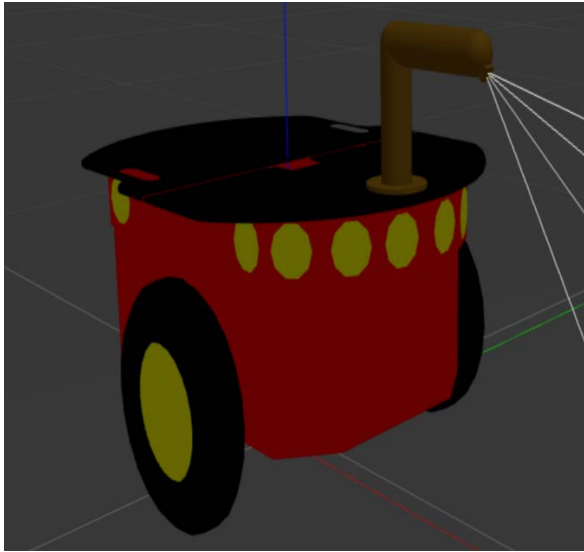


Fig.11 Pioneer 3-DX after modification

**Visual navigation without obstacle environment**

In this first simple example, let's say there are no obstacles in the path, so we don't implement the obstacle avoidance algorithm.

Now, by specifying the position the robot should go to with "Goal x" and "Goal y", the robot will launch from the position (x = -5, y = 5), and make its way to the given position. We'll use (x = 5, y = -5) in this example (Fig.12).

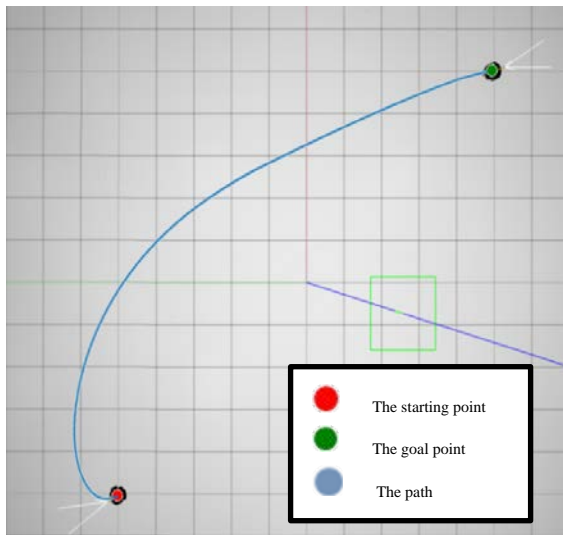


Fig.12 Simulation without Obstacles and Goal at (5, -5)

**Visual navigation in an environment with one obstacles**

Obstacle avoidance is a fundamental problem for any autonomous system as it tries to reach its destination. The

objectives of this research require the robot to be able to detect and avoid all existing obstacles. The system is developed based on the most restrictive and complex case. The camera was chosen as a sensor as one of the best devices for detecting obstacles (Fig.13).

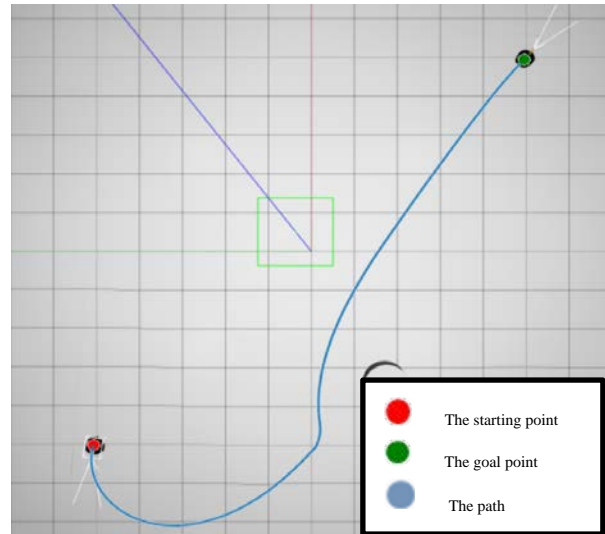


Fig.13 Simulation with one Obstacle and Goal at (10, -10)

**Visual navigation in an environment with Multiple obstacles**

At this point, we will see that the robot can navigate and reach the predetermined location in the four quadrants.

❖ **Quadrant I**

Goal coordinates used (x = 10; y = 10) (Fig.14).

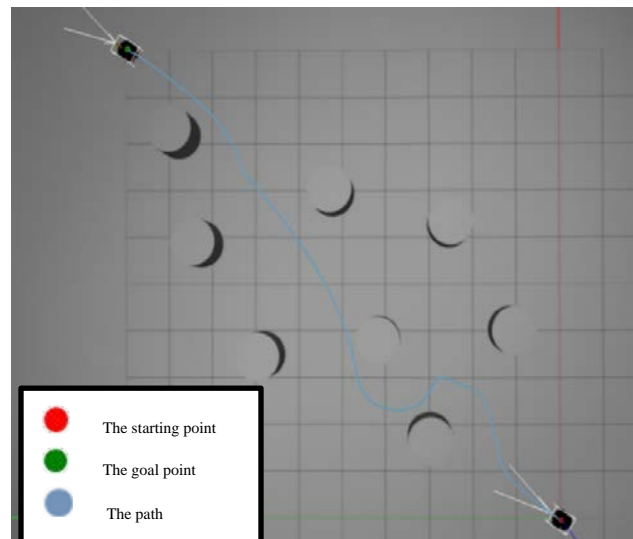


Fig.14 Simulation with Multiple Obstacles and Goal at (10, 10)

❖ *Quadrant II*

Goal coordinates used ( $x = 10; y = -5$ ) (Fig.15).

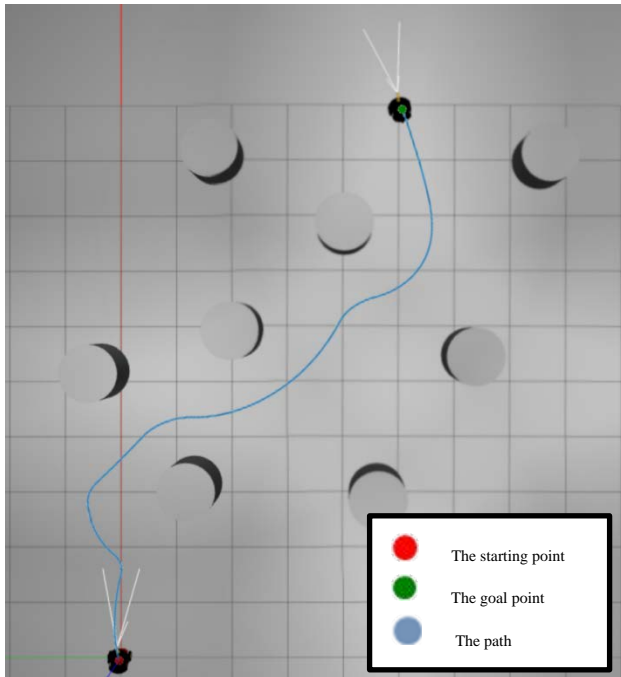


Fig.15 Simulation with Multiple Obstacles and Goal at (10, -5)

❖ *Quadrant III*

Goal coordinates used ( $x = -7; y = -6$ ) (Fig.16).

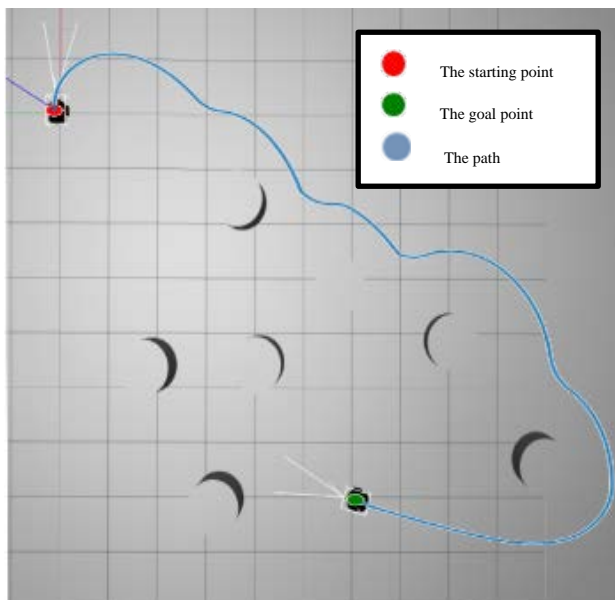


Fig.16 Simulation with Multiple Obstacles and Goal at (-7, -6)

❖ *Quadrant IV*

Goal coordinates used ( $x = -7; y = 8$ ) (Fig.17).

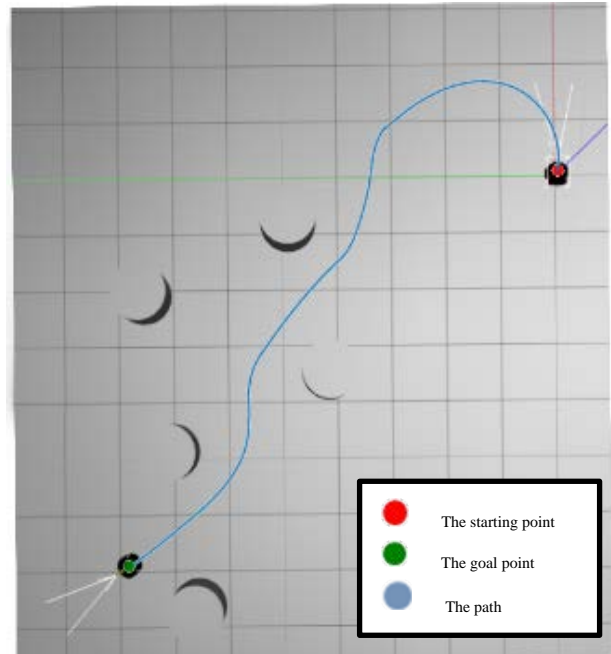


Fig.17 Simulation with Multiple Obstacles and Goal at (-7, 8)

*Visualization in OpenCV*

In order to get real time image visualization from the camera of the robot we need to use OpenCV libraries to import the necessary features, after we use the canny instruction to detect the edge between obstacles and the ground (Figs.18-19).

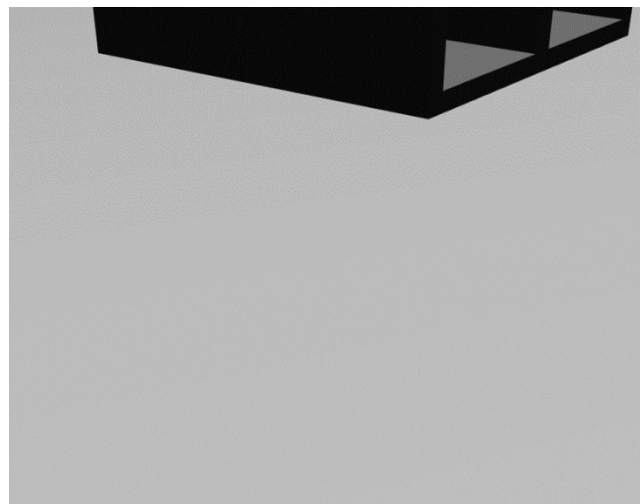
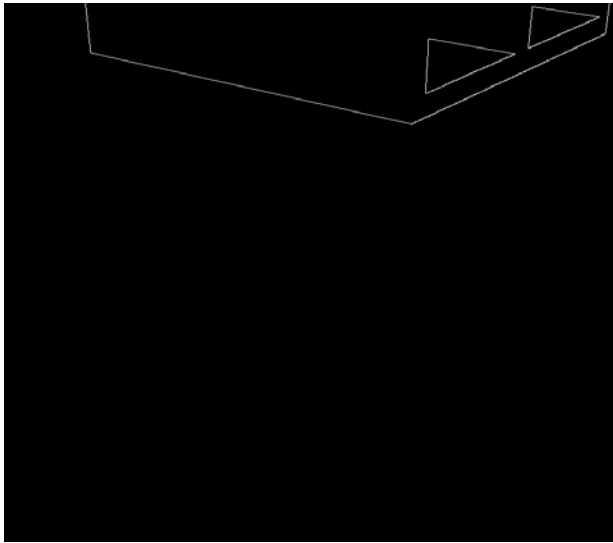


Fig.18 Real time image of the gazebo simulation with camera normal



**Fig.19** Real time image of the gazebo simulation with canny

## CONCLUSIONS

The study, development and testing conducted in this work resulted in the robot being able to navigate successfully in many different environments, it demonstrated the ability to reach the desired target location using the camera to detect and avoid obstacles. In this work, we provide an assessment of how successful the objectives of the work research have been achieved, and potential areas for future work.

## AUTHOR INFORMATION

### Corresponding Author

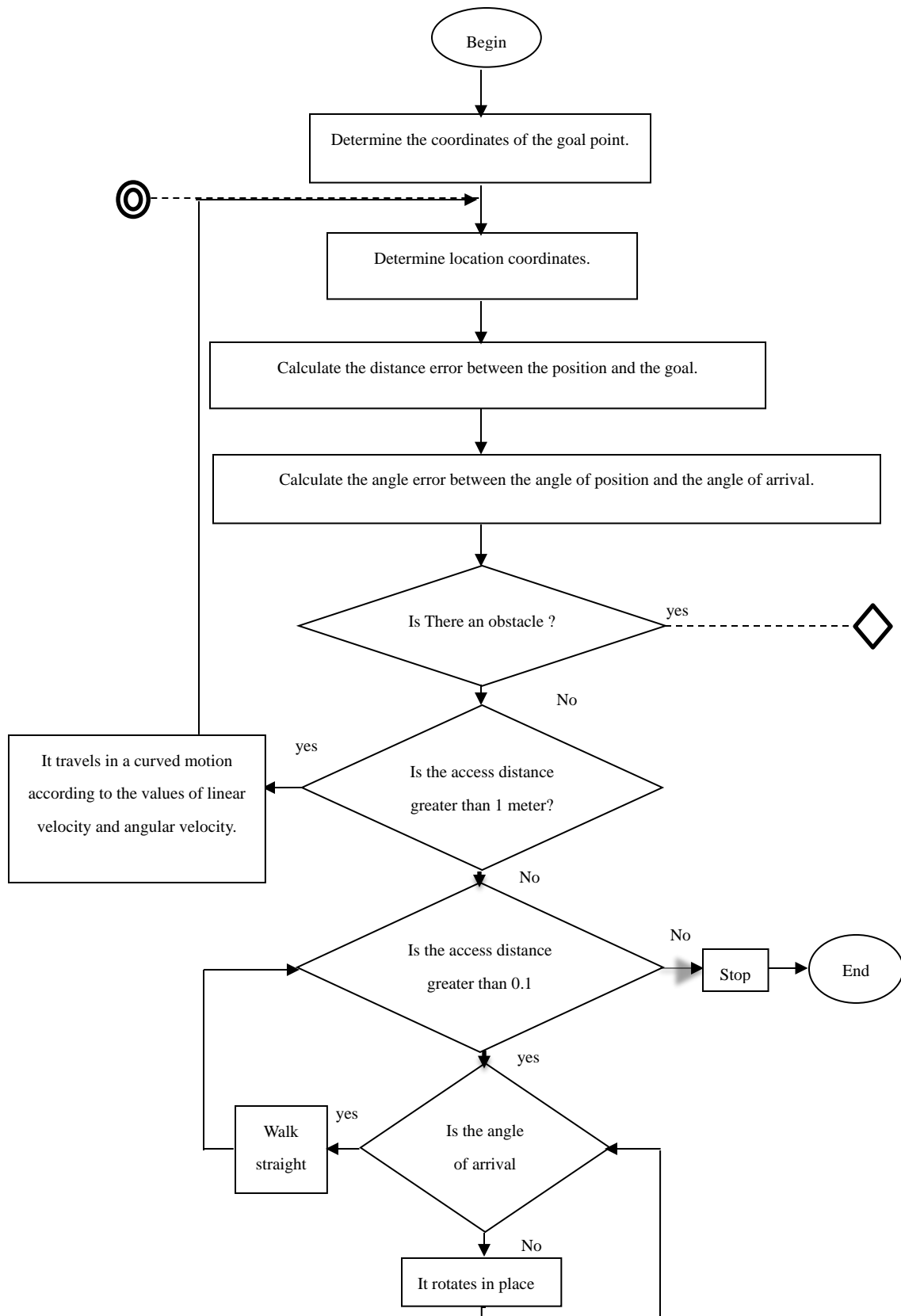
\*Salim Refoufi

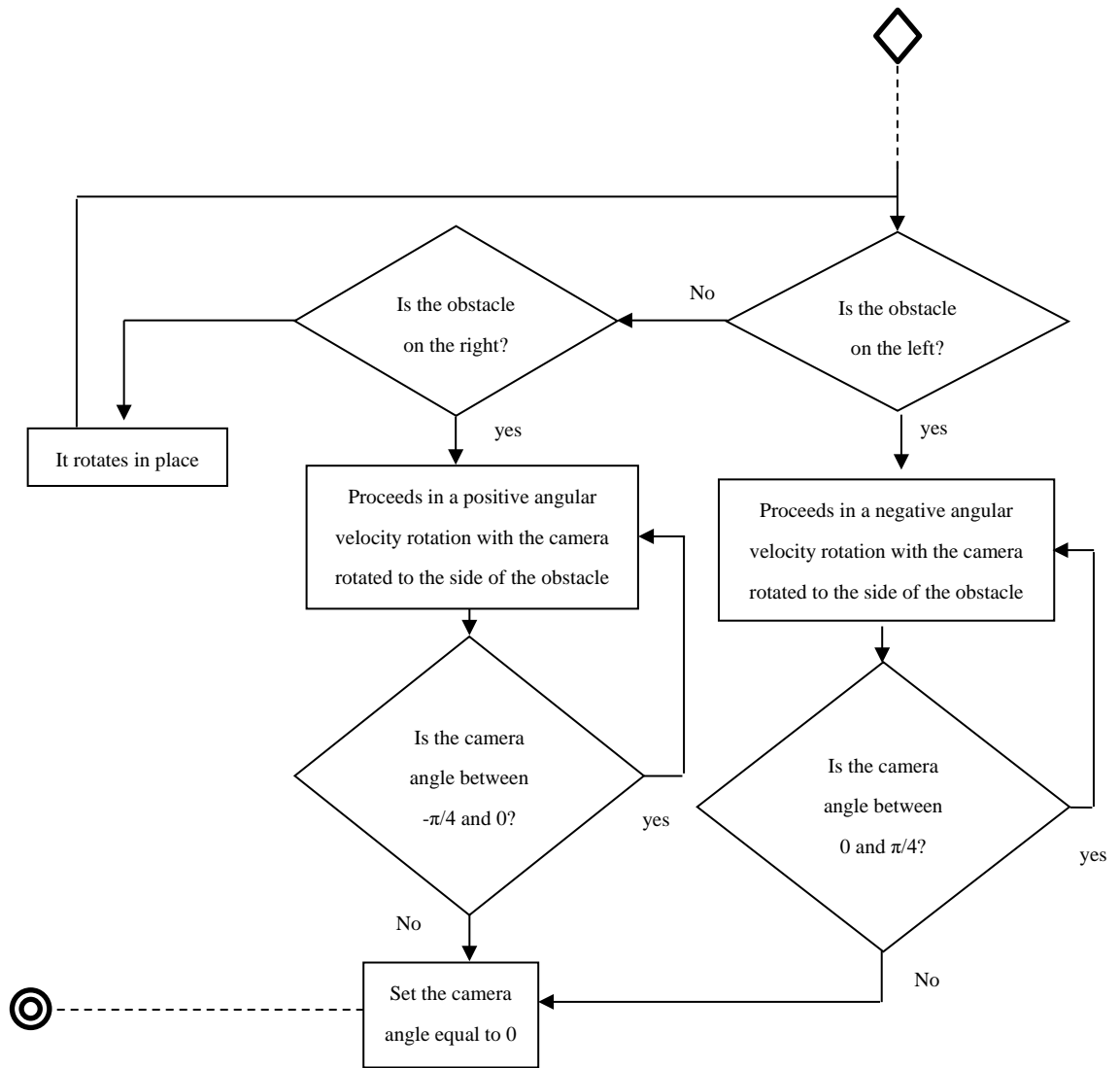
Email address: [refoufi2003@yahoo.fr](mailto:refoufi2003@yahoo.fr)

## REFERENCES

1. Laumond. J. P , La Robotique Mobile, Editions Hermès, 2001.
2. Tigli. J. Y , Vers une Architecture de contrôle pour Robot Mobile orientée Comportement, Thèse de doctorat, Université de Nice-Sophia, Antipolis, 1996.
3. Beaudry. E, Planification de tâches pour un robot mobile autonome, Faculté des sciences, université de Sherbrooke, Canada, 2006.
4. Latombe. J. C, Robot Motion Planning, Kluwer Academic Publishers, Norwell, 1991.
5. Cuesta. F, Ollero. A, Intelligent Mobile Robot Navigation, Springer-Verlag, Berlin Heidelberg, 2005.
6. Steels. L, When are robots intelligent autonomous agents, journal of robotics, Volume 15 pp 3-9, 1995.
7. Borenstein. J, Everett. H. R., Feng. L, Where am I, Sensors and Methods for Mobile Robot Positioning, University of Michigan, 1996.
8. Filliat. D, Robotique Mobile, Cours à l'école Nationale Supérieur des Techniques Avancées ENSTA, 2004.
9. A. BENMACHICHE, Approche de Navigation Coopérative et Autonome des Robots Mobiles, Doctorat, Dép d'Informatique, UNIVERSITE BADJI MOKHTAR –ANNABA, 2016.
10. Lentin. J, Learning Robotics using Python, second edition. Packt. 2018.
11. Harman. T. L, ROS Robotics By Example, Packt. 2016
12. Roseberock. A, Practical Python and OpenCV, 3rd edition "An introductory, example driven guide to image processing and computer vision". PyImageSearch. 2016.
13. Konstantina. F, Supervision of data transfer with python, Technological Educational Institute of Crete, 2016.

**Diagrams of the used algorithm**







2021

## Multi-Agents Segmentation for Mammography

Hayet Saadi <sup>a, \*</sup>, Hayet Farida Merouani <sup>a</sup>, Ahlem Melouah <sup>a</sup>, Nacereddine Boukabache <sup>b</sup>

<sup>a</sup>Computer Sciences Department, Laboratoire de Recherche en Informatique (LRI), Badji Mokhtar University, Annaba BP 12, Algeria

<sup>b</sup>Radiologist at Medical Imaging Center, 17 Rue de l'Independance, Azzaba, Algeria

**ABSTRACT:** Breast tumor segmentation in mammography is a critical and challenging task. Due to the similarities of the breast and tumor tissues, and the presence of a high amount of noise. Multi Agent System (MAS) is one of the powerful tools of Distributed Artificial Intelligence (DAI) employed for Medical Imaging processing. The presented approach is a hybridization between the classic Watershed segmentation and the concept of MAS. In the aim of, creating a new automatic tumor segmentation model for mammography images. This approach is proceeded as following; first, the classic object oriented watershed segmentation is applied on preprocessed mammography images, second, the MAS is introduced. Using two type of interactive agents, the MAS behavior is launched: Agent Pixel (AP) and Agent Territory (AT). As a result, the final segmentation is emerging. Pixels' intensity is the only information employed by the two types of agents to generate the final segmentation. . The results were encouraging with an accuracy (ACC) of 89% over three datasets, Mammographic Image Analysis Society (MIAS), INBreast, and Database of Digital Mammograms of Annaba (DDMA) a local dataset of LRI Lab.

**Keywords:** Segmentation; Mammography; Watershed; Multi Agents System.

## INTRODUCTION

From the statistics provided by the World Health Organization (WHO), on 2020, that the number of women diagnosed with breast cancer was 2.3 million<sup>1</sup>. Another fact, regarding breast cancer is that its early identification can effect positively the treatments' results. The standard test used to detect breast cancer at a very early stage is *mammography*. Mammography presents a list of interesting characteristics that can help radiologists and practitioners like a High detection rate, Safe to administer, Reasonable in cost...<sup>2</sup>. Computer-Aided Diagnosis (CAD) are the systems, which were developed to help radiologist and practitioners to deal with a large number of images and to assist in images analysis and interpretation<sup>3-4</sup>. CAD are used for mammography images in all processing phases<sup>5-6</sup>. The same concept of CAD is employed for other medical imaging modalities like: 3D MRI Preprocessing<sup>7</sup>, Retinal Fundus images enhancement<sup>8</sup>, CT COVID-19 images segmentation<sup>9</sup>, and Skin

Lesion preprocessing, segmentation and classification<sup>10</sup>. The urge to create systems and materiel, that go along with, the technological growth and Artificial Intelligence (AI) revolution sophisticated healthcare systems were introduced to hospitals and practices to facilitate the process and decision making<sup>11-12-13</sup>.

One of the famous fundamental concept of AI is Distributed Artificial Intelligence (DAI). Which was described with the fact of AI distributed by an entity or a group of entities. One of the strongest tools and the well-known notions of DAI are Agents and Multi Agents Systems (MAS)<sup>14</sup>. Agents and MAS represent the concepts and theories of societies, collective intelligence, the relationship between individual behaviors and phenomena observed at the global level, collaboration, conflict cooperation, and coordination<sup>15</sup>.

According to Ferber (1995)<sup>15</sup>, an Agent is a physical or virtual entity with: the ability to act in an environment, communication

directly with other agents, has its own resources, tends to satisfy its objectives, the most important fact of an agent is the autonomy...

In the other hand, a MAS is a system with: an environment, a group of agents, a set of relations and operations between the agents <sup>15</sup>.

The robustness of Agent and MAS made them an effective tool in medical domain. Therefore, they were included in different forms and takes Segmentation, Classification, Diagnosis, E-health, to improve time and quality. Benmazou et al. (2014)<sup>16</sup>, employed MAS and texture descriptors to classify mammography images. Bennai et al. (2020) <sup>17</sup> applied a segmentation of MRI brain to detect tumors.

Breast tumor segmentation in mammography is a critical and challenging task in healthcare and CAD systems. Due to textured nature of the breast tissues, similarities between tumor and breast tissues, and the presence of a high amount of noise. An enhanced automatic segmentation is presented in this paper, with a hybridization of classic *Watershed Segmentation* and *MAS*. The experimental results show an encouraging overall accuracy statistically and with a collaboration of an MD radiologist. The reminder of this paper is structured as following:

- The detailed proposed Mammography Segmentation approach based on MAS and Watershed Segmentation in (Section 2);
- Implementation details, Dataset, Experimental results, Analysis and discussions in (Section 3);
- Finally, conclusion in (Section 4).

## EXPERIMENTAL

This section contains the details of the proposed approach. Fig.1 represents its flowchart. Mainly, the proposed approach is divided into two phases, where the preprocessed mammography images Saadi and Merouani (2019) <sup>18</sup> were first passing by a classic watershed segmentation; second, a MAS is introduced with an Agent behavior was applied to generate the final segmentation.

### *Watershed segmentation*

The mathematical morphological concept is the base of watershed image segmentation. Which is a three dimensions visualization, of a two-dimensional large-scale image. These

dimensions are composed of two spatial coordinates and one intensity. The result of this topographic segmentation are *catchment basins* separated by *watershed lines*. In other terms, pixels are assigned to a region or a line. The main objective of this segmentation is to find the watershed lines<sup>19-20-21</sup>.

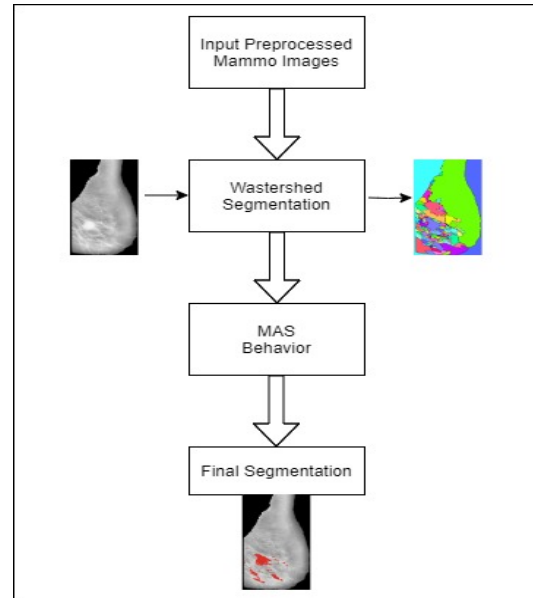


Fig. 1 Flowchart of the proposed approach

### *Multi Agents Behavior*

The outcome of the watershed segmentation is over-segmented images. To overcome this problem, a MAS was introduced as following:

**a- Types of Agents:** There is two types of reactive and interactive agents. *Agent Pixel (AP)* is a *pixel that* contains as information: the *original intensity of the mammography image* and *watershed catchment's color*. *Agent Territory (AT)* this agent owns a set of AP with the same watershed catchment's color, i.e. this set of AP is owned by one and only one AT. Another important information within AT is the average intensity of these AP (*AvrgCatch*).

**b- Agents' environment:** the whole number of APs represents the environment, except the APs of the background, i.e. only the breast area of the mammography.

**c- MAS Segmentation:** Before, starting the segmentation, the breast area's intensity average is calculated (*AvrgBrst*) as the environment information seen by all the agents (ATs and APs). The following algorithm presents the MAS behavior to emerge the final segmentation. This process is launched randomly, where, all ATs with *low brightness* will kill themselves, and only

ATs with *high brightness* stay alive to emerge the final tumor zone.

**Algorithm: MAS Segmentation**

```

If AT.AvgCatch <= AvgBrst
    This.AT (kill.themself)
    Change area's color to original mammography
Else
    Stay alive and change area's color to red
End
    
```

**RESULTS AND DISCUSSION**

*Data Sets and Tools*

The proposed approach was experimented on three different mammography datasets with (150) images. Where, (50) from Mammographic Image Analysis Society (MIAS), which is an organization of UK research groups interested in the understanding of mammograms, and had generated a dataset of digital mammograms<sup>22</sup>. INbreast with (50) images, from the Breast Center in the University Hospital of Porto Portugal<sup>23</sup>. In addition to, (50) images from the local dataset of LRI Lab called Database of Digital Mammograms of Annaba (DDMA), in collaboration with University Hospital of Ibn-Roched Annaba <sup>24</sup>.

The approach was in implemented in *Netbeans 8* for the part of *classic watershed* (<https://bit.ly/3radnzZ>). In the other hand, for the MAS segmentation *NetLogo* was employed as a modelling environment<sup>25</sup>, Fig.2 shows the main GUI of our proposed approach . On a PC *Windows 10* with an *Intel Core i5* with 2.2 *GHz processor* and 8 *GB RAM*.

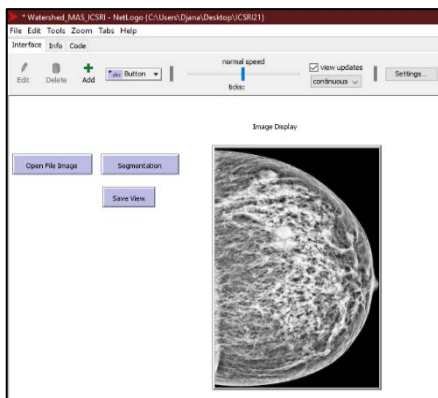


**Fig. 2** The main GUI on NetLogo of the proposed approach

**Evaluation Measures**

To evaluate the performance of our proposed approach, a quantitative analysis was carried out by the mean of the index of Accuracy (ACC). Equation eq.1 presents the mathematical representation of ACC.

$$ACC = \frac{TP + TN}{TP + TN + FP + FN} \tag{1}$$

Where:

*TP* , *TN*, *FP*, *FN* and represent respectively the True Positives, the True Negatives, the False Positives and the False Negatives.

**Performance analysis**

The proposed approach is a mammography breast tumor segmentation, by a combination between classic watershed segmentation and MAS concept of DAI. It obtains an overall ACC around (89%) over the three employed datasets. INbreast scored the highest ACC, over the other datasets, around (97%). The most important reason for this score is the nature of INbreast images, with a high quality even before applying the preprocessing. For MIAS the ACC scored around (90%), the presence of high amount of noise and the high breast density were the reasons to have this outcome for MIAS, and even for DDMA, which scored an ACC around (80%). Fig.3 represents the graphic visualization of the ACC of our proposed approach.

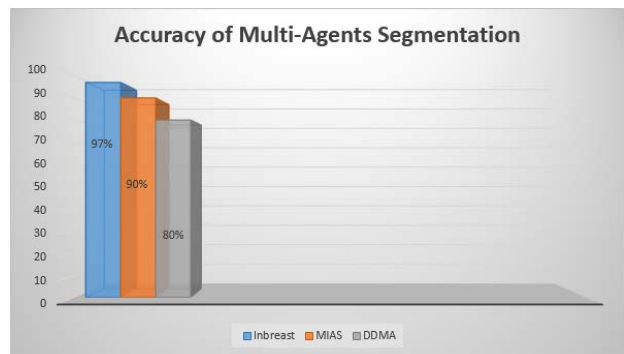


**Fig. 3** The graphical visualization of the results of the proposed approach

Fig.4, Fig. 5, and Fig. 6 represent the detailed process of the approach for the three datasets INbreast, MIAS and DDMA respectively. Sub figure (a) is the mammography image after



preprocessing. Sub figure (b) is the result of the classic watershed segmentation, as is obviously clear, watershed generates an over-segmentation in a way that makes the image hard to be understood or interpreted. Finally, sub figure (c), which represents the final result of the MAS segmentation.

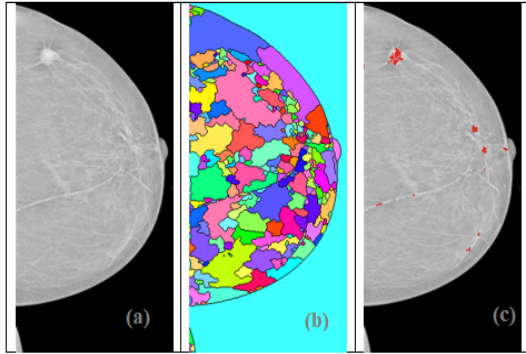


Fig. 4 The process of the proposed approach for INbreast

As is presented this segmentation localized relatively the tumor in the majority of the cases in a correct way. At this point, we can say that our proposed approach overcame practically the over-segmentation problem. The test phase was with a collaboration of an expert MD Radiologist, where, the results were analyzed and discussed.

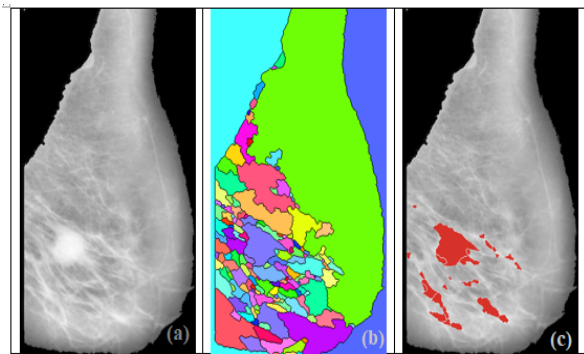


Fig. 5 The process of the proposed approach for MIAS

The qualitative comparison between our proposed approach and other existing approach in the literature related to mammography tumor segmentation in term of ACC, is presented in Table. 1.

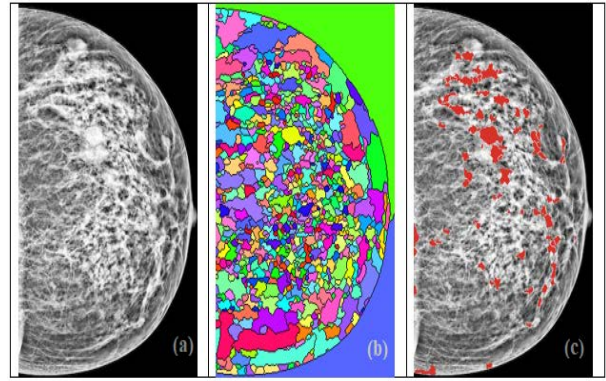


Fig. 6 The process of the proposed approach for DDMA

From Table 1, the overall of our proposed approach is encouraging. For INbreast our proposed approach scored better the approach presented by Dhungel et al. (2017)<sup>26</sup> with (97%) over (90%) respectively. Dhungel et al. (2017)<sup>26</sup> applied a deep structured output learning, that is refined by a Conditional Random Field, and finally smoothen by an active contour to finish the segmentation.

Table 1. Qualitative comparing table between our proposed approach and other existing approaches.

N°	References	Dataset	The approach	ACC %
1	Shrivastava and Bharti (2020)	MIAS	ROI extraction Seeded Region Growing	92.2
2	Dhungel et al. (2017)	INbreast	DL Conditional Random Field	90
	Our	MIAS		90
3	Proposed Approach (2021)	INbreast DDMA	Watershed and MAS	97 80

The approach presented by Shrivastava and Bharti (2020)<sup>27</sup>, scored a higher ACC for MIAS comparing to our approach with (92.2%) over (90%) respectively. Shrivastava and Bharti (2020)<sup>27</sup> worked on ROI extraction, and automatic seed extraction and thresholding in a seeded region growing. Finally, our approach presents an ACC of (80%) for DDMA, which is the lowest score due to the fact of the high amount of noise and the

high breast density.

Our proposed approach, works excellently comparing to the works presented in the literatures. The major problem of watershed related to the over-segmentation was overcome relatively.

## CONCLUSIONS

The proposed approach is an automatic enhanced watershed segmentation with MAS, for mammography images to detect breast tumor. The main problem of the over-segmentation in watershed was relatively overcome.

The interactive employed Agents were relying only on pixel intensity. They do not use any other information and they do not need any learning phase. The results were encouraging and promising for future enhancement

## AUTHOR INFORMATION

### Corresponding Author

\*Hayet Saadi

Email address: [hayet.saadi@univ-annaba.org](mailto:hayet.saadi@univ-annaba.org)

## ACKNOWLEDGMENT

We are grateful to the Direction Générale de la Recherche Scientifique et du Développement Technologique (DGRSDT) which kindly supported this research, as well as to the Laboratoire de Recherche Informatique (LRI) and its members where this study was conducted. As well as to NetLogo community. As well as to MD Nacereddine Boukabache for his medical and technical assistance and his hospitality into his practice during this extraordinary period.

## REFERENCE

- <sup>1</sup> World Health Organization, *Breast Cancer*, 2021 (Accessed April 16, 2021), <https://bit.ly/32RIDit> .
- <sup>2</sup> J. M. Seely, How Effective is Mammography as a Screening Tool?, *Current Breast Cancer Reports*,9, 251–258, 2017.

- <sup>3</sup> J. Katzen et K. Dodelzon, A Review of Computer Aided Detection in Mammography, *Clinical Imaging*,52,305-309, 2018.
- <sup>4</sup> S. Boudraa, A. Melouah et H. F. Merouani, Improving Mass Discrimination in Mammogram-CAD System using Texture Information and Super-Resolution Reconstruction, *Evolving Systems*, 1–10, 2020.
- <sup>5</sup> A. Melouah et S. Layachi, Novel Automatic Seed Selection Approach for Mass Detection in Mammograms, *International Journal of Computational Science and Engineering*, 18,80–88, 2019.
- <sup>6</sup> L. Viegas, I. Domingues and M. Mendes, Study on Data Partition for Delimitation of Masses in Mammography, *Journal of Imaging*, 7, 174, 2021.
- <sup>7</sup> F. Romdhane, F. Benzarti and H. Amiri, A new method for three-dimensional magnetic resonance images denoising, *International Journal of Computational Vision and Robotics*, 8, 1, 2018.
- <sup>8</sup> M. J. Alwazzan, M. A. Ismael and A. N. Ahmed, A Hybrid Algorithm to Enhance Colour Retinal Fundus Images Using a Wiener Filter and CLAHE, *Journal of Digital Imaging*, 34, 750–759, 2021.
- <sup>9</sup> K. Sahib, A. Melouah et A. Slim, Unet Model for COVID-19 Infected Area Segmentation in CT Images, *4th International Conference on Artificial Intelligence in Renewable Energetic Systems, Tipasa, Algeria*, 2020.
- <sup>10</sup> K. Sahib, A. Melouah, F. Touré and A. Slim, W-Net and Inception Residual Network for Skin Lesion Segmentation and Classification, *Applied Intelligence*, July 2021.
- <sup>11</sup> T. Sethi, A. Kalia, A. Sharma et A. Nagori, Interpretable Artificial Intelligence: Closing the Adoption Gap in Healthcare, chez *Artificial Intelligence in Precision Health*, D. Barh, Éd., Elsevier, 2020, 3–29.
- <sup>12</sup> K. Syed, W. C. Sleeman IV, J. J. Nalluri, R. Kapoor, M. Hagan, J. Palta et P. Ghosh, Artificial Intelligence Methods in Computer-Aided Diagnostic Tools and Decision Support Analytics for Clinical Informatics, chez *Artificial Intelligence in Precision Health*, D. Barh, Éd., Elsevier, 2020, p. 31–59.
- <sup>13</sup> H. Abuoud, A. Eldurrah et A. M. Abdulshahed, Internet of Things for Smart Healthcare (In Arabic), *Journal of Academic Research*,15, 1–19, 2020.
- <sup>14</sup> L. Monostori, Artificial Intelligence, L. Laperrière et G. Reinhart, Éd., CIRP Encyclopedia of Production Engineering, Springer Berlin Heidelberg, 2014, p. 47–50.
- <sup>15</sup> J. Ferber, Les Systèmes Multi Agents: Vers une Intelligence Collective, InterEdition, Éd., IIA: Informatique Intelligence Artificielle, 1995.
- <sup>16</sup> S. Benmazou, H. F. Merouani, S. Layachi and B. Nedjmeddine, Classification of Mammography Images based on Cellular Automata and

Haralick parameters, *Evolving Systems*, 5, 209–216, 2014.

<sup>17</sup> M. T. Bennai, Z. Guessoum, S. Mazouzi, S. Cormier et M. Mezghiche, A Stochastic Multi-Agent Approach for Medical-Image Segmentation: Application to Tumor Segmentation in Brain MR Images, *Artificial Intelligence in Medicine*, 110, 101980, 2020.

<sup>18</sup> H. Saadi et H. F. Merouani, Pectoral Muscle Segmentation in Mediolateral Oblique Mammograms, *International Congress on Health Sciences and Medical Technologies (ICHSMT'19)*, Tlemcen, Algeria, 2019.

<sup>19</sup> A. Hefnawy, An Improved Approach for Breast Cancer Detection in Mammogram Based on Watershed Segmentation, *International Journal of Computer Applications*, 75, 26–30, 2013.

<sup>20</sup> A. Seal, A. Das et P. Sen, Watershed: An Image Segmentation Approach, *International Journal of Computer Science and Information Technologies (IJCSIT)*, 6, 2295–2297, 2015.

<sup>21</sup> L. Vincent et P. Soille, Watersheds in Digital Spaces: An Efficient Algorithm Based on Immersion Simulations, *IEEE Transactions on Pattern Analysis & Machine Intelligence*, 13, 583–598, 1991.

<sup>22</sup> J. Suckling, J. Parker, D. Dance, S. Astley, I. Hutt, C. Boggis et I. Ricketts, *Mammographic Image Analysis Society (MIAS) database v1.21 [Dataset]*, 2015.

<sup>23</sup> I. C. Moreira, I. Amaral, I. Domingues, A. Cardoso, M. J. Cardoso et J. S. Cardoso, InBreast: Toward a Full-Field Digital Mammographic Database, *Academic Radiology*, 19, 236–248, 2012.

<sup>24</sup> H. F. Merouani, N. Beledjhem, Y. Tilili, S. Layachi et A. Melouah, *Système d'aide pour le suivi et le diagnostic des tumeurs mammaires (SASDUM)*, 2013.

<sup>25</sup> U. Wilensky, NetLogo Centre for connected learning and computer-based modelling, Northwestern University, Evanston, IL, <https://bit.ly/3sLDHiT>, 1999.

<sup>26</sup> N. Dhungel, G. Carneiro et A. P. Bradley, A deep learning approach for the analysis of masses in mammograms with minimal user intervention, *Medical image analysis*, 37, 114–128, 2017.

<sup>27</sup> N. Shrivastava et J. Bharti, Breast Tumor Detection and Classification based on Density, *Multimedia Tools and Applications*, 79, 26467–26487, 2020.



2021

## Segmentation of MRI images by the algorithm FPSO-FPCM for detection of multiple sclerosis

Hakima Zouaoui<sup>a,\*</sup>, Abdelouahab Moussaoui<sup>b</sup>

<sup>a</sup> Computer Science Department, Mohamed El Bachir El Ibrahimi University, Algeria

<sup>b</sup> Computer Science Department, Ferhat Abbas University, Algeria

**ABSTRACT:** Multiple Sclerosis (MS) is an autoimmune inflammatory disease that leads to lesions in the central nervous system. Magnetic Resonance Imaging (MRI) provide sufficient imaging contrast to visualize and detect MS lesions, particularly those in the white matter (WM). Medical image segmentation is an essential step for most consequent image analysis tasks. The proposed segmentation algorithm is composed of three stages: segmentation of the brain into regions using Fuzzy Particle Swarm Optimization (FPSO) in order to obtain the characterization of the different healthy tissues (White matter, grey matter and cerebrospinal fluid (CSF)). After the extraction of WM, atypical data (outliers) is eliminated using Fuzzy C-means algorithm, and finally, we introduce a Mamdani-type fuzzy model to extract MS lesions among all the absurd data. Although the FCM algorithm yields good results for segmenting noise free images, it fails to segment images corrupted by noise, atypical data (outliers) and other imaging artifact. The purpose of this study is to segment high dimensional data of WM lesions using Fuzzy Possibilistic C-means (FPCM). This approach is a generalized version of FCM algorithm. The objective of the work presented in this paper is to obtain an improved accuracy in segmentation of WM. Comparison results to the method of FPSOFPCM showed that the defuzzification of the atypical data of the segmentation was 56.79 showing that the proposed FPSOFPCM outperformed the other method (FPSOFPCM).

**Keywords:** Fuzzy Particle Swarm Optimization; Fuzzy Possibilistic C-Means; Multiple Sclerosis Lesions; Segmentation; Mamdani..

## INTRODUCTION

Multiple sclerosis (MS) is an inflammatory, demyelinating and neurodegenerative disease of the central nervous system involving immune-mediated destruction of myelin and axonal damage that affects both white matter (WM) and gray matter (GM). MS is characterized by the formation of focal inflammatory lesions, also called plaques<sup>1</sup>. It may cause various potential symptoms, including visual problems<sup>2</sup>, spasms<sup>3</sup>, numbness<sup>4</sup>, fatigue<sup>5</sup>, among others. MS is typically diagnosed by the presenting symptoms, together with supporting neuroimaging

methods, such as magnetic resonance imaging (MRI) to detect the damaged WM<sup>6</sup>.

Both MS lesions and brain atrophy, are usually measured in-vivo from MRI by means of automatic or semi-automatic segmentation algorithms. The most frequent modalities to segment WM lesions include proton density-weighted (PD-w), FLAIR and T2-weighted (T2-w), this is because lesions appear hyper-intense in these sequences which makes them easier to detect<sup>1</sup>. However, WM lesions in MS can be detected with standard MRI acquisition protocols without contrast injection. It

has been shown that many features of lesions, such as volume T. Kalincik et al.<sup>8</sup> and location P. Sati et al.<sup>9</sup> are important biomarkers of MS, and can be used to detect disease on set or even track its progression. Therefore accurate segmentation of WM lesions is important in understanding the progression and prognosis of the disease. With T2-w MR imaging sequences, most lesions appear as bright regions in MR images, which is useful for automatic segmentation. Although manual delineations are considered as the gold standard, manually segmenting lesions from 3D images is tedious, time consuming, and often not reproducible. Therefore automated lesion segmentation from MRI is an active area of development in MS research<sup>7</sup>.

In fact, robust and efficient segmentation of various tissues and structures in medical images is of crucial significance in many applications, such as the identification of brain pathologies from MR images<sup>10</sup>. Actually, image segmentation is regarded a crucial stage in the image processing system that straight for efficiently guiding the clinicians in the process of medical diagnosis. In Moreover, related tasks such as position detection, primitive extraction, or pattern recognition all strongly dependent on the quality of the segmentation. The accurate segmentation of lesions in MRI is important for the accurate diagnosis, adequate treatment development and patient follow-up of the MS disease.

This paper is an extension of a previous work where we proposed a new automated segmentation method that detects the lesions of MS<sup>11</sup>. The previously published MS segmentation algorithm follows three stages: We initially segment the brain into different tissues classes, namely: WM, Grey Matter (GM) and Cerebrospinal Fluid (CSF) using Fuzzy Particle Swarm Optimization (FPSO) algorithm. Secondly, we use Fuzzy C-Means (FCM) algorithm to eliminate the atypical data of the white matter. And finally, a decision-making system that uses Mamdani-type fuzzy model is employed in order to ascertain whether a given voxel is an MS lesion or not<sup>11</sup>. However, we found that our method failed in accurately for segmentation of white matter lesions in MR images because the FCM algorithm yields good results for segmenting noise free images, it fails to segment images corrupted by noise, atypical data (outliers) and other imaging artifact.

Lesion segmentation plays an important role in the diagnosis and follow-up of multiple sclerosis (MS). This task is very time-

consuming and subject to intra- and inter-rater variability. In this paper, we present an improved tool for automated MS lesion segmentation. Our approach is based on three main steps, initial brain tissue segmentation according to the gray matter (GM), WM, and cerebrospinal fluid (CSF) performed using the algorithm Fuzzy Particle Swarm Optimization (FPSO). This is followed by a second step where the lesions are segmented as outliers to the normal apparent WM brain tissue using a Fuzzy Possibilistic C-means (FPCM) algorithm and decision-making system that uses Mamdani-type fuzzy model.

The remaining of this paper is organized as, follows; related works are presented in Section 2. The proposed algorithm of automatic MS lesion detection and its various steps are highlighted in is described I and Section 3. Section 4 reports the experimental results. Finally, conclusion and future work are summarized in section 6.

## **RELATED WORK**

There are several methodologies available to detect MS from MR images. The degree to which the disease has affected can be known by estimating the volume of MS lesion through MR imaging and this helps in planning the treatment. Udupa, J.K. et al<sup>12</sup> have proposed a new system with which MS lesions can be segmented from dual-echo fast spin echo MRI and the computation of MS lesion volume can be eventually performed. Many automated lesion segmentation methods have been proposed in the past decade<sup>18</sup>. There are usually two broad categories of segmentations, supervised and unsupervised. Unsupervised lesion segmentation methods rely on intensity models of brain tissue, where image voxels containing high intensities in FLAIR images are modeled as outliers<sup>19-20</sup> based on the intensity distributions. The outlier voxels then become potential candidates for lesions. Eventually the segmentation can be refined by a simple thresholding technique<sup>21-23</sup>. Alternatively, Bayesian models such as mixtures of Gaussians<sup>24-26</sup> or Student's t mixture models<sup>27</sup> can be applied on the intensity distributions of potential lesions and normal tissues. Optimal segmentation is then achieved via an expectation-maximization algorithm. Additional information about intensity distributions and expected locations of normal tissues via a collection of healthy subjects<sup>28</sup> can be included to determine the lesions more accurately. Local intensity information can also be included via Markov random

field to obtain a smooth segmentation<sup>29</sup>. Ying Wu et al<sup>13</sup> have dealt with an automatic segmentation scheme that segments and classifies MS lesions into three sub-kinds from T2-w and contrast- enhanced T1-w brain images of 12 MR scans. On the other hand, S. Sivagowri, et al<sup>14</sup> have presented an automatic method for segmenting MS lesions from MR images. It uses a governed- classifier, namely, support vector machine (SVM) for differentiating the blocks that lie in MS lesion regions and non-MS lesion regions using textural features.

Supervised lesion segmentation methods make use of atlases or templates, which typically consist of multi-contrast MR images and their manually delineated lesions. As seen in the ISBI-2015 lesion segmentation challenge<sup>30</sup>, supervised methods have become more popular and are usually superior to unsupervised ones, with four out of top five methods being supervised. These methods learn the transformation from the MR image intensities to lesion labels (or memberships) on atlases, and then the learnt transformation is applied onto a new unseen MR image to generate its lesion labels. For instance, logistic regression<sup>31-32</sup> and SVM<sup>33</sup> have been used in lesion classification, where features include voxel-wise intensities from multi-contrast images and the classification task requires to label an image voxel as lesion or non-lesion. Instead of using voxel-wise intensities, patches have been shown to be a robust and useful feature<sup>34</sup>. As such, random forests<sup>35-37</sup> and k-nearest neighbors<sup>38</sup> based algorithms have used patches and other features, computed at a particular voxel, to predict the label of that voxel. Dictionary based methods<sup>39-41</sup>, use image patches from atlases to learn a patch dictionary that can sufficiently describe potential lesion and non-lesion patches. For a new unseen patch, similar patches are found from the dictionary and combined with similarity-based weighting. In the proposed methodology by Colm Elliott et al<sup>16</sup>, mutual fragmentation is performed on the sequential scans for carrying out a temporarily reliable tissue segmentation that produces lesions.

Class-based methods<sup>17-19</sup>, modeled the lesions as an independent class to be extracted. In<sup>36</sup>, a combination of intensity-based k-nearest neighbor classification (k-nn) and a template-driven segmentation (TDS) was designed to segment different types of brain tissue. Lesions were modeled as one of the expected tissue types, and the class parameters were obtained through a supervised voxel sampling scheme on two randomly selected scans. Since the manual training step is highly data-dependent, it

is expected to be conducted for each study or data set. A summary of the aforementioned techniques is given in Table 1.

**Table 1: Comparison of MS lesion segmentation methods**

Author	Method	Sequences	Evaluation
Udupa et al. <sup>12</sup>	Fuzzy Connectedness Principles	T1-w, T2-w and PD-w	NA
Wu et al. <sup>13</sup>	KNN	T1-w, T2-w and PD-w	Spe=0.53 Sen=0.80
Prastwa et al. <sup>17</sup>	Bayesian classification	T1-w, T2-w and FLAIR	Spe=0.99 Sen=0.03
Zhang et al. <sup>19</sup>	SWE+KNN	MS image	Spe=0.99 Sen=0.96
Souplet et al. <sup>21</sup>	EM	T1-w, T2-w and FLAIR	Spe=0.99 Sen=0.26
Jain et al. <sup>23</sup>	MSmetrix	3D T1-w 3D FLAIR	Sen=0.57 Pre=0.83
Strumia et al. <sup>25</sup>	Geometric Brain Model	T1-w, T2- w and FLAIR	Spe=0.56 Sen=0.70
Dworkin et al. <sup>32</sup>	CV	T1-w, T2-w, PD-w and FLAIR	NA
Maier et al. <sup>35</sup>	ET	T1-w, T2- w and FLAIR	NA
Deshpande et al. <sup>41</sup>	Sparse Representations and Adaptive Dictionary Learning,	T1-w MPRAGE, T2-w, PD and FLAIR	Sen=0.60

## PROPOSED APPROACH

In this study, we use information from T1- w, T2-w and proton density-weighted (PD) images. This is motivated by the fact that T1-w, T2-w and PD images contain information about WM lesions<sup>42</sup>. The proposed approach makes use of both unsupervised reasoning offered by a-two step segmentation method as well as an approach that mimics expert reasoning in order to identify whether a potential voxel is a lesion or not. An

optimization based approach involves initial identification of the WM class from each of the MR modality using a Fuzzy Particle Swarm Optimization (FPSO) algorithm assuming that the voxels can be WM, GM or CSF as hypothesized in<sup>42</sup>. The focus on WM is also rooted to related clinical studies<sup>43-44</sup>, which indicated that the infringement predominantly inflammatory present in the WM is likely in relate with the mechanisms of degeneration and achievement where the measurement of the load lesional provides insights about the degree of progress of the WM in the course of the disease<sup>11</sup>. Second, following the argumentation highlighted by Ait-Ali et al.<sup>45</sup>, WM tissue is often pervaded by atypical data, which often weakens the detection of lesions. Therefore, discarding the negative effect of atypical data becomes necessary. Lesion or not, a fuzzy like reasoning that imitates expert reasoning which gathers global information regarding image contrast as well as the signal type before making such decision<sup>11</sup>. Figure 1 shows the proposed workflow for the segmentation of MS lesions. The initial images are noisy, the inhomogeneities are corrected and all images are registered in the same space. Details of the different phases are provided in the subsequent subsections.

### Segmentation of the brain by Fuzzy particle swarm optimization algorithm

Brain MRI segmentation is an essential task in many clinical applications because it influences the outcome of the entire medical analysis pipeline. This is because subsequent processing steps rely on accurate segmentation of anatomical regions. For instance, MRI segmentation is commonly used for measuring and visualizing different brain structures, for delineating lesions, for analyzing brain development, and for image-guided interventions and surgical planning. This diversity of image processing applications has led to development of various segmentation techniques with variable accuracies and degrees of complexity. In this study, the segmentation of the brain tissues into different segments, namely: WM, GM and CSF is a key step in our approach. For this purpose, an optimization-based approach using Fuzzy Particle Swarm Optimization algorithm has been adopted in our approach. This is motivated by its simplicity, ability to deal with high dimensional datasets, as well as its proven efficiency in similar other segmentation tasks as pointed out in <sup>46-47</sup>. The application of Fuzzy Particle Swarm Optimization (FPSO) approach for clustering in our case yields three distinct classes corresponding to WM, GM and CSF. The outcome of this segmentation serves as the basis for implementing lesion-handling based strategies.

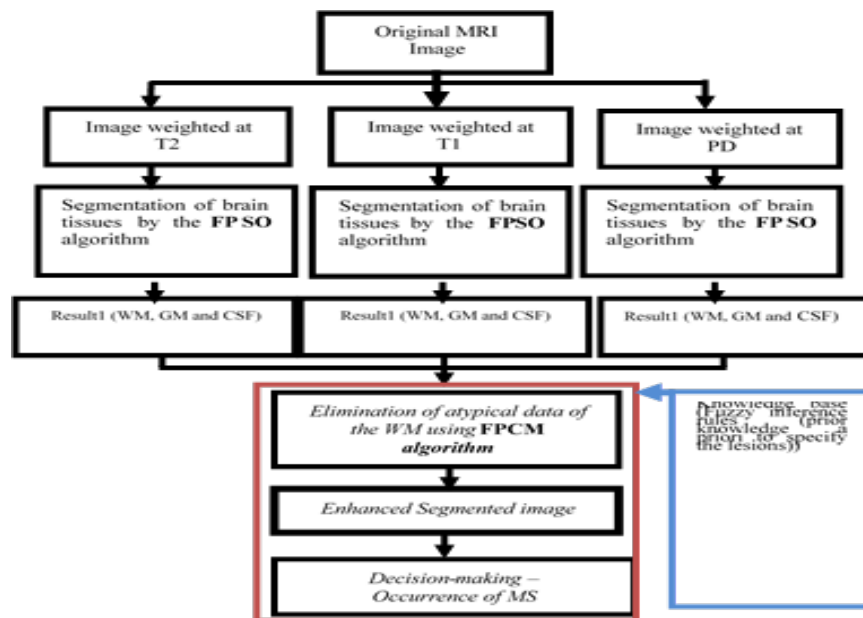


Fig. 1 Block diagram of the proposed approach for automatic segmentation of MS lesions

### Particle swarm optimization (PSO)

Particle swarm optimization (PSO) is a population-based stochastic optimization technique inspired by bird flocking and fish schooling originally designed and introduced by Kennedy and Eberhart<sup>48</sup> in 1995 and is based on iterations/generations. The algorithmic flow in PSO starts with a population of particles whose positions represent the potential solutions for the studied problem, and velocities are randomly initialized in the search space. In each iteration, the search for optimal position is performed by updating the particle velocities and positions. Also in each iteration, the fitness value of each particle's position is determined using a fitness function. The velocity of each particle is updated using two best positions, personal best position and global best position. The personal best position,  $pbest$ , is the best position the particle has visited and  $gbest$  is the best position the swarm has visited since the first time step. A particle's velocity and position are updated as follows.

$$v(t+1) = w \cdot v(t) + c_1 \cdot rand_1 \cdot (Pbest(t) - X(t)) + c_2 \cdot rand_2 \cdot (Gbest(t) - X(t)) \quad (1)$$

$$X(t+1) = X(t) + V(t+1) \quad (2)$$

Where:

$X$  and  $V$  are position and velocity of particle respectively.  $w$  is inertia weight,  $c_1$  and  $c_2$  are positive constants, called acceleration coefficients which control the influence of  $pbest$  and  $gbest$  on the search process,  $P$  is the number of particles in the swarm,  $r_1$  and  $r_2$  are random values in range  $[0, 1]$ .

PSO can be implemented and applied easily to solve various function optimization problems, or the problems that can be transformed to function optimization problems<sup>50</sup>. However, the PSO algorithm suffers a serious problem that all particles are prone to be trapped into the local minimum in the later phase of convergence. The optimal value found is often a local minimum instead of a global minimum<sup>51</sup>. Pang et al.<sup>52</sup> proposed a version of particle swarm optimization for TSP called fuzzy particle swarm optimization (FPSO).

### Fuzzy particle swarm optimization for fuzzy clustering

Peng et al.<sup>49</sup> proposed a modified particle swarm optimization for TSP called fuzzy particle swarm optimization (FPSO). In their

proposed method the position and velocity of particles redefined to represent the fuzzy relation between variables. In this subsection we describe this method for fuzzy clustering problem.

In FPSO algorithm  $X$ , the position of particle, shows the fuzzy relation from a set of data objects,  $O = \{O_1, O_2, \dots, O_n\}$ , to set of cluster centers,  $Z = \{z_1, z_2, \dots, z_n\}$ .  $X$  Can be expressed as follows:

$$X = \begin{bmatrix} \mu_{11} & \cdots & \mu_{1c} \\ \vdots & \ddots & \vdots \\ \mu_{n1} & \cdots & \mu_{nc} \end{bmatrix} \quad (3)$$

In which  $\mu_{ij}$  is the membership function of the  $i^{th}$  object with the  $j^{th}$  cluster with constraints stated in (1) and (2). Therefore, we can see that the position matrix of each particle is the same as fuzzy matrix  $\mu$  in FCM algorithm. In addition, the velocity of each particle is stated using a matrix with the size  $n$  rows and  $c$  columns the elements of which are in range  $[-1, 1]$ . We get the equations (4) and (5) for updating the positions and velocities of the particles based on matrix operations<sup>53</sup>.

$$V(t+1) = w \otimes V(t) \oplus (c_1 r_1) \otimes pbest(t) \ominus X(t) \oplus (c_2 r_2) \otimes (gbest(t) \ominus X(t)) \quad (4)$$

$$X(t+1) = X(t) \oplus X(t+1) \quad (5)$$

After updating the position matrix, it may violate the constraints given in (1) and (2). So it is necessary to normalize the position matrix. First we set all the negative elements in matrix to zero. If all elements in a row of the matrix are zero, they need to be re-evaluated using series of random numbers within the interval  $[0, 1]$  and then the matrix undergoes the following transformation without violating the constraints:

$$X_{normal} = \begin{bmatrix} \mu_{11} / \sum_{j=1}^c \mu_{1j} & \cdots & \mu_{1c} / \sum_{j=1}^c \mu_{1j} \\ \vdots & \ddots & \vdots \\ \mu_{n1} / \sum_{j=1}^c \mu_{nj} & \cdots & \mu_{nc} / \sum_{j=1}^c \mu_{nj} \end{bmatrix} \quad (6)$$



In FPSO algorithm the same as other evolutionary algorithms, a function is needed to evaluate the generalized solutions called fitness function. In this paper Eq. (7) is used for evaluating the solutions:

$$f(\mathbf{X}) = \frac{K}{J_m} \quad (7)$$

There in  $K$  is a constant and  $J_m$  is the objective function of FCM algorithm. The smaller is  $J_m$ , the better is the clustering effect and the higher is the individual fitness  $f(X)$ . The FPSO algorithm for fuzzy clustering problem can be stated as follows:

---

### Algorithm 1

---

**Input** original image.

1. Initialize the parameters including population size  $P$ ,  $c_1$ ,  $c_2$ ,  $w$ , and the maximum iterative count.
2. Create a swarm with  $P$  particles ( $X$ ,  $pbest$ ,  $gbest$  and  $V$  are  $n*c$  matrices).
3. Initialize  $X$ ,  $V$ ,  $pbest$  for each particle and  $gbest$  for the swarm.
4. Calculate the cluster centers for each particle using Eq. (11).
5. Calculate the fitness value of each particle using Eq. (7).
6. Calculate  $pbest$  for each particle.
7. Calculate  $gbest$  for the swarm.
8. Update the velocity matrix for each particle using Eq. (4).
9. Update the position matrix for each particle using Eq. (5).
10. If terminating condition is not met, go to step 4.

**Output** segmented image

---

The termination condition in the proposed method is the maximum number of iterations or no improvement in  $gbest$  after a number of iterations.

### Segmentation of the white matter using Fuzzy Possibilistic C-Means algorithm

The next stage in our methodology consists in removing the clearly hyper-intense voxels in the previously identified WM voxels in order to highlight the different MS lesions. This is because the lesions of the MS are not well contrasted due to the partial volume in the surrounding tissues, which renders their segmentation rather a difficult task. Motivated by the lack of a fully comprehensive labeled database as reported in<sup>55</sup> a non-supervised like strategy based on Fuzzy Possibilistic C-Means algorithm has been advocated. The FPCM algorithm solves the noise sensitivity defect of Fuzzy C-Means algorithm and overcomes the problem of coincident clusters of Possibilistic C-

means algorithm<sup>54</sup>. This is backed by its reported success in image analysis and medical diagnosis including magnetic imaging regardless of the modality and the type of acquisition (mono or multimodal)<sup>56-58</sup> its reduced complexity, easy implementation (especially for large and high dimension dataset).

### Formulating of FPCM algorithm clustering

Clustering is a process of finding groups in unlabelled dataset based on a similarity measure between the data patterns (elements)<sup>54</sup>. A cluster contains similar patterns placed together. One of the most widely used clustering methods is the FPCM algorithm. The FPCM algorithm solves the noise sensitivity defect of Fuzzy C-Means algorithm and overcomes the problem of coincident clusters of Possibilistic C-Means algorithm. The FPCM algorithm allows to partition the pixels of  $X$  into  $C$  classes (here  $C=3$ ) pertaining to WM, GM and CSF by calculating the centres  $b_j$  ( $j=1, C$ ) of  $j$ -th class and the membership matrix ( $U$ ), Given a set of  $N$  total number of pixels of the image  $\mathbf{X} = \{ x_1, x_2, \dots, x_N \}$  the Fuzzy Possibilistic C-Means (FPCM) clustering algorithm minimizes the objective function given below<sup>32-33</sup>:

$$J(\mathbf{B}, \mathbf{U}, \mathbf{T}, \mathbf{X}) = \sum_{i=1}^C \sum_{j=1}^N (u_{ij}^m + t_{ij}^\lambda) d^2(x_j, b_i) \quad (8)$$

Where  $x_j$  is the  $j$ -th  $P$ -dimensional data vector,  $b_i$  is the centre of cluster  $i$ ,  $m > 1$  is the weighting exponent,  $\lambda \in [3,5]$  is the typicality exponent,  $d^2(x_j, b_i)$  is the Euclidean distance between data  $x_j$  and cluster centre  $b_i$ ,  $[U]_{C \times N}$  is the fuzzy matrix and  $[T]_{C \times N}$  is the typicality matrix.

The minimization of objective function  $J(\mathbf{B}, \mathbf{U}, \mathbf{T}, \mathbf{X})$  can be guided by an iterative process in which updating of membership degrees  $u_{ij}$ , typicality degrees  $t_{ij}$  and the cluster centers are done for each iteration by :

$$u_{ij} = \left[ \sum_{k=1}^c \left( \frac{d(x_j, b_i)}{d(x_j, b_k)} \right)^{\frac{2}{(m-1)}} \right]^{-1} \quad (9)$$

$$t_{ij} = \left[ \sum_{k=1}^c \left( \frac{d(x_j, b_i)}{d(x_j, b_k)} \right)^{\frac{2}{(\lambda-1)}} \right]^{-1} \quad (10)$$

$$b_i = \frac{\sum_{k=1}^N (u_{ik}^m + t_{ik}^\lambda) x_k}{\sum_{k=1}^N (u_{ik}^m + t_{ik}^\lambda)} \quad (11)$$

Where :

$$\forall i \in \{1 \dots C\}, \forall j \in \{1 \dots N\} \begin{cases} u_{ij} \in [0,1] \\ 0 < \sum_{i=1}^N u_{ij} \end{cases} \quad (12)$$

$$\forall j \in \{1 \dots N\} \sum_{i=1}^c u_{ij} = 1 \quad (13)$$

$$\forall i \in \{1 \dots C\} \sum_{j=1}^N t_{ij} = 1 \quad (14)$$

FPCM algorithm consists then of iteratively applying equations (9), (10) and (11) until stability of the solutions. The above equations show that membership  $u_{ik}$  is affected by all  $c$  cluster centres, while possibility  $t_{ik}$  is affected only by the  $i$ -th cluster centre  $C_i$ . The possibilistic term distributes the  $t_{ik}$  with respect to all  $n$  data points, but not with respect to all  $c$  clusters. Thus, membership can be called relative typicality, it measures the degree to which a point belongs to one cluster relative to other clusters and is used to crisply label a data point. And possibility can be viewed as absolute typicality, it measures the degree to which a point belongs to one cluster relative to all other data points, it can reduce the effect of outliers. Combining both membership and possibility can lead to a better clustering result<sup>59</sup>.

Overall, the FPCM algorithm consists of the following steps and rules (Table 2)<sup>15</sup>:

**Table 2. Rules' base in the form of a matrix.**

	T1-w	T2-w	DP-w
Hyper signal	Low/Normal	High	High
Hyper signal	Low	High	High
Hyper signal after injection of Gadolinium	Normal	High	High

### Algorithm 2

**Input** WM image.

S1: Given a preselected number of clusters  $c$  and a chosen value for  $m$ , initialize the fuzzy partition matrix and typically the partition matrix with constraint in (13) and (14), respectively.

S2: Calculate the center of the fuzzy cluster,  $b_i$  for  $i = 1, 2, \dots, c$  using Eq. (11).

S3: Use Eq. (9) to update the fuzzy membership  $u_{ij}$ .

S4: Use Eq. (10) to update the typically membership  $t_{ij}$ .

S5: If the improvement in  $J(B, U, T, X)$  is less than a certain threshold ( $\epsilon$ ), then stop; otherwise, go to S1

**Output** The images of extracted MS

### Decision-making

The last step determines whether a given WM voxel is an MS lesion or not. For this purpose, a Mamdani-type fuzzy inference system has been adopted. In the latter, (global) information about the image contrast and signal's type are used as global variables. The outcome corresponds to the extent to which the MS attribute is persistent in the underlying WM voxel. Especially, the weighted images in T2 and PD underline the myelin component in the lesions characterized by the edemas with hyper-intense appearance in comparison to the WM. Furthermore, T1-w underlines the irreversible destruction of the tissues with the appearance in the white matter of persistent "black holes" (Hypo-signal)<sup>50</sup>.

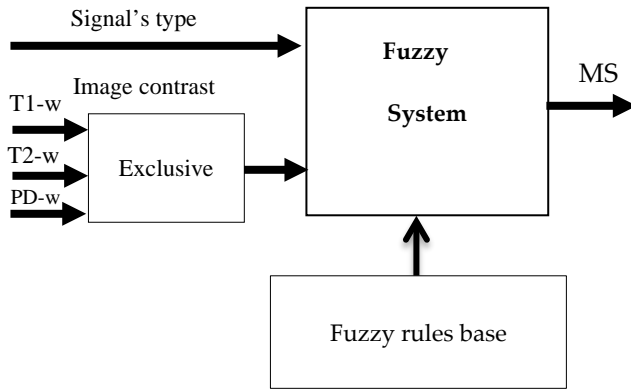


Fig. 2 Diagram of fuzzy system of the MS disease

An instance of fuzzy rules is described below:

1. **If** [(the image contrast is T1-w active) AND (the signal is hyperintense)] **then** (MS is low).
2. **If** [(the image contrast is T1-w active) AND (the signal is hyperintense)] **then** (MS is normal).
3. **If** [(the image contrast is T2-w active) AND (the signal is hyperintense)] **then** (MS is high).
4. **If** [(the image contrast is PD -w active) AND (the signal is hyperintense)] **then** (MS is high).
5. **If** [(the image contrast is T1-w active) AND (the signal is hypointense)] **then** (MS is low).
6. **If** [(the image contrast is T2-w active) AND (the signal is hypointense)] **then** (MS is high).
7. **If** [(the image contrast is PD-w active) AND (the signal is hypointense)] **then** (MS is high).
8. **If** [(the image contrast is T1-w active) AND (the signal is hyperintense after injection of gadolinium)] **then** (MS is normal).
9. **If** [(the image contrast is T2-w active) AND (the signal is hyperintense after injection of gadolinium)] **then** (MS is high).
10. **If** [(the image contrast is PD-w active) AND (the signal is hyperintense after injection of gadolinium)] **Then** (MS is high).

The quantification of image contrast, signal type and the MS disease is described in the as follows:

For the fuzzification of the signal's type, we choose two fuzzy intervals and belonging functions of Gaussian types. Figure 3 shows the fuzzy repartition of the input variable of signal's type.

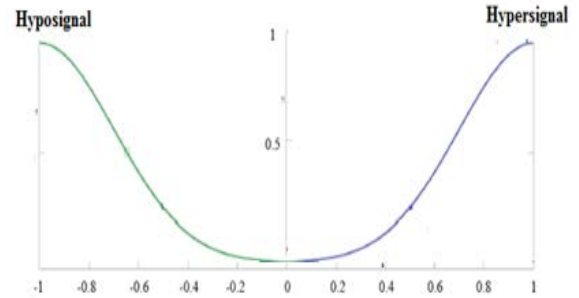


Fig. 3 Fuzzy repartition of input variable of signal's type<sup>11</sup>

For the output variable, we choose three fuzzy intervals and Gaussian membership functions, which define predicates: *low*, *normal* and *high* of the MS disease in comparison to the white matter. Figure 4 shows the fuzzy repartition of the output variable of the decision of the MS disease.

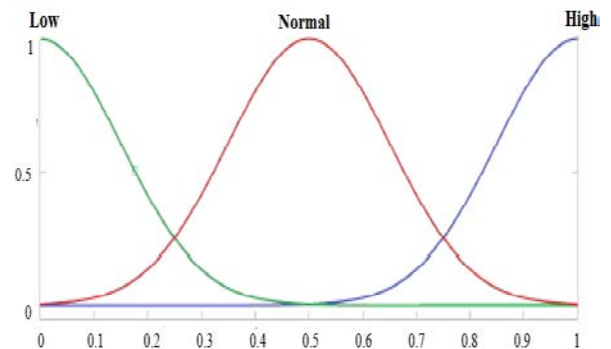


Fig. 4 Fuzzy repartition of the output variable giving the decision of the MS disease<sup>11</sup>

The selected inference method is Mamdani's method. Consequently, the operator is realized by the calculation of the minimum, while the operator OR is realized by the calculation of the maximum. The defuzzification step is done using the method of calculating the centre of attraction.

## RESULTS AND DISCUSSION

### Dataset

The dataset was provided as part of a collaboration agreement between LSI laboratory (Laboratory Intelligent Systems: image and signal team) Ferhat Abbas University of Sétif and LAMIH UMR CNRS 8201 (Laboratory of Industrial and Human Automation control, Mechanical engineering and Computer Science) University of Valenciennes. The various T1-w, T2-w

and PD images corresponding to relatively older patients. These images are in the form of DICOM (Digital Imaging and Communications in Medicine) and were already pre-processed and spatially normalized.

### Computational requirement

The proposed algorithm was implemented in Net-Beans IDE 8.2 and run on a laptop with 2.40 GHz Intel(R) Core (TM) i5-4210U CPU and 4 GB RAM. The operating system was 64-bit Windows 8.1. To compare the performance of these images, we compute different coefficients reflecting how well two segmented volumes match. Four measures are used as follows<sup>43</sup>:

$$Overlap (ovrl) = \frac{TP}{TP + FN + FP} \quad (15)$$

$$Similarity (Si) = \frac{2TP}{2TP + FN + FP} \quad (16)$$

$$Sensitivity (Sen) = \frac{TP}{TP + FN} \quad (17)$$

$$Specificity (Spc) = \frac{TN}{TN + FP} \quad (18)$$

Where, TP (True Positive) means an MS patient is correctly identified as MS, FP (False Positive) means healthy people were incorrectly identified as MS, TN (True Negative) means healthy people were correctly identified as healthy, and FN (False Negative) means MS patients incorrectly identified as healthy.

### Analysis of the results

The brain segmentation was successfully applied on some real images and results are shown in Figure 5.

### Automatic tissues and white matter lesion segmentation by FPSO and FPCM algorithms

The following figure 5 illustrates axial slices of the segmentation results by the FPSO algorithm for the T2-w, PD-w and T1-w MR images in order to obtain a characterization of the different

healthy tissues WM, GM and CSF. After the segmentation by FPSO algorithm we extracted the WM. Then, the use of FPCM allowed us to eliminate the atypical data of the WM for each image (T2-w, PD-w, T1-w) as exhibited in figure 5.

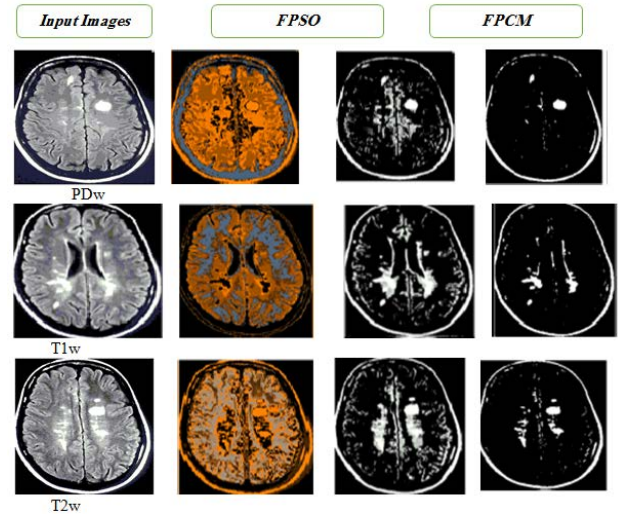


Fig. 5 Scheme of the full MS lesion segmentation process. The left column shows the the used strategy for of tissues (WM, GM, and CSF) segmentation steps, while the right column depicts the used strategy for MS lesion segmentation.

Comparative results are presented in Table 3 below:

Table 3. Comparison of the results obtained by FPSO and FPCM

		algorithms			
		GSF	WM	GM	MS lesions
T1-w	<i>Si</i>	0.81	0.91	0.85	0.93
	<i>Ovrl</i>	0.63	0.88	0.84	0.94
	<i>Sen</i>	0.70	0.95	0.91	0.91
T2-w	<i>Spc</i>	0.75	0.96	0.90	0.93
	<i>Si</i>	0.92	0.94	0.92	0.99
	<i>Ovrl</i>	0.89	0.93	0.90	0.95
PD-w	<i>Sen</i>	0.90	0.93	0.92	0.94
	<i>Spc</i>	0.92	0.96	0.93	0.96
	<i>Si</i>	0.77	0.81	0.81	0.96
PD-w	<i>Ovrl</i>	0.58	0.77	0.70	0.95
	<i>Sen</i>	0.66	0.83	0.72	0.85
	<i>Spc</i>	0.88	0.86	0.85	0.93

The results obtained by FPSO and FPCM algorithms are very satisfactory and confirm the validity of the algorithms, its ease of implementation gives us a substantial advantage. We have made an improvement in optimizing the white matter and atypical localization data for all tissues using T1-w, T2-w and PD-w.

**Decision-making**

The implementation of the Mamdani fuzzy inference system makes use of min operator for AND connective and max for OR connectives. The result of the implementation is shown in Table 4.

**Table 4. Results of MS lesions of the defuzzification values for the different sequences**

	T1-w(%)	T2-w(%)	PD-w(%)
MS	49.64	59.51	51.71

Involving people with MS proactively in decision-making and in managing their disease is also key to the successful management of MS. The decision-making depends always on the expertise, it is evident from the Table 4 that the patient suffers from the multiple sclerosis and the MS lesions are detected in all the sequences by a normal or a high characterization.

**Experimental Results**

In this section, we compare the proposed algorithm with the FPSO, FPCM, FPSOFCM algorithms and the segmentation realized by the expert on a set of MRI brain images. In order to study the robustness of the proposed algorithm for MRI brain segmentation, test images (256x256 pixels) are from three MRI modalities (T1-w, T2-w and PD-w), corrupted by different levels of white Gaussian noise (0%, 3%, 4%) and intensity non-uniformity (RF)(0%, 20%, 40%). Segmentation results are shown in Figure 6.

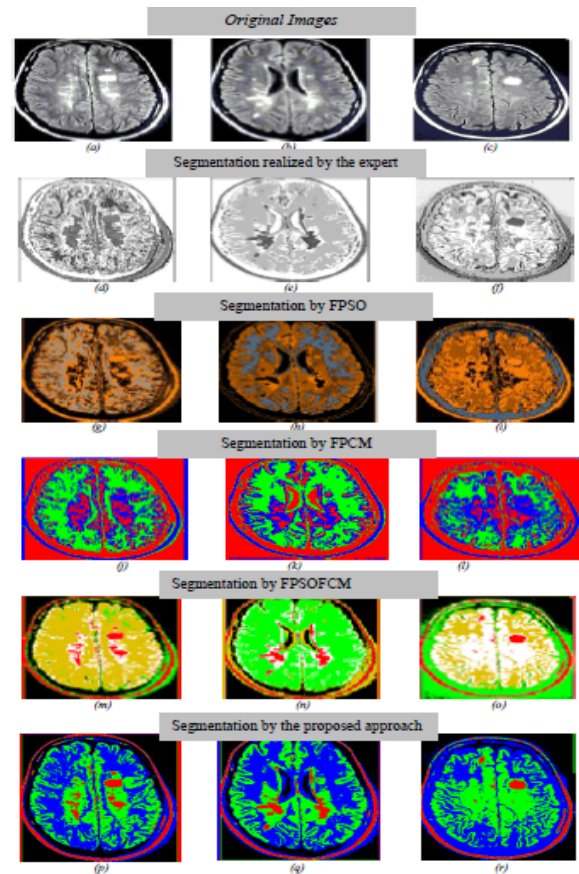


**Fig. 6 Comparison of segmentation results on T1-w, T2-w and PD-w images.**

The interpretation of our results is done by an expert (hospital center of Ain Naadja Algiers) on simulated and real images. By analyzing the images of figure 6, the expert has established the following statement:

- \_ **Image (d):** The interpretation of the classes is totally improved in relation to (FPSO, FPCM), we notice the distinction between the three classes of the brain and the class of the pathology SEP.
- \_ **Image (g):** FPSO is unsuitable in this segmentation in relation to the image (FPSOFCM).
- \_ **Image (j) :** The FPCM does not bring much compared to the FPSO.
- \_ **Image (m):** The class CSF does not conform to the class of the original image. The lack of information about the small grooves (image (a)) and the poor discrimination CSF/GM make that the segmented CSF class does not well represent the fluid distribution. The distributions of the WM and GM get closer to those given by the original image. The detection of the pathology

is indicated according to the expert but the details are not well expressed.

– **Image (p)**: the proposed approach brings a great performance to the segmentation for the three classes and especially for the fourth one which is the pathology that specifies well the size and the details about this later.

Next, we compare in figure 7 the segmentation of T2-w MRI between segmentation made by the expert, FPSO, FPCM, FPSOFCM for a given time of acquisition and the segmentation by the proposed approach.

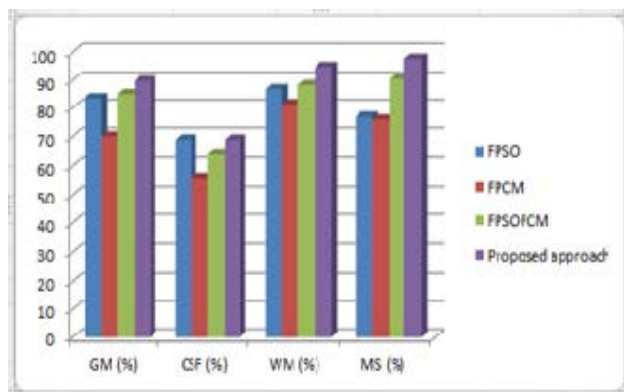


Fig. 7 Performance measures of the results gotten by different algorithms

Table 5 summarizes the results of the lesion detection algorithms reviewed in terms of reproducibility and agreement with the experts. The results highlighted in this Table and Fig.7 underline the advantages of the proposed approach in comparison to the segmentation by FPSO, FPCM and FPSOFCM for all tissues CSF, WM, GM and MS lesions. From these outcomes, it is evident that our extension of a previous work provides a very good performance method for the segmentation of abnormal anatomy in MRI data, such as MS lesions.

Table 5. Comparison of the results gotten by different algorithms.

	GM (%)	CSF (%)	WM (%)	MS (%)
<b>FPSO</b>	83.7	69	87	77
<b>FPCM</b>	70.2	55.9	81.5	76
<b>FPSOFCM</b>	85.2	64.1	88.4	90.6
<b>Proposed approach</b>	89.9	69	95	97.9

## CONCLUSIONS

The goal of the research presented in this article was to propose an automatic approach of segmentation of the MS lesions images based on FPSOFCM algorithm. Comparison results to other similar approaches shows that the proposed method outperforms is better than the other previous ones in extracting MS lesions. The prospects of improvement and development of this work are multiple: we can consider improving the post-treatments done after the detection of outliers in order to keep only the SEP lesions. At present, only the outliers for which the segmentation of the WM given by the FPCM algorithm will be kept. The main limitation of this method is that it depends on the employed method of registration. Another solution may consist of using the obtained segmentation of tissues. Thus, we can keep the outliers situated in the mask of the obtained segmentation of the WM.

## AUTHOR INFORMATION

\*ZOUAOUI Hakima

Email address: [hak\\_soraya@yahoo.fr](mailto:hak_soraya@yahoo.fr)

## REFERENCES

1. S. González-Villà, A. Oliver, Y. Huo, X. Lladó, B. A. Landman. "Brain structure segmentation in the presence of multiple sclerosis lesions". *NeuroImage: Clinical*, Volume 22, 101709, (2019).
2. F. Costello, "Vision Disturbances in Multiple Sclerosis". (*Semin. Neurol.*) 36, 185–195. (2016).
3. C. Pozzilli, "Overview of MS Spasticity". *Eur. Neurol.* 71, 1–3. (2014).
4. G. Koutsis, P. Kokotis, A.E. Papagianni, M.E. Evangelopoulos, C. Kilidireas, N.A. Karandreas, "neurophysiological study of facial numbness in multiple sclerosis: Integration with clinical data and imaging findings". *Mult. Scler. J.* 22, 764–765. (2016).
5. E. Sebastião, E.A. Hubbard, R.E. Klaren, L.A. Pilutti, R.W. Motl, "Fitness and its association with fatigue in persons with multiple sclerosis". *Scand. J. Med. Sci. Sports*, 27, 1776–1784. (2017).
6. S. H. Wang, H. Cheng, P. Phillips and Y. D. Zhang, "Multiple Sclerosis Identification Based on Fractional Fourier Entropy and a Modified Jaya Algorithm". *Entropy*, Volume: 20 Issue: 4, Article ID. 254, pp. 1-19, (2018).
7. S. Roy, A. John S. Butman, Daniel, A. Reich, Peter, Calabresi, Dzung L. Pham. "Multiple Sclerosis Lesion Segmentation from Brain MRI via Fully Convolutional". *Computer Vision and Pattern Recognition*. 1803.09172. (2018).
8. T. Kalincik, M. Vaneckova, M. Tyblova, J. Krasensky, Z. Seidl, E. Havrdova, D. Horakova, Volumetric MRI markers and predictors

- of disease activity in early multiple sclerosis: *A longitudinal cohort study*. *PLoS One* 7 (11), e50101. (2012).
9. P. Sati, et. al., 2016. The central vein sign and its clinical evaluation for the diagnosis of multiple sclerosis: a consensus statement from the North American Imaging in Multiple Sclerosis Cooperative. *Nature Rev. Neurology* 12, 714-722. 2016.
  10. E. H. Jason, N. Brian, M. Sunanda, "An information theoretic approach via IJM to segmenting MR images with MS lesions". *In Proceedings of the 2014 IEEE 27th International Symposium on Computer-Based Medical Systems (CBMS), New York, NY, USA, 27-29 May*, pp. 180-192. (2014).
  11. H. Zouaoui, A. Moussaoui, M. Oussalah, A. Taleb-Ahmed. A Robust Method for MR Image Segmentation and Multiple Scleroses Detection. *Journal of Medical Imaging and Health Informatics*, Volume 9, Number 6. (2019).
  12. J.K.. Udupa L. Wei, S. Samarasekera, Y. Miki, M.A. Van Bucham, R.I, Grossman, "Multiple sclerosis lesion quantification using fuzzy-connectedness principles", *IEEE Transactions on Medical Imaging*, 16(5), pp. 598-609. (1997).
  13. Y. Wu, S. Warfield. K, et al, 2006, "Automated segmentation of multiple sclerosis lesion subtypes with multichannel MRI", *Neuro Image*, 32(9), pp. 1205-1215. (2006).
  14. S. Sivagowri, and M.C. Jobin Christ, "Automatic lesion segmentation of multiple sclerosis in MR images using supervised classifier", *International Journal of Advanced Research in Electrical, Electronics and Instrumentation Engineering*, 2(12), pp. 6081-6089. (2013).
  15. Ö. Özdemir , A. Kaya. "Comparison of FCM, PCM, FPCM and PFCM Algorithms in Clustering Methods" *Afyon Kocatepe University Journal of Science and Engineering*, 19 (2019) 011304 (92-102).
  16. C. Elliott, D. L. Arnold, D. Louis Collins, T. Arbel, "Temporally consistent probabilistic detection of new multiple sclerosis lesions in brain MRI", *IEEE Transactions on Medical Imaging*, 32(8), pp. 1490-1503. 2013
  17. M. Prastawa, G. Guido, "Automatic MS Lesion Segmentation by Outlier Detection and Information Theoretic Region Partitioning". *In proceedings of the Grand Challenge II: workshop of MICCAI 2008*, vol, 11(WS), (2008)
  18. D. Garcia-Lorenzo, S. Francis, S. Narayanan, D.L. Arnold, D. L. Collins, "Review of automatic segmentation methods of multiple sclerosis white matter lesions on conventional magnetic resonance imaging". *Med. Image Anal.* 17 (1), 1-18. (2013)
  19. Y. Zhang, S. Lu, X. Zhou, M. Yang, L. Wu, B. Liu, P. Phillips and S. Wang, "Comparison of machine learning methods for stationary wavelet entropy-based multiple sclerosis detection: decision tree, k-nearest neighbors, and support vector machine.Simulation", *Transactions of the Society for Modeling and Simulation International*. Vol. 92(9) 861-871. (2016).
  20. N. Shiee, P.L. Bazin, A. Ozturk, D.S. Reich, P.A. Calabresi, D.L. Pham, " A Topology-Preserving Approach to the Segmentation of Brain Images with Multiple Sclerosis Lesions". *NeuroImage* 49 (2), 1524-1535. (2009).
  21. J. Souplet, C. Lebrun, N. Ayache, G. Malandain, "An automatic segmentation of T2-FLAIR multiple sclerosis lesions". *In: Multiple Sclerosis Lesion Segmentation Challenge Workshop (MICCAI 2008 Workshop)*. (2008).
  22. E. Roura, A. Oliver, M. Cabezas, S. Valverde, D. Pareto, J. C. Vilanova, L. Ramio-Torrenta, A. Rovira, X. Llado, "A toolbox for multiple sclerosis lesion segmentation". *Neuroradiology* 57, 1031-1043. (2015).
  23. S. Jain, D. M. Sima, A. Ribbens, M. Cambron, A. Maertens, W. V. Hecke, J. D., Mey, F. Barkhof, M. D. Steenwijk, M. Daams, F. Maes, S. V. Hu\_el, H. Vrenken, D. Smeets, "Automatic segmentation and volumetry of multiple sclerosis brain lesions from MR images". *NeuroImage: Clinical* 8 (5), 1229-1239. (2015).
  24. P. Schmidt, C. Gaser, M. Arsic, D. Buck, A. Forschler, A., Berthele, M. Hoshi, R. Ilg, V. J. Schmid, C. Zimmer, B. Hemmer, M. Muhlau,, "An automated tool for detection of FLAIR hyperintense white-matter lesions in multiple sclerosis". *NeuroImage* 59 (4), 3774-3783. (2012).
  25. M. Strumia, F. R. Schmidt, C. Anastasopoulos, C. Granziera, G. Krueger, T. Brox, "White matter MS-lesion segmentation using a geometric brain model". *IEEE Trans. Med. Imag.* 35 (2), 1636-1646. (2016).
  26. C. H. Sudre, M. J. Cardoso, W. H. Bouvy, G. J. Biessels, J. Barnes, S. Ourselin, "Bayesian model selection for pathological neuroimaging data applied to white matter lesion segmentation". *IEEE Trans. Med. Imag.* 34 (10), 2079-2102. (2015).
  27. P. G. Freire, R. J. Ferrari, "Automatic iterative segmentation of multiple sclerosis lesions using Student's t mixture models and probabilistic anatomical atlases in FLAIR images". *Computers in Biology and Medicine* 73, 10-23. (2016).
  28. X. Tomas-Fernandez, S. K. Warfield, "A model of population and subject (MOPS) intensities with application to multiple sclerosis lesion segmentation". *IEEE Trans. Med. Imag.* 34 (6), 1349-1361. (2015).
  29. R. Harmouche, N. K. Subbanna, D. L. Collins, D. L., Arnold, T. Arbel, Probabilistic multiple sclerosis lesion classification based on modeling regional intensity variability and local neighborhood information. *IEEE Trans. Biomed. Engg.* 62 (5), 1281-1292. (2015).
  30. A. Carass, et. al., "Longitudinal multiple sclerosis lesion segmentation: resource & challenge". *NeuroImage* 148, 77-102. (2017).
  31. E. M. Sweeney, R. T. Shinohara, N. Shiee, F. J. Mateen, A. A. Chudgar, J. L. Cuzzocreo, P. A. Calabresi D. L. Pham, D. S. Reich, "OASIS is automated statistical inference for segmentation, with applications to multiple sclerosis lesion segmentation in MRI". *NeuroImage: Clinical* 2, 402413. (2013).
  32. J. D. Dworkin, E. M. Sweeney, M. K. Schindler, S. Chahin, D. S. Reich, R. T. Shinohara, "PREVAIL: Predicting recovery through estimation and visualization of active and incident lesions". *NeuroImage: Clinical* 12, 293-299. (2016).
  33. Z. Lao, D. Shen, D., Liu, A. F. Jawad, E. R. Melhem, L. J. Launer, R. N. Bryan, C. Davatzikos, "Computer-assisted segmentation of white matter lesions in 3D MR images, using support vector machine". *Academic Radiology* 15 (3), 300-313. (2008).
  34. S. Roy, Q. He, A. Carass, A., Jog, J.L. Cuzzocreo, D. S. Reich, J. L. Prince, D. L. Pham, "Example based lesion segmentation". *In: Proceedings of SPIE Medical Imaging (SPIE)*. Vol. 9034. p. 90341Y. (2014).
  35. O. Maier, M. Wilms, J. von der Gablentz, U. M. Kramer, T. F., Munte, H. Handels, "Extra tree forests for sub-acute ischemic stroke lesion segmentation in MR sequences". *Journal of Neuroscience Methods* 89, 89-100. (2015).
  36. D. Surya Prabha and J. Satheesh Kumar, "Performance Evaluation of Image Segmentation using Objective Methods", *Indian Journal of Science and Technology*, Vol 9(8), pp. 1-8, February (2016).
  37. A. Jog, A. Carass, D.L. Pham, J. L. Prince, " Multi-output decision trees for lesion segmentation in multiple sclerosis". *In:*

- Proceedings of SPIE Medical Imaging (SPIE)*. Vol. 9413. p. 94131C. (2015).
38. L. Griffanti, G. Zamboni, A. Khan, L. Li, G. Bonifacio, V. Sundaresan, U. G. Schulz, W. Kuker, M. Battaglini, P. M. Rothwell, "BIANCA (Brain Intensity AbNormality Classification Algorithm: A new tool for automated segmentation of white matter hyperintensities". *NeuroImage* 141, 191205. (2016).
  39. S. Roy, Q. He, E. Sweeney, A. Carass, D.S. Reich, J.L. Prince, D.L. Pham, "Subject specific sparse dictionary learning for atlas based brain MRI segmentation". *IEEE Journal of Biomedical and Health Informatics* 19 (5), 1598-1609. (2015).
  40. N. Guizard, P. Coupe, V. S. Fonov, J.V. Manjon, D.L. Arnold, D.L. Collins, "Rotation-invariant multi-contrast non-local means for MS lesion segmentation". *NeuroImage: Clinical* 8, 376-389. (2015).
  41. H. Deshpande, P. Maurel, C. Barillot, "Adaptive dictionary learning for competitive classification of multiple sclerosis lesions". In: *Intl. Symp. on Biomed. Imag. (ISBI)*. pp. 136-139. (2015).
  42. D. Garcia-Lorenzo, S. Prima, S.P. Morrissey, C. Barillot, "A Robust Expectation-Maximization Algorithm for Multiple Sclerosis Lesion Segmentation". *Segmentation in the Clinic: A Grand Challenge II: lesion segmentation, New York, United States*. pp. 1-9, (2008).
  43. F. Barkhof, "MRI in multiple sclerosis: correlation with expanded disability status scale (EDSS)". *Multiple Sclerosis* 5, 283-286 (1999).
  44. A. El Dor, J. Lepagnet, A. Nakib, P. Siarry, "PSO-2S optimization algorithm for brain MRI segmentation. In: Genetic and Evolutionary Computing", pp. 13-22. *Springer* (2014).
  45. L. S. Ait-Ali, S. Prima, G. Edan, C. Barillot, "Longitudinal segmentation of MS lesions in multimodal brain MRI". In: *15eme Congres Francophone AFRIF/AFIA de Reconnaissance des Formes et Intelligence Artificielle (RFIA)*, Tours, France, Janvier (2006).
  46. V. Selvi, Dr. R. Umaramani, "Comparative analysis of ant colony and particle swarm optimization techniques. International Journal of Computer Applications". (0975-8887), Volume 5- No.4, pp 1-6, (2010).
  47. Y. Shi, R. C. Eberhart, Empirical study of particle swarm optimization. vol. 3, pp. 1945-1950 (1999).
  48. J. Kennedy, R. C. "Eberhart, Particle Swarm Optimization", In: *Proceedings of the IEEE International Conference on Neural Networks*, pp. 1942-1948 (1995).
  49. W. Pang, K. Wang, C. Zhou, L. Dong, "Fuzzy Discrete Particle Swarm Optimization for Solving Traveling Salesman Problem", In: *Proceedings of the Fourth International Conference on Computer and Information Technology, IEEE CS Press*, pp. 796-800, (2004).
  50. H. Izakian and A. Abraham, "Fuzzy c-means and fuzzy swarm for fuzzy clustering problem", *Expert Systems with Applications*, 38(3): 1835 - 1838, (2011).
  51. F. Rehab A. Kader, Fuzzy Particle Swarm Optimization with Simulated Annealing and Neighborhood Information Communication for Solving TSP. (*IJACSA International Journal of Advanced Computer Science and Applications*, Vol. 2, No. 5, pp. 15-21, (2011).
  52. W. Pang, K. P Wang, C. G Zhou, and L. J Dong, "Fuzzy discrete particle swarm optimization for solving traveling salesman problem". In *The Fourth International Conference on Computer and Information Technology*, pp. 796-800, (2004).
  53. H. Izakian, A. Abraham, V. Snášel. "Fuzzy Clustering Using Hybrid Fuzzy c-means and Fuzzy Particle Swarm Optimization" *2009 World Congress on Nature & Biologically Inspired Computing (NaBIC 2009)*, pp.1690-1694, (2009).
  54. C. Lamiche, A. Moussaoui, "Evaluation of the Segmentation by Multispectral Fusion Approach with Adaptive Operators: Application to Medical Images" (*IJACSA International Journal of Advanced Computer Science and Applications*, Vol. 2, No. 9, (2011).
  55. J. Bezdek, I. Hall, L. Clarke, "Review of MR image segmentation techniques using pattern recognition," *Med. Phys.* 20, 1033-1048, (1993).
  56. R. Nikhil, Pal, Kuhu Pal, James M. Keller, and James C. Bezdek, "A Possibilistic Fuzzy c-Means Clustering Algorithm". *IEEE transactions on fuzzy systems*, vol. 13, no. 4, August (2005).
  57. J.C. Bezdek, "Fuzzy mathematics in pattern classification," *Ph.D dissertation*, Cornell University, Ithaca, NY, (1973).
  58. N. R. Pal, K. Pal and J. C. Bezdek, "A mixed c-means clustering model", *Proceedings of the Sixth IEEE International Conference on Fuzzy Systems*, Vol. 1, pp. 11-21, (1997).
  59. S.Sivakumar, Dr.C.Chandrasekar. "Lung Nodule Detection Using Fuzzy Clustering and Support Vector Machines," *International Journal of Engineering and Technology (IJET)*. ISSN: 0975-4024 Vol 5 No 1 Feb-Mar (2013).
-





2021

## Evaluation of Effective Delivered Dose from Computed Tomography Head Scans by OSL&TL dosimetry

Khaoula Sari<sup>a</sup>, Morodian Diallo<sup>a</sup>, Karim Benkahila<sup>b,c</sup>, Serrine Sara Bouacid<sup>b</sup>, Faycal Kharfi<sup>a,b,\*</sup>

<sup>a</sup>Department of Physics, Faculty of Science, Ferhat Abbas-Setif1 University, Setif, Algeria

<sup>b</sup>Laboratory Dosing Analysis and Characterization in high resolution, Ferhat Abbas-Setif1 University, Setif, Algeria

<sup>c</sup>Fighting Against Cancer Centre, Setif, Algeria

**ABSTRACT:** In CT-scan, applying the ALARA-principle (i.e. the dose to the patient should be as low as reasonably achievable) is of the most interest to take benefit from the diagnostic capability of medical imaging by avoiding any post-diagnostic hazard due the absorbed dose. In such medical imaging modality effective delivered dose is a single parameter that can be used to assess the relative risk from exposure to ionizing radiation. In this study, we will apply computed tomography dose index (CTDI) method to determine effective dose in case of head CT-Scan. The objectives of this study are the measurement of the effective dose by TL and OSL dosimetry and CTDI method and the comparison of the measured doses to the scanner' calculated ones as well as to some worldwide measured doses for the same head CT-scan protocol. The average absorbed dose and the CTDI values were evaluated for the head scan protocol around a Siemens CT Scanner (Somatom128) used for radiotherapy simulation at the Fighting Against Cancer Medical Centre, Setif, Algeria. The calculated effective dose were found in good agreement with some international values. According to the results of the present study, the determined CTDI for head CT-scan and the measured TL and OSL point-doses allow the accurate determination of the effective dose. The Siemens dose control and optimization system "CARE Dose-4D" was found to be adequate for effective dose estimation and optimization. The followed methodology of CT-scan effective dose determination based on CTDI and TL&OSL dosimetry was found to be appropriate for modern CT scanners.

**Keywords:** CT-scan; Head CT-scan; effective dose; Clinical CT-scan objective; TL/OSL dosimetry.

## INTRODUCTION

Currently, it is universally accepted that the generalization of computed tomography (computed tomography), while it has led to considerable medical progress, has been accompanied by an increase in the radiation dose delivered to patient. In addition, if the CT-scan is combined with radiotherapy treatment, the effective dose delivered during CT-scanning, for some cases of radiotherapy treatment, should be taken into account in the total treatment dose. It, therefore, becomes particularly important to know and optimize the dose to be delivered in CT-scan. Modern

scanners display dosimetric data relating to a given examination at the desk and allow a rough estimate of the average effective dose delivered (per organ and for the whole body). This calculation involves the use of a formalism based on the calculation of CTDIs and PDLs (Dose length product) for a water equivalent dose deposition media represented by simple cylindrical geometries with diameters of 16 cm and 32 cm (adult head and neck and pediatrics). This estimation by pure calculation also involves the consideration of the kV and mAs

CT-scan data. To have even more representative and precise dose values, CTDIs are also measured on a real phantom. The Polymethyl methacrylate (PMMA) CTDI phantoms, generally supplied with CT scanners present problems of adequacy with the structure, morphology and heterogeneity of the human body made-up of biological matters of different densities (bones, muscles, air, liquids, etc.)<sup>1-2</sup>. The actual study was carried out at the radiotherapy department at the fighting against cancer (CLCC) of Sétif and at the high-resolution dosage, analysis and characterization (LDAC) laboratory of Ferhat Abbas-Sétif1 University. The objective of this work is the evaluation of the effective dose delivered following a CT-scan examination of the head by CTDI method, and OSL and TL luminescence dosimetry. The additional value of this experimental study is also to determine the additional dose administered to a patient to be also treated with external radiotherapy. In this context, we chose to work with the radiotherapy simulation CT scanner “Siemens Somatom Definition AS128” used in the radiotherapy department of the CLCC-Sétif. The dose measurements were performed on the anthropomorphic Rando phantom. Indeed, the structure and morphology of this phantom are closest to those of human. This is to obtain results close to the doses really delivered during CT-scan and, thus, to partially overcome the problem of the homogeneity of conventional CTDI phantoms.

The doses determined by the CTDI method following dose measurements by TL and OSL dosimetry are compared to those calculated by the scanner system. Comparisons with other international results are also made for the same considered test case.

## MATERIAL AND METHODS

In this work, we have used the following material:

1. The TLD-700 (LiF:Mg, Ti) and OSL-BeO dosimeters for measuring absorbed point-doses.
2. Luminescence reader OSL/TL Risø DA-20 from for the measurement of TL/OSL signals and the determination of the point-dose.
3. The Rando anthropomorphic phantom to simulate the human body with its heterogeneity.
4. The Siemens Somatom Definition AS 128 radiotherapy simulation CT-scanner<sup>3</sup>.

### *TL and OSL dosimetry*

For TL and OSL dosimetry, two types of dosimeters are used:

1. **TLD-700:** The TLD-700 are based on Lithium Fluoride but composed mainly of the isotope Li-7 (99.99%)<sup>4</sup>. TLD-700 (LiF: Mg, Ti) is considered to be a virtually tissue-equivalent material ( $Z_{\text{eff}} = 8.2$ )<sup>5</sup>. The TLD-700 is suitable for gamma, beta, and

environmental dosimetry applications<sup>4</sup>. The TLD-700 dosimeters used are manufactured by BICRON-NE HARSHAW (USA) in different forms (chips, powder, and sticks). In our work, we used discs with a diameter of 3.2 mm and a thickness of 0.9 mm.

2. **Beryllium oxide OSLD:** BeO optically stimulated luminescence (OSL) can be used for photon and beta dosimetry in scientific, medical and industrial applications. Due to the effective atomic number ( $Z_{\text{eff}} = 7.14$ ), BeO can be considered a human tissue equivalent in dosimetric practice<sup>6</sup>. In this work, we have used BeO OSL dosimeters of German origin and marketed by a Turkish company Radkor Co. These dosimeters are in the form of a square ceramic pellet with dimensions of 4 mm × 4 mm × 1 mm and a mass of 32 mg<sup>7</sup>.

The Risø TL/OSL reading system was originally developed for dating geological and archaeological samples (Fig.1). It has also been used for retrospective dosimetry and for characterizing the luminescence of materials. This reader, which allows both thermoluminescence (TL) and optically stimulated luminescence (OSL) measurements, is equipped with a 48-positions rotating carousel to automatically process as many samples. The emitted luminescence is measured by a light detection system composed of a photomultiplier tube and suitable detection filters. The light stimulation of the reader includes a source emitter and heating plate that can be used separately to make optically stimulated luminescence (OSL) or thermally stimulated luminescence TL. Both luminescence are used in this work for dosimetry purpose. Additional in-situ irradiations can be also ensured for test and calibration by a beta source and an X-ray generator.



Fig. 1 Used RISØ TL/OSL-DA20 Reader, a) Reader, b) Controller, c) The X-ray generator controller

Table 1 below shows the main characteristics and main operating conditions of the Risø TL/OSL DA-20 reader. The delivered dose rate for test and calibration are also given.

**Table 1. Main characteristics of the RISØ TL/OSL DA-20 reader**

<b>Photomultiplier</b>	CsSb crystal with maximum detection efficiency between 200 and 400 nm and 0.4sr as solid detection angle
<b>Heater material</b>	Khantal with maximal temperature of 700°C and heating rate varying from 0.1 to 10°C/s
<b>Beta source</b>	<sup>90</sup> Sr/ <sup>90</sup> Y, E <sub>max</sub> : 2.27 MeV, Strength: 1.48GBq, Dose rate 0.1Gy/s in the quartz
<b>X-ray Generator</b>	Tungsten, 50 kV, 1 mA, 50 W, Dose rate in the quartz 2Gy/s

### CT-Scan and Rando phantom irradiation

The Rando anthropomorphic phantom is a phantom that well simulates the human body with its various densities. The main characteristics and advantages of this phantom are:

#### 1. Meeting global radiotherapy quality assurance standards:

The Alderson Radiotherapy Phantom (ART) and its earlier version Alderson Rando have been used for more than 30 years in radiology and radiotherapy quality assurance (Fig.2). ART has been refined and improved in the design of its materials. This phantom is an essential quality assurance tool; around 10,000 are used worldwide. It provides integrated testing of the entire chain in CT-scan and radiotherapy treatment planning. Rando anthropomorphic phantom is made from a material equivalent to tissue; it is designed under very sophisticated technological constraints and follow ICRU-44 standards. It is also designed for precision and ease of use<sup>8</sup>.



**Fig. 1 Used male ART representing a man 175 cm high and 73.5 kg in weight**

**2. Anatomy:** The ART phantom is cut horizontally into slices of 2.5 cm thick (Fig.1). Each slice has holes that are plugged with Bone tissue-equivalent material, Soft tissue-equivalent material, Lung tissue-equivalent material, and TLD and OSLD<sup>8</sup>.

#### 3. Materials:

**Soft Tissues:** There are limitless small variations in density and absorption throughout the human body. The soft tissues of the phantom are tightly controlled to have the average density of these tissues.

**Skeletons:** Skeletons are highly detailed polymer casts that mimic the shape, mass density, and attenuation coefficients of cortical bone and sponginess. They allow the continuous production of phantoms, instead of the sporadic production required by the limited availability, variable size and uncertain chemical composition of human skeletons. These problems, along with the loss of squash in dried natural skeletons, make the upper skeletons “real bone”. The molds for cortical bone and sponginess were made from human skeletons that are compatible with the sizes of the soft tissue molds. The skeletons closely conform to the standards set by the International Commission on Radiation Units and Measurements (ICRU Report No. 44). the mass density is slightly reduced to account for a small decrease in calcium content in older patients<sup>8</sup>.

**4. Slots for passive dosimeters:** The phantom contains cylindrical holes for the location of TL/OSL dosimeters. These holes are originally filled with rods to be removed and cut for the location of the dosimeter at the required location on the axis. Z scan holes. The holes can accommodate dosimeters up to 5mm in diameter with varying thicknesses. The location holes go through the slices of the phantom end to end, about 2.5 cm thick<sup>8</sup>.

**5. Assembly:** The slices of the ART phantom are held between two aluminum plates by nylon tie rods (threaded rods). The nuts at the end of the threaded rods firmly clamp the slices in proper alignment<sup>8</sup>.

The necessary ART phantom CT-scans were performed around Seimens scanner principally devoted to radiotherapy treatment

simulation. Siemens has simplified its range of scanners. They are all called "Definition" and have many characteristics in common. They all have a tunnel with a diameter of 78 cm and have the same restraint options and the "interventional" option with in particular a box placed on the bed, which controls the table and the acquisition system. They all use the "Straton" tube, which has the particularity of having a directly cooled anode. It is actually the entire tube that rotates so that the flow of electrons does not always hit the same part of the anode.

With a dissipation of 7.3 MHU/ min (170 kW), the anode does not need to have a large heat capacity and the tube is therefore smaller and lighter than its competitors. It has a floating focal spot which, with a frequency of 4600Hz, allows switching from one position to another and thus being able to obtain two cuts per detector strip.

The power of the generator is 80 kW except for the "Definition AS 128" and they have the UFC detector (The detectors are made of Low Resistance Ceramic Material allowing the acquisition of nearly 4,608 projections per turn, and access to the Ultra High Definition imaging with fast acquisitions)

The Siemens Definition AS 128 scanner produces up to 128 slices with a 64-strip detector covering 38.4 mm per rotation, and a 78 cm-wide tunnel for better handling and comfort.

Some features and details of the scanning mode are presented below:

**1. Acquisition console and scanning execution:** In terms of console, Siemens is launching a Syngo post-processing server, through its new generation of application servers. The server has the computing power and can be accessed by any computer (subject to not exceeding the agreed number of concurrent use rights). A large number of image processing software are already available on this architecture. The acquisition station allows complete management of the control of the scanner. This computer console actually contains multiple features aimed at simplifying routine clinical use and providing optimal performance<sup>3</sup>.

**2. Scheduling of the CT examination:**

- Choice of protocols by anatomical regions.
- Possibility to save modified protocols.
- Possibility of rebuilding with an extended Hounsfield unit scale.

The « Definition » scanners all have « CARE » devices to limit the dose delivered to patients' which are the followings:

CARE Topo: the topogram can be stopped at any time without blocking the device (dose saving)

CARE Bolus: For all injected exams, monitoring of the arrival of the contrast product and automatic triggering of the spiral when the desired opacification is reached.

CARE Profile: Visualization of the dose distribution along the

topogram before acquisition.

CARE Dose4D: for anatomical modulation of exposure in real time. This allows you to adjust the dose depending on the patient's anatomy and position during acquisition.

CARE Dashboard: Visualization of dose reduction tools activated in real time.

CARE kV (Kilovolt Optimization): Automated organ-based voltage adjustment, improving image quality and contrast-to-noise ratio while reducing dose.

**Dose measurement and determination methods**

The absorbed effective dose was determined experimentally by TL and OSL dosimetry and calculated by the scanner on-board scanner algorithm (CARE Dose-4D). For the TL and OSL dosimetry, the dose was measured after the calibration the dosimeters, the subtraction of their backgrounds, the determination of their elementary correction factors, and the establishment of their responses. CARE Dose-4D calculate the computed tomography dose index (CTDI) for the determination of effective absorbed dose<sup>9</sup>.

The on-board program (algorithm) for calculating the dose of the scanner estimates the absorbed dose (*D*) according to the scanning protocol used and the scanning parameters that refer. This program also uses topogram data and other dose optimization (reduction) algorithms ensuring optimum image quality. In fact, the automatic tube current modulation (MACT) and angular modulation allow such optimization. Since the effective mAs and the intensity of the anode current vary according to the thickness of the tissues crossed, these algorithms allow dose reductions varying between 10 and 60% and this, depending on the patient's morphology and the examined region. The CARE Dose-4D dose calculation module (Siemens) combines two actions: the first is an automatic adjustment based on the size of the patient and the absorption measured in a single topogram; this step determines the maximum mA of each slice; the second is a real-time adjustment based on the attenuation of the X-ray beam according to the different regions crossed<sup>10</sup>.

For estimation of the effective delivered dose (*E*) to the studied phantom, CARE dose-4D compute first the values of volumetric *CTDI* (*CTDI<sub>vol</sub>*) and the corresponding Dose Length Product (*DLP*) from the calculated absorbed dose (*D*) from the phantom scan parameters used with the selected protocol. Calculation steps given by equations (1-6) are followed.

$$CTDI(mGy) = \int_{-\infty}^{+\infty} \frac{D(z)}{N.T} dz \tag{1}$$

$$CTDI_{100} (mGy) = \int_{-50}^{+50} \frac{D(z)}{N \times T} dz \tag{2}$$

$$CTDI_w = \frac{1}{3} CTDI_{C100} + \frac{2}{3} CTDI_{P100} \quad (3)$$

$$CTDI_n = CTDI_w / mAs \quad (4)$$

$$CTDI_{vol}(mGy) = \frac{CTDI_w}{Pitch} \quad (5)$$

$$DLP (mGy.cm) = CTDI_{vol} \times L \quad (6)$$

$$E = DLP * k \quad (7)$$

Where:

- $D(z)$ : Absorbed dose calculated on the Z scanning axis
- $N$ : Number of CT slices
- $T$ : Slice thickness
- $CTDI_{100}$ : Computed Tomography Dose Index over 100 mm
- $CTDI_{100c}$ :  $CTDI_{100}$  at the centre
- $CTDI_{100p}$ :  $CTDI_{100}$  at the periphery
- $CTDI_w$ : Weighted Computed Tomography Dose Index
- $CTDI_n$ : Standardized Computed Tomography Dose Index
- mAs: X-ray tube charge in milliampère-second
- $L$ : Scanner length
- $k$ : Weighting factor depending on the scanned organ.

## EXPERIMENTAL

### CT-scan and dose determination by CARE dose-4D

In the TL and OSL dosimetry work that we performed on the Rando phantom, we chose to use a brain scan with the “Head” Protocol. Indeed, in radiotherapy, toxicity at small doses is rather problematic for this region of the human body. The TLD and OSLD dosimeters were placed in three (3) positions to obtain the necessary point-doses to apply the CTDI method. The Siemens Somatom Definition AS' scanner dedicated to radiotherapy simulation allows on the one hand the volume acquisition of the external contours, anatomical structures and target volumes of patients and on the other hand the construction of reference images. This data will then be used to calculate dose distributions and position the patient under the treatment device.

A “Brain SPC” scanning protocol for an adult is used for this TL / OSL dosimetry work with standard scanning parameters that are already used in clinical practice. The scanner to calculate the

CTDI and the DLP, and thus estimate the effective dose E by the algorithm implemented on the scanner uses the selected scan parameters. Table 2 provides the scanning parameters: kV, mAs, slice thickness, pitch and scan length, which we had used and which are adopted in clinical practice.

**Table 2. CT-scan parameters**

TL Dosimetry	
Scanning Protocol	Cerebral_SPC (Adult)
kV	120 Kv
mAs	423 mAs (Topo à 100 kV)
Slice thickness	1 mm
Topogram length L	25.6 cm
Pitch	0.55
OSL Dosimetry	
Scanning Protocol	Cerebral_SPC (Adult)
kV	120 kV
mAs	363 (Topo à 100 kV)
Slice thickness	1 mm
Topogram length L	22.5 cm
Pitch	0.55

### Dose measurement by TL-OSL dosimetry and CTDI method

The CTDI method is applied in this work to determine the effective dose for the CT examination in question. The CDITs are determined by TL and OSL dosimetry performed on the Rando phantom by measuring the dose on the three points A, B, and C. The TL / OSL intensities measured around the Riso DA-20 reader are converted into dose using the established response curves and elementary correction factors for the intensities measured for each dosimeter (ECF). For the determination of the dose, it is necessary to take into account the fact that the dose rates are given in relation to quartz, that the exposures are carried out in the materials of the dosimeters (LiF and BeO), and that the doses which interest us are those which should be absorbed by the material of the phantom (water equivalent). In addition, we must also consider the variation in energy between that used in the calibration of dosimeters (50keV) and those used in the scanning examination (120 keV).

For each type of dosimeter, (TLD and OSLD) two dose correction factors (CF) are therefore necessary. These correction factors are given by the following formulas:

$$CF_1 = CF \left[ \frac{LiF}{Quartz} \right]_{50keV} = \frac{\frac{\mu_{en}}{\rho}(LiF)}{\frac{\mu_{en}}{\rho}(Quartz)} = 0.486 \quad (8)$$

$$CF_2 = CF \left[ \frac{Water}{LiF} \right]_{120keV} = \frac{\frac{\mu_{en}}{\rho}(Water)}{\frac{\mu_{en}}{\rho}(LiF)} = 1.16 \quad (9)$$

$$CF_3 = CF \left[ \frac{BeO}{Quartz} \right]_{50keV} = \frac{\frac{\mu_{en}}{\rho}(BeO)}{\frac{\mu_{en}}{\rho}(Quartz)} = 0,192 \quad (10)$$

$$CF_4 = CF \left[ \frac{Water}{BeO} \right]_{120keV} = \frac{\frac{\mu_{en}}{\rho}(Water)}{\frac{\mu_{en}}{\rho}(BeO)} = 1,17 \quad (11)$$

These factors allow the dose to be corrected, for the two types of dosimeters used, as follows:

$$D_{corr}(TL) = D_{meas}(TL) \times FC[LiF/Quartz]_{50keV} \times FC[Water/LiF]_{120keV} \quad (12)$$

$$D_{corr}(OSL) = D_{meas}(OSL) \times FC[BeO/Quartz]_{50keV} \times FC[Water/BeO]_{120keV} \quad (13)$$

Once all the doses have been measured and corrected, the  $CTDI_w$ ,  $CTDI_{vol}$ ,  $DLP$  and effective dose  $E$  are determined by the following formulas:

$$CTDI_w = \frac{1}{3}CTDI_c + \frac{2}{3}CTDI_p = \frac{1}{3}CTDI_B + \frac{2}{3} \left[ \frac{1}{2}(CTDI_A + CTDI_C) \right] \quad (14)$$

$$CTDI_{vol} = CTDI_w/0.55 \quad (15)$$

$$DLP = CTDI_{vol} \times L \quad (16)$$

$$E = DLP \times k \quad (17)$$

For the adult head protocol,  $k = 0.0021 \text{ mSv.mGy}^{-1}.\text{cm}^{-1}$ .

For each type of dosimetry and after the step of calibrating and establishing the response curves of the TLD and OSLD dosimeters, the latter were placed on the Randon phantom and exposed according to the scanning protocol already described in the previous sections. The dosimeters were placed at the different holes of the slice number 4 located at the level of the phantom head. Dosimeters A and C are placed on the periphery of the slice and dosimeter B in the center as shown in figures 2 (Top face of the slice) and 3 (bottom face of the slice). After the

preparation and assembly of the Rando phantom, it was exposed according to the selected head-scan protocol with the recommended clinical position. The topogram is first collected then the CT-scan was done after performing the necessary adjustment. After CT-scan, the dosimeters were collected in order to read the induced TL and OSL signals.

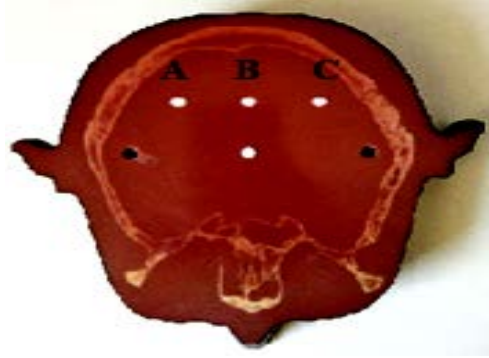


Fig 2 Phantom slice on which the dosimeters are placed: Top face



Fig 3 Phantom slice on which the dosimeters are placed Top: Bottom face

### ***TL-OSL Dosimeters calibration and dose responses establishment***

In this CT-scan effective dose measurement, three (3) dosimeters are used for each TL or OSL dosimetry. For the calibration of these dosimeters, these dosimeters were irradiated in situ with X-rays. The X-ray generator of the Riso DA-20 reader was used to deliver the required doses under a voltage of 50 kV and a variable current. This generator is equipped with a collimator, a mechanical shutter; a controlled high voltage power supply, a control and command system, and a safety interlock system<sup>11</sup>. The dosimeters are placed on stainless steel discs 9.7 mm in diameter. Luminescence signals are recorded as a count as a function of temperature (TL) or time (OSL). The exposure rate is given relative to quartz. The distance between the x-ray tube and the sample is 35.5 mm, and the average

dose rate in quartz is 2 Gy /s<sup>12</sup>.

Prior to use, the dosimeters were annealed using a Riso TL / OSL DA-20 reader to remove any residual TL / OSL signal and leave only background noise. Thus, thanks to a tweezer, the dosimeters are placed on the carousel for their emptying by gradually heating them up to 450 ° C with a heating rate of 5 ° C/s. This step is necessary. To empty the dosimeters and know the background noise level and its adequacy with the measurements that will be carried out. The following figure 4 represents the background noise signals for the TL and OSL dosimeters obtained.

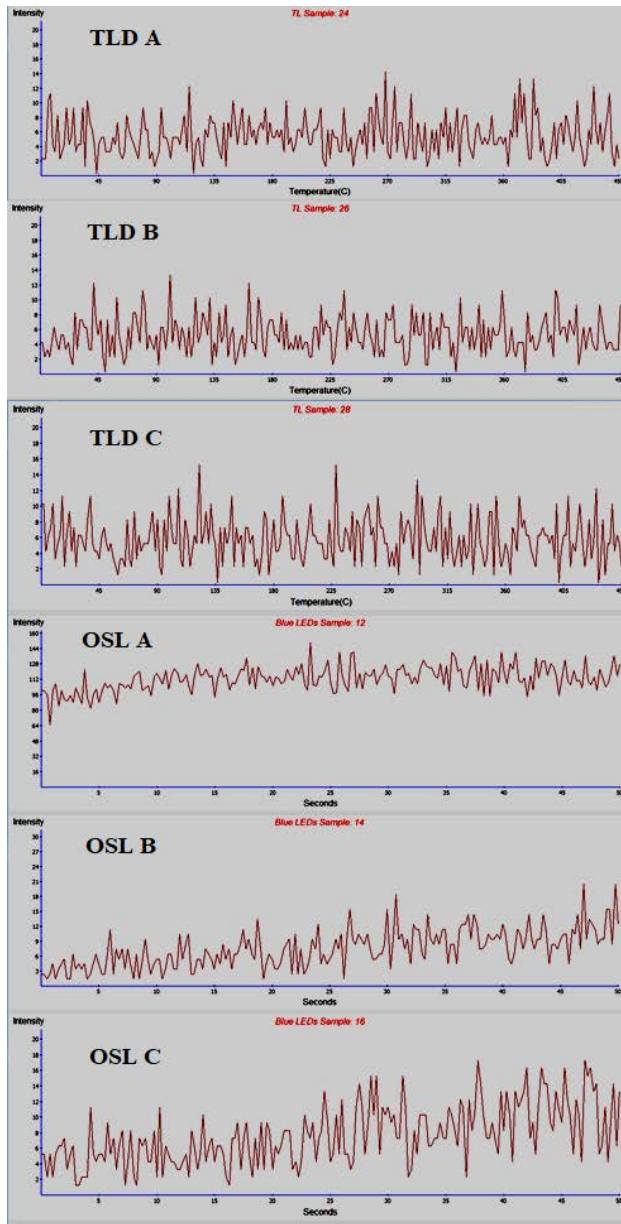


Fig. 4 Background noise signals for TLDs and OSLs

Dosimeters, by virtue of their geometric and structural properties, do not respond identically and in the same way to the same dose. This is why it is generally recommended by the dosimeters to choose to use a reference dosimeter and to align the responses of the other dosimeters with respect to this one for the same dose. Thus, elementary correction factors can be identified for all the dosimeters used to overcome this drawback and have precise and uniform measurements. To determine the elementary correction factors, all three TL dosimeters were exposed to the same x-ray dose of 500 mGy using dosimeter A as a reference. The same goes for OSL dosimeters with a dose of 100 mGy and dosimeter A as a reference. Table 3 shows the TL intensities of dosimeters A, B and C for a dose of 500 mGy.

Table 3. TL intensities of dosimeters A, B, and C for a dose of 500 mGy

Dosimeter		Measured Intensity
T	A (reference)	466142
L	B	357013
D	C	476664
O	A (reference)	1378
S	B	1287
L	C	1357

The elementary correction factor for each used dosimeter (ECF) is given by:

$$ECF_{TL/OSL} = \frac{I_{TL/OSL(A,ref)}}{I_{TL/OSL(A,B,C)}} \quad (18)$$

To establish the TL and OSL responses of the dosimeters used as a function of the x-ray dose, the reference TLD and OSLD dosimeters (A) were exposed to different x-ray doses of 0.24, 0.5, 1, 1.5, 2 and 4 Gy . The exposure is carried out under suitable operation conditions of the X-ray generator in terms of high voltage (kV), anode current (mA) and exposure time (s).

The determined ECFs are presented in the following table for the different TLDs and OSLDs following the measurements of the TL and OSL signals for the same dose of 2 Gy.

Table 4. Elementary Correction Factors

Dosimeter		ECF
T	A (reference)	1
L	B	1.30
D	C	0.98

O	A (reference)	1
S	B	1.07
L	C	1.01

$$I_{TL} = 780839 \pm 20854 \times D + 46923 \pm 11797 \quad (19)$$

The TL signals obtained (Fig.5) for the reference TL dosimeter (A) enabled us to determine the TL intensities for the different doses considered and to establish the response curve (TL = f (D) (Fig.6). The linear data adjustment by the least squares method allow generating the Fit equation (Eq.19) that is used for the determination of the doses during the CT-scan examination. The response curve seems well linear with a regression factor of 0.99.

Likewise, the OSL signals obtained (Fig. 7) for the reference OSL dosimeter (A) are also used to establish the response curve (OSL = f (D) (Fig.8). The linear data adjustment allow too the objection of the relation between dose to OSL intensity (Eq. 20).

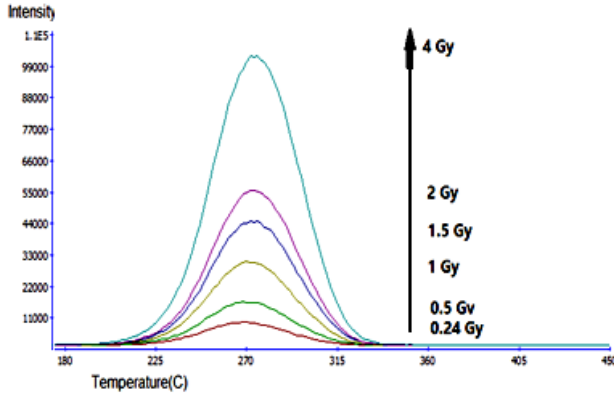


Fig. 5 TL signals obtained for the reference TLD (A)

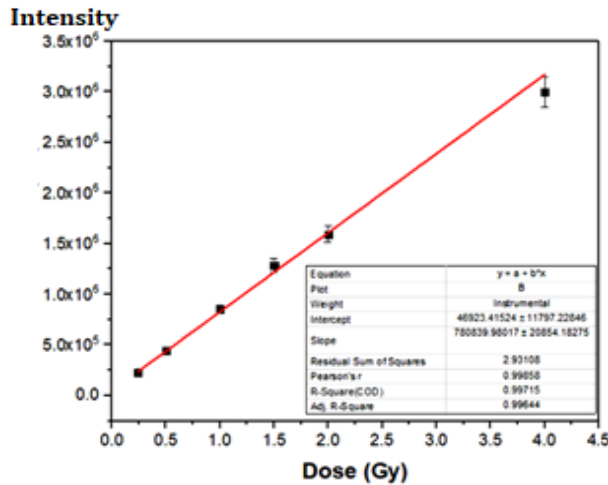


Fig. 6 TL-Dose response curve of the reference TLD (A)

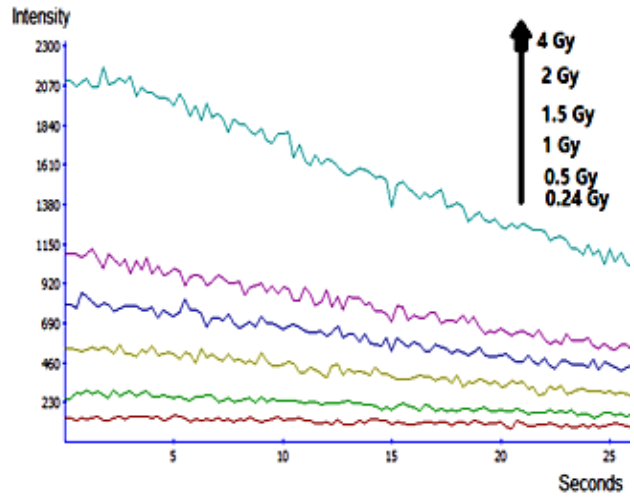


Fig. 7 OSL signals obtained for the reference TLD (A)

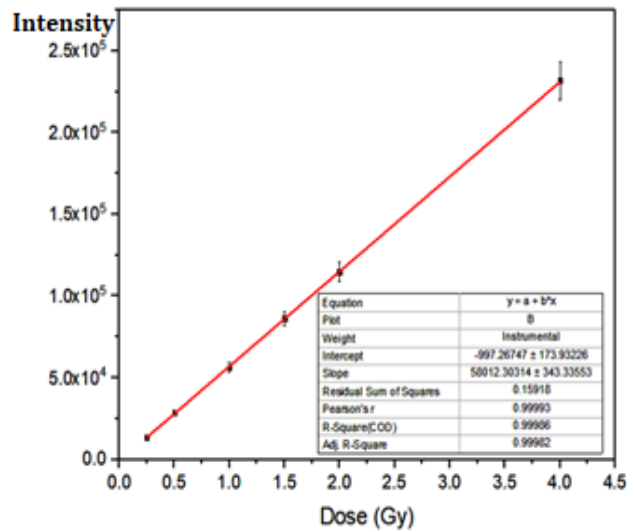


Fig. 8 TL-Dose response curve of the reference OSL (A)

$$I_{OSL} = 58012 \pm 343 \times D - 997 \pm 174 \quad (20)$$

## RESULTS AND DISCUSSION

### CT-scan and dose determination by CARE dose-4D

In the CT-scan performed, the slice thickness is 1mm. Thus, and depending on the lengths of the scanning topograms, 241 slices were acquired for TL dosimetry and 219 for OSL dosimetry. For TL dosimetry, slices N ° 100, 101 and 102 cover the axial positions



of the used dosimeters (A, B and C) on the phantom (Fig. 9). Likewise, for OSL dosimetry, slices N ° 92, 93 and 94 cover the axial positions of the used OSL dosimeters (A, B and C) on the phantom (Fig.10). The CT-slices obtained are of very good quality from a visual point of view (contrast and definition).

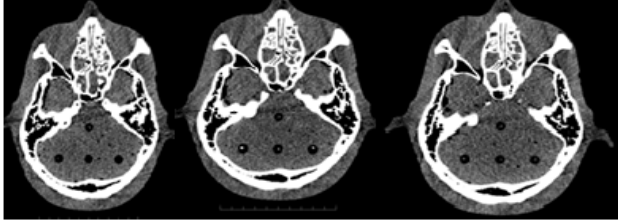


Fig. 9 CT slices 100, 101 and 102 for TL dosimetry

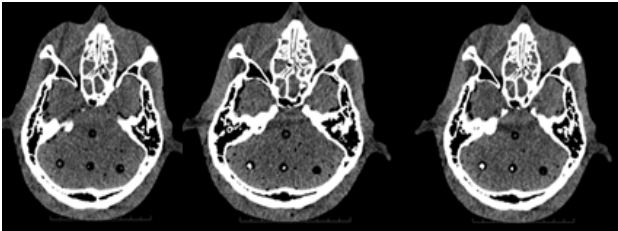


Fig. 10 CT slices 92, 93 and 94 for OSL dosimetry

The values of  $CTDI_{vol}$  and  $DLP$  calculated by CARE Dose-4D are presented in table 5. From these values, the effective doses  $E (DLP \times k)$  are determined for both TL and OSL dosimetry (Table 5).

Table 5.  $CTDI_{vol}$  and  $DLP$  calculated by CARE Dose-4D and corresponding effective doses E

$CTDI_{vol}$ (mGy)	$CTDI_w$ (mGy)	$DLP$ (mGy. cm)	$E = k \times DLP$ (mSv)
<b>TL dosimetry</b>			
46.43	46.43	1188.6	2.5
<b>OSL Dosimetry</b>			
39.85	39.85	896.6	1.88

**Measured effective doses by TL and OSL dosimetry**

Following the exposure of the Rando Phantom, the point-doses in A, B and C positions are measured and corrected. The measured and corrected TL and OSL intensities are presented in table 6.

Table 6. Measured and corrected TL and OSL Intensities

TLD/OSL	Measured Intensity	ECF	Corrected Intensity
<b>TL dosimetry</b>			
A	74596±3730	1	74596±3730
B	66057±3302	1.30	85874±4292
C	80846±4042	0.98	79229±3961
<b>OSL Dosimetry</b>			
A	5997±280	1	5997±280
B	4471±224	1.07	4783.97±240
C	3860±185	1.01	3898.6±187

The point-doses at positions A, B and C are determined by the TL/OSL-Dose response equations and corrected by the various corrections factors (Table 7). From the doses measured by TL and OSL dosimetry, the effective doses are determined by the CTDI method according to the formalization already presented. Table 7 summarizes the values of the average absorbed point-doses with the used correction factors..

Table 7. Measured and corrected doses

	Measured dose	$CF_{1/3}$	$CF_{2/4}$	Corrected dose
<b>TL dosimetry</b>				
A	35.44± 1.8	0.486	1.16	19.97 ± 1.53
B	49.88 ± 2.31	0.486	1.16	28.12 ± 2.19
C	41.37 ±3.52	0.486	1.16	23.33 ±1.62
<b>OSL Dosimetry</b>				
A	120.56 ± 5.23	0.192	1.17	27.08 ± 3.31
B	99.65 ± 4.51	0.192	1.17	22.38 ± 3.05
C	84.38 ± 4.06	0.192	1.17	18.95 ± 2.88

From the point-doses measured by TL and OSL dosimetry, the effective doses are determined by the CTDI method according to the formalization already presented. Table 8 summarizes the values of determined effective doses for each dosimetry (TL and OSL).

**Table 8. Measured effective doses by TL and OSL dosimetry, and CTDI method**

CTDI <sub>w</sub> (mGy)	CTDI <sub>vol</sub> (mGy)	DLP (mGy.cm)	E (mSv)
<b>TL dosimetry</b>			
23.8 ± 1.7	43.3 ± 1.8	1107.7 ± 55.7	2.33 ± 0.09
<b>OSL Dosimetry</b>			
22.8 ± 1.1	41.45 ± 1.3	932.6 ± 51.1	1.96 ± 0.08

**Comparison between TL&OSL dosimetry and CARE dose-4D**

The results of tables 5 and 8 allow us to make the following remarks and conclusions:

1. The differences between the doses estimated by CARE Dose-4D and the CTDI method associated with TL and OSL dosimetry are 6.8% for TL and 4.08% for OSL. This shows that, on the one hand, CARE Dose-4D estimates and optimizes well the dose in CT-scan well. On the other hand, the two used dosimetries are very efficient for dose measurement with a slight advantage for OSL dosimetry.

2. The doses of the two CT-scans carried out for the TL and OSL dosimetries, whether estimated by CARE Dose-4D and determined by the CTDI and TL and OSL dosimetry, are different because of the lengths of topograms were not the same (25.6 and 22.5 cm) and therefore the doses absorbed by the two different volumes should be different. Indeed, we notice that the ratio between the two topogram lengths is 1.13, and that between the CARE Dose-4D doses is 1.32, while that between the CTDI-dosimetry-TL/OSL doses is 1.18. This shows that TL-OSL dosimetry tracks the change in dose deposition volume better than CARE Dose-4D.

**Comparison to others studies**

The effective dose calculated and measured for a the head CT-scan with a standard scanning protocol around the Siemens Somatom 128 scanner were also compared to other results internationally obtained for the same CT-scan. Table 9 compares *CTDI<sub>vol</sub>*, *DLP* and effective doses from various origins.

**Table 9. Comparison of effective doses E for the head CT-scan from various origins**

Origin	L	DLP (mGy.cm)	E (mSv)
<b>Our Study</b>			
CARE Dose-TL	25.6	1188,6	2,5

CARE Dose-OSL	22.5	896,6	1,88
CTDI-TL	25.6	1107.71	2,33
CTDI-OSL	22.5	932,63	1,95
<b>Worldwide results</b>			
South Africa <sup>13</sup>	25	989,92	2,07
Nigeria <sup>14</sup>	21.5	1310	2,75
Canada <sup>15</sup>	13.2	1098	2,31
Kenya <sup>16</sup>	26.4	1612	3,38
Egypt <sup>17</sup>	45.3	1360	2,85
Greece <sup>18</sup>	15.8	1053	2,21
United States <sup>19</sup>	18.1	1120	2,35
Australia <sup>20</sup>	16.7	1000	2,1
France <sup>21</sup>	16.2	1050	2,21

Although, the *CTDI<sub>vol</sub>* compared are representative in terms of absorbed dose level, the comparison of effective doses is not objective unless one proceeds to standardize and normalize the dose against the length of the topogram used in the CT-scan. The following figure 11 shows graphical comparison of standardized and normalized effective doses with respect to the topogram length. The results of the comparison clearly show that the dose is very well optimized in the scanning protocol of the Egyptian reference. The worst optimization is that relating to the Canadian reference. Our Siemens Somatom-128 scanner optimizes the dose relatively better compared to other scanners as shown in figure 11 by ensuring a very good image quality as shown on the CT-slices obtained. However, the objective comparison between these doses remains depending on quality of the produced CT images and the dose level to be not exceeded for this kind of CT-scan. If such CT-scan is combined with radiotherapy treatment, the determined dose levels should be taken into consideration in the total dose to be administered to the patient to avoid overdose problems although for low doses.

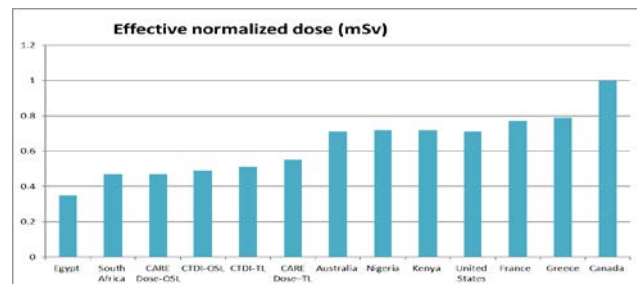


**Fig. 11 Comparison of standardized and normalized effective doses**

## CONCLUSIONS

In this project, it was a question of applying TL and OSL dosimetry after calibration of the dosimeters for the measurement of the point-doses necessary for the application of the CTDI method for the determination of the effective dose in CT-scan.

In this work, effective dose is measured for a specific head CT-scan around a Siemens Samaton 128 radiotherapy simulation scanner. This protocol was specially chosen because it is the one that poses the most dose toxicity problems for patients to be treated with radiotherapy. TL and OSL dosimetries were performed under clinical CT-scan conditions. All dosimetric response functions of the used dosimeters were effectively established and found to be linear.

The differences between the doses estimated by CARE Dose-4D and the CTDI method with TL and OSL dosimetry are 6.8% for TL and 4.08% for OSL. This shows that CARE Dose-4D correctly estimates and optimizes the dose of the CT-scan. It was also observed that TL and OSL dosimetries follow the change in absorbed dose as a function of deposition volume better than CARE Dose-4D.

This study show that for an objective comparison between effective absorbed doses, the CT image quality and the dose level not to be exceeded must be taken into consideration. If CT-scan is associated with radiotherapy treatment, the determined dose levels in CT-scan should be taken into account in the total dose to be administered to the patient to avoid problems of overdose and radiotoxicity.

## AUTHOR INFORMATION

### Corresponding Author

\*Faycal Kharfi

Email address: [kharfifaycal@univ-setif.dz](mailto:kharfifaycal@univ-setif.dz)

## REFERENCES

1. F. Kharfi. Mathematics and Physics of Computed Tomography (CT): Demonstrations and Practical Examples in: Imaging and Radioanalytical Techniques in Interdisciplinary Research - Fundamentals and Cutting Edge Applications, INTECH, ISBN 978-953-51-1033-0, 2013.
2. I. Gardin, S. Hapdey, Apport du TDM en imagerie multimodalité: le point de vue du physicien médical. Médecine Nucléaire, Elsevier/Masson, 2010, pp.426-430.
3. <https://www.siemens-healthineers.com/fr-ch/computed-tomography/single-source-ct/somatom-definition-as>.
4. AAPM TG 191: Clinical use of luminescent dosimeters: TLDs and OSLDs, 2019.

5. A. Lisbona, Groupe de Travail « Dosimétrie des explorations diagnostiques en radiologie » Societe Française de Physique Medicale, Rapport S.F.P.M. N° 21, [https://inis.iaea.org/collection/NCLCollectionStore/\\_Public/43/054/43054872.pdf](https://inis.iaea.org/collection/NCLCollectionStore/_Public/43/054/43054872.pdf).
6. A. Jahn, M. Sommer, J. Henniger, OSL efficiency for BeO OSL dosimeters, Technische Universität Dresden, Institute for Nuclear and Particle Physics, Radiation Physics Group, D-01062 Dresden, Germany. Radiation Measurements (2014), <http://dx.doi.org/10.1016/j.radmeas.2014.03.024>.
7. E. Aşlar et al., Thermally and optically stimulated luminescence properties of BeO dosimeter with double TL peak in the main dosimetric region, Applied Radiation and Isotopes 170, 2021, 109635.
8. Quality Control Instrumentation, Alderson Radiation Therapy Phantom (ART) <https://www.supertechx-ray.com>
9. D. Brenner, W. Huda. Effective dose: a useful concept in diagnostic radiology Radiat. Prot. Dosim. 2008, 128 503–8.
10. SIEMENS, Guide pratique pour la réduction de dose, 11-2010. <https://www.yumpu.com/fr/document/read/12815669/guide-pratique-pour-la-reduction-de-dose-siemens-healthcare>.
11. A. Krleski, S. Petkovska, M. Ginovska. Characterization of Thermoluminescent Dosimeter with Thermal and Optically Stimulated Luminescence Reader Riso TL/Osl Da-20 at Low and Upper Dose Limit, International Medical Physics and Bioengineering Workshop, CORFU 2017.
12. Guide to the Risø TL/OSL Reader (2015). DTU Nutech, Denmark
13. M. Nyathi. Establishment of Diagnostic Reference Levels and Estimation of Effective Dose from Computed Tomography Head Scans at a Tertiary Hospital in South Africa. Iranian Journal of Medical Physics 2020; 17: 99-106. 10.22038/ijmp.2019.39685.1531.
14. E.U. Ekpo, T. Adejoh, J.D. Akwo, O.C. Emeka, A.A.Modu, M. Abba, K.A. Adesina, D.O. Omiyi and U.H.Chiegwu. Diagnostic Reference Levels for Common Computed Tomography (CT), Examinations: Results from the First Nigerian Nationwide Dose Survey, 13 March 2018, Journal of Radiological Protection, Volume 38, Number 2.
15. G.M. Wardlaw. Diagnostic Reference Levels (DRLs): Concepts, Canada, and Constraints, 2017, Health Canada Medical Imaging Division, Montebello. <https://www.canada.ca/en/health-canada/services/publications/health-risks-safety/canadian-computed-tomography-survey-national-diagnostic-reference-levels.html>.
16. K.K. Geoffrey, J.S. Wambani, I.K. Korir, M.A. Tries and P.K. Boen, National Diagnostic Reference Level: Initiative For Computed Tomography Examinations in Kenya, Radiation Protection Dosimetry (2016), Vol. 168, No. 2, pp. 242 – 252.
17. D.H.Salama, J. Vassileva, G. Mahdaly, M. Shawki, A.Salama.D. Gilley, et al.. Establishing national diagnostic reference levels (DRLs) for computed tomography in Egypt. PhysMed, 2017, 39:16-24.
18. G. Simantirakis, C.J. Hourdakakis, S. Economides, I. Kaisas, M. Kalathaki, C. Koukorava, et al. Diagnostic reference levels and patient doses in computed tomography examinations in Greece. Radiat Prot Dosimetry, 2015, 163(3):319-24.
19. R. Bindman, M. Moghadassi, N. Wilson, T.R. Nelson, J.M. Boone, C.H. Cagnon et al. Radiation Doses in Consecutive CT

Examinations from Five University of California Medical Centers. *Radiology*, 2015, 277(1):134-41.

20. A. Hayton, A. Wallace, P. Marks, K. Edmonds, D. Tingey, P. Johnston. Australian diagnostic reference levels for multi detector computed tomography, *Australas Phys Eng Sci Med*, 2013, 36:19–26.
21. Doses délivrées aux patients en scanographie et en radiologie

conventionnelle, résultats d'une enquête multicentrique en secteur public, direction de la radioprotection de l'homme, Service d'Etudes et d'Expertises en Radioprotection, Rapport DRPH/SER N°2010-12.

[https://www.irsn.fr/FR/expertise/rapports\\_expertise/Documents/radioprotection/IRSN-Rapport-dosimetrie-patient-2010-12.pdf](https://www.irsn.fr/FR/expertise/rapports_expertise/Documents/radioprotection/IRSN-Rapport-dosimetrie-patient-2010-12.pdf)

---



2021

# Simulation of dynamic $^{18}\text{F}$ FDG-PET images for lesion detectability investigation using kinetic modeling and 4D-XCAT phantom

Fethi Bezoubiri,<sup>a,\*</sup> Tahar Zidi,<sup>b</sup> Fayçal Kharfi<sup>c,d</sup>

<sup>a</sup>Medical Physics Department, Radiology Physics Division, Nuclear Research Center of Algiers, 16000, Algiers, Algeria.

<sup>b</sup>Atomic Energy Commission (COMENA), 16000, Algiers, Algeria.

<sup>c</sup>Laboratory of Dosing, Analysis and Characterization with High Resolution (DAC), Campus El-Bèz, 19000, Sétif, Algeria.

**ABSTRACT:** The simulation in nuclear medicine is an effective approach to test new mathematical methods of image processing and lesion detection. These methods are used to extract information inaccessible by conventional PET-image analysis. Dynamic  $^{18}\text{F}$ FDG-PET is a powerful tool for the examination of malignant tumors. The aim of this work was to simulate dynamic  $^{18}\text{F}$ FDG-PET images for a better detectability of lesion. In this work the three-compartment model with four kinetic parameters and blood volume component ( $k_1$ ,  $k_2$ ,  $k_3$ ,  $k_4$  and  $V_p$ ) was, firstly, used to simulate the time-activity curves (TAC's) of  $^{18}\text{F}$ FDG. The arterial input function of  $^{18}\text{F}$ FDG was, then, modeled using a parametric function. In total, the TAC's of thirteen tissues were simulated, namely: lung, stomach, spleen, pancreas, marrow, gray and white matter, skeletal muscle, liver, kidney and tumors. Secondly, a typical  $^{18}\text{F}$ FDG dynamic PET protocol has been adopted to generate 28 time frames [9 x 10 s, 3 x 30 s, 4 x 60 s, 4 x 120 s, 8 x 300 s]. To generate dynamic phantom, the activity values were calculated from the TAC's according to the scan duration of each frame. These activity values were assigned to each voxel of the realistic XCAT human torso phantom in order to produce 28 activity maps. Finally, the STIR platform was used to reconstruct and to generate the  $^{18}\text{F}$ FDG PET images from the XCAT phantom. **Results:** the arterial input function was calculated and used in the simulation of the TAC's of each tissue. Then, the TAC's were generated using the three-compartment model. The consistency of our results was assessed through the comparison between the calculated TAC's and those reported in literature that showed good agreement. Finally, a total number of 28 frames of XCAT phantom were generated. Realistic dynamic  $^{18}\text{F}$ FDG-PET images were simulated using kinetic modeling and XCAT phantom. The obtained findings can be used to study the impact of the reconstruction parameters on the detectability of lesions in the  $^{18}\text{F}$ FDG PET images.

**Keywords:** Simulated dynamic;  $^{18}\text{F}$ FDG-PET images; 4D-XCAT phantom; STIR;  $^{18}\text{F}$ FDG kinetic modeling.

## INTRODUCTION

Positron Emission Tomography with 2-deoxy-2-[ $^{18}\text{F}$ ] fluoro-D-glucose ( $^{18}\text{F}$ FDG-PET) play important role in detection and treatment of malignant tumours. The dynamic  $^{18}\text{F}$ FDG-PET acquisition is often used with a kinetic modelling to estimate the physiological parameters that characterise the functional state of

tissue. It is also used in lesion detection<sup>1</sup>, since the difference of tracer uptake of normal and malignant tissues taken over the time can provide additional feature to improve the lesion detectability. In this type of acquisition, the use of short time frame to capture the peak of activity concentration leads to a noisy  $^{18}\text{F}$ FDG-PET images. In these images, the lesion detection task becomes a tough work, and several researchers work on developing new

methods to improve the lesion detectability in the <sup>18</sup>F-DG-PET images. The most drawback of using the clinical images in image processing process is to obtain a sufficient set of clinical images with known truth about the presence or absence of lesions. To overcome this drawback, the simulation approach is highly needed. It is considered as a substantial way for the researchers to provide images for developing and testing new mathematical methods for image processing and lesion detection. The simulated images can be highly clinically realistic if a validate PET imaging system combined with a realistic model of human body and an actual <sup>18</sup>F-DG activity distribution is used<sup>2</sup>. This work aims to simulate dynamic <sup>18</sup>F-DG-PET images to study the impact of the reconstructed parameters on lesion detection. To do so, we have used the well-known 4D eXtended CARDiac-Torso (4D-XCAT) phantom and <sup>18</sup>F-DG kinetic modelling. The Time Activity Curves (TAC's) of different tissues of 4D-XCAT phantom are calculated using three-compartments model and simulated input function. For the reconstruction procedure, Software for Tomographic Image Reconstruction (STIR) software is employed.

## MATERIALS AND METHODS

### Numerical phantom

We have used the realistic 4D-XCAT human torso phantom to model the time-dependent activity and the 511-keV attenuation maps for the tissues listed in table 1<sup>3,4</sup>. To model the lesion, a lesion size of 9 mm diameter was simulated and inserted at the top of the liver in the main phantom 4D-XACT. The attenuation maps generated were used for the attenuation correction in the image reconstruction procedure. The activity maps were generated by calculating the TAC's of different tissues of 4D-XCAT phantom. The TAC's were calculated using an actual <sup>18</sup>F-DG kinetic micro-parameters, an effective blood plasma volume values cited in table 1<sup>5,6</sup> and a modeled input function. To produce a series of dynamics activity maps, a real acquisition protocol were adopted in this study. This protocol consists of 28 frames recorded during 55 min: 9\*10s, 3\*30s, 4\*60s, 4\*120s and 8\*300s<sup>7</sup>. The activities values calculated, according to each time frame, were assigned to the voxels of each region of the 4D-

XCAT phantom to produce 28 frames. The image matrix size of the activity maps and the attenuation map was 256 × 256 pixels, with a pixel size of 2.5 x 2.5 mm<sup>2</sup>.

### Modelization of the <sup>18</sup>F-DG Time Activity Curves

To generate the TAC's of <sup>18</sup>F-DG, we have used the standard three-compartment model<sup>8</sup>. A descriptive schema of this model is illustrated in fig. 1.

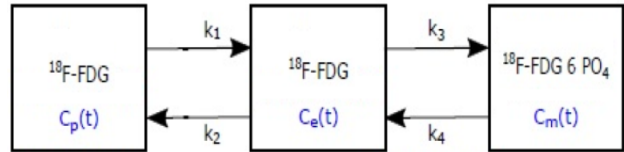


Fig. 1 A schema showing the three-compartment model of <sup>18</sup>F-DG uptake

In this model,  $C_p(t)$  is the input function,  $C_e(t)$  and  $C_m(t)$  are the concentrations of unmetabolized, metabolized and trapped <sup>18</sup>F-DG in tumor cells, respectively, expressed in kBq/mL.  $k_{1 \rightarrow 4}$  are parameters describing the exchanges between the compartments.

- $k_1$  ( $\text{min}^{-1}$ ) and  $k_2$  ( $\text{min}^{-1}$ ) represent the reversible exchanges of FGD between the blood and tissue compartments;
- $k_3$  ( $\text{min}^{-1}$ ) represents the phosphorylation of the FGD <sup>18</sup>F-DG-6-PO<sub>4</sub> ;
- $k_4$  ( $\text{min}^{-1}$ ) represents the effect of possible dephosphorylation of FGD-6-PO<sub>4</sub> to <sup>18</sup>F-DG.

The values of these parameters, as reported in the literature, are presented in the Table 1.

The <sup>18</sup>F-DG kinetics is described by the following differential equations:

$$\frac{dC_e(t)}{dt} = k_1 C_p(t) - (k_2 + k_3) C_e(t) + k_4 C_m(t) \quad (1)$$

$$\frac{dC_m(t)}{dt} = k_3 C_e(t) - k_4 C_m(t) \quad (2)$$

$$C_{FDG}(t) = C_e(t) + C_m(t) + V_p C_p(t) \quad (3)$$

$C_{FDG}(t)$  being the total concentration of the <sup>18</sup>F-DG in an Region

Of Interest (ROI), and  $V_p$  represents the effective blood plasma volume contained in the ROI.

The solution of this system of equation gives:

$$C_{FDG} = K_i \int C_p(t)dt + V_p C_p(t), \quad (4)$$

$$\text{with: } K_i = \frac{k_1 * k_3}{k_2 + k_3} \quad (5)$$

**Table 1. The <sup>18</sup>FDG kinetic micro-parameters and the effective blood plasma volume  $V_p$  of different organs used in this study.**

organs	$k_1$ (min <sup>-1</sup> )	$k_2$ (min <sup>-1</sup> )	$k_3$ (min <sup>-1</sup> )	$k_4$ (min <sup>-1</sup> )	$V_p$
kidney	0.2630	0.2990	0.0000	0.0000	0.4380
spleen	1.2070	1.9090	0.0080	0.0140	0.0000
liver	1.2560	1.3290	0.0020	0.0020	0.1650
marrow	0.4250	1.0550	0.0230	0.0130	0.0400
myocardium	0.1960	1.0220	0.1490	0.0100	0.5450
lung	0.1080	0.7350	0.0160	0.0130	0.0170
aorta	0.0000	0.0000	0.0000	0.0000	1.0000
soft tissue	0.0470	0.3250	0.0840	0.0000	0.0190
ventricle	0.0000	0.0000	0.0000	0.0000	1.0000
stomach	0.6140	1.8850	0.0710	0.0310	0.0630
tumour	0.1860	0.4380	0.3360	0.0000	0.0800

In order to generate the <sup>18</sup>FDG TAC's, we have modeled the input function  $C_p(t)$  using the parametric function proposed by feng<sup>9-12</sup>. The mathematical expression of this model is given as follows:

$$C_p(t) = (A_1 t - A_2 - A_3)e^{\lambda_1 t} + A_2 e^{\lambda_2 t} + A_3 e^{\lambda_3 t} \quad (6)$$

with:

- $\lambda_1$  (min<sup>-1</sup>),  $\lambda_2$  (min<sup>-1</sup>) and  $\lambda_3$  (min<sup>-1</sup>) are the eigenvalues of the model.
- $A_1$  (μCi/ml/min),  $A_2$  (μCi/ml) and  $A_3$  (μCi/ml) are the coefficients of the model.

The values of the  $\lambda_{1 \rightarrow 3}$  and  $A_{1 \rightarrow 3}$  are reported in Table 2.

**Table 2. Parameters of the Input function used in this study.**

$A_1$ (μCi/ml/min)	$A_2$ (μCi/ml)	$A_3$ (μCi/ml)	$\lambda_1$ (min <sup>-1</sup> )	$\lambda_2$ (min <sup>-1</sup> )	$\lambda_3$ (min <sup>-1</sup> )
851.1225	21.8798	20.8113	-4.1339	-0.1191	-0.0104

### Scanner geometry and image reconstruction

For the reconstruction procedure, STIR software version 4.0.0-alpha has been used<sup>13</sup>. Firstly, we have employed STIR ray tracing technique to perform the forward projection of the 4D-XCAT activity maps in order to generate a free-noise sinograms using parameters that define the geometry of the scanner General Electric (GE) Discovery 710. This scanner contains 25 rings with 576 detectors per ring. It has also 6 and 9 crystals per block in axial and transaxial directions, respectively. The inner ring diameter is 81.02 cm with 0.654 cm distance between the rings. The average depth of interaction and the default bin size are 0.94 and 0.21306 cm, respectively. The effective central bin size was set to 0.213 cm. Secondly; The free-noise sinograms generated were attenuation corrected by calculating the attenuation coefficient from the 4D-XCAT attenuation maps. Then, a noisy sinograms were obtained by corrupting the corrected sinograms with Poisson noise. Finally, these sinograms were reconstructed using Ordered Subsets-Maximum a posteriori Probability-One Step late (OSMAPOSL) algorithm with 35 iterations and 1 subset. The same reconstruction procedure was applied to all the 28 frames covering the liver region. The reconstructed image size was 256 x 256 pixels, with the voxel size of 2.5 x 2.5 mm<sup>2</sup>.

## RESULTS AND DISCUSSION

The Input function obtained using equation 6 and the parameters values reported in table 2, is given in fig. 2. The pic shown in fig. 2 is corresponding to the dose injection. Using this input function with the <sup>18</sup>FDG kinetic micro-parameters reported in table 1 and the kinetic modelling equations 1-5, TAC's of 11 tissues were generated and illustrated in fig. 3. From the TAC of the tumour, we can see clearly the trapping of the <sup>18</sup>FDG. This is due to the high value of  $k_3$  and  $k_4 = 0$ , as can be seen in table 1. We can see also that the TAC of the ventricles and the aorta are identical and similar to the Input function since all the kinetic micro-parameters of these organs equal zero and the effective blood plasma volume equal to one. The TAC's simulated were used to generate the <sup>18</sup>FDG dynamic activity maps.

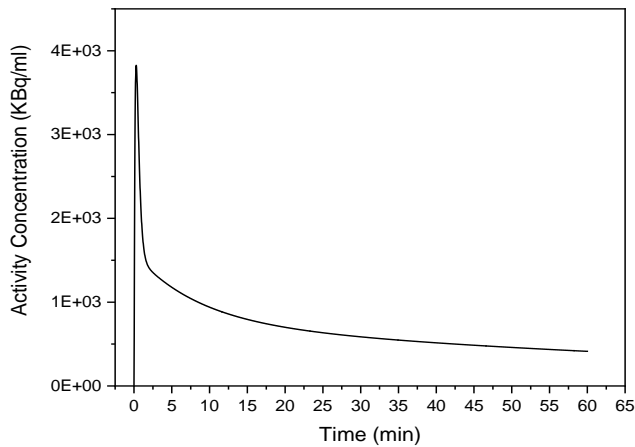


Fig. 2 <sup>18</sup>FDG Input function used in this study.

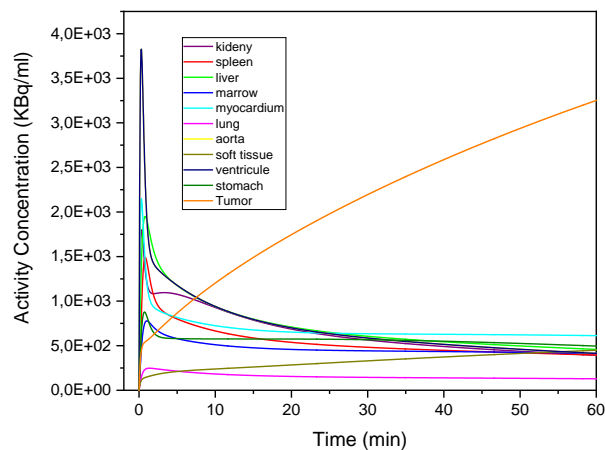


Fig. 3 TAC's of <sup>18</sup>FDG generated for different tissues of 4D-XCAT phantom.

Representative transverse, coronal and sagittal slices selected from early, intermediate and late time frames of dynamic <sup>18</sup>FDG activity map corresponding to frame 1, frame 17 and frame 28 are given in fig. 4. From the early frame, one can observe that the activity is high in the ventricles and the aorta among the other organs. For the lesion detection, as we know the detection is occurred when the activity of the lesion is higher or lower than the surrounding tissue. So, we can see the lesion inserted in the liver as a cold spot since the activity of this later was greater than the activity of the former. In the intermediate frame, we cannot easily differentiate the lesion from the liver because the activity in the tumor and in the liver is almost similar. In the late frame, we can see clearly the lesion with a high activity. This is due to the irreversible trapping in the lesion and the increased activity

concentration in the late frame.

All the 28 frames generated were forward projected and reconstructed following the procedure described in paragraph II.c. An example of projection data of frame 28 is shown in fig. 5. The reconstructed images from an early, intermediate and late frame time correspond to those illustrated in the fig. 4 are displayed in figure 6. The images reconstructed are qualitatively identical to the simulated ones, demonstrating the reliability of the reconstruction procedure followed. However, the lesion that we have hardly observed in the frame 17 since the lesion and liver activity values were close, can be not seen in the corresponding reconstructed image. This is perhaps due to the technical limitations of the scanner used in this study.

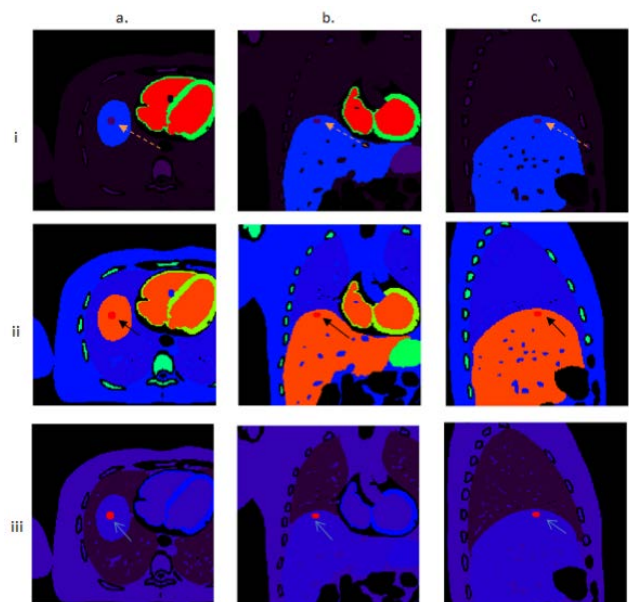


Fig. 4 Transverse (a), coronal (b) and sagittal (c) simulated images of <sup>18</sup>FDG activity maps taken at 3 different time points corresponding to : i = frame 1, ii = frame 17 and iii = frame 28

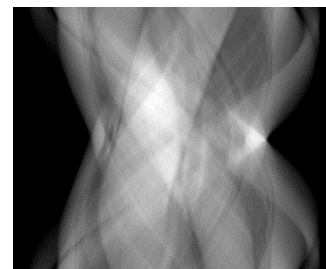
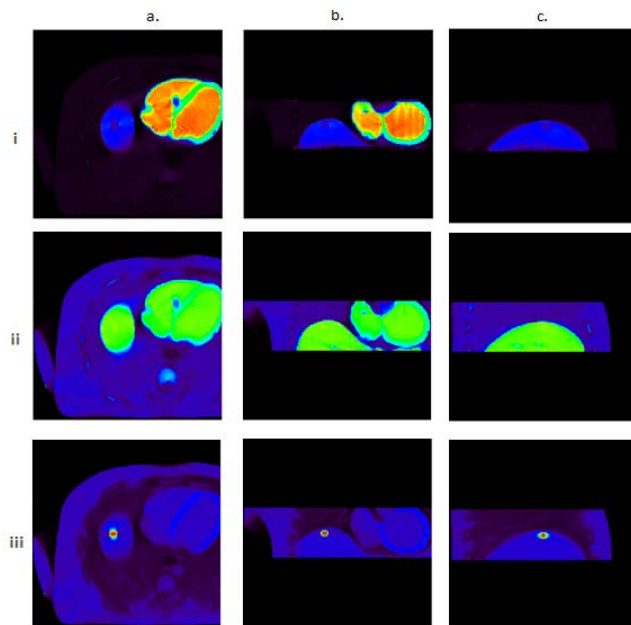


Fig. 5 Sinogram after forward projecting the activity maps of frame





**Fig. 6** Transverse (a), coronal (b) and sagittal (c) reconstructed simulated TEP images taken at 3 different time points corresponding to i = frame 1, ii = frame 17 and iii = frame 28

## CONCLUSIONS

In this work, the 3-compartment model was used to generate the  $^{18}\text{F}$ FDG temporal activity concentration curves. These curves were calculated using the parametric model of the arterial input function and the physiological parameters of the organs reported in the literature. A real data acquisition protocol was adopted to create 28 frames. The activity concentrations of  $^{18}\text{F}$ FDG in each frame were calculated from previously simulated time activity curves. The calculated concentrations for each organ were injected into the voxels of the 4D-XCAT Digital Phantom. The created phantom was reconstructed to generate dynamic PET images using the STIR software.

In perspective, the obtained findings can be used to study the impact of the reconstruction parameters on the detectability of lesions in the  $^{18}\text{F}$ FDG PET images.

## AUTHOR INFORMATION

### Corresponding Author

\*Mr. Fethi Bezoubiri

Email address: [f.bezoubiri@crna.dz](mailto:f.bezoubiri@crna.dz)

## IV. REFERENCES

1. Li, Z., Li, Q., Yu, X., Conti, P. S., & Leahy, R. M. (2008). Lesion detection in dynamic FDG-PET using matched subspace detection. *IEEE transactions on medical imaging*, 28(2), 230-240.
2. Lee, C. (2014). *Monte carlo calculations in nuclear medicine second edition: Applications in diagnostic imaging*.
3. Segars, W. P., Sturgeon, G., Mendonca, S., Grimes, J., & Tsui, B. M. (2010). 4D XCAT phantom for multimodality imaging research. *Medical physics*, 37(9), 4902-4915.
4. Segars, W. P., & Tsui, B. M. (2009). MCAT to XCAT: The evolution of 4-D computerized phantoms for imaging research. *Proceedings of the IEEE*, 97(12), 1954-1968.
5. Qiao, H., & Bai, J. (2011, May). Dynamic simulation of FDG-PET image based on VHP datasets. In *The 2011 IEEE/ICME International Conference on Complex Medical Engineering* (pp. 154-158). IEEE.
6. Dimitrakopoulou-Strauss, A., Georgoulas, V., Eisenhut, M., Herth, F., Koukouraki, S., Mäcke, H. R., ... & Strauss, L. G. (2006). Quantitative assessment of SSTR2 expression in patients with non-small cell lung cancer using  $^{68}\text{Ga}$ -DOTATOC PET and comparison with  $^{18}\text{F}$ -FDG PET. *European journal of nuclear medicine and molecular imaging*, 33(7), 823-830.
7. Wienhard K. (2002) Measurement of glucose consumption using  $^{18}\text{F}$  fluorodeoxyglucose. *Methods*, 27(3), 218-225.
8. Sokoloff, L., Reivich, M., Kennedy, C., Rosiers, M. D., Patlak, C. S., Pettigrew, K. E. A., ... & Shinohara, M. (1977). The  $^{14}\text{C}$  deoxyglucose method for the measurement of local cerebral glucose utilization: theory, procedure, and normal values in the conscious and anesthetized albino rat 1. *Journal of neurochemistry*, 28(5), 897-916.
9. Feng, D., Huang, S. C., & Wang, X. (1993). Models for computer simulation studies of input functions for tracer kinetic modeling with positron emission tomography. *International journal of biomedical computing*, 32(2), 95-110.
10. Feng, D., & Wang, X. (1993). A computer simulation study on the effects of input function measurement noise in tracer kinetic modeling with positron emission tomography (PET). *Computers in biology and medicine*, 23(1), 57-68.
11. Feng, D., Li, X., & Huang, S. C. (1996). A new double modeling approach for dynamic cardiac PET studies using noise and spillover contaminated LV measurements. *IEEE transactions on biomedical engineering*, 43(3), 319-327.
12. Feng, D., & Wang, X. (1995). A method for biomedical system modelling and physiological parameter estimation using indirectly measured input functions. *International journal of systems science*, 26(4), 723-739.
13. Thielemans, K., Tsoumpas, C., Mustafovic, S., Beisel, T., Aguiar, P., Dikaios, N., & Jacobson, M. W. (2012). STIR: software for tomographic image reconstruction release 2. *Physics in Medicine & Biology*, 57(4), 867.



2021

# Commissioning of a brachytherapy treatment Planning system and its validation with Gafchromic film EBT3 using 2D gamma index distribution

Mohamed Lahlabou,<sup>a</sup> Rachid Khelifi,<sup>b</sup> Cheikh Tayeb<sup>a</sup>

<sup>a</sup>Radiotherapy department, Central Hospital of the Army, Kouba / Algiers, Algeria

<sup>b</sup>Laboratory of PTHIRM, University of Saad Dahleb, Blida, Algeria

**ABSTRACT:** In brachytherapy, the accuracy of the commissioning is very important for the prescription of treatment for the patients. The aim of this study is to perform a commissioning for a treatment planning system (TPS) and check its accuracy in order to ensure a good treatment of the patients. In this study, sources of Cesium-137 CIS BIO international CSM11 type were used for the commissioning of Elekta XiO brachytherapy TPS. The necessary irradiations were performed by the BEBIG Eckert & Ziegler Curietron machine. EBT3 Gafchromics films were used for the dose measurement after their calibration around the Elekta Synergy linear accelerator. Necessary data for the TPS were first collected and, then, used to extract the dose distribution for each source. The dose distributions were also measured by Gafchromic films. The measured and calculated dose distributions were compared. For each source, the majority of dose distribution points are conform to the passing criteria of gamma index. The studied TPS was commissioned for clinical use in brachytherapy treatment planning with the considered sources.

**Keywords:** Brachytherapy; TG43; Gamma index; Commissioning.

## INTRODUCTION

A commissioning of a treatment planning system (TPS) passes by three stages. First step is the acquisition of the data of the machine (or source for brachytherapy). It consists in collecting the data of the radioactive sources such as geometry, activity, reference air kerma rate (RAKR)...etc. Then, modelling the source by accomplishing a model for the source so that the algorithm can generate a dose distribution by using the data already introduced. Finally, check of the accuracy of the calculation by checking the dose distribution by comparing calculated dose distribution with TPS and that measured with a

detector. The aim of this study is to perform a commissioning for the sources of cesium137 and checking the accuracy of the algorithm to ensure a good planning for the patients.

## EXPERIMENTAL

We have use Elekta Xio 4.8 brachytherapy TPS to achieve the commissioning of Cesium 137 type CSM11 radioactive sources (CIS Bio International, Saclay, France). XiO supports two methods TG43 formalism and Sievert Integral. We have chosen the TG43 formalism due to its accuracy.

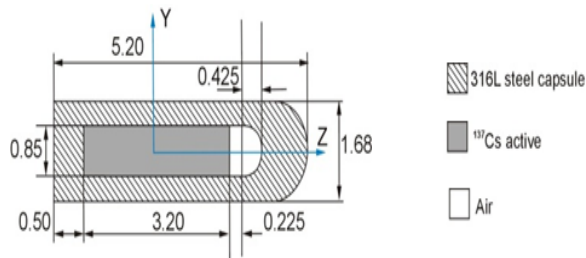


Fig.1 E&Z BEBIG Low Dose Rate cesium 137 type CSM11

$$\dot{D}(r, \theta) = S_K \cdot \Lambda \cdot \frac{G_L(r, \theta)}{G_L(r_0, \theta_0)} \cdot g_L(r) \cdot F(r, \theta) \quad (1)$$

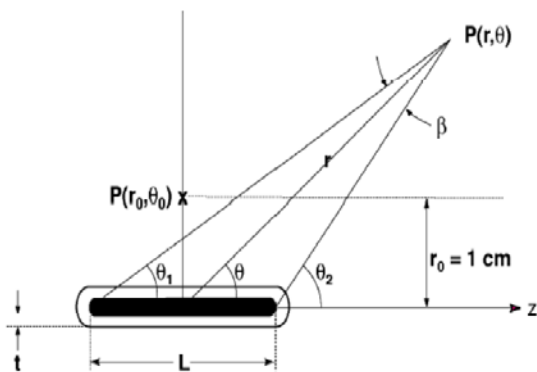


Fig.2 Brachytherapy dose calculation geometry

We have used as a machine of treatment the Curietron (BEBIG Eckert & Ziegler Company). In this work, five (5) “Curiestock” linear sources of Cesium-137 with different lengths have been considered. Each linear source is composed of two or several sub sources of Cesium 137 of type CSM11 according to its length.

Necessary data for the source of Cesium-137 CSM11 type was taken from the report of the AAPM and ESTRO<sup>1</sup>.

To validate the model of the radioactive source that was created, we must perform some checking task by comparing distribution of dose calculated by TPS to measured one by the detector. We have chosen Gafchromic (Ashland Specialty Ingredients, Bridgewater, NJ, USA) EBT3 radiochromic films as a detector because of its high space resolution to measure the dose distribution of the linear sources considered.

To obtain the distribution of dose calculated by the TPS for the different radioactive sources, we have used a phantom composed of six plates of PMMA (PolyMethylMethAcrylate) with 1 cm in thickness to avoid any backscatter. We have put an applicator of

“Dellouche” type on the top of the sixth plate. Figure 3 shows the disposition of the applicator on the phantom.



Fig.3 Applicator and Gafchromic film disposition on phantom

CT-images acquisition for the applicator on the phantom with a Big Bore Brilliance CT were successfully accomplished by PHILIPS scanner. With these CT images, we planned with TPS for the five different linear sources considered (five different lengths) a treatment of ten hours. Finally, the calculated dose distribution for each radioactive source was extracted.

To validate the model of the radioactive source which was created, we make a check by comparing calculated dose distribution by TPS and that measured by films.

For the comparison of the dose distribution of the different linear sources, we have used the PTW-VERISOFT 6.0 software package. The comparison is based on the gamma index criteria by using the dose difference (DD) in % and the distance-to-agreement (DTA) parameters in mm.

## RESULTS AND DISCUSSION

Figure 4 shows both measured and calculated dose distribution for a 40 mm length linear radioactive source normalized at 5 Gy. The 2D gamma index distribution for this linear radioactive source for 2% of dose difference to the maximum dose of calculated volume and 2 mm of distance-to-agreement is illustrated in Figure 5. The comparison results between measured and calculated dose distribution with different criterion of gamma index for the five different linear radioactive sources are presented in Table 1. The calculated dose distribution by the TPS is validated with more than 95% of checked points for a difference to the maximum dose of the calculated volume of 3% and a distance-to-agreement of 5mm.

**Table 1. Comparison results between measured and calculated dose distribution with different criterion of gamma index**

Source ID	Active							
	length [mm]	2%,2mm	2%,3mm	3%,2mm	3%,3mm	3%,5mm	5%,3mm	5%,5mm
51814	17	59.2	86.5	65.4	89.7	98.7	92.3	98.7
51813	40	100	100	100	100	100	100	100
51811	50	79.6	94.2	82.2	94.4	100	95.2	100
51818	60	49.9	63.6	53.2	66.4	97.5	74.2	97.5
51820	70	73.7	87.5	75.2	88.2	99	90.3	99

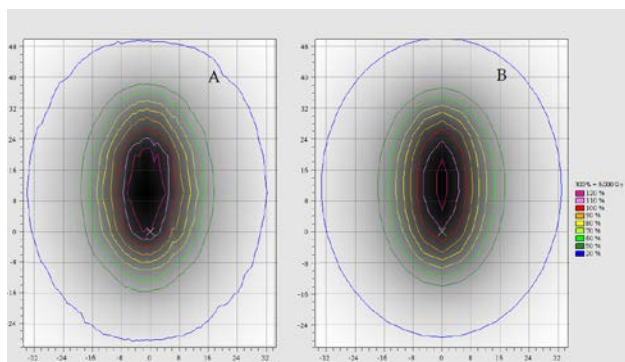


**Fig.4 Measured dose distribution (A) and calculated dose (B) distribution for the radioactive source 51813/40mm normalized at 5 Gy**

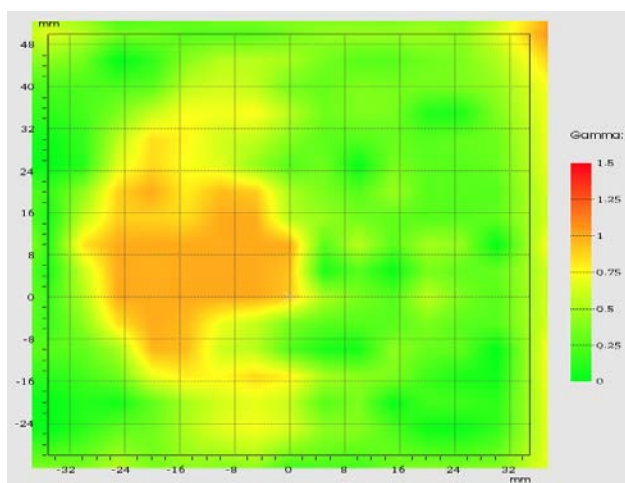


**Fig. 5 2D gamma index distribution for the radioactive source 51813/40mm for 2% of dose difference with maximum dose of calculated volume and 2mm distance to agreement**

## CONCLUSIONS

On the basis of the of gamma index 2D criterion, results of the actual study show clearly that the calculated dose distributions by the considered TPS is validated with more than 95% of checked points for a DD of 3% and a DTA of 5 mm taken as passing criteria. Therefore, the Elekta XiO planning system can be safely used to plan brachytherapy treatment with the models of the linear radioactive sources considered.

## AUTHOR INFORMATION

### Corresponding Author

\*Mohammed Lahlabou

Email address: [mohammed.lahlabou@hotmail.fr](mailto:mohammed.lahlabou@hotmail.fr)

## REFERENCES

1. Nashrulhaq Tagiling, Raizulnasuha Ab Rashid, Siti Nur Amirah Azhan, Norhayati Dollah, Moshi Geso, Wan Nordiana Rahman. Effect of scanning parameters on dose-response of radiochromic films irradiated with photon and electron beams. *Heliyon* 4 (2018) e00864. doi: 10.1016/j.heliyon.2018. e00864.
2. Dose calculation for photon-emitting brachytherapy sources with average energy higher than 50 keV: Full Report of the AAPM and ESTRO. *Med. Phys.* 39 (2012) 2904-2929
3. M.J.Rivard, B.M.Coursey, L.A.DeWerd, W.F.Hanson, M.Saiful Huq, G. S. Ibbott, M. G. Mitch, R. Nath, and J. F. Williamson, "Update of AAPM Task Group No. 43 Report: A revised AAPM protocol for brachytherapy dose calculations," *Med. Phys.* 31, 663–674 2004.



2021

# Monte-Carlo Code for Modeling and simulation of tomographic image

Fayçal Kharfi,<sup>a,c,\*</sup> Naziha Benaskeur,<sup>a,b,</sup> Serine Sara Bouacid<sup>c</sup>

<sup>a</sup>Department of Physics, Faculty of Science, University of Setif1, Setif, Algeria

<sup>b</sup>Nuclear Research Centre of Birine, Djelfa, Algeria

<sup>c</sup>Laboratory Dosing Analysis and Characterization with high resolution, Ferhat Abbas-Setif1 University, Setif, Algeria

**ABSTRACT:** Neutron tomography is a developed technique for non-destruction examination. It is widely used in industrial fields for the determination of internal structures of objects. This examination is, generally, based on the exploitation of neutron transmission data. In our work, a three-dimensional model was reconstructed using the neutron transmission data obtained by Monte Carlo simulation on a virtual object. 2D images are reconstructed using the Filtered Back Projection (FBP) method using MatLab software. Projection data simulated from different angles were considered and Shepp-Logan filter was used for the tomographic reconstruction. The reconstructed image obtained has a configuration similar to that modelled geometrically. When optimal number of projections is used, the gray levels areas become uniform allowing high quality reconstructed image with less artifacts.

**Keywords:** Neutron transmission, Monte-Carlo code, Simulation, Modeling, Projection, Reconstruction.

## INTRODUCTION

Neutron tomography has acquired great importance in nuclear installations for scientific and industrial applications<sup>1-3</sup>. It is based on the attenuation physical principle of a neutron beam passing through a material.

Neutron attenuation can be measured or simulated using appropriate codes. In the neutron imaging this parameter can be used for the neutron characterization of shielding materials entering sensitive structures such as nuclear reactors or neutron sources. Also, the neutron attenuation can be used for the projection data determination in a large number of pixels of a detector plane as in the transmission neutron tomography<sup>4-5</sup>.

Monte Carlo simulation of the radiation transport within a system, using appropriate computer codes, provides a better understanding and interpretation of the neutron transmission

process<sup>3</sup>. These calculation codes can give particle counts exactly analogous to experimental measurements<sup>4-6</sup>.

It can collect the particle transmitted through studied materials on a rectangular plane image grid, which was used in our simulation work. This option makes synthetic radiography applications possible with Monte-Carlo simulation code<sup>7-8</sup>.

In this work, we try to generate tomographic projections for a high speed bearing 6202z made of stainless steel materials by using a Monte-Carlo simulation code. This bearing is containing a spherical foreign body as a result of corrosion made of ferric oxide. The results will be used for the reconstruction of tomographic image representing the internal structure.

Using the appropriate codes, the neutron attenuation (parameter related to neutron transport in material) can be measured and

simulated. This simulation provides a better understanding and interpretation of the neutron transmission process.

## SIMULATION

### Studied phantom description

In this work, we have proposed to study a single row deep groove ball bearing 6202z (15x35x11) NSK (Fig.1). It is having an axis of symmetry. It is composed principally of two ring incorporated one in the other. Distributed between the two rings, ten balls made of iron of diameter 0.6 cm. The inner ring and the second one are composed of iron and having diameters of 1.5 cm and 3.264 cm, and thickness of 0.15 cm and 0.118 cm, respectively.

In this phantom, we assume the formation of a foreign body as a result of the corrosion phenomena. This body is composed, for example, of ferric oxide with a spherical shape of diameter 0.4 cm staked on the internal side of the outer ring.



Fig. 1 Single row deep groove ball bearing

### Geometric modeling by Monte-Carlo code

The geometric modeling and the complete description of the object are represented in the input file: The shape, size and materials of each part are well defined. The studied-materials compositions; Iron (Fe) and Ferric Oxide (Fe<sub>2</sub>O<sub>3</sub>), are defined in 'Material card' of the Monte-Carlo code where their mass densities are 7.86 and 5.2 g/cm<sup>3</sup>, respectively. In order to model

the proposed configuration, cylinder and sphere geometries were used.

In Fig. 2, we have represented 3D visualization and the three slices (XY, XZ and YZ) of the configuration studied by Monte-Carlo simulation code.

### Neutron transmission data simulation

The emerging beam intensity (I) is normalized with respect to the beam intensity measured without sample (I<sub>0</sub>) for obtaining the neutron transmission data by simulation using the following equation:

$$Tr = \frac{I}{I_0} \quad (1)$$

The results obtained by Monte-Carlo code are used to create a 50x100 matrix in the Excel software.

The neutron transmission data was simulated by running the Monte-Carlo code for a number of neutron histories. Using this code, the distribution of relative uncertainty on neutron flux in a Sample Radiograph was illustrated in the output file. The results obtained are acceptable only if the relative uncertainty is less than 5%. For that, several tests have been executed for the maximum number of neutron histories selection. The obtained values can be used for the projection data determination in a large number of pixels of a detector plane.

### Projection data generation

The projections are radiographic images taken at several projection angles varying from 0 to 180° with a fixed step according to the projection number<sup>9</sup>. They are presented as 2D gray level images (digitized in several pixels lines) with a variation in blackening proportional to the neutron intensities distribution in the neutron beam transmitted from the object after interaction. The projection data is calculated using the Beer-Lambert equation<sup>10</sup>:

$$P = -\ln\left(\frac{I}{I_0}\right) = \Sigma_{tot}d = \Sigma_{Fe} d_{Fe} + \Sigma_{Fe_2O_3}d \quad (2)$$

where  $\Sigma_{tot}$  and  $d$  are the macroscopic cross-section and thickness of the studied material, respectively. The macroscopic cross-section values of Iron and Ferric Oxide were presented in table 1 where the deference between the two attenuations is clearly.

Table 1. Studied Samples

N°	Component	Materials	Macroscopic cross section (cm <sup>-1</sup> )			Density (at/cm <sup>3</sup> )
			Absorption	Scattering	Total	
1	Single row deep groove ball bearing	Iron (Fe)	0.216	0.925	1.141	7.86
2	Defect (foreign body)	Ferric Oxide (Fe <sub>2</sub> O <sub>3</sub> )	0.100	0.649	0.749	5.2

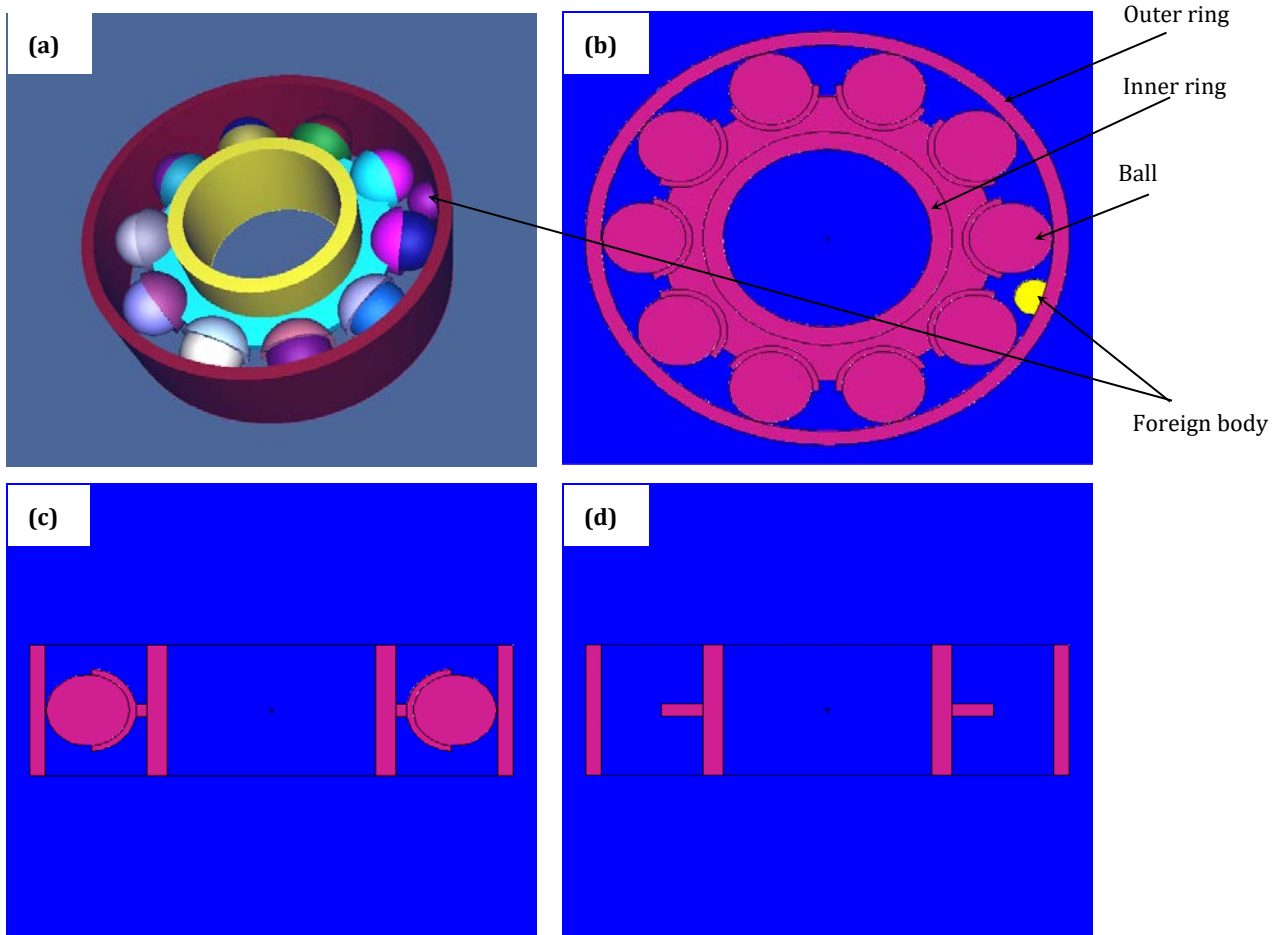


Fig. 2 Monte-Carlo configuration geometries of studied phantom (a) 3D visualization, (b) slice XY, (c) XZ and (d) YZ.

## RESULTS AND DISCUSSION

### Neutron transmission data simulation

In the Fig. 3 we show the relative uncertainty variation as a function of pixel fraction. It can be seen that the statistical uncertainties on the neutron fluxes decrease with the increase in the number of neutrons histories up to  $5E4$  histories (Table 2). Beyond this value we notice the divergence of relative uncertainty. After that we conclude as the  $5E4$  histories is the adequate value at which we have collected several projections.

On the other hand, the transmitted neutron profile through the phantom with oxide obtained at  $0^\circ$  for different lines is presented in Fig. 4. The comparison between the transmitted neutron profiles ( $I/I_0$ ) through the phantom with and without oxide for  $0^\circ$  angle at center line was illustrated in Fig. 5 where a small difference in the transmission is shown.

### Projection data generation

Using the neutron transmission data obtained by Monte-Carlo

simulation code the projection data was calculated by eq. 2 and represented on radiographic images. The projection data should be collected on many angles by rotation of the studied sample.

The Fig. 6 shows a projection data in terms of gray level for several projection angles. We note that, the projection data present an identical gray level each  $36^\circ$  angle where the material attenuation effect of the foreign body is not visible clearly. It is may be very weak, but it should appear clearly on the reconstructed images.

Using a reconstruction method, the combined projection data result can be transformed into a series of cross-sectional images of the sample<sup>11</sup>.

### Tomographic image reconstruction

The collected projection data simulated from different angles are processed together to obtain a sample tomographic reconstruction using the Filtered Back Projection (FBP) method under a MatLab program and a Shepp-Logan filter<sup>12</sup>. For this, sinograms indicating the detected cross section lines under

different projection angles  $\theta$  were considered<sup>13</sup>. This sinograms grouping the projection data simulated by Monte-Carlo code for the studied phantom have presented in Fig. 7. In this figure there are several blackening regions. The appearance of these gray level regions reflects well the existence of embedded objects made of materials with different attenuation coefficients. The lightest region corresponds to the more attenuating neutron material. The black bands correspond to the direct beam (without object).

Using a reconstruction method, the combined projection data can be transformed into a series of cross-sectional images of the sample Fig. 8. When we use more projections, the gray levels have uniform distribution, with a decrease in artifacts and the

result becomes acceptable. The reconstruction results obtained by simulation are illustrated for several slices using 90 projections where the foreign body position is detected and localized clearly Fig. 9.

The images reconstructed along the height (all sections) of the studied object are stacked using the "VGStudio"<sup>14</sup> software for the 3D image visualization of the object internal structure (Fig. 10). We clearly observe: the two rings incorporated one in the other, the ten balls and a foreign body composing the studied phantom from which the distinction becomes easy.

**Table 2. Relative uncertainty variation as a function of number of neutron histories**

Number of neutron histories	Statistical uncertainties (%)	
	< 5%	< 10%
1E3	66.13	95.71
5E3	97.68	100.00
1E4	98.06	100.00
<b>5E4</b>	<b>98.16</b>	<b>100.00</b>
1E5	84.00	98.39
5E5	85.03	98.52
1E6	81.29	89.42

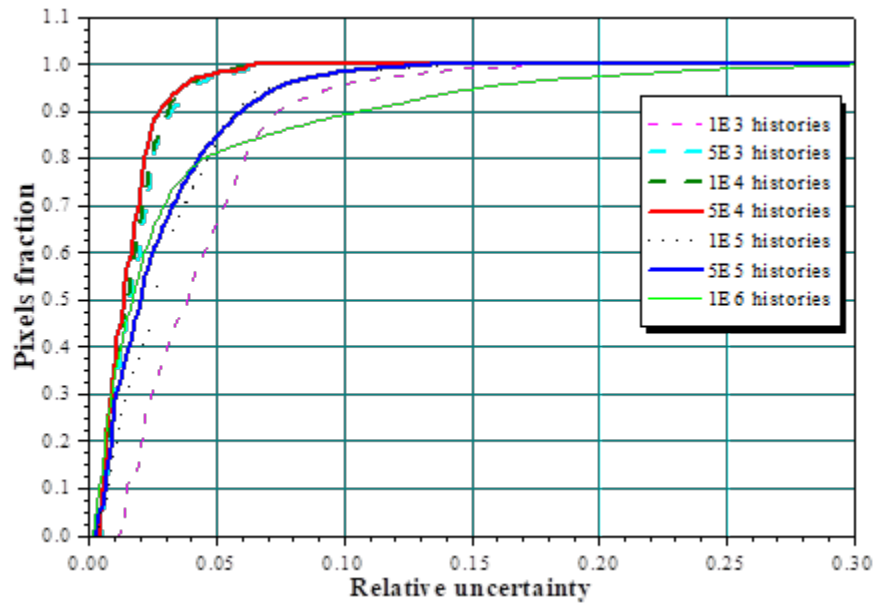


**Fig 3 Relative uncertainty variation as a function of pixel fraction.**



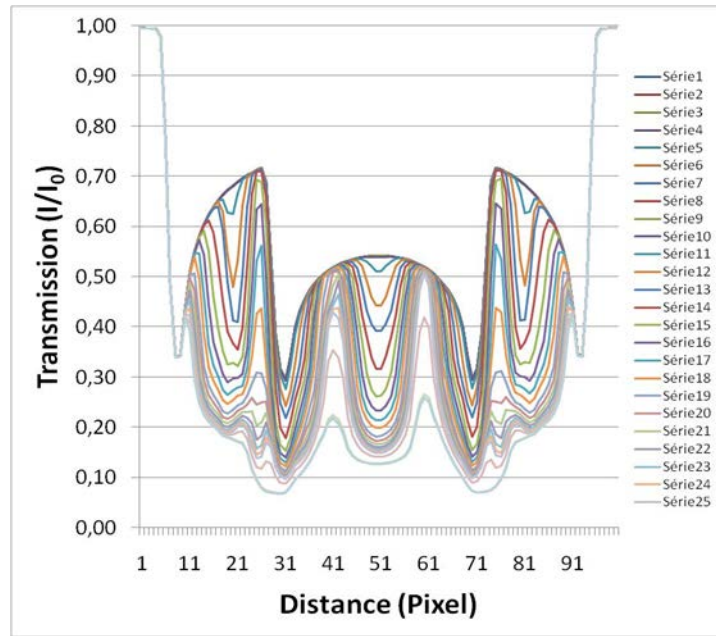


Fig 4 Transmitted neutron profile through the phantom with oxide obtained at 0° for different lines.

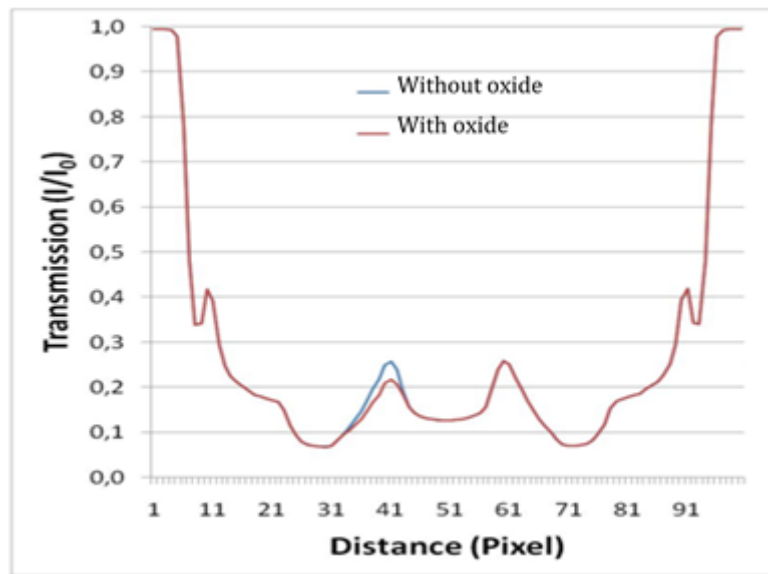


Fig 5 Comparison of transmitted neutron profile ( $I/I_0$ ) through the phantom with and without oxide at 0° (centre line).

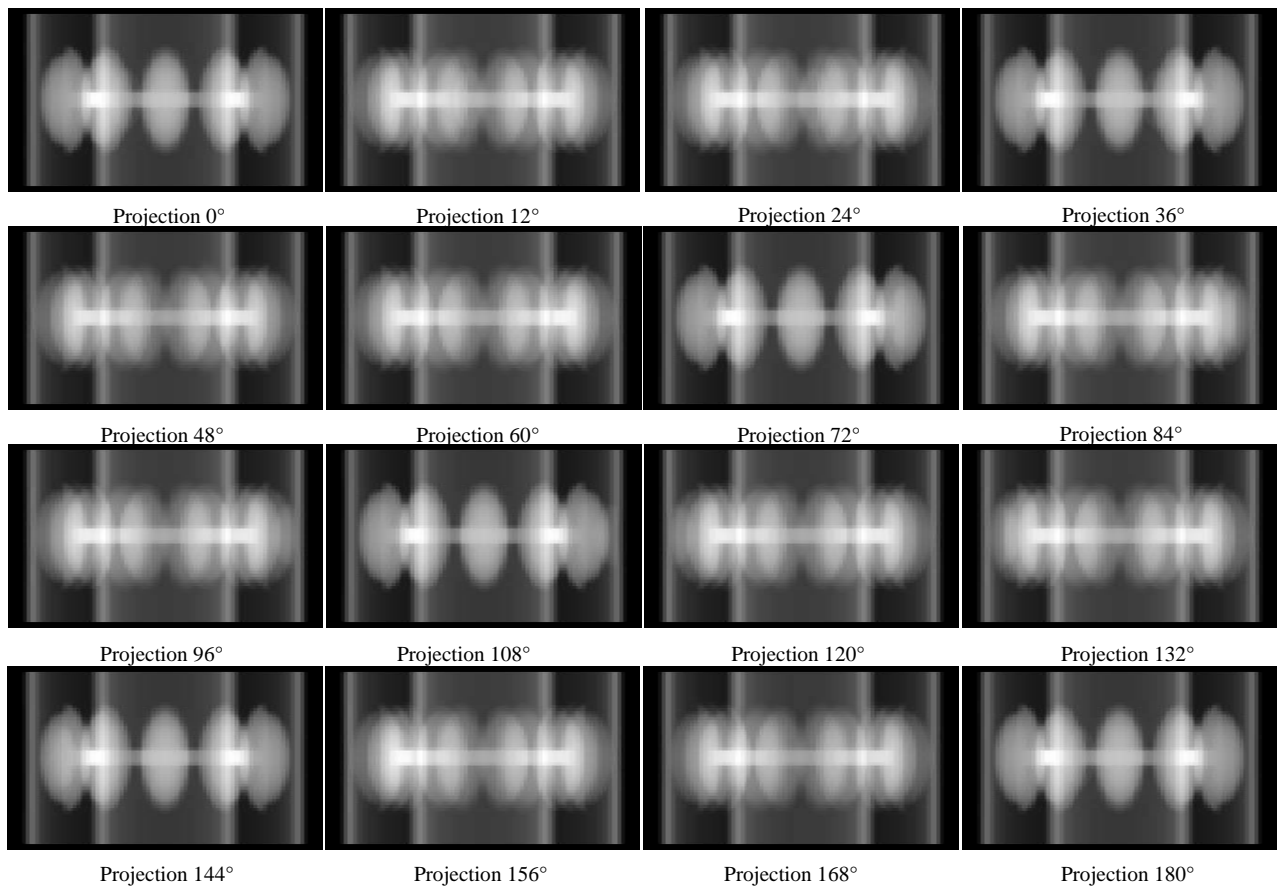


Fig. 6 Projection data of the studied phantom at different angles  $\theta$ .

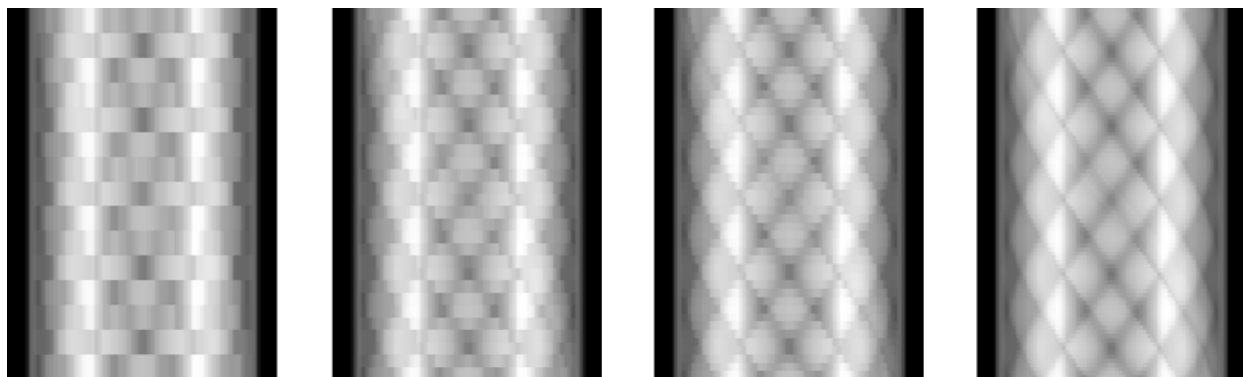


Fig. 7 Sinogram grouping the projection data simulated by Monte-Carlo code.

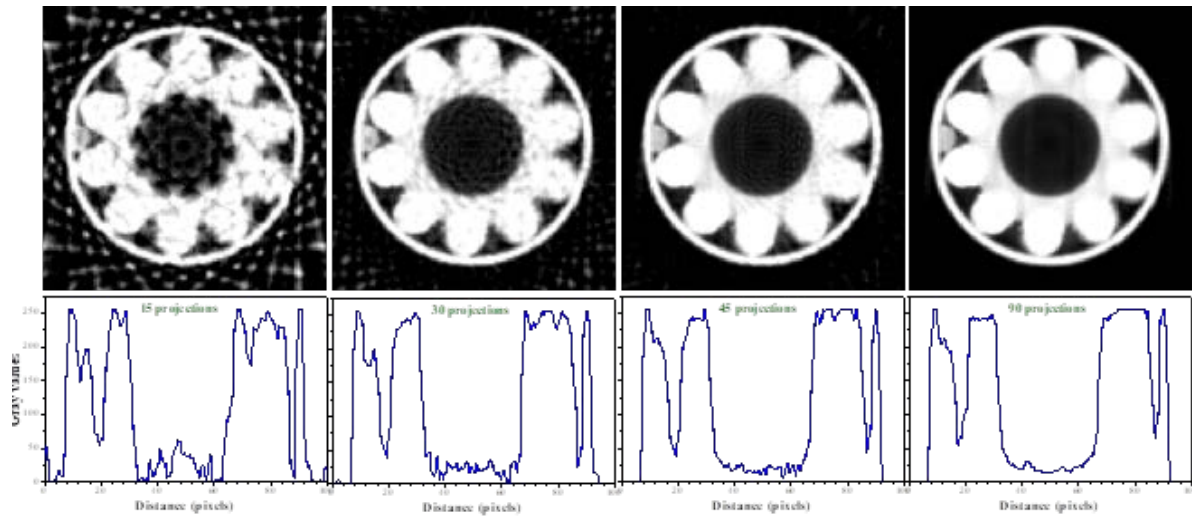


Fig. 8 2D reconstructed image for different number of projection.

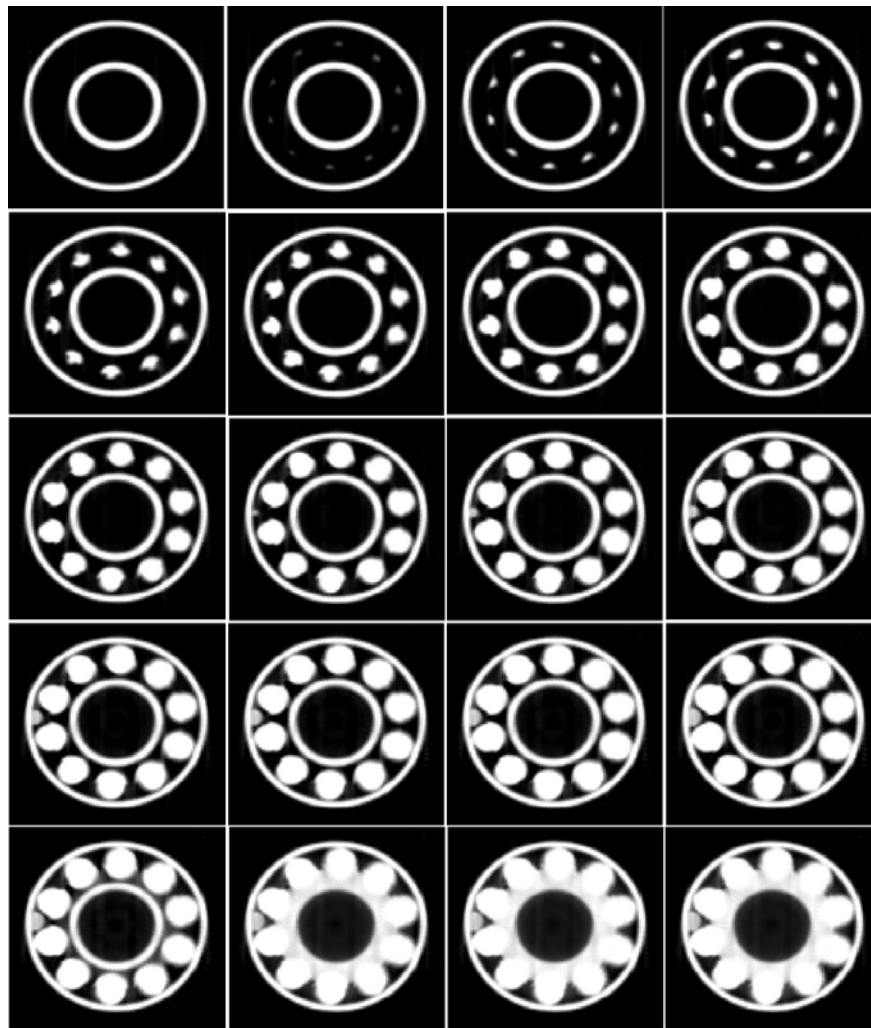


Fig. 9 2D reconstructed image at different line for 90 projections.

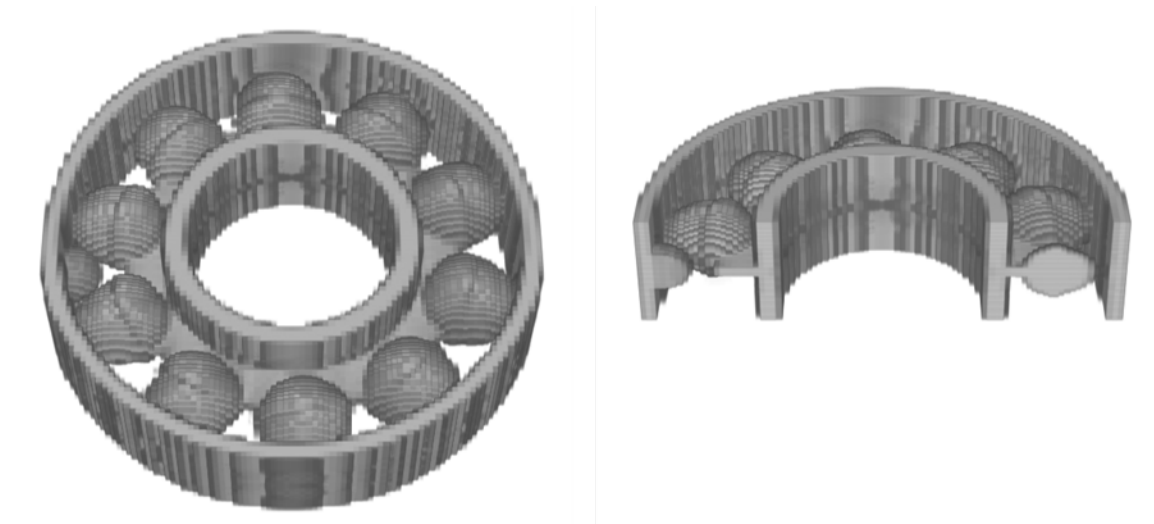


Fig. 10 Stacking results of all reconstructed sections of the studied phantom.

## CONCLUSIONS

In this study, a high speed bearing 6202z containing a spherical foreign body made of ferric oxide was analyzed by Monte-Carlo simulation code. The Monte-Carlo code can successfully simulate projection data for transmission neutron tomography. The simulation code allowed the determination of the internal structure and composition of the object based on the transmission data collected. This allows the detection and localization of materials incorporated into each other due to neutron attenuation coefficients.

The reconstruction tomography processes gives a better quality image that reflects correctly the internal structure; the foreign body was detected.

## AUTHOR INFORMATION

### Corresponding Author

\*Fayçal Kharfi.

Email address: [kharfifaycal@univ-setif.dz](mailto:kharfifaycal@univ-setif.dz).

## REFERENCES

1. M. N. Dawson, Applications of neutron radiography and tomography. *Ph. D. Thesis, University of Leeds*, 2008.
2. W. J. Richards, M. R. Gibbons, K. C. Shields, Neutron tomography developments and applications. *Appl. Radiat. Isotopes*. 2004, 61, 551-559.
3. P. Vontobel, E. H. Lehmann, R. Hassanein, G. Frei, Neutron tomography: method and applications. *Physica B*. 2006, 385, 475-480.
4. N. Hachouf, F. Kharfi, A. Boucenna, Characterization and MCNP simulation of neutron energy spectrum shift after transmission through strong absorbing materials and its impact on tomography reconstructed image. *Appl. Radiat. Isotopes*. 2012, 70, 2355-2361.
5. N. Hachouf, F. Kharfi, M. Hachouf, A. Boucenna, New analytical approach for neutron beam hardening correction. *Appl. Radiat. Isotopes*. 2016, 107, 353-358.
6. M. Looman, P. Peerani, H. Tagziria, Monte Carlo simulation of neutron counters for safeguards applications. *Nucl. Instrum. Methods*, 2009, A598, 542-550.
7. J. F. Briesmeister, MCNP a General Monte Carlo N-Particle Transport code. 2003, Vols 1-4, Version 5.
8. SCALE: A Comprehensive Modeling and Simulation Suite for Nuclear Safety Analysis and Design, ORNL/TM-2005/39. Version 6.1, Jun. Available from Radiation Safety Information Computational Center at Oak Ridge National Laboratory as CCC-785. 2011.
9. B. Schillinger, Neutron Tomography. *Paul Scherrer Institute, Summer School on Neutron Scattering*, 2000.
10. E. H. Lehmann, P. Vontobel, R. Hassanein, Neutron tomography as tool for applied research and technical inspection. *Solid State Phys.* 2005, 45, 389-405.
11. A. C. Kak, M. Slaney, Principles of Computerized Tomographic Imaging. *IEEE Press. New York*, 1988.
12. L.A. Shepp, B.F. Logan, The Fourier reconstruction of a head section. *IEEE Trans. Nucl. Sci.* 1974, NS-21 21-43.
13. J. Benech, Spécificité de la mise en œuvre de la tomographie dans le domaine de l'ARC électrique – validité en imagerie médicale. *Thèse de Doctorat, Université de Toulouse*, 2008.
14. VGStudio 1.2.1, User's Manual. Volume graphics GmbH, Heidelberg, Germany, 2005.



2021

## Neutron Imaging Denoising with a Deep Learning Method

Mohamed Laid Yahiaoui,<sup>a,b,\*</sup> Faycal Kharfi,<sup>b,c</sup> Layachi Boukerdja<sup>a,b</sup>

<sup>a</sup>Nuclear Research Centre of Birine, 17001, Algeria

<sup>b</sup>Laboratory of Dosing, Analysis, and Characterization in high resolution, University of Ferhat Abbas-Setif1, 19000, Algeria

<sup>c</sup>Department of Physics, University of Ferhat Abbas-Setif1, 19000, Algeria

**ABSTRACT:** Neutron imaging is a non-destructive testing technique, similar in principle to X-ray imaging. It is based on the attenuation of neutrons as they pass through the material. The conventional film-based neutron imaging system implemented around Es-Salam research reactor has been renewed and replaced by a scintillator and CCD-camera based system allowing 3D imaging<sup>1</sup>. Even though this newly enhanced system ensures many imaging advantages, the production of digital images is suffering from the drawback of noise caused mainly by gamma rays and the recording system itself.

In order to restore a high-quality image, it is required to remove noise from the raw captured images. In this work, we develop an approach to reduce noise in neutron images. We attempt to achieve this by using a pre-trained convolutional neural network (DnCNN) model with a Python deep learning based program. Furthermore, a clear neutron image has been modeled by MCNP5. Based on the simulation, the efficiency comparison of the classical methods and the pre-trained DnCNN is achieved. In addition, we also apply the DnCNN technique to denoise the experimental neutron image.

Based on quantitative and qualitative analysis, the DnCNN model proved its efficiency in guaranteeing better and more efficient neutron image denoising results when compared to traditional tested techniques.

**Keywords:** Neutron imaging; Noise processing; Deep learning; Python.

## INTRODUCTION

Neutron radiography expanded in influence in recent years to reach several fields such as: engineering, biology, archaeology, metallurgy ... etc. The benefits rate depends heavily on the images' resolution and clarity. However, in reality, neutron images are distorted by noise<sup>2</sup>. The principle sources of noise in neutron images arise during image acquisition due to gamma rays effect and recording system. To overcome this problem, we should use the denoising methods. In recent decades, some image denoising methods based on deep learning have developed. In this work, we focus on studying the efficiency of the pre-trained DnCNN model<sup>3</sup> on neutron images that were created around the neutronography facility of the Algerian Es-Salam research reactor. Our study is summarized as follows:

1. Noising of neutron image modeled by MCNP5 code<sup>4</sup> by adding Gaussian white noise.
2. Denoising this image using the classical methods and the pre-trained Convolutional Neural Network (DnCNN).
3. Qualitative and Quantitative analysis of the denoised image.
4. Denoising experimental neutron image through the application of a pre-trained DnCNN.

## MATERIAL AND METHODS

In this section, we present the simulation that we developed in this study, in which we used five denoising methods. Two methods of the spatial filter<sup>5</sup> (Mean filter and Median filter), as

well as two methods of the frequency filter<sup>6</sup> (Gaussian filter and Wiener filter), also the method of denoising convolutional neural network (DnCNN).

In addition, we present the experimental neutron image denoised by DnCNN method.

Figure 1 illustrates the architecture of the DnCNN

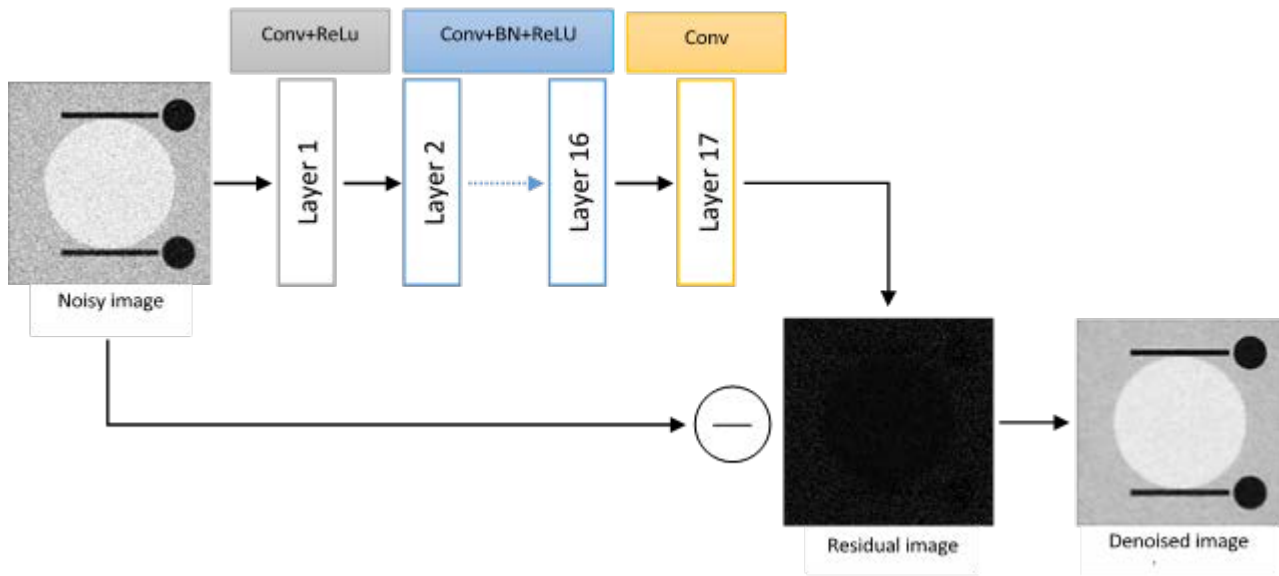


Fig. 1 The architecture of the DnCNN network

After the function is learned, features about the noise subtract from the noisy image. In this work, a pre-trained model is used. The model is trained by 400 noisy images with several noise levels of Gaussian white noise where the neural network parameter configuration is as follows:

- The neural network has a total of 17 layers.
- Conv+ReLU (Rectified Linear Unit): for the first layer, 64 filters of size 3x3 are used to generate 64 feature maps.
- Conv+BN+ReLU: for layers 2 to 16, 64 filters of size 3x3x64

are used, and batch normalization is added between convolution and ReLU.

- Conv: for the last layer, filters of size 3x3x64 are used to reconstruct the output.

### Simulation

In this part, we run a simulation in order to examine the denoising methods we introduced previously. First, we have modeled a clear neutron image (Beam purity indicator) using an MCNP5 code (Figure 2).

Table 1 shows the characteristics of this piece.

Table 1. Characteristics of the beam purity indicator

Materials	Chemical composition	The sub-compounds	Atomic fractions
Lead	Pb	-	1
Cadmium	Cd	-	1
Boron nitride	BN	B, N	0.4, 0.6
Poly-tetra-fluoro-ethylene (PTFE)(Jr, 2010)	C <sub>2</sub> F <sub>4</sub>	C, F	0.33331, 0.66669

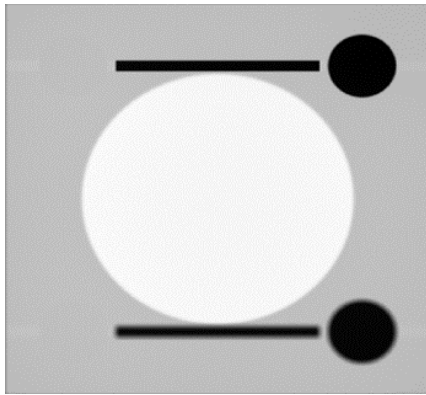


Fig. 2 The image of the Beam purity indicator simulated by a neutron flux grid. We used the Fmesh4 feature of the MCNP5 code

Then, we create a noisy image by adding white Gaussian noise to this image. Next, we restore the denoised image by applying the five methods of denoising. Finally, we performed a quantitative analysis of the obtained images by calculating the Peak Signal to Noise Ratio<sup>7</sup> (PSNR) and qualitative analysis (visual aspect) as well.

Figure 3 illustrates the scheme of the simulation.

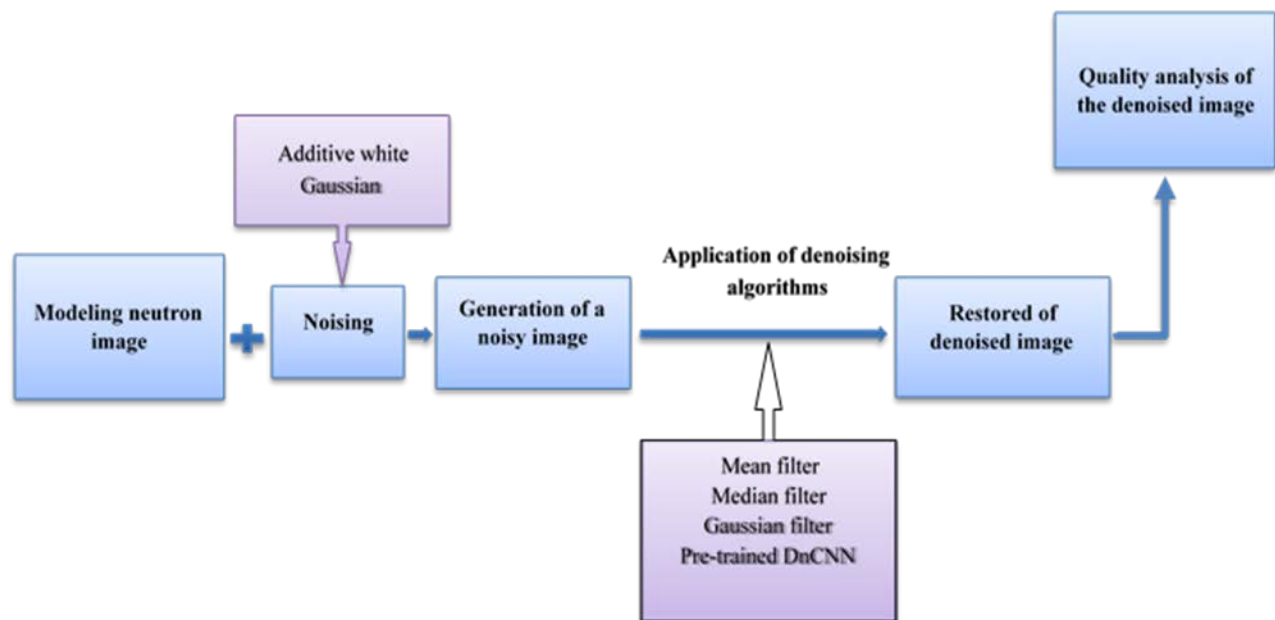


Fig. 3 The simulation scheme

### Experimental

In this part, we have used an experimental neutron image. This image is taken around the neutronography facility of the Algerian Es-Salam research reactor<sup>8</sup>.

This system is composed of a neutron source, a neutron collimation system, a scintillator screen, an object turntable, a

mirror, a cooled CCD camera, and computer support (Figure 4).

After adjusting the appropriate parameters for our neutron imaging system (gain and frame rate), we obtained a neutron image of our object. Then, we denoised our image by applying the DnCNN technique.

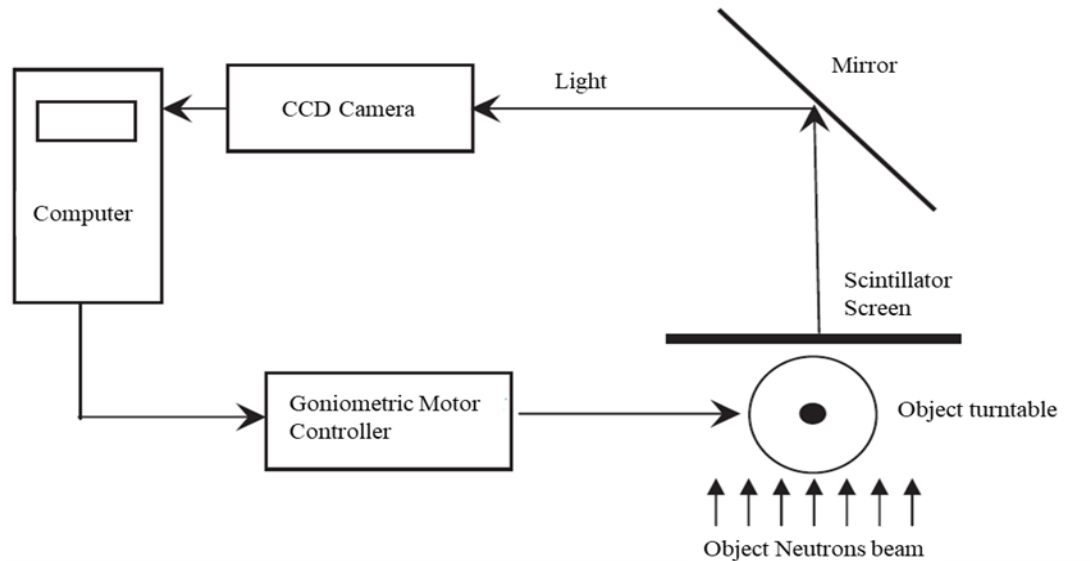


Fig. 4 Neutron tomography system of the Es-Salam research reactor

## RESULTS AND DISCUSSION

The results obtained in the simulation are shown in Figure 5.

Table 2 and Figure 6 represent the results obtained (PSNR values as a function of the noise variance) by four classical methods and the DnCNN method on the reference image.

The comparison between the aforementioned different methods shows that the DnCNN method is the best approach in the values of the PSNR (Figure 6). The Mean filter and median filter have reduced the noise, but these filters generated a blurring effect in the image (Figures 5.b and 5.c).

Figure 5.d shows that the Gaussian filter gives better results than the Mean and Median filters. However, the images are blurry

because the Gaussian filter also removes the high frequencies corresponding to the details of the image.

The Wiener filter is the best filter in the PSNR values compared to the four classical methods. However, the Wiener filter allows smoothing and artifacts on neighboring contours (Figure 5.e). Remarkably, the DnCNN method gives a less blurry and clearer image (Figure 5.f). The results of the experimental work are shown in Figure 7, which shows the results of applying the pre-trained DnCNN method on the experimental neutron image. Based on the subjective criterion (visual aspect), we can say that the application of the method of convolutional neural networks is effective in terms of noise reduction and clarity of the restored images.

Table 2. PSNR results for simulation images denoised by several techniques

$\sigma$	Noisy image	Mean filter	Median filter	Gaussian filter	Wiener filter	DnCNN
10	28.7508	34.1927	35.2968	36.9275	37.2242	<b>39.1426</b>
20	22.9457	30.4224	30.1230	31.9767	32.1834	<b>34.6939</b>
30	19.5252	27.3093	26.8016	28.4494	28.4925	<b>31.1114</b>
40	17.2911	25.0398	24.4991	25.9932	26.2799	<b>28.4920</b>
50	15.5972	23.2469	22.5994	23.9737	24.0558	<b>26.3826</b>



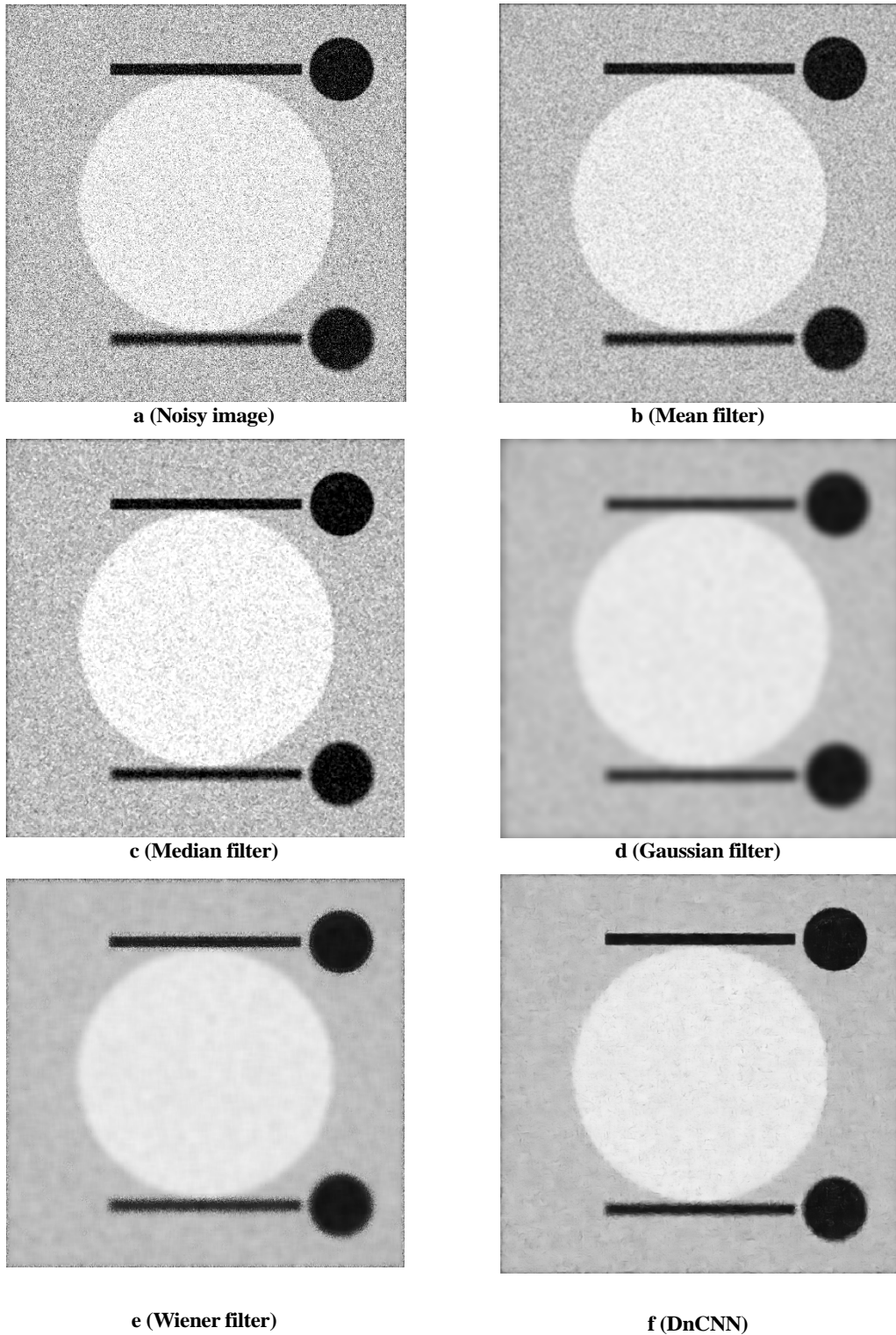


Fig. 5 Noise reduction results on the image by different denoising methods (Simulation results)

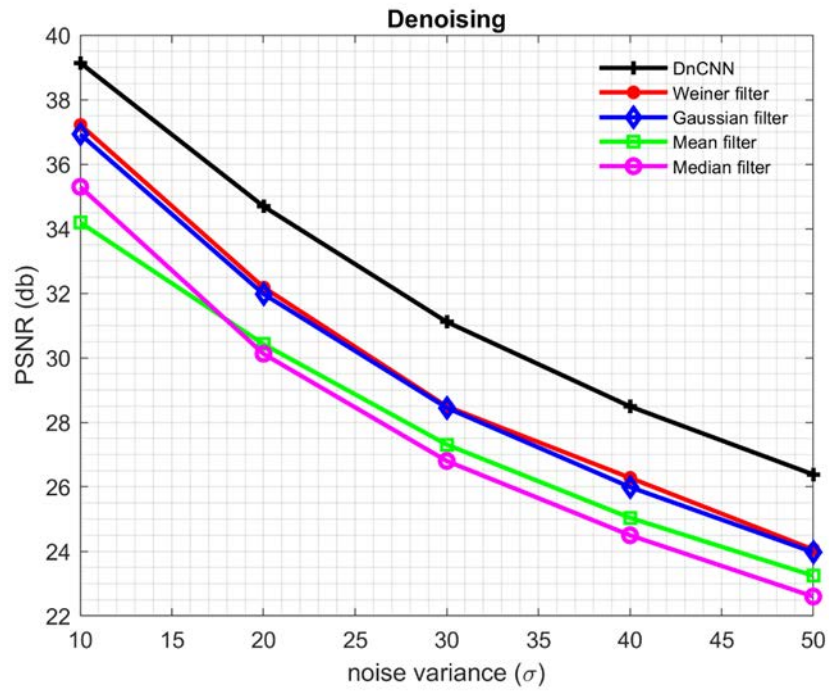


Fig. 6 Representation of the PSNR of the denoised images as a function of the noise variance, by different denoising techniques on the simulation images

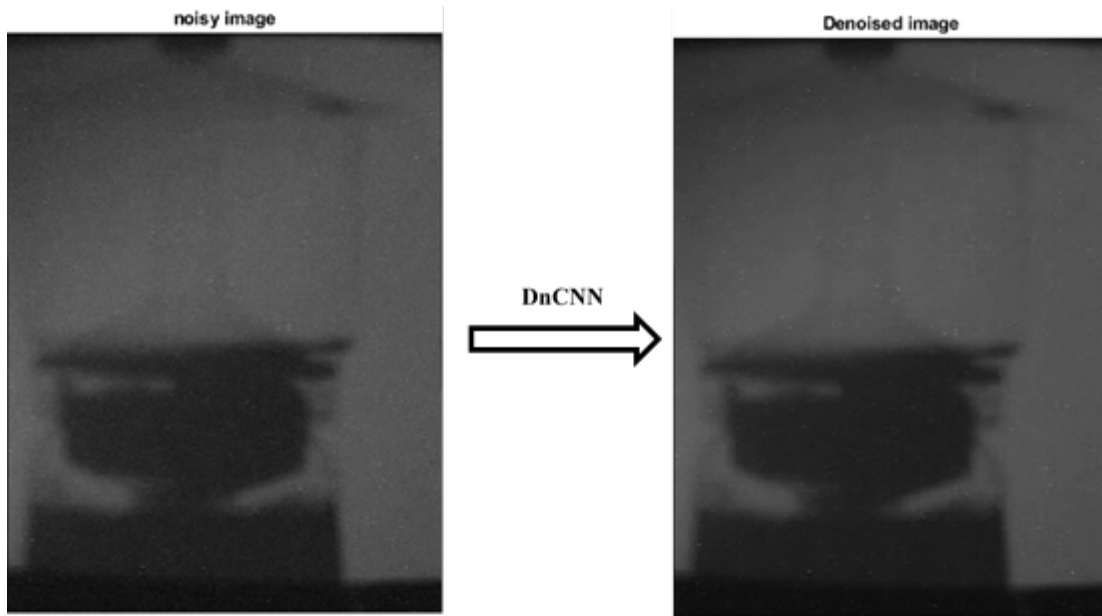


Fig. 7 Denoising results on the neutron image by DnCNN methods (Experimental results)

## CONCLUSIONS

In this work, five denoising algorithms were evaluated and compared by simulation in order to best select those that were used in the experimental part. Furthermore, we have obtained the conclusion that the use of classical denoising methods has several inconveniences such as: generating a blur effect in the image due to removing the high frequencies corresponding to the details of the image, allowing very large smoothing on neighboring contours, and displaying visible artifacts near the contours.

In the experimental part, we used the DnCNN method on an experimental neutron image because the simulation results show the superiority of the DnCNN method (better PSNR and better contour conservation) compared with the traditional methods. The evaluation of the denoised experimental neutron image quality confirmed the efficiency of DnCNN method.

The results of the DnCNN method can be improved by creating a dataset of neutron images, training the pre-trained DnCNN network again, as well as taking into account the compound noise. These suggestions hold the potential of future extensive research.

## AUTHOR INFORMATION

### Corresponding Author

\*Mohamed Laid YAHIAOUI

Email address: [laidastro@hotmail.fr](mailto:laidastro@hotmail.fr)

## REFERENCES

1. Kharfi, F., Boukerdja, L., Attari, A., Abbaci, M., & Boucenna, A. Implementation of neutron tomography around the Algerian Es-Salam research reactor: preliminary studies and first steps. *Nuclear Instruments and Methods in Physics Research Section A: Accelerators, Spectrometers, Detectors and Associated Equipment*, 2005, 542(1-3), 213-218.
2. Zhao, C., Yan, Y., Wang, Y., & Qiao, S. White spots noise removal of neutron images using improved robust principal component analysis. *Fusion Engineering and Design*, 2020, 156, 111739.
3. Zhang, K., Zuo, W., Chen, Y., Meng, D., & Zhang, L. Beyond a gaussian denoiser: Residual learning of deep cnn for image denoising. *IEEE transactions on image processing*, 2017, 26(7), 3142-3155.
4. Monte Carlo Team, X. Mcnp-a general Monte Carlo N-particle transport code, version 5, *volume III: Developer's guide*. 2008, LA-CP-03-0284.
5. de Cheveigné, A., & Simon, J. Z. Denoising based on spatial filtering. *Journal of neuroscience methods*, 2008, 171(2), 331-339.
6. Motwani, M. C., Gadiya, M. C., Motwani, R. C., & Harris, F. C. Survey of image denoising techniques. In *Proceedings of GSPX, 2004*, Vol. 27, pp. 27-30.
7. Hore, A., & Ziou, D. Image quality metrics: PSNR vs. SSIM. In *2010 20th international conference on pattern recognition*, 2010, (pp. 2366-2369). IEEE.
8. Kharfi, F., Denden, O., Bourenane, A., Bitam, T., & Ali, A. Spatial resolution limit study of a CCD camera and scintillator based neutron imaging system according to MTF determination and analysis. *Applied Radiation and Isotopes*, 2012, 70(1), 162-166.



2021

# Neutron beam characterization at the neutron radiography facility of a Es-salam research reactor by SCALE 6.1 simulations

Widad Titouche,<sup>a,\*</sup> Layachi Boukerdja<sup>b</sup>

<sup>a</sup>Nuclear physics Department, Nuclear Research Centre of Birine, 17200, Algeria

<sup>b</sup>Neutron Radiography Department, Nuclear Research Centre of Birine, 17200, Algeria

**ABSTRACT:** Es-salam nuclear research reactor has several horizontal and vertical experimental channels; one of its horizontal channels is equipped by a neutron radiography facility. The design of this facility required the determination of the energetic neutron beam spatial distribution. This can be achieved by simulation, through powerful calculation codes. These allow to predict, to understand and to optimize the behavior of such installation. The purpose of this work was the determination of the thermal neutron flux at the neutron radiography facility. The calculation has been done by the means of SCALE 6.1 Monte Carlo simulation codes. The simulation results are in good agreement with experimental measurements. The concordance between simulation results and experimental values allow a precise characterization of the neutron radiography beam as well as a validation of the adopted methods of simulation and variance reduction.

**Keywords:** Neutron beam, spatial distribution, simulation, Monte Carlo, MCNP5, SCALE6.1.

## INTRODUCTION

Modeling and simulation can be an important element in the prediction of nuclear reactor core behavior. The development of a simulation model have to be validated. The purpose of validation is to provide confidence in the ability of computer code to predict, realistically, reactor core parameters. Experimental data are the best source of information in the validation process.

In this work, the neutron radiography facility of Es-salam research reactor has been modeled by SCALE 6.1 code package<sup>1</sup>. Simulation consist of both criticality and transport calculations. A three-dimensional modeling capability within SCALE6.1 has been created to model Es-salam research reactor core and its experimental channels, by linking the KENO-VI criticality code to the MAVRIC transport sequence. KENO-VI has been used for criticality calculations and MAVRIC (Monaco with Automated Variance Reduction using Importance Calculations) for radiation

transport calculations.

Monte Carlo codes use variance reduction (VR) methods to reduce calculation times, and uncertainties, but many of these involve a great deal of experience on the part of the user. Over the past decade, progress has been made developing hybrid methods for VR that use discrete ordinates solutions. These hybrid approaches have been automated in MAVRIC reducing burden on the user. These automated systems use CADIS (Consistent Adjoint Driven Importance Sampling) or FW-CADIS, which forms an importance map and biased source distribution from the results of coarse mesh adjoint discrete ordinate calculation<sup>2,3</sup>.

This paper details the Monte Carlo simulation of the neutron imaging facility and the use of VR technique to achieve acceptable precision for the Monte Carlo results in reasonable time.

## NEUTRON IMAGING FACILITY AT ES-SALAM RESEARCH REACTOR

The neutron imaging facility is implemented around Es-salam reactor at the nuclear research center of Birine. It is mainly composed with a neutron collimator, installed inside the horizontal channel N° 6 (H6) of the reactor, an imaging detection system based on a cooled CCD camera, a turntable for neutron tomography and a beam stop (see fig.1). The entire installation is surrounded by biological protection made of concrete.

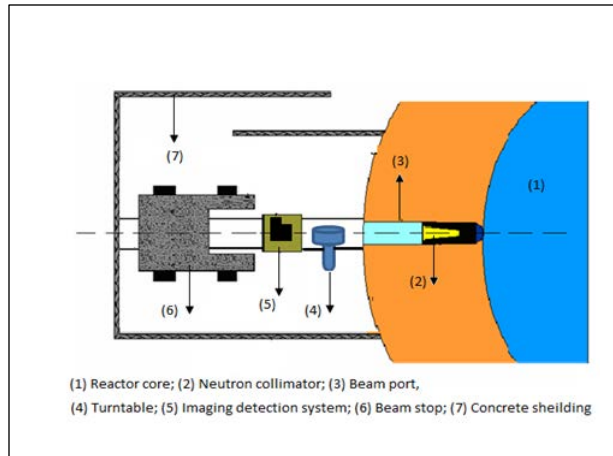


Fig.1 General layout of the neutron imaging facility

## THE SCALE6.1 CODE PACKAGE

The SCALE6.1 code system was developed for the U.S.NRC to satisfy a need for a standardized method of analysis for the evaluation of nuclear facilities. In its present form, the system has the capability to perform criticality, shielding, radiation source term, spent fuel depletion/decay, reactor physics, and sensitivity analyses using well established functional modules tailored to the SCALE6.1 system.

The criticality-eigenvalue sequence (CSAS6) uses a 3D multigroup MC transport code KENO-VI to provide the problem-dependent, cross-section processing followed by the calculation of the neutron multiplication factor  $k_{\text{eff}}$ <sup>1</sup>. KENO-VI has the ability to save the space-energy fission distribution of a critical system into a file over the user-specified 3D mesh grid and energy structure of the cross section library. This methodology was first implemented into SCALE6.0 code package to enable modeling of criticality accident alarm systems (CAAS)<sup>2,3</sup>. The MC shielding sequence MAVRIC is based on the Consistent Adjoint Driven Importance Sampling (CADIS) methodology<sup>3</sup> which is used to create space-energy mesh-based VR parameters: the importance map (weight windows) and a biased source distribution<sup>3,4</sup>. The integrated SN code Denovo<sup>1</sup> is

used for a quick estimate of the deterministic adjoint fluxes (xyz mesh) which are used by the MAVRIC for the VR preparation. The Monaco is a multigroup, fixed-source, 3D MC transport code<sup>1</sup>, which uses these VR parameters to bias MC simulation in the last step of the hybrid deterministic stochastic methodology. When computing several tallies at once or a mesh tally over a large volume of space, an extension of the CADIS method called the FW-CADIS can be used to obtain the uniform relative uncertainties<sup>3</sup>.

## METHODOLOGY ADOPTED IN SCALE 6.1

The CAAS capability in SCALE6.1 is a two-step approach using KENO-VI and MAVRIC. The first step is the determination of the source distribution, typically done with the CSAS6 control sequence, which uses the KENO-VI functional module. In the second step MAVRIC use this mesh source to perform transport calculations. For best results, the critical system geometry was modeled with only the closest surrounding materials but in fine details while the transport geometry could leave out small details but would include large level components of the in-pile part of the neutron imaging facility.

### KENO-VI calculations

Full-sized reactor core has been modeled using the SCALE General Geometry Package (SGGP). The KENO-VI criticality calculations for Es-salam reactor core use ENDF/B-VII 238 group library, a total of 250 generations, with 50 skipped generations and 10000 source particles per generation. The fission distribution was accumulated on a 17x17x20 mesh covering a cylinder surrounding the fissionable material.

### MAVRIC calculations

The MAVRIC transport calculations were performed for the experimental channel; first without the collimator for neutron radiography facility and second with the collimator. The MAVRIC calculations for both models use the same fission source distribution from KENO-VI. The CADIS case was used with ENDF/B-VII-27n19g library for faster Denovo Sn calculations and ENDF/B-VII-200n47g library for Monaco, with  $S_8/P_3$  parameters. For the importance maps/biased source a coarse mesh of about 56 cells in 380 cm<sup>2</sup> was defined for Sn calculations and number of mesh planes including all the core model with significant material boundaries. One adjoint source was located at the end of the channel. The adjoint source spectrum for CADIS was response 9029 (neutron dose). MAVRIC was executed for 10 batches with 100000 neutrons per batch (10<sup>6</sup> histories) for the NR facility without collimator system, and 10 batches with 900000 neutron per batch (9x10<sup>6</sup> histories) for calculations with collimator system.

## RESULTS AND DISCUSSION

The calculated  $k_{eff}$ , is within the range of the experimental value with a deviation of 0.06%. The fission source distribution is sketched in figure 2, where one can notice the spatial gradient of the fission neutron over the core.



Fig.2 Fission source spatial distribution for the reactor mid-plane (z=0)

To show the effect of the automated VR in MAVRIC, an analog calculation using the KENO-derived mesh source, but without importance map and biased source distribution, was run for 5767.75 minutes (~96h), in case of neutron imaging facility without collimator system, while with the CADIS methodology (VR) the total Monaco CPU time, for the same flux calculation, was 200.0 minutes (~3h).

The calculated thermal neutron flux in the horizontal channel N°6 (H6) with and without collimator system are presented in Table 1 and compared with experimental values measured at 1 MW reactor power.

Table 1. Comparison results

	MAVRIC Thermal neutron flux	Experimental values	Errors
H6 without collimator system	1.01050 E+8 ±0.02469	0.96 E+8	5.26%
H6 with collimator system	1.45749 E+6 ±0.02650	1.6 E+6	8.91%

SCALE6.1 create a file, which can be displayed using the ChartPlot 2D Interactive Plotter, to visually check the convergence behavior of the tally; in this case the neutron flux (Fig.3). As we can see there is a stability between the ten batches and the flux converge well.

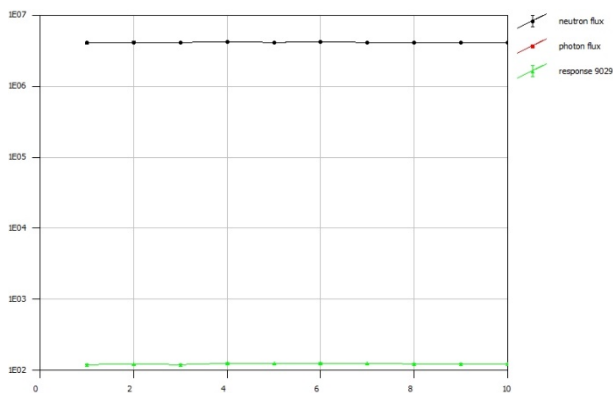


Fig.3 Batch convergence data for neutron flux

imaging facility. The total neutron fluxes are shown in Figure 4 for several of the neutron energy groups.

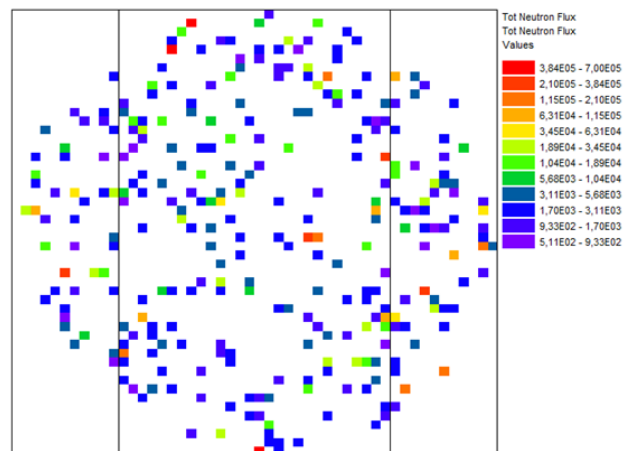


Fig.4 Energetic neutron flux spatial distribution at the level of the analyzed object

The SCALE6.1 also includes the Java Mesh File Viewer utility to view the flux distribution and its homogeneity at the analyzed object position, which is an important parameter in neutron

## CONCLUSIONS

Detailed criticality and transport calculations of Es-Salam

research reactor with neutron imaging facility were performed using KENO-VI and the hybrid deterministic-stochastic methodology in MAVRIC sequence of SCALE6.1 code package. SCALE6.1 capability to do detailed simulations were proved. The automated variance reduction capabilities of MAVRIC allow for the full three dimensional analysis of the reactor core and the imaging facility in reasonable time limit. The thermal neutron flux was obtained with satisfactory MC statistics and match the experimental values.

This qualification scheme means that the simulation tools are suitable to improve the neutron radiography facility and to updated.

## AUTHOR INFORMATION

### Corresponding Author

\*Widad Titouche

Email address: [w.titouche@cmb.dz](mailto:w.titouche@cmb.dz)

## REFERENCES

1. SCALE: A Comprehensive Modeling and Simulation Suite for Nuclear Safety and Design, ORNL/TM-2005/39, Version 6.1, June 2011. Available from Radiation Safety Information Computational Center at Oak Ridge National Laboratory as CCC-785.
2. D. E. Peplow, L. M. Petrie Jr, Criticality Accident Alarm System Modeling With SCALE, International Conference on Mathematics, Computational Methods & Reactor. Physics (M&C 2009), Saratoga Springs, 2009, New York, May 3-7.
3. E. Douglas, E. Peplow, Monte Carlo Shielding Analysis Capabilities with MAVRIC, Nuclear Technology, Vol. 174, May 2011.
4. M. Matijevic, D. Pevec, K. Trontl, Modeling of PWR Biological Shield Boration Using SCALE6.1 Hybrid Shielding Methodology, 23<sup>rd</sup> International Conference Nuclear Energy for New Europe, 2014, Portoroz Slovenia.



2021

## Neutron irradiation effects on topological properties of CZ-silicon

Nadjet Osmani<sup>a,\*</sup>

<sup>a</sup> Department Neutron Transmutation Doping of Silicon, Nuclear Research Center of Birine , Djelfa

**ABSTRACT:** In this work, the change in the structural properties of CZ-silicon (CZ-Si) are studied before and after irradiation at three different fast neutron fluence values:  $0.74 \times 10^{18}$ ,  $1.98 \times 10^{18}$  and  $3.96 \times 10^{18}$  n/cm<sup>2</sup>. The neutron irradiation was performed around the Es-Salam research reactor. The induced surface topography characteristics on the studied CZ-Si material was observed using Atomic Force Microscope AFM in contact mode. The effect of the isochronal annealing on the topological property CZ-Silicon was studied. 3D-AFM technique is used to characterize the surface quality and roughness. The neutron irradiation has induced an increase in the surface roughness in case of higher neutron fluence. It was also observed that the roughness increases with the increase of the neutron fluence and decreases by increasing of the post-irradiation annealing temperature. This phenomenon can be related to the smoothing aspect of the material surface.

**Keywords:** Neutron fluence; Silicon; AFM; Roughness

### INTRODUCTION

Defects in semiconductors play a crucial role in determining the performance of electronic and photonic devices<sup>1</sup>. Understanding the role of defects is crucial to explain several phenomena, from diffusion to guttering, or to draw theories on the materials behavior, in response to electrical, optical, or mechanical fields. Studies of neutron irradiation structural defects and their influence on the characteristics of Silicon were investigated and several papers were published<sup>2-6</sup>. The effect of neutron irradiation on the some mechanical properties of such materials was also of great interest. Indeed, many investigations have been undertaken to understand the silicon damage due to neutron irradiation. Results on surface's roughness of silicon, irradiated at different fluences at the level of  $10^{18}$  n/cm<sup>2</sup>, are described and discussed in this paper. The purpose of this research is to examine structural defects in neutron irradiated silicon using atomic force microscopy, which may illustrate the evolution of defect from

atomic to large clusters. In this paper, very interesting information was also obtained by using the topography techniques for averaged surface roughness analysis.

### EXPERIMENTAL

In this work, CZ-Silicon samples were irradiated around the Es-Salam research reactor under neutron fluences of  $0.74 \times 10^{18}$ ,  $1.98 \times 10^{18}$ , and  $3.96 \times 10^{18}$  n/cm<sup>2</sup>. Isochronal annealing procedures of 60 min at two different temperatures, 550 and 750 °C, were carried out in a quartz tube furnace under Argon atmosphere. The surface topology of the boron doped CZ-Silicon was observed using "Pacific Nanotechnology" Atomic Force Microscope (AFM) in contact mode. The data obtained are real two- and three-dimensional images of the investigated surface.



## RESULTS AND DISCUSSION

Neutron irradiation is a powerful mechanism for semiconductor doping. In this study, the neutron irradiation has induced increase of the surface roughness at higher neutron fluence. Figure 1 shows clearly the increase of roughness as a function of the neutron fluence. Figures 2 and 3 show the 2D (a) and 3D (b) AFM surface topology images of CZ-Si before and after irradiation for a neutron fluence of  $0.74 \times 10^{18}$ . For this neutron fluence, the surface roughness changes from 8.28 to 9.42 nm. It is well known that neutron irradiation may induce various types of structural changes that can modify the material mechanical properties. Annealing at suitable temperature is a very efficient post-irradiation treatment that may reduce some irradiation effects such as change in roughness. Figures 4 and 5 demonstrate well the effect of annealing processing at two-selected temperatures of 550 and 750°C for the sample irradiated with a neutron fluence of  $0.74 \times 10^{18}$  n/cm<sup>2</sup>. Indeed, the average roughness decreases with the increase of the annealing temperature. The surface roughness of silicon wafer is one of the most important issues that degrade characteristics of semiconductor devices. The importance of

spatial roughness frequency as an influential parameter has been pointed. In this research, the effect of roughness due to neutron irradiation was studied using samples irradiated with different fluences and annealed with two-selected temperatures. From the obtained results, it was found that that higher temperature decreases the surface roughness due to neutron irradiation.

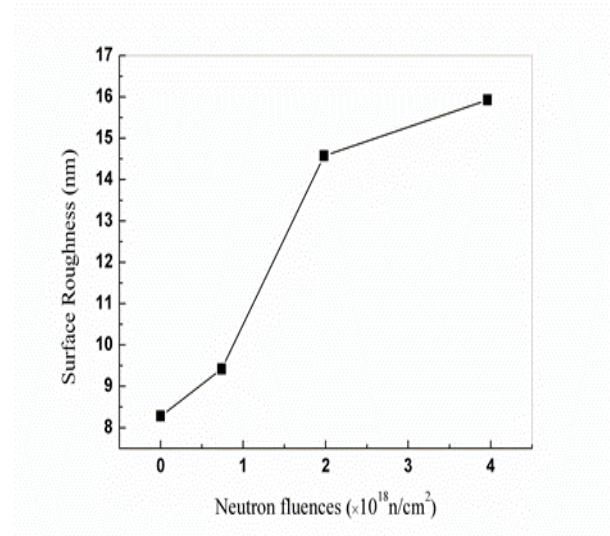


Fig.1 The average roughness of Si as a function of neutron fluence

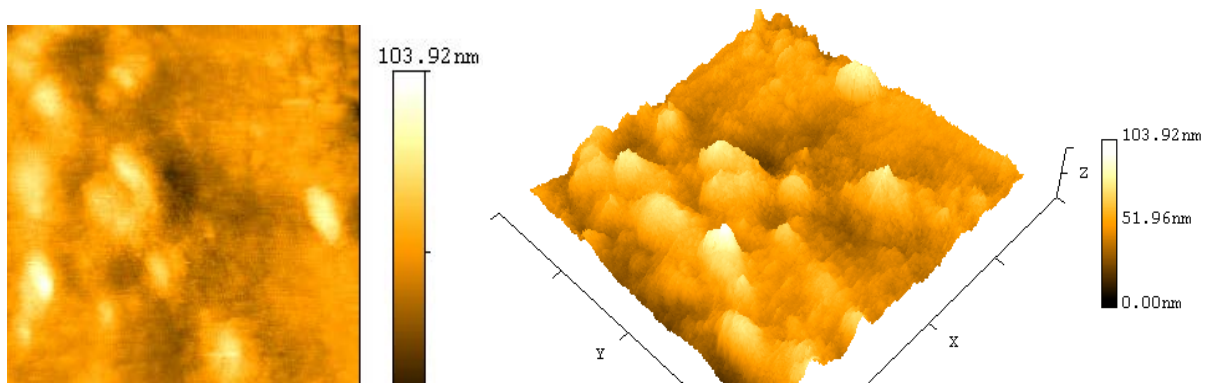


Fig.2 (a) 2D and (b) 3D AFM surface topology images of CZ-Si before irradiation

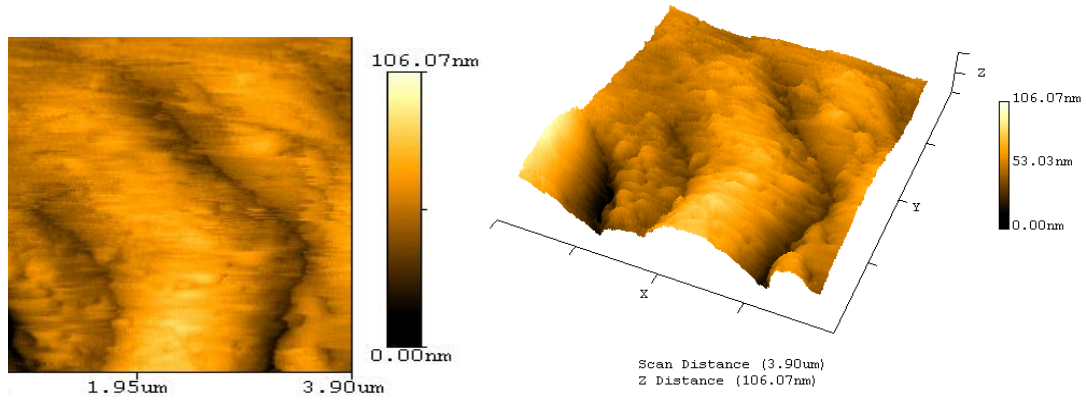


Fig.3 (a) 2D and (b) 3D AFM surface topology images of CZ-Si after irradiation at  $0.74 \times 10^{18} \text{ n/cm}^2$

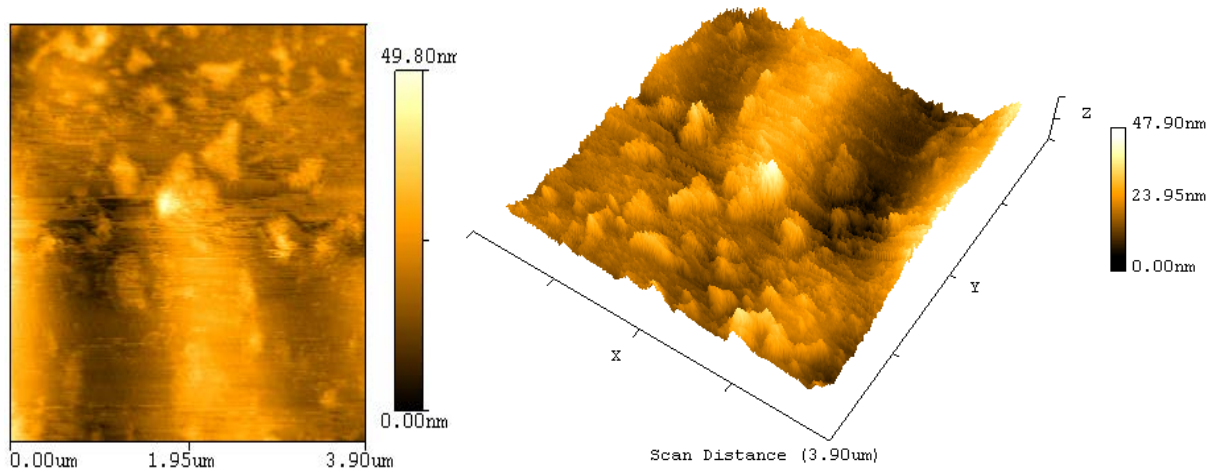


Fig.4 (a) 2D and (b) 3D AFM surface topology images of CZ-Si after irradiation with  $0.74 \times 10^{18} \text{ n/cm}^2$  and annealing at  $550^\circ\text{C}$

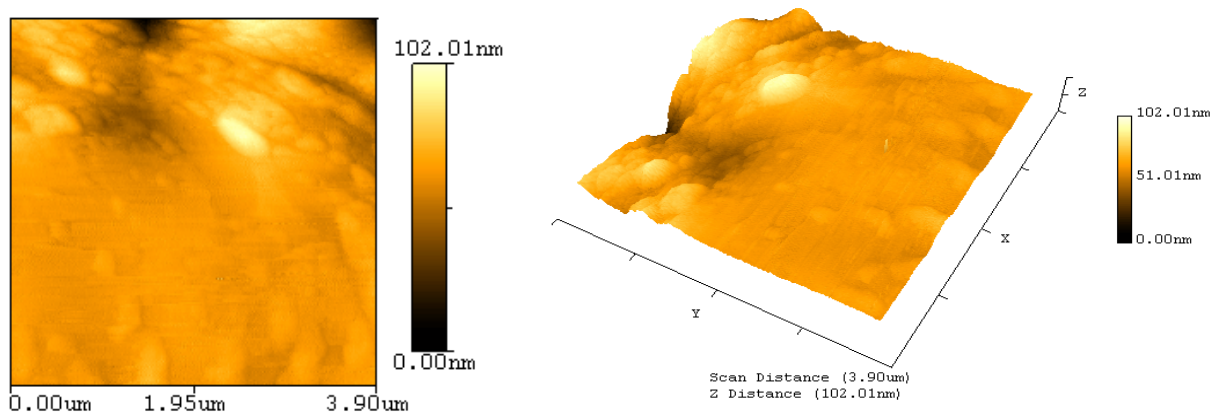


Fig.5 (a) 2D and (b) 3D AFM surface topology images CZ-Si after irradiation with  $0.74 \times 10^{18} \text{ n/cm}^2$  and annealing at  $750^\circ\text{C}$

## CONCLUSIONS

In the present study, we have pointed out the change in topological properties on boron doped CZ-Silicon induced by fast neutron irradiation with different higher neutron fluences. The induced surface defects is proportional to the neutron irradiation fluence and induce an increase in average surface roughness. The studied material when subjected to a post-irradiation thermal annealing find its roughness decreasing by the increase of the annealing temperature.

## AUTHOR INFORMATION

### Corresponding Author

\*Nadjet Osmani

Email address: [osmaninadjet@yahoo.fr](mailto:osmaninadjet@yahoo.fr)

## ACKNOWLEDGMENT

---

The author acknowledges the technical support of S.A. Amzert and all the operators of the Es-Salam research reactor.

## REFERENCES

1. P.Kaminski ,R. Kozlowski, E.Nossazewska-Orlowska, "Formation of electrically active defects in neutron irradiated silicn", Nucl,Instr ad Meth B. 186(2002) 152.
2. N. Osmani, A. Boucenna, A. Cheriet, (2015). DOI:10.1109/WSMEAP.7338207, an IEEE journal.
3. Nadjet Osmani, L. Guerbous et A. Boucenna(2018). "Structural, topological, electrical and luminescence properties of CZ-Silicon (CZ-Si) irradiated by neutrons" Applied Physics A Materials Science & Processing 124:709
4. N. Osmani, ACheriet.(2020) "Complexes defects induced by neutron irradiation of Cz-silicon" <https://doi.org/10.1007/s00339-020-03519-0> Applied Physics A126:329.
5. Bosetti M, Croitoru N, Furetta C, Pensotti S, Rancoita P, Rattaggi M, Redaelli M, Seidman A. Nucl Instr Methods B 1995;95:21.
6. Croitoru N, Dahan R, Rancoita PG, Rattaggi M, Rossi G, Seidman A. Nucl Instr Methods B 1997;124:542.



2021

# Overview of tracers' techniques using in CFD modeling of Boron Behaviour and Pressurized thermal shock

Youcef Bouaichaoui,<sup>a,\*</sup> Abderahman Belkaid,<sup>a</sup> Thomas Höhne<sup>b</sup>

<sup>a</sup>Centre de Recherche Nucléaire de Birine /CRNB/COMENA/ALGERIA BP 180 – Ain Oussera - 17 001 – Djelfa- Algérie

<sup>b</sup>Helmholtz-Zentrum Dresden-Rossendorf (HZDR), Institute of Safety Research, P.O. Box 510119, D-01314 Dresden, Germany

**ABSTRACT:** The present article documents the two main techniques used in Computational Fluid Dynamics (CFD) code validation activity carried out at the Nuclear Research Center of Birine as part of the Coordinated Research Project initiated by the International Atomic Energy Agency (IAEA), entitled: "Application of Computational Fluid Dynamics (CFD) Codes for Nuclear Power Plant Design". The work consists in modeling phenomena such as: boron dilution and pressurized thermal shock (PTS) by simulating the cooling fluid in the downcomer and the lower plenum of KONVOI German PWR reactor type represented by ROCOM test facility designed on a reduced scale 1/5 by the German Research Center HZDR. The simulation results were evaluated against the experimental data collected from the ROCOM test. Good quantitative and qualitative agreement with the experimental data was obtained.

**Keywords:** ANSYS-CFX; PTS; Boron Dilution; ROCOM; CRP.

## INTRODUCTION

Recognizing the growing interest in using CFD codes to contribute to the technological progress of their verification and validation (V & V) for the purpose of using these codes in nuclear reactor design studies, at the IAEA it was decided to set up a benchmarking exercises to improve the degree of maturity as reliable tools in the safety analysis of nuclear reactors.

In this context, the CFD software packages ANSYS CFX<sup>1</sup> code was used to simulate one of the experiments conducted in order to examine coolant mixing in the reactor pressure vessel (RPV) of a German-type PWR, and provide data to validate the associated numerical models, the Rossendorf COolant Mixing Model (ROCOM) test facility. Indeed, the essential problem related to the distribution of coolant properties, is whether an Emergency Core Cooling (ECC) injection following a Small Break Loss-of-Coolant Accident (SB-LOCA) may lead or not to

a Pressurized Thermal Shock (PTS) scenario, due to the relatively cold injected water being not sufficiently mixed with the water already present in the cold legs.

From the entire set of data, the experiment D10m10 with 10% flow rate in one loop and 10% density difference between ECC and loop water has been selected for the calculations to be performed during this benchmark exercise<sup>2-4</sup>. The Froude number for this test is  $Fr = 0.85$ , and may therefore be regarded as density dominated

Objectives:

A set of ROCOM CFD-test data are used to calculate the behaviour of boron free water slugs arriving from the cold legs with a low concentration of boron resulting from the condensation of the vapor by creating a slug of non-borated water which is at the origin of reactivity accidents. The objective here is to obtain a reliable core inlet map for boron concentration

for a given scenario, in order to be able to predict the subsequent neutronic behaviour within the core region. The sodium chloride (Na-Cl) injected as a tracer can significantly modify the electrical conductivity of the water allowing the use of the conductance method to measure the electrical conductivity of the mixed solution within the water.

In addition, the ANSYS CFX code<sup>1</sup> was used to replicate the PTS and boron dilution experiments performed in the ROCOM test facility for the prediction of tracer distribution profiles by solving the transport equation for a pseudo tracer component as a user-defined function (UDF).

## ROCOM FACILITY AND TEST DESCRIPTION

The ROCOM test facility<sup>2,3</sup> consists of a Perspex model of the RPV (Fig. 1) with four inlet and four outlet nozzles. The facility is equipped with four fully independent operating loops (Fig. 2), each with its own dedicated circulation pump, driven by motors with computer-controlled frequency transformers. As a result of this set-up, a wide variety of operating regimes can be realized: four-loop operation; operation with pumps off; simulated natural circulation modes; and flowrate ramps. For the investigation of natural circulation modes, the pumps are operated at low speed, by means of the frequency-transformer system.

Geometric similarity between the actual Konvoi reactor and the scaled ROCOM facility is maintained from the inlet nozzles to the downcomer, and through to the core inlet. The core itself is excluded from the similarity principle; rather, a core simulator with the same Euler number (pressure drop vs. flow head) as in the original reactor is utilized. All the component parts of the ROCOM test facility are manufactured from Perspex for visualization purposes (Fig. 1).



Fig.1 Perspex model of the RPV in ROCOM

An overview of the ROCOM test facility is given in Fig. 2. The model of the Reactor Pressure Vessel (RPV) incorporates, at 1:5 scale, the geometry of the original PWR with respect to the design of the nozzles (diameter, radii of curvature and diffuser sections), the characteristic extension of the downcomer cross-section below the nozzle zone, the perforated drum in the lower plenum, as well as the design of the core support plate, with its orifices for the passage of the coolant into the core. The flow rate in the loops is scaled according to the transit time of the coolant through the RPV. That is, the transit time of the coolant in the model is identical to that of the reactor when the actual coolant flow rate is scaled by 1:5

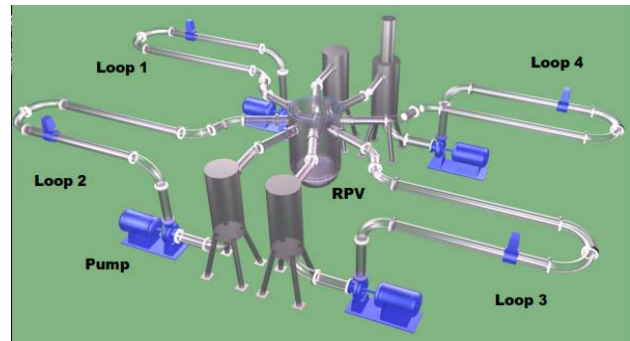


Fig 2 Overview of the ROCOM test facility with its four loops and individual frequency-controlled circulation pumps

From these scaling laws, the nominal flow rate in ROCOM is 185 m<sup>3</sup>/h per loop. The Reynolds numbers are approximately two orders of magnitude smaller than in the reactor. As a result of the down-scaling in geometry, a factor of 25 applies for the mass flow rates, and hence the velocities. The remaining differences derive from the operation at room temperature, and at ambient pressure. In particular, at room temperature, the viscosity of water is approximately a factor of 8 higher than under typical reactor conditions. Since coolant mixing is mainly induced by turbulent dispersion (i.e. largely independent on the exact fluid molecular properties), it is possible to use a tracer substance to model differences in both boron concentration<sup>4-7</sup> and coolant temperature. The coolant in the disturbed loop is marked by injecting a sodium chloride (common salt) solution into the main coolant flow upstream of the reactor inlet nozzle.

### Instrumentation

The distribution of the tracer in the water flow field was measured using electrode mesh sensors, which sample the distribution of electrical conductivity over the cross section of the flow. The development of these sensors was aimed at producing a direct conductivity measurement between pairs of crossing wires to avoid the use of tomographic reconstruction algorithms<sup>8</sup>, and to achieve a time resolution of up to 10 000

frames per second. By this technique, two crossing grids of electrodes (insulated from each other) are placed across the cross-section of the flow duct. The electrodes of the first grid (transmitter electrodes) are successively charged with short voltage pulses. The currents arriving at the electrodes of the second grid (receiver electrodes) are recorded. After a complete cycle of transmitter activation, a full2D matrix of local conductivities is obtained.

Special methods of signal acquisition<sup>5</sup> guarantee that each value of the matrix depends only on the local conductivity in the immediate vicinity of the corresponding crossing point between transmitter and receiver electrodes.

In the current test, the mesh sensors are placed at four positions in the flow path. The first sensor (Fig. 3) is flanged to the reactor inlet nozzle in Loop N°1, and records the tracer concentration at the reactor inlet. The second and third sensors are located at the inlet and outlet of the downcomer.

The downcomer sensors consist of 64 radial fixing rods with orifices for four circular electrode wires (Fig. 4). Small ceramic insulation beads separate the rods and wires electrically. The rods act as radial electrodes; i.e. each rod corresponds to a circumferential measuring position (Fig. 5).

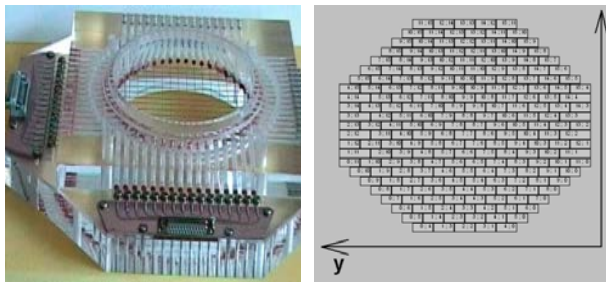


Fig 3 Mesh sensor for measuring tracer distributions in front of the reactor inlet nozzle (left) and measurement positions (right)

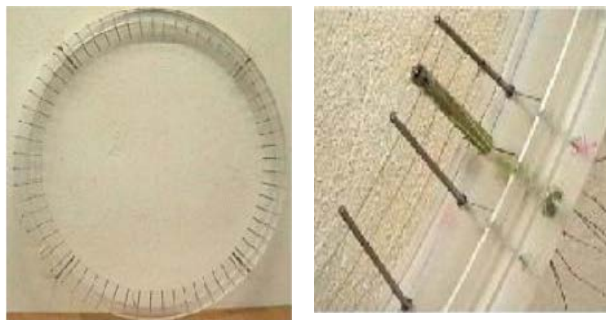


Fig 4 Wire mesh sensor in the downcomer for radial measurements (64x4 measuring positions)

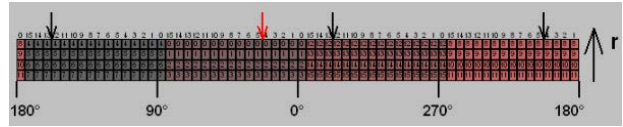


Fig 5 Measurement positions at the two downcomer sensors (upper and lower)

The fourth sensor is integrated into the core support plate: 2X15 electrode wires are arranged such that the wires of the two planes cross in the centres of the coolant inlet orifices of each fuel element (Fig. 6). In this way, the tracer concentration can be measured for each individual fuel element channel. 193 conductivity measurements at the core entrance were applied to the test facility (Fig. 7). All sensors provide 200 measurements per second. A measuring frequency of 20 Hz is sufficient; only ten successive images are averaged into one conductivity distribution.



Fig 6 Wire mesh sensor at the core entrance

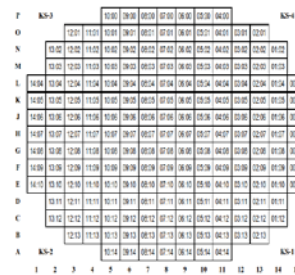


Fig 7 Measurement positions at the core sensors

## EXPERIMENTAL

As the ROCOM facility cannot be heated, the higher density of the cold ECC water is simulated by adding sugar (glucose). In this case of experiment described here, a density difference of 10% was used. A sugar solution with a density of 1100 kg/m<sup>3</sup> has a viscosity a factor 3 higher than that of pure water. This lead to creating a density difference and stratification potentially

dangerous between the relatively cold Emergency Cooling Water (ECC) and the primary loop inventory allowed simulating a Loss Of Coolant Accident (LOCA) lead to a Pressurized Thermal Shock (PTS) scenario, due to the relatively cold injected water being not sufficiently mixed with the water already present in the cold legs.

Assuming similarity between the tracer concentration and the temperature and boron concentration fields, a variety of different experiments can be carried out, which gives the ROCOM facility great flexibility. As standard, the reference values correspond to the unaffected coolant (index „0“) and to the coolant at the „disturbed“ reactor inlet nozzle (index „1“). The difference between the two reference values is the magnitude of the perturbation. A mixing scalar  $\Theta_{x,y,z,t}$  may thus be defined as follows:

$$\Theta_{x,y,z,t} = \frac{\sigma_{x,y,z,t} - \sigma_0}{\sigma_1 - \sigma_0} \cong \frac{T_{x,y,z,t} - T_0}{T_1 - T_0} \cong \frac{C_{B,x,y,z,t} - C_{B,0}}{C_{B,1} - C_{B,0}} \quad (1)$$

In which  $\sigma$ ,  $x$ ,  $y$ ,  $z$ ,  $t$  denotes the (measured) electrical conductivity;  $T$  is the (derived) temperature, and  $CB$  the (derived) boron concentration. Which of the two parameters – temperature or boron concentration – is represented by the measured mixing scalar depends on appropriate choice of the reference values, and the stipulation of the boundary conditions in the experiment.

## NUMERICAL MODELLING

The analysis has been performed with CFD ANSYS CFX-17.0 code for simulations of turbulent flow and mixing in ROCOM facility by solving the Reynolds Averaged Navier Stokes (RANS) equations with k-w-SST turbulence model associated to a transport equation of an additional, user-defined, scalar variable simulating the tracer. For the study presented here, the Boussinesq approximation is applied to take into account density effects on the momentum equation. The density is taken constant in all terms of the Navier-Stokes equations with exception of the gravity term. There, the density is a function of the local temperature or concentration, respectively.

The discretization in space is a 2<sup>nd</sup> order element-based finite-volume method with 2<sup>nd</sup> order time integration. It uses a coupled algebraic multigrid algorithm to solve the linear systems arising from discretization. The discretization schemes and the multigrid solver are scalably parallelized. CFX works with unstructured hybrid grids consisting of tetrahedral, hexahedral, prism and pyramid elements.

### Meshing of the calculation domain

This meshing was created by ANSYS ICEMCFD with unstructured hybrid grids consisting of tet, hex, prism and

pyramid elements. The investigated mixing phenomena occur in the cold leg n°1 during the ECC injection, in the downcomer and the lower plenum. All domain from the cold leg to the core support plate has been discretized with fine meshes. The total mesh contains about 2,377,780 hexa 3,222,496 tetra, 8,594,10 prisms and 29,131 pyramids; i.e. about 6,488,817 total number of cells. A total view of the mesh is shown in Fig.8.

Table 1. Grid information

	Mesh type	Number of cells
1	Hex	2,377,780
2	Tet	3,222,496
3	Prisms	8,594,10
4	Pyramids	29,131
5	Total number of cells	6,488,817

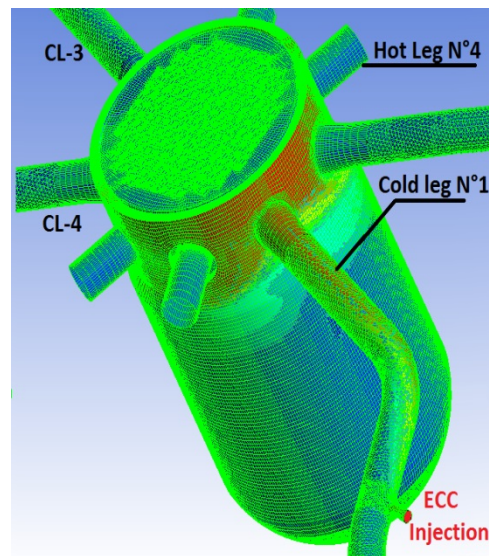


Fig.8 View of mesh

### Boundary conditions

For the simulation calculation, the boundary conditions of the experiment were scrupulously reproduced namely:

- The velocity of the ECC injection line is 0.64297 m/s. The injection time is from 5 s to 15 s (Dirac impulse) after start of loop circulation in Cold Leg N.1. The injection is initiated by opening the upstream valve.
- The fluid used in the ECC injection line is glucose-water (10% density difference to tap water density) with a density of

1100 [kg/m<sup>3</sup>]

- The velocity in Cold Leg No.1 is 0.291 [m/s].
- The other 3 loops are left open.
- Pressure-controlled outlet boundary condition
- Uniform inlet turbulent intensity profile (5%)
- Upwind discretization scheme for advection terms

### CFD setup

In the current study a convergence criterion of  $1 \times 10^{-6}$  was used to ensure negligibly small iteration errors. The time step used was 0.05 s. Glucose-water, which had a higher density, was used as a tracer. It has been modeled with the multi-component model of ANSYS CFX. In this case, the components share the same fields of speed, pressure and temperature. The properties of multi-component fluids are calculated assuming that the constituent components form an ideal mixture. Glucose-water is modeled as a component with a different density and viscosity than water. The mass fraction of the glucose water can be directly related to the mixing scalar described in Eq. (1).

However, the use of simplified models to describe turbulence imposes restrictions on the resolution in space and time that can be used in a CFD calculation. This leads to modeling errors and numerical errors that give more or less inaccurate results. A higher level of quality assurance in the validation of CFD codes has been achieved by consequently applying BPG<sup>9</sup>.

## RESULTS AND DISCUSSION

### Qualitative and quantitative assessment of the CFX simulation versus experiment results

In order to demonstrate the capability of CFD codes to predict the complex phenomena of mixing flow, a comparison was carried out between the calculated results performed with the commercial code ANSYS CFX and the measurements from the experimental setup.

### Qualitative analysis

In Figs 9a, 9b and 9c are plotted the distribution of the mixing scalar in the cold leg n°1 with contours in color shade, which gives a better illustration of the mixing profile for the instant “end of ECC injection”. A horizontal cut plane through the Centre of the cold leg, a vertical cut plane trough the inlet nozzle and ROCOM 3D are shown. The non-homogeneous distribution of the mixing scalar is good visible.

Fig. 10 shows the tracer path and its distribution in ROCOM since the end of the injection from  $t = 15s$  to  $t = 100s$ . After

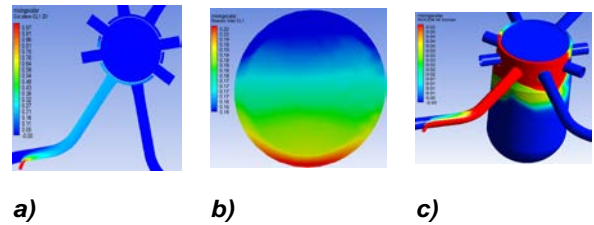


Fig. 9 Mixing scalar in ROCOM, at the end of ECC injection

completion of the injection, the cold leg flow transports the ECC water towards the reactor inlet. It is clear that the flow entering the downcomer is divided into two streams flowing right and left in a downward spiral around the central barrel. The surface covered by the ECC water is first larger under the inlet nozzle under the effect of buoyancy. As the ECC flow is still present, the ECC water is then transported laterally along the spillway on the opposite side of the cold branch no. 1 caused by the pulse of the injected jet. In order to better illustrate the trajectory of the tracer and its distribution in ROCOM, the opposite part of the ECC injection was also represented in Fig.10.

The mixing scalar is much more expressed for instances between 15 and 45 s. The two streaks of the flow merge together after 35 s of the end of the injection and move down through the measuring plane of the upper downcomer sensor as illustrated in Fig. 11 and after the path of tracer goes to into the lower downcomer Fig. 12. Such a flow distribution is typical for single-loop operation. It is dominated by the momentum insertion due to the operating pump or high natural circulation flow rate.

This ECC water transport on the opposite side of the injection is visible in Fig. 13 representing the main plans of Rocom Mesh Sensors. Almost the entire amount of ECC water exceeds the measurement plane of the upper downcomer sensor with a more concentrated azimuthal distribution on the opposite side of the affected loop to reach the plane of the cold branches ( $Z = 0$ ) at the instance between 55s and 100s.

Figure 14 show the snapshots of the the core inlet distribution of the mixing scalar in the three times 45s, 55s and 100s. This snapshot is deduced from the experimental results ROCOM D10M10, the first tracer appears at two positions on the opposite



side of the input plane of the core with respect to the position of the ECC injection loop. This same qualitative behavior is reproduced by ANSYS-CFX shown in Fig. 15 at a given instant.

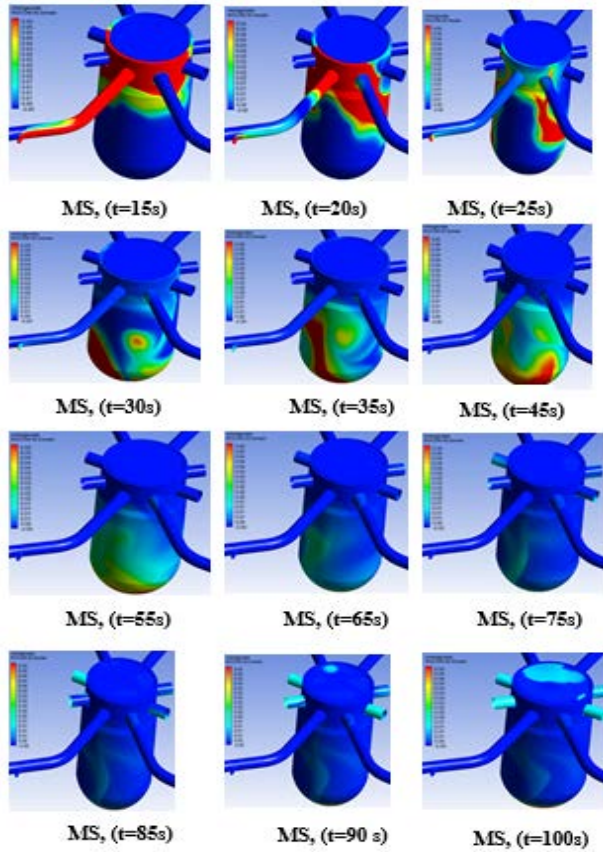


Fig. 10 Instantaneous mixing scalar distributions in ROCOM, from t =15s to 100s

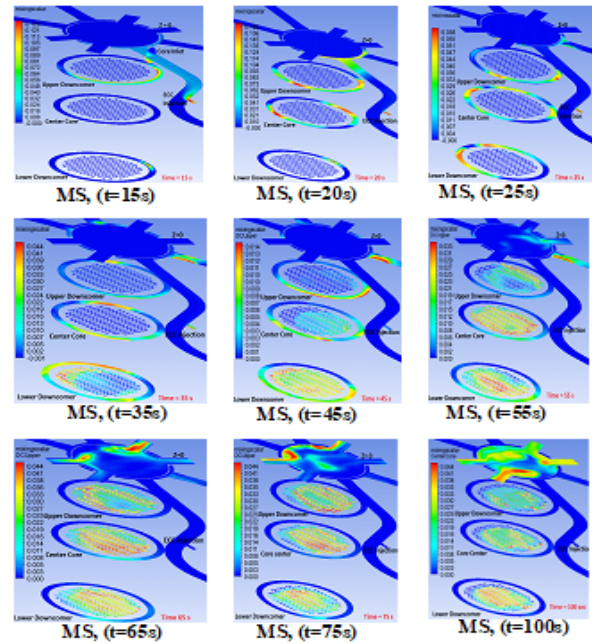


Fig. 13: Instantaneous mixing scalar distributions in ROCOM, from t =15s to 100s

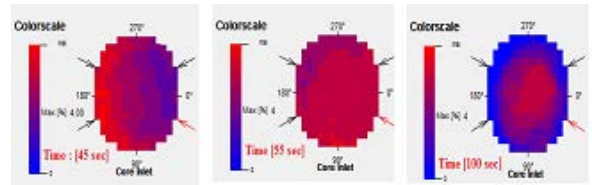


Fig 14 Snapshots of the core inlet distributions from time instants 45, 55, 100

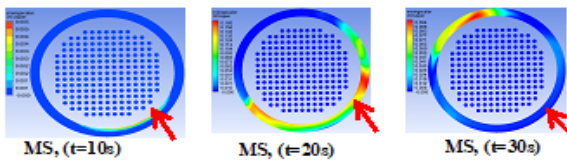


Fig. 11 CFX calculations of the Upper Downcomer distributions from time instants 10, 20, 30

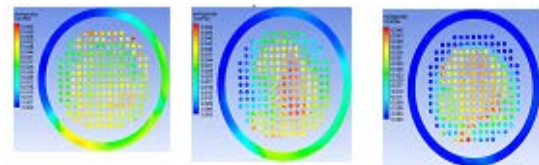


Fig 15 CFX calculations of the core inlet distributions from time instants 45, 55, 100s

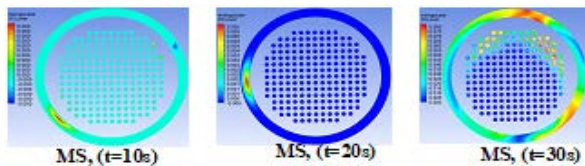


Fig 12 CFX calculations of the Lower Downcomer distributions from time instants 10s, 20s, 30s

## CONCLUSIONS

This paper shows results of test numerical simulations of ROCOM PTS experiments proposed by IAEA as an international benchmark kindly made available by Helmholtz Zentrum Dresden-Rossendorf, Dresden Institute

(HZDR)/Germany to perform detailed calculations of the proposed test.

Experimental data obtained for density difference between ECC and loop water inventory were compared to numerical predictions from the CFD software packages CFX in terms of tracer concentration space and time distribution both in the downcomer and at the core inlet.

Qualitatively, the formation of the perturbed region in the downcomer and in the lower plenum was correctly predicted.

## AUTHOR INFORMATION

### Corresponding Author

\*Surname Family name

Email address: [y.bouichaoui@cmb.dz](mailto:y.bouichaoui@cmb.dz)

## ACKNOWLEDGMENT

The authors express their thanks to Birine Nuclear Research Center for the supply of the Ansys CFX code license. This document contains experimental data that were produced in the ROCOM experimental facility at Helmholtz Zentrum Dresden-Rossendorf made available to us by the IAEA as part of the Co-ordinated Research Project (CRP-I31022). The authors of this article are grateful to the ROCOM test facility team and would

like to thank.

## REFERENCES

1. ANSYS CFX, 2016. ANSYS CFX User Manual.
2. T. Höne, Specifications of the PTS experiment D10M10, IAEA, FZDR, Rossendorf, Germany Benchmark, 2016
3. T. Höhne, S.Kliem, U. Bieder, Modeling of a buoyancy-driven flow experiment at the ROCOM test facility using the CFD-codes CFX-5 and TRIO, Nuclear Engineering and Design, 2006, 236 (12), 1309–1325
4. T. Höhne, S. Kliem, T. Sühnel, U. Rohde, , H.-M.. Prasser, F.-P.Weiss, Experiments at the mixing test facility ROCOM for benchmarking of CFD codes, Nuclear Engineering and Design, 2008, 238, 566–576
5. U.Rohde, S. Kliem, T. Höhne, R. Karlsson, et al., Fluid mixing and flow distribution in the reactor circuit: measurement data base, Nuclear Engineering and Design, 2005b, 235, 421–443
6. U. Grundmann, U. Rohde, Investigations on a boron dilution accident for a VVER-440 type reactor by the help of the code DYN3D, ANS Topical Meeting on Advances in Reactor Physics, Knoxville, 1994, 3, pp. 464471
7. H.-M. Prasser, J. Zschau, D. Peters, G. Pietzsch, W. Taubert, M. Trepte, Fast wire-mesh sensors for gas-liquid flows - visualisation with up to 10 000 frames per second. International Congress on Advanced Nuclear Power Plants (ICAPP) Hollywood Florida, USA, paper 1055.
8. H.-M. Prasser, A.Bottger, J.Zschau, A new electrode-mesh tomograph for gas-liquid flows, Flow Measurement and Instrumentation, 2001, 9, 111-119.
9. OECD, NEA/CSNI/R, Best Practice Guidelines for the use of CFD in Nuclear Reactor Safety Applications, 2007, p 166

---

## Author Index

Azizi, H., 20  
Belkaid, A., 116  
Benaskeur, N., 93  
Benkahila, K., 73  
Bessou, S., 10  
Benmahammed, K., 33  
Berrimi, F., 25  
Bezoubiri, F., 85  
Bouacid, S. S., 73, 93  
Bouaichaoui, Y., 116  
Boukabache, N., 54  
Boukerdja, L. 101, 108  
Cheikh, T., 90  
Diallo, M., 73  
Doukhi, O., 42  
Frahta, N., 33  
Guezzout, F., 42  
Hamdi, S., 29  
Hedli, R., 25  
Höhne, T., 116  
Kara-mohamed, C., 25  
Khalal, D. M., 20  
Kharfi, F., 73, 85, 93, 101  
Khelifi, R., 90  
Laghmara, Y., 42  
Lahlabou, M., 90  
Melouah, A., 54  
Merouani, H. F., 54  
Messalti, A. Z., 10  
Moussaoui, A., 29, 33, 60  
Osmani, N. 112  
Ousalah, M., 29  
Refoufi, S., 42  
Saadi, Y., 54  
Saidi, M., 29  
Sari, K., 73  
Titouche, W., 108  
Yahiaoui, M. L., 101  
Zidi, T., 85  
Zouaoui, H., 60



# First International Conference and School on Radiation Imaging (ICSRI-2021)

26-30 September 2021, Setif, Algeria

## 2<sup>nd</sup> Call for Papers

With great pleasure, the Organizing Committee announces the first call for abstract submission and school application for the 1<sup>st</sup> International Conference and School on Radiation Imaging (ICSRI-2021), to be held virtually at Ferhat Abbas-Setif1 University, in Setif, Algeria, from **26 to 30 September, 2021**. The conference is supported by the Algerian Atomic Energy Commission (COMENA).

The conference will include plenary sessions with conferences presented by eminent scientists, and orally and in poster sessions covering the different conference topics. The invited talks will be chosen to review recent advances in different areas covered by the conference.

The conference will be followed by a three

(3) days school for doctorate students and newly qualified academics and researchers in the field of radiation imaging and applications (25 participants max.). The program of the school will include lectures and practical sessions on three topics: 1. X-ray tomography, 2. Scanning Electron Microscopy (SEM), and 3. Artificial intelligence, Deep learning, and Image processing in Radiation Imaging.

The conference proceedings will be published in a special issue via an academic publisher.

The conference will be held virtually by videoconference while the school will be face-to-face in classroom and laboratory.

### Important Dates

- Registration and Abstract Submission Opening  
**February 1, 2021.**
- Abstract Submission Deadline  
**August 20, 2021.**
- Acceptance notification  
**September 1, 2021**

Secretary of the ICSRI-2021

Mobile: +213(0) 557363347

Phone: +213(0) 36620136

Fax: +213(0) 36620136

E-mail: icsri2020@univ-setif.dz

icsri2020@outlook.dz

Website:

<https://www.univ-setif.dz/OCS/ICSRI-2020/ICSRI2020>

## Conference Topics:

The 1<sup>st</sup> International Conference and School on Radiation Imaging (ICSRI-2021) will be held for the first time at the University of Sétif1 and will provide an international forum for discussing current research and developments in the domain of radiation imaging and applications that includes all kind of medical and industrial techniques.

Conference topics will include:

**Track 1:** Non-medical radiation imaging (X-ray,  $\gamma$ -ray, neutrons, electrons...)

**Track 2:** Radiation Imaging methods and systems development

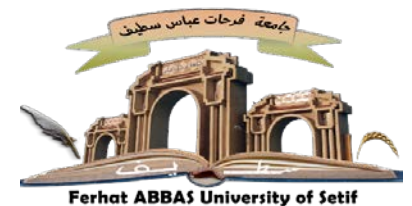
**Track 3:** Radiation Imaging Simulation and modeling

**Track 7:** Image Processing and Data Analysis Techniques

**Track 4:** Molecular Imaging and Nuclear Medicine (SPECT, SPECT/CT, PET/CT, PET/MR, etc)

**Track 5:** Medical Radiation Imaging (CT, Mammography, Fluoroscopy, MRI, US, etc)

**Track 6:** Advanced Imaging Methods (Image Reconstruction, Artificial Intelligence, Radiomics, Theragnostic, etc)



Ferhat ABBA University of Setif



UFAS.1 Lab.DAC



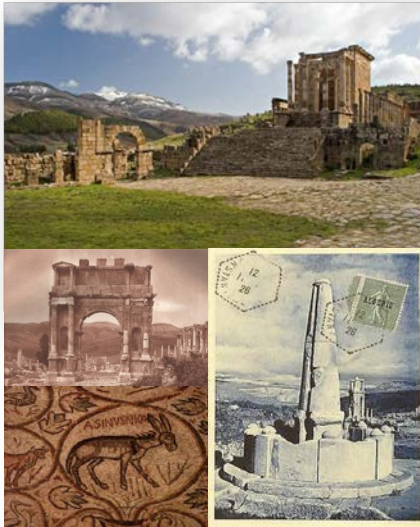
1st ICSRI

## Organizing Committee

**General Chair:** Pr. Fayçal Kharfi (UFAS1);

**Deputy Chair:** Dr. Layachi Boukerdja (CRNB);

**Committee:** Dr. Belkhiat Djamel Edine Chouaib (UFAS1), Pr. Azizi Hacene (UFAS1), Pr. Moussaoui Abdelouahab (UFAS1), Dr. Hamici Melia (UFAS1), Dr. Chouaba Self Eddine (UFAS1), Dr. Mosbah Ammar (UFAS1), Dr. Khelifi Djilali (COMENA), Mrs. Benachour Lilia (UFAS1)



Cuicul (Djémila- 55 km from Setif city-) was built at 900 meters of altitude during the 1st century AD as a Roman military garrison. It became a UNESCO World Heritage Site for its unique adaptation of Roman architecture to a mountain environment. Significant buildings in ancient Cuicul include a theatre, two fora, temples, basilicas, arches, streets, fountain and houses. The exceptionally well preserved ruins surround the forum of the Harsh, a large paved square with an entry marked by a majestic arch.

## Registration Fees

### • The registration fees include:

- o Lunch, banquet,
- o Conference proceedings and conference bag
- o City tour & Gala dinner
- o For the school participants diners are included in registration fees.

- Students are required to provide a copy of a valid ID that certifies their full-time student status.

### The registration fees are:

Regular scientists:	12000DZD 6000DZD	AI * ANI**
Doctorate students	8000DZD 4 000 DZD	AI ANI
Participant to the school	15000DZD 5000DZD	AI ANI
Industrial:	30 000 DZD	ANI

\*: Accommodation included, \*\*: Accommodation not included

## International Program Committee

- |  |   |
|--|---|
| Pr. Atef El-Taher (Al-Azhar Univ, Eg)            | Pr. Kharfi Fayçal (UFAS1, Dz)                           |
| Pr. Amrani Naima (UFAS1, Dz)                     | Pr. Maalej Nabil (KFUPM, KSA)                           |
| Pr. Azizi Hacene (UFAS1, Dz)                     | Pr. Maouche Djamel (UFAS1, Dz)                          |
| Pr. Babahenini Mohamed Chaouki (Biskra Univ, Dz) | Pr. Merouani Hayet Farida (Annaba Univ, Dz)             |
| Pr. Benamrane Nacéra (USTO, Dz)                  | Pr. Meziane Abdelkrim (CERIST, Dz)                      |
| Pr. Boucenna Ahmed (UFAS1, Dz)                   | Pr. Mimi Malika (Mostaghanem Univ, Dz)                  |
| Pr. Bouchareb Yassine (Sultan Qaboos Univ, Om)   | Pr. Mongy Tarek (ECAE, Eg)                              |
| Pr. Bouyoucef Salahedine (Bab El Oued CHU, Dz)   | Pr. Moussaoui Adelouahab (UFAS1, Dz)                    |
| Pr. Cherfa Yazid (SD-Blida Univ, Dz)             | Pr. Meriç Niyazi (Ankara University, Tr)                |
| Pr. Djedi Noureddine (Biskra Univ, Dz)           | Pr. Oussalah Mourad (Oulu University, Fi)               |
| Pr. Doghmane Noureddine (BM-Annaba Univ, Dz)     | Pr. Saint-Gregoire Jean-pierre (ASCA, Fr)               |
| Pr. Draï Redouane (CRTI, Dz)                     | Dr. Şahiner Eren (Ankara University, Tr)                |
| Pr. Guemmmaz Mohamed (UFAS1, Dz)                 | Pr. Schillinger Burkhard (TUM, De)                      |
| Pr. Hadid Abdenour (Oulu University, Fi)         | Pr. Seghier Mohamed (ECAE, Abu Dhabi, UAE)              |
| Pr. Hachouf Fella (Constantine Univ, Dz)         | Pr. Seghour Abdessalem (CRNA, Dz)                       |
| Pr. Hamidatou Algham Lylia (CRNB, Dz)            | Pr. Taleb-Ahmed Abdelmalik (Valencienns University, Fr) |
| Pr. Kambiz Shahnazi (PHIC, China)                | Pr. Zaidi Habib (Geneva University Hospital, Ch)        |
|  | Dr. Zidi Tahar (COMENA, DZ)                             |

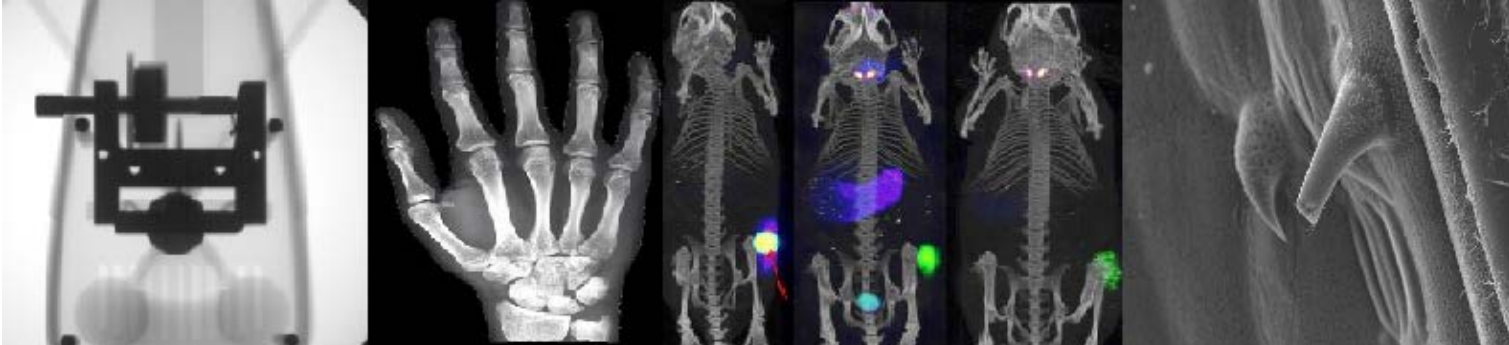
## Welcome to Setif

Sétif (the capital of Sétif Province) is a town in north-eastern Algeria, 1096 meters above sea level. It is the second most populated Province after the country's capital. The streets are tree-lined with a fountain and theater, giving the town French feel. A large amusement park is located in the center of the city where the city Zoo can be found. The ruins from Roman, Byzantine, Islamic and colonial eras adorn the city center.

The local economy deals both with trade and industries. The trade is mainly in grain and livestock from the surrounding region. Sétif has become the commercial center of a region where textiles are made, phosphates are mined and cereals grown. Other industries are woodworking, manufacture of carpets and metal handicrafts.

Sétif is connected by rail as well as the main national highway. The city has also an international airport.





The first International Conference and School on Radiation Imaging (ICSRI-2021) was held, for the first time, at the University of Sétif1. The conference has provided a forum to scientists, researchers and students to discuss current research and development in the field of radiation imaging and image processing. Due to the Covid-19 pandemic, the conference was organized via online mode from 26 to 27 September 2021. The Algerian Atomic Energy Commission (COMENA) has kindly supported the organization of the conference with its research centres (CRNB, CRNA and CRND). The conference has included plenary sessions with conferences presented by eminent scientists, and orally and in poster sessions covering the different conference topics. The invited talks have reviewed recent advances in radiation imaging. In total 43 interesting works were presented during the conference. A three days practical school for doctorate students and newly qualified academics and researchers was also organized for 25 participants. The program of the school included lectures and practical sessions on three main topics: 1) X-ray tomography, 2) Scanning Electron Microscopy (SEM), and 3) Image processing.

**General Chair:** Pr. Fayçal Kharfi, Ferhat Abbas-Setif1 University, Algeria

**Deputy Chair:** Dr. Layachi Boukerdja, Nuclear Research Centre of Birine, Algeria

**Committee Members:**

Dr. Djamel Edine Chouaib Belkhiat, Ferhat Abbas-Setif1 University, Algeria

Pr. Hacene Azizi, Ferhat Abbas-Setif1 University, Algeria

Pr. Adelouahab Moussaoui, Ferhat Abbas-Setif1 University, Algeria

Dr. Melia Hamici, Ferhat Abbas-Setif1 University, Algeria

Dr. Chouaba Seif Eddine, Ferhat Abbas-Setif1 University, Algeria

Dr. Ammar Mosbah (Ferhat Abbas-Setif1 University, Algeria)

Dr. Djilali Khelfi, Atomic Energy Commission, Algeria

Dr. Bilal Sari, Ferhat Abbas-Setif1 University, Algeria

Mrs. Lilia Benachour, Ferhat Abbas-Setif1 University, Algeria

